

Syracuse University

SURFACE

Dissertations - ALL

SURFACE

June 2018

Structure-Property Relationships in Novel Electrospun Composites for Advanced Applications

Melodie Lawton
Syracuse University

Follow this and additional works at: <https://surface.syr.edu/etd>



Part of the [Engineering Commons](#)

Recommended Citation

Lawton, Melodie, "Structure-Property Relationships in Novel Electrospun Composites for Advanced Applications" (2018). *Dissertations - ALL*. 891.

<https://surface.syr.edu/etd/891>

This Dissertation is brought to you for free and open access by the SURFACE at SURFACE. It has been accepted for inclusion in Dissertations - ALL by an authorized administrator of SURFACE. For more information, please contact surface@syr.edu.

Abstract

Active polymeric materials that alter shape in response to an external stimulus offer unique avenues for the design and study of dynamic structures. This research focused on developing elastomeric polymer composites with multiple functionalities by exploring the design and properties for various applications including controlled drug delivery and shape memory.

The first part of this dissertation describes the fabrication and characterization of a soft, elastomeric polymeric composite with inherent shape memory properties capable of localized, long-term tunable drug release. In Chapter 2, the fibers were loaded with a hydrophilic drug model, Rhodamine B, and embedded within a siloxane-based elastomeric matrix to form a composite, which is critical to regulating water transport from the environment to the fibers to liberate the drug. *In vitro* drug release studies were conducted in PBS under physiological conditions to evaluate the effect of drug concentration, fiber size, fiber crystallinity, drug loading and the addition of the crosslinked siloxane. The effect of the microstructural properties of the fibrous phase on drug release were explored and tuned through thermal treatment of the composite.

The findings from Chapter 2 were then applied to Chapter 3 for the development of a vascular graft with controlled and sustained nitric oxide (NO) releasing capabilities and suitable mechanical properties for the prevention of restenosis. To avoid the unwanted systemic side effects associated with a free radical such as NO, our approach delivered NO locally by supplying it from the vascular graft material. It was found that reducing the tin catalyst used for crosslinking the silicone constituent significantly improved cell viability, however, the NO interacted with the catalyst activity, affecting the silicone crosslinking reaction. The NO-releasing composite was demonstrated to be a strong chemottractant to endothelial cells.

The next part of this research focused on the development of a shape memory elastomeric composite featuring thermoplastic fibers imbibed by polyanhydride-based elastomer. It was determined in Chapter 4 that the polyanhydride elastomer is capable of dynamic covalent exchange reactions at elevated temperatures among the network chains that allowed near-complete reconfiguration of the permanent shape in the solid state. Together, these features were combined to create a shape memory elastomer capable of arbitrary programming of both temporary and permanent shapes. The degradation properties of this composite were then studied in Chapter 5 under *in vitro* conditions, where it was revealed that the degradation rate of the PAH matrix was strongly influenced by the selection of the composition of polymeric fibrous phase. The degradation of this composite was found to occur as a modified surface to bulk degradation, although the PAH by itself erodes heterogeneously. A hydrophilic model drug was incorporated in the fibrous phases and used to study the *in vitro* controlled release properties of these composites, where drug release correlated with the matrix degradation. The shape memory properties of these polyanhydride-based compositions were also examined.

Lastly, Chapter 6 investigated the design, fabrication, and characterization of a polymeric composite composed of oriented semicrystalline polymeric fibers embedded within a crosslinked epoxy matrix. This anisotropy enabled the construction of complex three dimensional geometries featuring latent mechanical programming. Rather than relying on specific molds to manipulate a new shape, this system capitalized on strain conditioning to influence a new structure. Additionally, we found that by compressing the oriented fibers of each ply during composite cure, the composites constructed from such plies exhibited actuation.

The shape memory composites studied in this dissertation demonstrated the potential be broadly applicable from drug releasing implants, tailorable degradability, and the self-assembly of complex shapes. Chapter 7 provides some recommendations for future directions.

STRUCTURE-PROPERTY RELATIONSHIPS IN NOVEL ELECTROSPUN COMPOSITES
FOR ADVANCED APPLICATIONS

by

Melodie I. Lawton

B.S., Polytechnic University, 2004

M.S., Rochester Institute of Technology, 2010

Dissertation

Submitted in partial fulfillment of the requirements for the degree of
Doctor of Philosophy in Bioengineering.

Syracuse University
June 2018

Copyright © Melodie Iris Lawton 2018
All Rights Reserved

*To Bruce and Kieran,
Thank you for your unconditional love and support.*

Acknowledgements

First and foremost, I would like to thank my advisor, Prof. Patrick T. Mather for his support and mentorship throughout my graduate career. His passion for research, teaching and pursuit of knowledge is inspirational and drives me to do more. I will always be grateful to Prof. Mather for the opportunities he has given me that have been essential to both my academic and personal growth.

I would also like to thank my committee members, Prof. Julie M. Hasenwinkel, Prof. Teng Zhang, Prof. James H. Henderson, Prof. Ian D. Hosein, and Prof. Zhen Ma for their support, insights and invaluable suggestions to my dissertation.

I am also thankful for the opportunity to engage in several collaborations throughout this research. Specifically I want to thank Dr. Vivian Gahtan of SUNY Upstate Medical, Dr. Devon A. Shipp of Clarkson University, and Dr. Joe Lenhart of the Army Research Laboratory. I would also like to especially thank Dr. Eric Finkelstein, Dr. Ariel Ash-Shakoor, and Dr. Wenbin Kuang, who have provided invaluable support.

I would like to also acknowledge the undergraduate mentees I have had the pleasure of working with: Julia Tumbic, Michael Robertson, Emily Mihalko, and Tackla S. Winston. Julia's riddles and pranks maintained the morale through some very long days. I also cannot thank Tackla enough for her tireless support, dedication and hard work, which is reflected in this thesis.

I wish to thank past and current members of the Mather Research Group, whom have been helpful in more ways than one. I am also thankful for all of the administrative support from Karen Low, Lynore De La Rosa, and Jason Markle. I would also like to give a special thanks to Supreme I. Lambert for keeping my computer running for the duration of my time at Syracuse University.

I would not have pursued my doctoral studies had it not been for the loving support and encouragement of my husband, who has been my foundation. I am thankful to Kieran for all of his patience, listening to my presentations, and always making laugh. And lastly, I would also like to thank my friends and family for their unwavering support through the years.

Table of Contents

List of Tables	xv
List of Schemes	xvii
List of Figures	xviii
Chapter 1: Introduction and Scope of Dissertation	1
1.1 Polymers and Composites	1
1.1.1 Polymers	1
1.1.2 Polymer Composites	3
1.2 Multi-Functional Materials	5
1.2.1 Biocompatibility for Biomedical Applications	6
1.2.2 Degradation	7
1.2.3 Controlled Drug Delivery	8
1.2.4 Shape Memory	10
1.3 Shape Memory Elastomeric Composite	11
1.4 Scope of Dissertation	12
1.5 References	14
Chapter 2: Shape Memory Elastomeric Composite with Controlled Drug Release of a Hydrophilic Drug Model	22
2.1 Synopsis	22
2.2 Introduction	22
2.3 Materials and Methods	24
2.3.1 Materials	24
2.3.2 Fabrication of RhB-Loaded Electrospun Fibers	25
2.3.3 Preparation of RhB-Loaded Fibrous Elastomeric Composite	25
2.3.4 Morphological Characterization	26
2.3.5 Thermal Characterization	27
2.3.6 <i>In Vitro</i> RhB Release	28
2.3.7 Thermal Treatment to Induce Crystallization	29

2.3.8 Mechanical Properties.....	29
2.4 Results.....	29
2.4.1 Fiber Characterization and Composite Morphology.....	29
2.4.2 <i>In Vitro</i> RhB Release from PCL fibers.....	30
2.4.3 Thermal Characterization and RhB Release.....	31
2.4.4 RhB Release from Thermally Treated Fiber Mats.....	31
2.4.5 RhB Release from PCL/PDMS Composites.....	32
2.4.6 RhB Release from Thermally Treated PCL/PDMS Composites.....	33
2.4.7 Mechanical Properties.....	34
2.5 Discussion.....	35
2.6 Conclusions.....	40
2.7 References.....	40
Chapter 3: Nitric Oxide Releasing Shape Memory Elastomeric Composite for Vascular Graft Applications.....	60
3.1 Synopsis.....	60
3.2 Introduction.....	60
3.3 Methods.....	66
3.3.1 Materials.....	66
3.3.2 Fabrication of NO-Loaded Electrospun Fibers.....	66
3.3.3 Preparation of NO-Loaded Fibrous Elastomeric Composite.....	67
3.3.4 Morphology.....	67
3.3.5 Thermal Characterization.....	68
3.3.6 <i>In Vitro</i> NO Release.....	68
3.3.7 Suture Retention Strength.....	69
3.3.8 Burst Pressure.....	70
3.3.9 Kink Resistance.....	71
3.3.10 Cytotoxicity.....	72
3.3.11 Mechanical Characterization.....	73
3.3.12 Cell Migration Assay.....	73
3.4 Results.....	75

3.4.1 Fabrication	75
3.4.2 Thermal Characterization.....	75
3.4.3 NO Release	76
3.4.4 Suture Retention.....	77
3.4.5 Burst Pressure	77
3.4.6 Kink Resistance	78
3.4.7 Cytotoxicity.....	79
3.4.8 Migration Assay.....	81
3.5 Discussion	82
3.6 Conclusions.....	91
3.7 Acknowledgements.....	92
3.8 References.....	92

Chapter 4: Anhydride-Based Reconfigurable Shape Memory Elastomeric Composite	124
4.1 Synopsis	124
4.2 Introduction.....	124
4.3 Methods.....	127
4.3.1 Materials	127
4.3.2 Thiol-ene Elastomer Syntheses.....	127
4.3.3 Polycaprolactone Polyurethane Synthesis	128
4.3.4 Electrospinning	128
4.3.5 PAH/PCL PU Composite Fabrication	128
4.3.6 Morphology.....	129
4.3.7 Differential Scanning Calorimetry.....	129
4.3.8 Thermomechanical Characterization	129
4.3.9 Tensile Testing.....	130
4.3.10 Stress Relaxation.....	130
4.3.11 Qualitative Shape Memory and Reconfiguration Testing	131
4.3.12 Quantitative Shape Memory and Reconfiguration Testing	131
4.4 Results.....	132

4.4.1 Thiol-ene Elastomer Synthesis	132
4.4.2 PAH/PCL-PU Composite Fabrication and Morphology	133
4.4.3 Thermal Properties.....	133
4.4.4 Thermomechanical Properties	134
4.4.5 Mechanical Properties.....	134
4.4.6 Stress Relaxation.....	134
4.4.7 Qualitative Shape Reconfiguration	135
4.4.8 Qualitative Shape Memory and Reconfiguration	135
4.4.9 Quantitative Shape Memory and Reconfiguration	136
4.5 Discussion	137
4.6 Conclusions.....	140
4.7 Acknowledgements.....	141
4.8 References.....	142

**Chapter 5: Biodegradable Shape Memory Elastomeric Composites with
Controlled Release of a Model Drug158**

5.1. Synopsis	158
5.2. Introduction.....	158
5.3. Methods.....	164
5.3.1 Materials	164
5.3.2 Electrospinning of PCL.....	164
5.3.3 Electrospinning and Thermal Treatment of PVAc	165
5.3.4 PAH Monomer Preparation	165
5.3.5 PCL/PAH Composite Fabrication.....	165
5.3.6 PVAc/PAH Composite Fabrication	165
5.3.7 Thermal Characterization.....	166
5.3.8 <i>In Vitro</i> Degradation	167
5.3.9 Mechanical Properties.....	168
5.3.10 Morphology.....	168
5.3.11 Qualitative Shape Memory	169
5.3.12 Quantitative Shape Memory	169

5.3.13 Fixed Shape during Degradation	170
5.3.14 <i>In Vitro</i> RhB Release	170
5.4. Results.....	171
5.4.1 Fabrication of PAH-based composites.....	171
5.4.2 <i>In Vitro</i> Degradation Mass Loss	173
5.4.3 Morphology.....	174
5.4.4 Thermal Properties.....	175
5.4.5 Tensile Mechanical Properties.....	177
5.4.6 <i>In Vitro</i> Drug Release	177
5.4.7 Shape Memory.....	178
5.4.8 Fixed Shape Preservation during Degradation	179
5.5. Discussion.....	180
5.6. Conclusions.....	186
5.7 Acknowledgements.....	187
5.8 References.....	187

Chapter 6: Latent Mechanical Programming of a Shape Memory Composite with Reversible Anisotropic Actuation.....	217
6.1 Synopsis.....	217
6.2 Introduction.....	218
6.3 Methods.....	220
6.3.1 Materials	220
6.3.2 Electrospinning	220
6.3.3 Anisotropic Composite Fabrication	221
6.3.4 Thermal Analysis	222
6.3.5 Morphology.....	222
6.3.6 Thermomechanical Characterization	223
6.3.7 Quantitative Triple Shape Memory	223
6.3.8 Latent Triggering of Mechanically Programmed, Anisotropic Shape Change.....	225
6.3.9 Reversible Anisotropic Actuation.....	226
6.4 Results.....	226

6.4.1 Composite Fabrication and Morphology	226
6.4.2 Thermal Analysis	227
6.4.3 Thermomechanical Properties	228
6.4.4 Quantitative Triple Shape Memory	228
6.4.5 Latent Anisotropic Shape Change	229
6.4.6 Reversible Anisotropic Actuation.....	230
6.5 Discussion	233
6.6 Conclusions.....	238
6.7 References.....	239
Chapter 7: Conclusions & Future Work	263
7.1 Overall Conclusions.....	263
7.2 Future Directions	266
7.2.1 Shape Memory Elastomeric Composite with Controlled Drug Release of a Hydrophilic Drug Model.....	266
7.2.2 Nitric Oxide Releasing Shape Memory Elastomeric Composite for Vascular Graft Applications.....	268
7.2.3 Anhydride-Based Reconfigurable Shape Memory Elastomeric Composite	269
7.2.4 Biodegradable Shape Memory Elastomeric Composites with Controlled Model Drug Release of a Model Drug.....	270
7.2.5 Latent Mechanical Programming of a Shape Memory Composite with Reversible Anisotropic Actuation	272
7.3 References.....	273
Appendix 1: Properties and Ballistic Performance of Epoxy-Based Thermoset-Thermoplastic Composites	281
Vita	311

List of Tables

- Table 2-1: DSC thermograms of various fiber diameters of electrospun PCL with 0.5 wt % RhB.
- Table 2-2: Summary of tensile mechanical properties of the PCL/PDMS composite.
- Table 3-1: Thermal properties of the NO releasing PCL/PDMS composite and fibrous components at two NO donor concentrations.
- Table 3-2: Linear regression parameters of NO release profiles used to calculate the flux..
- Table 3-3: Average suture retention strength for the composite at three different tensile speeds.
- Table 3-4: Summary of mechanical properties of PDMS crosslinked using different DBTDL concentrations.
- Table 4-1: Summary of mechanical properties for the PAH/PCL PU elastomeric composite.
- Table 5-1: Summary of tensile engineering stress-strain curves for the PAH/PCL and PAH/PVAc composites and individual components.
- Table 5-2: Fraction of PCL in the PCL/PAH composite as a function of degradation time.
- Table 5-3: Fraction of PVAc in the composite as a function of degradation time.
- Table 5-4: Mechanical properties of PAH/PCL composite after different degradation times.
- Table 5-5: Mechanical properties of PAH/PVAc composite after different degradation times.
- Table 5-6: One way shape memory fixing and recovery ratios for the PVAc/PAH composite.

Table 6-1: Thermal transitions of the different crosslinked epoxy formulations, the epoxy/PCL composite and the electrospun PCL component. All measurements were taken from the second heating cycle. *NM* denotes not measured and *N/A* means not applicable.

Table 6-2: Fixing and recovery ratios for the triple shape memory quantification of the epoxy/PCL composite as single-ply with fibers oriented parallel to the uniaxial strain (0°) or perpendicular to the uniaxial strain (90°), and the cross-ply(0) bilayer composite.

Table 6-3: Thermal characterizations for epoxy/PCL composites fabricated using different compression factors. *NM* denotes not measured and *N/A* means not applicable.

List of Schemes

- Scheme 2-1: Chemical structures of (A) poly(ϵ -caprolactone) and (B) Rhodamine B, and (C) synthesis of cross-linked silanol-terminated PDMS.
- Scheme 3-1: Decomposition of diethylenetriamine nitric oxide donor (DETA-NO) upon exposure to water.
- Scheme 4-1: (A) (Top to bottom) Synthesis of PAH- and TMPDAE-based networks, (B) Hard-block-free PCL PU-based polyurethane, and (C) Preparation of anhydride-based reconfigurable shape memory elastomeric composite with representative scanning electron microscopy images (SEM) of (D) as electrospun PCL PU, and (E) the surface of the PAH/PCL PU composite after curing. The scale bar represents 50 μm for both SEM micrographs
- Scheme 4-2: Dynamic covalent exchange activated thermally and involving rearrangement of adjacent anhydride groups.
- Scheme 5-1: (A) Synthesis of polyanhydride elastomer, and chemical structures of (B) poly(ϵ -caprolactone) and (C) poly(vinyl acetate)..
- Scheme 6-1: The chemical structures of the epoxy components and PCL used to fabricate the PCL/epoxy composite.
- Scheme 6-2: Fabrication of the bilayer anisotropic epoxy-PCL composite by (A) first electrospinning aligned PCL fibers followed by (B) infiltration of aligned PCL fiber mats in the cross-ply(0) orientation.
- Scheme 6-3: Method for controlling clamping force by varying the spacer thickness during epoxy/PCL composite fabrication.

Scheme 6-4: Various cutting angles (top row) of rectangular samples (bottom row) used to mechanically program 3D shapes. The blue lines correspond to the fiber direction of the top layer and the red lines were maintained on the bottom layer.

List of Figures

- Figure 1-1: Example of erosion mechanisms in degradable polymers where (A) bulk (homogenous) erosion occurs throughout the polymer and (B) surface (heterogeneous) erosion degrades at the surface, while the sample maintains its shape and properties but decreases in size.
- Figure 1-2: One way shape memory depicted (A) quantitatively and (B) morphologically.
- Figure 2-1: Scanning electron microscopy micrographs of PCL fibers containing 0.5 wt % RhB with an average fiber diameter of A) $0.23 \mu\text{m} \pm 0.13 \mu\text{m}$, B) $0.41 \mu\text{m} \pm 0.23 \mu\text{m}$, C) $0.50 \mu\text{m} \pm 0.24 \mu\text{m}$, D) $0.61 \mu\text{m} \pm 0.34 \mu\text{m}$, E) $0.91 \mu\text{m} \pm 0.40 \mu\text{m}$, and F) $1.29 \mu\text{m} \pm 0.63 \mu\text{m}$. Fiber diameter are reported as mean \pm standard deviation for $n > 250$ fibers ($p < 0.05$).
- Figure 2-2: Optical microscopy at two magnifications of 2 % RhB/PCL fibers melted at 80 °C. Letters denote areas of light (L) and dark (D) pink regions indicating low and high concentrations of RhB. White regions are air pockets formed during melting, as marked by an asterisk.
- Figure 2-3: Representative scanning electron microscopy micrographs of RhB/PCL-PDMS composite showing the (A) surface and (B) cross-section
- Figure 2-4: A) Cumulative RhB release from electrospun 0.5 % RhB/PCL fibers of various diameters and (B) a comparison of the cumulative RhB release at 48 h with fiber morphology

- Figure 2-5: First heat DSC thermograms of various fiber diameters of electrospun PCL containing 0.5% RhB in comparison to amount of RhB released at 48 h.
- Figure 2-6: (A) Controlled RhB release results and (B) thermal characterization comparing drug release performance following annealing of two concentrations of RhB electrospun in PCL fibers.
- Figure 2-7: Comparison of RhB release from 0.5 % RhB/PCL (fibers only) and 0.5 % RhB/PCL/PDMS (composite) in PBS at 37 °C for samples fabricated from the same parent fiber mat.
- Figure 2-8: Representative samples of (A) 1.5 % RhB/PCL fiber mat and (B) 1.5 % RhB/PCL/PDMS composite after several time points of drug release in PBS at 37 °C. Color loss is due to the release of RhB from the fibers into the surrounding media.
- Figure 2-9: (A) Controlled RhB release results and the (B) corresponding thermal characterizations comparing drug release performance following thermal treatment of the PCL/PDMS composite.
- Figure 2-10: Tensile stress-strain curves for the PCL/PDMS composite at various fiber fraction values.
- Figure 2-11: Phase separation between hydrophilic model drug Rhodamine B within the PCL fiber.
- Figure 2-12: Thermogravimetric characterizations of the (i) 0.5 % RhB/PCL, (ii) 1.5 % RhB/PCL, (iii) PDMS, and (iv) 1.5 % RhB/PCL/PDMS composite.

Figure 3-1: SEM micrographs of electrospun DETA-NO loaded PCL fibers showing the (A) 0.5 % DETA-NO/PCL fiber mat, (B) the 1.5 % DETA-NO/PCL fiber mat, (C) the fiber mat surface following following PDMS infiltration,(D) the cross-section of the DETA-NO/PCL/PDMS composite, (E) the composite in tubular form, and (F) the cross-section of the tubular composite. The micrographs in C - D are shown for 0.5% DETA-NO donor concentration.

Figure 3-2: DSC thermograms comparing melting transitions of NO releasing PCL/PDMS composite and fibrous components at two NO donor concentrations. Solid lines denote second heating cycle and dashed lines denote first heating cycle.

Figure 3-3: (A) Overall cumulative NO profiles comparing electrospun fibers and as fibers embedded in the PDMS matrix for two NO donor concentrations. The plots in (B) and (C) are magnified views of (A).

Figure 3-4: (A) Cumulative NO release of 0.5% DETA-NO/PCL/PDMS composite divided into five stages. A magnified view of the release pattern in stages I and II are shown in (B). A linear regression (dashed line) was used to calculate the flux in each of NO release phase.

Figure 3-5: (A) Cumulative NO release of 1.5% DETA-NO/PCL/PDMS composite divided into five stages. A magnified view of the release pattern in stages I and II are shown in (B). A linear regression (dashed line) was used to calculate the flux in each of NO release phase.

- Figure 3-6: (A) Suture retention testing set-up and (B) representative force-displacement plot for the composite using a tensile speed of $50 \text{ mm} \cdot \text{min}^{-1}$. The suture retention strength is denoted by an asterisk.
- Figure 3-7: Average suture retention strength for the composite at three different tensile speeds.
- Figure 3-8: (A) Burst pressure testing set-up and (B) representative images of sample dilation and failure.
- Figure 3-9: Results of burst pressure testing showing (A) representative pressure-diameter and hoop stress displacement curves and (B) representative sample following high pressure burst failure. The arrow indicates the area where point of failure occurred.
- Figure 3-10: Kink-free bends for surgical placement using thermal shape programming feature showing (A) the bend radius measurement and the (B) supporting substrate used to fix a looped shape. Representative fixed shapes are shown for the 6 mm graft in (C) and (D), with respective recovered shapes in (E) and (F). Representative fixed shapes for the 3 mm graft are shown in (G) and (H), with respective recovered shapes in (I) and (J). The wall thickness classification is denoted on the photos.
- Figure 3-11: Results of kink resistance testing demonstrating (A) the critical curvature, which was the curvature value limit before a kink will occur with increased bending, and (B) shape fixing ratio dependence on graft tube wall thickness and diameter.

Figure 3-12: Cell viability of L929 fibroblast cells cultured in extracts from (A) the NO releasing PCL/PDMS composite and its components at different extraction times, (B) the PDMS elastomer with various catalyst concentrations, (C) the composite, both with and without NO donor, fabricated using different PDMS catalyst concentrations (% w/w), and (D) varying concentrations of the NO donor DETA-NO in cell culture media. The results for (B) – (D) were measured following 24 h of incubation in media. The results of the doped composite in (C) containing 0.1 % DBTDL could not be tested due to NO donor interference with PDMS crosslinking. All testing was conducted in triplicate. Dashed line indicates acceptable cytocompatibility level of 70 %.

Figure 3-13: Mechanical properties of crosslinked PDMS using different concentrations of DBTDL catalyst showing (A) representative engineering tensile stress-strain curves, (B) Young's moduli, and (C) strain-to-failure.

Figure 3-14: Effect of NO release from the 0.5 % DETA-NO/PCL/PDMS composite on BAEC and BSMC migration. Comparisons were made to the positive controls (media and DETA-NO in media) and negative control (serum-reduce media). The data shown are the mean and standard deviation of three experiments.

Figure 3-15: Representative micrographs of stained BAECs on the lower surface of the Transwell membrane taken with fluorescence microscope (10 X magnification). The cells visible on this surface are a result of migration over 48 h. The various conditions are (A) serum-reduced media, (B) media only, (C) 10 μ M DETA-NO in media, (D) PCL/PDMS, and (E) 0.5 % DETA-NO/PCL/PDMS composite. The cells were stained for nuclei (green) and cytoskeleton (red), and the arrow points to the open pores on the Transwell membrane. The scale bar represents 50 μ m.

Figure 3-16: Representative micrographs of stained BSMCs on the lower surface of the Transwell membrane taken with fluorescence microscope (10 X magnification). The cells visible on this surface are a result of migration over 48 h. The various conditions are (A) serum-reduced media, (B) media only, (C) DETANO in media, (D) PCL/PDMS, and (E) DETANO/PCL/PDMS composite. The cells were stained for nuclei (green) and cytoskeleton (red), and the arrow points to the open pores on the Transwell membrane. The scale bar represents 50 μ m.

Figure 4-1: (A) Differential scanning calorimetry (DSC) second heating curves, and (B) first cooling curves of (i) neat PAH elastomer, (ii) PAH/PCL PU composite, and (iii) electrospun PCL PU.

Figure 4-2: Dynamic mechanical analysis (DMA) (A) storage modulus curves and (B) loss modulus curves of (i) neat PAH elastomer, (ii) PAH/PCL PU composite, and (iii) electrospun PCL PU.

- Figure 4-3: (A) Differential scanning calorimetry first cooling and second heating results and (B) dynamic mechanical analysis of pTMPDAE-based elastomer.
- Figure 4-4: Representative engineering stress-strain curves of (i) PAH elastomer, (ii) the PAH-PCL PU composite, and (iii) electrospun PCL PU, where the composite and its components are shown in (A). More details of the PAH elastomer and the composite are shown in (B).
- Figure 4-5: Shape reconfiguration as measured by stress relaxation. The relaxation modulus versus time are shown for: (A) varying the network composition at 80 °C for (i) PAH and (ii) TMPDAE, and (B) varying reconfiguration temperatures for the PAH elastomer.
- Figure 4-6: Shape reconfiguration response of elastomers synthesized using: (a) anhydride (PAH) and (b) TMPDAE diene monomers, in the flat configuration (left) and resulting shape following shape reconfiguration at 80 °C (right).
- Figure 4-7: Shape memory and reconfiguration behavior of PAH/PCL PU polyurethane composite. (A) Images of qualitative study demonstrating one way shape memory where (i) a temporary shape is fixed and then (ii) recovered to the original shape, followed by (iii) reconfiguration of the permanent shape; (iv) the reconfigured shape does not recover to the original geometry. (B) Quantitative shape memory and shape reconfiguration cycles for the PAH/PCL PU composite

- Figure 4-8: Shape memory stress-temperature-strain plot for PAH/PCL PU composite.
- Figure 4-9: Stress relaxation results for PAH network showing (A) peak modulus dependence on temperature and (B) Arrhenius dependence of PAH relaxation time with associated activation energy of 7.7 kcal/mol.
- Figure 4-10: Isothermal tensile storage modulus of the PAH elastomer as temperature is increased in a stepwise manner.
- Figure 5-1: Effect of thermal treatment implemented to minimize shrinkage of electrospun PVAc fibers prior to composite fabrication. (A) The resulting composite (right) when no thermal treatment or PAH pre-cure is used in comparison to its original geometry (left) (B) Pre-curing the PAH monomer enabled the PVAc to maintain its fibrous phase within the composite, however significant shrinkage occurred (right). Distinct regions of excess PAH denoted by the blue arrow. (C) Comparison of the effect of heat treatment on electrospun PVAc following hydration in DI water revealed significantly less shrinkage for samples previously treated. The foil substrate shows the original size of the fiber mat. (D) The addition of a heat treatment and pre-cured PAH resulted in a composite with minimal shrinkage and conservation of its original geometry. The excess PAH is trimmed as part of the fabrication process.

Figure 5-2: (A) Thermal and (B) thermomechanical characterizations of the (i) PAH elastomer, (ii) electrospun PVAc (heat treated), (iii) PVAc/PAH composite (iv) PCL/PAH composite, (v) electrospun PCL, and (vi) electrospun PVAc (untreated).

Figure 5-3: Scanning electron microscopy micrographs of (A) electrospun PCL and (B) electrospun PVAc following thermal treatment. The surface and cross-section of PAH/PCL are shown in (C) and (D). The surface and cross-section of PAH/PVAc are shown in (E) and (F).

Figure 5-4 Representative tensile engineering stress-strain curves of both the composite and individual components for PAH/PCL and PAH/PVAc composites showing (A) the strain-to-failures and (B) the linear elastic regions for (i) electrospun PVAc (heat treated), (ii) electrospun PVAc (untreated), (iii) electrospun PCL, (iv) PCL/PAH composite, (v) PAH, and (vi) PVAc/PAH composite.

Figure 5-5 Mass loss during *in vitro* degradation in PBS at 37 °C for the PAH/PCL and PAH/PVAc composites.

Figure 5-6: Morphological changes during degradation of the PCL/PAH composite in PBS at 37 °C at the A) surface and B) cross-section, revealed using scanning electron microscopy (SEM).

Figure 5-7: Morphological changes during degradation of the PVAc/PAH composite in PBS at 37 °C at the A) surface and B) cross-section, revealed using scanning electron microscopy (SEM).

- Figure 5-8: Thermal properties of the PCL/PAH composite during degradation. Dotted line indicates crystallization temperature for electrospun PCL.
- Figure 5-9: Fraction of PCL in the PCL/PAH composite as a function of degradation time.
- Figure 5-10: Thermal characterization by DSC of the PVAc/PAH composite following different degradation times. The dotted lines denote the glass transitions for PAH and PVAc.
- Figure 5-11: Evolution of the glass transition temperature of the PVAc component of the PVAc/PAH composite at different stages of PAH degradation.
- Figure 5-12: Comparison of PCL and PVAc content during degradation of the PCL/PAH and PVAc/PAH composites, respectively. The fiber composition was calculated based on the relative melting or glass transition temperatures as determined by DSC.
- Figure 5-13: Comparison of PCL and PVAc content during degradation of the PCL/PAH and PVAc/PAH composites, respectively. The fiber composition was calculated based on the relative melting or glass transition temperatures as determined by DSC.
- Figure 5-14: Representative engineering stress-strain plots of PVAc/PAH at various degradation points of (i) as fabricated, $t = 0$, (ii) 10 h, (iii) 48 h, (iv) PAH for reference, and (v) as-fabricated heat-treated electrospun PVAc for reference.

- Figure 5-15: *In vitro* release of hydrophilic model drug Rhodamine B from the PCL/PAH and PVAc/PAH composites with comparisons to (A) Rhodamine B release from fibers without the PAH matrix, and with mass loss results in (B) and (C).
- Figure 5-16: Qualitative demonstration of one way shape memory of the PVAc/PAH composite.
- Figure 5-17: Shape memory stress-temperature-strain plot for the PVAc/PAH composite.
- Figure 5-18: Preservation of arbitrarily deformed shapes during *in vitro* degradation of the PCL/PAH composite in PBS at 37 °C.
- Figure 6-1: Representative SEM micrographs of the (A) aligned electrospun PCL fibers, (B) PCL/epoxy composite surface, (C) cross-section of the single-ply composite with fibers aligned longitudinally (0° to long dimension), (D) cross-section of the single-ply composite with fibers aligned perpendicular (90° to long dimension), and (E) cross-section of the cross-ply bilayer composite. The micrographs in (B) – (E) were visualized following removal of the PCL phase.
- Figure 6-2: DSC thermograms of (A) the crosslinked epoxy using different relative weight fractions of DGEBA and NDGE, and (B) the PCL/epoxy composite and its individual components.
- Figure 6-3: Thermomechanical characterization of the D41N59D230 epoxy/PCL cross-ply(0) composite fabricated using a compression factor of 1.1 showing (A) the storage modulus and (B) the loss modulus and tan delta.

- Figure 6-4: Triple shape memory quantification of the epoxy/PCL composite (A) single-ply with fibers oriented parallel to the uniaxial strain (0°), (B) single-ply with fibers oriented perpendicular to the uniaxial strain (90°), and (C) the cross-ply(0) bilayer composite. The annotations denote the first fixed shape (F1), second fixed shape (F2) and the recovered shape (R).
- Figure 6-5: Example of mechanical shape programming sequence with shape recovery (shown for the cross-ply(0) composite), where 0° refers to the layer containing longitudinally oriented fibers.
- Figure 6-6: Various fiber orientations between the top and bottom fibrous phases within the composite and resulting shapes. (Row A) original shape with fiber orientation depiction (blue = top layer/red = bottom layer) (Row B) and original shapes (Row C) temporary fixed shape
- Figure 6-7: Effect of strain during mechanical shape programming on the cross-ply(0) composite.
- Figure 6-8: DSC thermograms for epoxy/PCL cross-ply(0) composites fabricated using different compression factors.
- Figure 6-9: Upon increasing the compression factor (CF) of the fiber mats within the composites, the samples begin to immediately change shape when strips are cut from the parent composite batch. The fiber orientation is depicted such that the blue vertical lines are the top layer and the red horizontal lines indicate the bottom layer).

- Figure 6-10: Stress-free strain of single-ply oriented epoxy/PCL composites in response to heating and cooling for fiber alignment oriented (A) longitudinal and (B) perpendicular to the long axis.
- Figure 6-11: Actuation behavior of the epoxy/PCL bilayer composites upon thermal cycling with the cross-ply(0) sample showing the (A) testing set-up and (B) magnification of the samples during actuation.
- Figure 6-12: Actuation behavior of the epoxy/PCL bilayer composites upon thermal cycling with the cross-ply(45) sample showing the (A) testing set-up and (B) magnification of the samples during actuation.
- Figure 6-13: (A) Curvature of the cross-ply(0) bilayer epoxy/PCL composite after 10 consecutive actuation cycles for the shape at room temperature (cooled) and the shape upon heating. (B) Representative photos of the shape change under cooling (left column) and heating (right column) conditions. The curvature of the heated activated shape was opposite to that of the cooled shape, as indicated by the negative curvature value.
- Figure 7-1: Cumulative release of RhB from PCL/Pellethane composite. RhB diffusion originated from the PCL matrix.
- Figure 7-2: Water uptake comparison between electrospun Pellethane and crosslinked silanol-terminated PDMS film following 24 h immersion in water. Sample size of three per group was used. The water uptake was calculated by dividing the difference in the mass of the wet and dried samples by the mass of the dried sample.

Figure 7-3: Results of hemolysis assay showing (A) photos of human blood clot formation over time comparing blood exposure to no samples (blood alone), the PCL/PDMS composite without drug, and the DETA-NO/PCL/PDMS composite, and (B) lysate absorbance values from the clotting assay.

Figure 7-4: Feasibility of remolding PAH-based materials following grinding. (A) A crosslinked PAH film is cut into small cubes that are then compression molded into a single object, and (B) the PAH/PCL composite is grinded and then compression molded into a film.

Figure 7-5: Healing potential of the PAH/PCL composite. A rectangular sample is fragmented into two pieces and then repaired back into a single piece following applying heat and pressure to the fractured surfaces under constant contact.

Figure 7-6: Sequence for attaining degradation-induced shape recovery for the electrospun Pellethane fibers imbibed in PAH composite showing: (A) original shape, (B) arbitrarily thermally programmed shape, (C) degradation of the newly shaped composite (D) recovery of the original shape following PAH matrix degradation, and (E) retention of fibrous morphology following degradation of the PAH matrix.

Figure 7-7: Time lapsed mechanically programmed displacement of an object by the anisotropic PCL/epoxy composed of oriented PCL arranged orthogonally. A rectangular strip was topped with a glass cover slip and placed on a hot plate at 45 °C. As the mechanically programmed shape was thermally activated, the sample began to curl and lift the glass slide in under 30 s. The schematic above demonstrates the thermally activated sequence of free-standing object displacement by the sample shown below.

Chapter 1

Introduction and Scope of Dissertation

1.1 Polymers and Composites

1.1.1 Polymers

Polymers are non-metallic macromolecules composed of smaller repeating units that form long molecular chains resulting in characteristically high molecular weights.¹ One may be more familiar with polymers in its final, processed form, colloquially known as plastics. Considering that plastics, and therefore polymers, affect daily life, these materials encompass all industries including automotive, textiles, food packaging, electronics, and biomedical, and are also produced naturally as part of hair, spider silk, starch, and even DNA. Accordingly, polymers comprise a significant subject of research.

Polymers are either semi-crystalline or amorphous, a classification that forecasts material design and processability. Amorphous polymers do not possess crystallizable regions in their molecular arrangement, which is principally due to structural hindrances of the atoms along the polymer backbone, or the presence of irregularly ordered side groups that can lead to a randomized molecular organization, thus preventing crystallization. Consequently, amorphous polymers do not exhibit a melting transition temperature, but instead a glass transition temperature (T_g), above which the onset of coordinated chain motion softens the polymer, resulting in rubbery to viscous flow behavior; below T_g the polymer vitrifies.² Crystallization of polymers occurs when the polymer chains are packed favorably to produce distinct oriented, folded lamellae, such as when cooling a polymer from a melt through the melting transition temperature (T_m) to below the crystallization transition temperature (T_c). Given that polymer

chains are inherently long, any misalignment of the chain folding prevents this regular packing, resulting easily into intermediary amorphous regions. In semicrystalline polymers, these regions tend to exist between the crystallites and will also exhibit a T_g , in addition to T_m and T_c . Intrinsically, the motion of the polymer chains, such as those produced by thermal or mechanical stimuli, greatly influence crystallization, and thus ultimately the mechanical behavior, opacity, and thermal properties. While crystallization generally occurs during cooling, it may also result from solvent evaporation or tensile strain and is further affected by the rate of each these variables as well as its molecular architecture.^{3,4}

Polymers are also classified as either thermoplastic or thermoset, based on their ability to be processed thermally. Thermoplastics are those polymers, either amorphous or semi-crystalline, that can reversibly melt and re-solidify. These types of polymers can also completely dissolve in a compatible solvent, which is useful for cast molding or electrospinning. Typical thermoplastics include linear polymers or those with simple branching such as polyethylene, polypropylene, and polystyrene. Poly(ϵ -caprolactone) is another example of a semicrystalline thermoplastic, whereas poly(vinyl acetate) is an amorphous thermoplastic, both of which are studied in more detail in this work. Thermosets are distinct from thermoplastics in that these polymers cannot reversibly become a liquid once solidified following the cross-linking reaction of their polymer or monomer precursors, which typically originate in liquid form. Unlike thermoplastics, thermosets will not dissolve in a compatible solvent, but instead will swell to a maximum expansion governed by the extension of its cross-links. Examples are vulcanized rubbers, polyimides, epoxies, and silicones, the latter two, which are studied and discussed in further detail in this dissertation.

In any design of a polymeric material, it is important to consider the variables that affect the processability, manufacturability, and final properties of the material. As mentioned above, the thermal properties such as the glass, melting and crystallization transition temperatures will influence the conditions which will enable microstructural as well as macrostructural changes to the polymer, which are critical for determining molding or end-use parameters. Other thermal considerations include the temperature at which the polymer degrades, which can lead to irreversible damage of the primary covalent bonds and cause failure. In processing the polymer, solvent selection is dependent on the chemical properties and molecular weight of the polymer, where it is often followed that “like dissolves like”, referring to the similar polarities between the polymer and the solvent. Molecular factors include molecular weight and hydrophilicity/hydrophobicity. If different polymers are combined at the molecular level, the miscibility and resulting morphology are important features to investigate. Other design parameters to consider are the mechanical properties such as the Young’s modulus, storage and loss moduli, and strain-to-failure, which indicate the elasticity and structural capacities, and are also affected by molecular weight, cross-link density, microstructure and morphology.

1.1.2 Polymer Composites

Composites are a class of engineering materials fabricated from a combination of other chemically or physically distinct materials such as the coupling of metals, polymers, and/or ceramics.^{5,6} Akin to polymers, composites are found in all industries. Some familiar examples are the combination of cellulose fibers and lignin that produce wood, and the dispersion of gravel and sand in cement that becomes concrete. Composites are especially advantageous when a single material cannot meet specific design criteria or when designing such a material requires

costly and complicated customization. The goal of composite material development is to achieve a set of properties that each material alone cannot provide, offering additional degrees of freedom to devise new material properties. Hence, composites accrue new properties not observed in either component in isolation, producing a superior material. A polymeric composite resolves a major problem within polymer engineering by overcoming the inherent poor mechanical properties of polymers compared to metals, while taking advantage of the plethora of properties that polymers have to offer.⁷ Additionally, there is a significant benefit and cost-savings in the ability to use commercially available or existing materials to create new materials while avoiding the need to invent new chemistry.

Many polymeric composites consist of a matrix and a reinforcing component. The matrix, which generally constitutes the largest volume fraction, serves as a continuous phase that encases the reinforcing (or dispersed) phase that is typically composed of fibers or spheres or particles.⁶ As a result of these physical differences, the microstructure of composites are heterogeneous with a discrete interface between the continuous and reinforcing phases, often termed interphase; here, the transfer of stress from the “weaker” matrix to the “stronger” fibers occurs.⁸ Additionally, the matrix also provides a protective barrier to the fibrous phase from the external environment.^{9,10} Most polymer composites are fabricated from thermoset matrices since the low viscosity of these monomers enables ease of traditional molding and greater fiber wetting, although thermoplastics matrices have become increasingly utilized.⁷ Some specific variables that affect composite properties include fiber or particle size, distribution and orientation. The composition of materials as well as the processing methods is a source of study and challenge for advanced applications.

1.2 Multi-Functional Materials

Many materials possess only one function beyond load bearing and often necessitate complementary materials or additional components in order to accommodate growing complex design requirements. Consequently, many researchers have sought to develop multifunctional materials, as these materials can simultaneously perform more than one independent functional capability beyond structural, such as self-healing, stimuli-responsiveness, self-cleaning, biodegradability, conductivity, biocompatibility, and drug delivery, with some even inspired by biology.¹¹⁻¹⁷ These types of materials differ from systems containing multiple components in that they are more efficient in weight and volume, given that these materials are typically single constituents or, in most cases, composites with integrated properties.¹⁸ Composite materials providing multifunctionality can be classified based on the dimensional scale at which integration between its constituents occur, ranging from coating or lamination between phases, to incorporation at the molecular level.^{19,19} Polymer composite materials lend themselves well to achieving multifunctionality considering they are the result of the synergistic combination of differing properties into a single, new material. This demand for multifunctionality has even influenced the expanding development of polymer composite materials.²⁰

As is the case for polymers, the development of multifunctional materials also spans many industries including energy storage, healthcare, automotive, communications, and consumer goods. For example, to address the multifaceted requirements in healthcare, Neffe et al. developed a smart polymer that is thermally deployable to allow for minimally invasive surgery, with controlled drug release for infection management, and biodegradability to avoid additional surgery for implant removal.²¹ Other examples include incorporating battery function

within load-bearing structures, transparent polymer nanocoatings for lenses or windows, wear- and scratch-resistance, self-healing materials, and shape memory polymers, which are covered in several review articles on the subject.^{17,20,22-25} The following sections briefly describe several material functions studied in this dissertation.

1.2.1 Biocompatibility for Biomedical Applications

Given that biological tissues are essentially polymers or composites, it is a natural tendency to for many researchers to utilize polymer composite materials for biomedical use.^{26,27} Since these materials must come into contact with living tissue, whether externally or internally, it is crucial that these materials exhibit biocompatibility. A material is considered biocompatibility when it does not trigger an adverse biological response from the host cells or tissues, whether locally or systemically, under specific circumstances.²⁸ Additionally, the material must also perform as intended, such that it has a positive therapeutic effect, rather than exist simply a non-toxic placement in the body. As such, biocompatibility is affected by the biological site selection, the intended function of the material, device size, and treatment duration. Several properties make up biocompatibility such as cytotoxicity, hemocompatibility, surface compatibility, and mechanical compatibility; these properties are typically first studied *in vitro* to screen new materials. In polymeric materials, biocompatibility is affected by mechanical properties, surface energy, hydrophilicity/hydrophobicity, surface and bulk chemical composition, and surface topography, to name a few.²⁹⁻³¹ Since composites are composed of more than one material, it is not sufficient to know the biocompatibility of each material, but to demonstrate both as a system.

Biocompatible materials may be classified as biomaterials when used to supplant or support the function of human tissues.³² One of the biggest challenges in biomaterials research is matching the properties of soft tissues such as skin, arteries, cartilage, muscles, organ walls, and tendons. Mechanical compatibility with the host tissue of a biomaterial or device is important to prevent complications such as stress-shielding or thrombosis.^{33,34} Most biomaterials are polymer-based, due to their low cost versatility and low modulus.. Polymer composites, such as those reinforced with fibers, offer tailorable tensile strength and functional microstructural properties, and are closer to mimicking the complex structures of native tissues, where a combination of collagen, elastin and fibronectin provide elasticity and tensile strength.³⁵ Nevertheless, polymers and their composites are still limited in soft tissue applications due to poor strength and elasticity.³⁶

1.2.2 Degradation

Degradable polymers are used in many biomaterials applications such as degradable implants, resorbable sutures, and, as further discussed in Section 1.4, a mechanism to control drug delivery. These polymers also find utility in environmental applications, where degradable consumer goods such as packaging and diapers can reduce environmental impact. Degradable polymers contain labile bonds in their chemical structure that upon contact with an aqueous environment, undergo hydrolytic cleaving of their chains. Degradation of polymers is classified as either surface/heterogeneous or bulk/homogenous degradation. As depicted in **Figure 1-1**, surface degradation occurs when the material loss is localized at the surface and is quicker than the rate of water diffusion, resulting in the polymer maintaining its overall geometry during degradation.³⁷ In contrast, bulk degradation loses material through its matrix as water penetrates

through to its interior, and does not maintain its shape during degradation; most polymers are bulk eroding.³⁸ Typical degradable biomaterials are based on homopolymers or copolymers of poly(glycolic acid), poly(lactic acid), polyesters, and polydioxanones, bacterial-derived polymers, polyanhydrides, or natural polymers.^{39,40} Several variables affect the degradation properties beyond chemical composition such as whether the degradation products are acidic and cause autocatalysis, addition of any drugs or excipients, and even size and shape in the case of surface erosion. **Chapter 5** further discusses and studies degradation.

1.2.3 Controlled Drug Delivery

Drug delivery is the supply and introduction of drugs in the body to treat diseases and is one of the most rapidly growing areas of biomedical engineering, encompassing many disciplines. A controlled drug delivery system is one where an active molecule is combined with a material.⁴¹ Familiar examples of drug delivery systems include tablets, creams, aerosols, liquids, and injections. The ideal drug delivery system would administer a drug at an optimum concentration that maximizes the therapeutic outcome without side effects, and maintains this efficacious concentration range for the duration of the treatment time.⁴² Toxicity occurs when the drug concentration is above the maximum therapeutic range, whereas a concentration below is ineffective. The challenge with conventional drug delivery systems, such as ingesting a tablet or administering an injection, is that while this enables immediate delivery of a therapeutic dosage, multiple administrations are required to maintain its therapeutic effects, particularly for those with chronic conditions, which can be unwieldy, painful, difficult to maintain, and/or expensive, and decrease patient quality of life.⁴³ Consequently, the study and development of controlled (or

sustained or prolonged) drug delivery systems target minimizing dosing frequency by providing a therapeutic concentration for an extended period of time.⁴⁴

Drug release systems are designed and structured as reservoir, hydrogel or matrix delivery systems. Reservoir delivery systems are constructed by sandwiching the drug between two or more layers of membrane material, typically a non-degradable, hydrophobic polymer.⁴¹ Diffusion of the drug through the polymer membrane determines the drug release rate. Hydrogel drug delivery systems utilize cross-linked water soluble polymers that contain entrapped drugs with a release rate are influenced by the degree of swelling and diffusion of drug through the material.⁴⁵ In a matrix delivery system, which is studied in **Chapters 2 and 5**, drugs are either dissolved or dispersed throughout the polymer bulk and rate limited by diffusion. Generally, drug release rate is limited by drug diffusion through the polymer and is affected by the diffusion coefficient of the drug, the chemical and structural properties of the polymer.

Drug release systems are also characterized by their drug release profiles, which quantify the amount of drug released over time and fall into three main categories: controlled release, burst release, or pulsatile (cyclic) release.⁴⁴ Drug release profiles are influenced by the mode of drug release and preferably follow zero-order release kinetics in order to maintain a constant drug concentration; however, first-order or variable release kinetics are more common and may be more desirable in certain applications.^{44,46} Polymer composite materials are a logical choice for drug delivery systems as these systems enable custom material property combinations that would tailor controlled release. Some of the variables to consider studying drug release include drug loading efficiency, ratio of drug to polymer, mechanical properties, surface chemistry, morphology, and polymer crystallinity. Polymer degradation can serve as another way to control

drug release, with surface erosion widely studied for drug release, since drug release profiles tend to be more constant, though in reality, drug diffusion from the bulk can also occur independent of the erosion front.⁴¹

1.2.4 Shape Memory

Shape memory polymers (SMPs) are a category of mechanically active smart materials that can memorize a programmed temporary shape and return to its pre-programmed shape in response to external stimuli such as heat⁴⁷, electricity⁴⁸, ultrasound⁴⁹, solvent^{50,51} and irradiation⁵²⁻⁵⁵. Thermally induced shape memory is the most widely studied system. SMPs have strong potential in biomedical applications such as by allowing bulky devices to become deployable following implantation through small incisions, self-tightening sutures in compact areas, artificial muscles, self-anchoring stents, and adaptable surfaces to direct cellular traffic, to name a few.^{56,57} Other applications include actuators, sensors, dimmable windows,^{58,59} smart textiles,^{60,61} and self-peeling adhesives.⁶² Several review articles discuss this topic in depth.^{55,63}

In order to exhibit shape memory, polymers must contain a combination of molecular features such as crosslinks (i.e. covalent, physical, or ionic), which serve to determine and “memorize” the original, permanent shape. These crosslinks are typically produced during fabrication in a stress-free state and contain some degree of extensibility to enable macroscopic shape shifting. The temporary shape “programming” (or “fixing”) of SMPs originates from the physical immobilization of the crosslinked network. Specifically, this is accomplished by exposing the deformed shape through a thermal transition to enable reversible crystallization or vitrification transitions for thermally triggered shape memory systems. The recovery of a fixed shape back to its original shape is achieved by exposure to a temperature exceeding its melting or

glass transition temperatures to enable the molecular mobility back to its permanent shape. An example of one way shape memory is presented in **Figure 1-2**.

1.3 Shape Memory Elastomeric Composite

To address the deficits of many soft smart polymer systems, the Mather Research Group previously developed a shape memory elastomeric composite (SMEC).^[Luo 2009] The goal of this composite was to develop a soft and elastic shape memory material by combining two commercially available polymers. Thermoplastic poly(ϵ -caprolactone) (PCL) was electrospun into a porous, non-woven fiber mat. The fibers were then embedded into Sylgard 184, a cross-linked polydimethylsiloxane matrix, which imparted elasticity and infiltrated the free space between the fibers. This system showed excellent shape memory performance, where the crystallizable PCL served as the switching phase and the crosslinks of the PDMS would serve to “remember” the original shape. This composite is advantageous structurally in that the fibrous structure imparts greater strength compared to PDMS due to its load distribution. The versatility of this system is that the properties are customizable by simply adjusting the fiber to matrix ratio, cross-link density of the matrix, fiber morphology or substituting the fibers or matrix with a different polymer with different properties. All of this utilizes much simpler chemistries and even commercially available materials. Rodriguez et al. later introduced anisotropy into this SMEC system, substituting the fibrous semicrystalline PCL phase with fibrous amorphous poly(vinyl acetate) PVAc.⁶⁴ They found that in the case of aligned fibers, shape fixing became a function of fiber angle orientation. Onyejekwe studied adding a drug, however undesirable shrinkage occurred and the biocompatibility properties were deficient.⁶⁵ In all of these studies, controlled drug delivery, biocompatibility, or degradation were not introduced into this system.

Outside of our group, several researchers have developed SMPs with additional material functionalities, though only few exhibit soft and elastomeric properties. For example, a SMP was developed by Wischke et al. to deliver a variety of model drugs that released over several months; however the Young's modulus was greater than that required for soft tissue applications such as vascular grafts.⁵⁴ Other drug-releasing SMPs were developed with soft, elastomeric properties comparable to native arterial tissue, however these materials have a biodegradation profile that falls short of that required for certain vascular applications such as arteriovenous access grafts, where mechanical stability is required over years instead of days or weeks.⁶⁶ For example, Serrano et al. developed polydiolcitrate based shape memory soft elastomeric films capable of controlled drug release of up to 30 days of hydrophobic model drugs, however these polymers degraded within two months.⁶⁶ A similar degradation profile was achieved by Kashif et al. by using a blended PCL/POSS nanocomposite also capable of shape memory, with controlled drug release; however, like others, their modulus was too stiff for soft tissue applications.⁶⁷ In addition, these SMP systems do not use commercially available materials and instead require laborious custom polymer syntheses. In another instance, Wang and coworkers recognized the limited available elastomeric shape memory materials and sought to develop a shape memory composite with thermally-triggered self-healing capabilities. This was accomplished by combining two commercially available non-degrading materials, however was focused on non-medical applications.⁶⁸

1.4 Scope of Dissertation

This dissertation examines the design, development and properties of electrospun composites for various applications such as controlled drug delivery and shape memory. In

Chapter 2, a hydrophilic drug model is incorporated into an electrospun polyester fiber mat and its drug releasing properties were studied relative to the microstructure of the fibers. The drug release from these fibers embedded into a siloxane elastomer was also investigated. **Chapter 3** examines the applicability of this composite for use as a biomimetic vascular graft with the incorporation of a nitric oxide donor in the fibrous phase. The nitric oxide releasing properties were investigated and its impact on cell migration was evaluated. The mechanical and biocompatibility properties were studied relative to the design requirements for this medical device. Additionally, it was discovered that the tin catalyst affected cell viability and a maximum concentration was determined that preserved the mechanical properties. In **Chapter 4** (adapted from Lawton et al.⁶⁹), a fully degradable shape memory elastomeric composite was developed with the ability to reconfigure its original, permanent shape. This composite was composed of a simple polyurethane electrospun fibers embedded in a cross-linked polyanhydride matrix. **Chapter 5** studied the degradation behavior of the polyanhydride-based composite developed in **Chapter 4**, comparing two different fibrous compositions as well as the drug releasing properties. Anisotropy of the polyester fibrous phase was introduced into a cross-linked epoxy matrix in **Chapter 6**, where dormant mechanically programmed shapes were investigated and reversible actuation was explored. Finally, a summary of the findings and conclusions of this work are presented in **Chapter 7** with suggested directions for continued research. Additional work is included in the **Appendix** of this dissertation.

1.5 References

1. Callister Jr., W. D. & Rethwisch, D. G. Materials science and engineering: an introduction. *John Wiley & Sons, Inc.*, 9th Edition (2003).
2. Sperling, L. H. Introduction to Polymer Science. *Introduction to Physical Polymer Science* 4th Edition (2005).
3. Yin, C., Dong, J., Tan W., Lin, J., Chen, D. & Zhang, Q.. Strain-induced crystallization of polyimide fibers containing 2-(4-aminophenyl)-5-aminobenzimidazole moiety. *Polymer* **75**, 178 (2015).
4. Wu, N., Lang, S., Zhang, H., Ding, M. & Zhang, J. Solvent-Induced Crystallization Behaviors of PLLA Ultrathin Films Investigated by RAIR Spectroscopy and AFM Measurements. *The Journal of Physical Chemistry B* **118**, 12652 (2014).
5. Jose, J. P. & Joseph, K. Advances in Polymer Composites: Macro- and Microcomposites—State of the Art, New Challenges, and Opportunities. *Polymer Composites: Vol. I*. Wiley-VCH Verlag GmbH & Co.: New York, 1st Edition (2012).
6. Wang, R. M., Zheng, S. R. & Zheng, Y. G. *Polymer matrix composites and technology*. Woodhead Publishing Limited (Science Press), Cambridge, UK, (2011).
7. McCrum, Norman Gerard, C. P. Buckley, and Clive B. Bucknall. *Principles of polymer engineering*. Oxford University Press, USA, 1997.
8. Qin, H. & Mather, P.T. Combined One-Way and Two-Way Shape Memory in a Glass-Forming Nematic Network. *Macromolecules* **42**, 273 (2009).
9. Herrera-Franco, P. J. & Valadez-Gonzalez, A. A study of the mechanical properties of short natural-fiber reinforced composites. *Elsevier* (2005).
10. Haque, A. & Ramasetty, A. Theoretical study of stress transfer in carbon nanotube reinforced polymer matrix composites. *Composites Part B: Engineering* **36**, 597 (2005).
11. Wischke, C. & Lendlein, A. Shape-memory polymers as drug carriers—A multifunctional system. *Pharmaceutical Research* **27**, 527 (2010).
13. Teo, W. E. & Ramakrishna, S. Electrospun nanofibers as a platform for multifunctional, hierarchically organized nanocomposite. *Composites Science and Technology* **69**, 1804 (2009).
14. Liu, K. & Jiang, L. Multifunctional integration: from biological to bio-inspired materials. *ACS Nano* **5**, 6786 (2011).

15. Misra, S. K., Ansari, T. I., Valappil, S. P., Mohn, D., Philip, S. E., Stark, W. J., Roy, I., Knowles, J. C., Salih, V. & Boccaccini, A. R. Poly (3-hydroxybutyrate) multifunctional composite scaffolds for tissue engineering applications. *Biomaterials* **31**, 2806 (2010).
16. Julich-Gruner, K. K., Lowenberg, C., Neffe, A. T., Behl, M. & Lendlein, A. Recent Trends in the Chemistry of Shape-Memory Polymers. *Macromolecular Chemistry and Physics* **214**, 527 (2013).
17. Bai, G., Tsang, M. K. & Hao, J. Luminescent ions in advanced composite materials for multifunctional applications. *Advanced Functional Materials* **26**, 6330 (2016).
18. Momoda, L.A. The future of engineering materials: Multifunction for performance-tailored structures. *Frontiers of Engineering: Reports on Leading-Edge Engineering from the 2004 NAE Symposium on Frontiers of Engineering*.
19. Matic, P. Overview of multifunctional materials. *Smart Structures and Materials 2003: Active Materials: Behavior and Mechanics* (2003).
20. Gibson, R. F. A review of recent research on mechanics of multifunctional composite materials and structures. *Composite Structures* **92**, 2793 (2010).
21. Neffe, A. T., Hanh, B. D., Steuer, S. & Lendlein, A. Polymer networks combining controlled drug release, biodegradation, and shape memory capability. *Advanced Materials* **21**, 3394 (2009).
22. Gowri, S., Almeida, L., Amorim, T., Carneiro, N., Souto, A. P., & Esteves, M. F. Polymer nanocomposites for multifunctional finishing of textiles-a review. *Textile Research Journal* **80**, 1290 (2010).
23. Pandey, G. & Thostenson, E. T. Carbon nanotube-based multifunctional polymer nanocomposites. *Polymer Reviews* **52**, 355 (2012).
24. Ragesh, P., Ganesh, V. A., Nair, S. V. & Nair, A. S. A review on 'self-cleaning and multifunctional materials'. *Journal of Materials Chemistry A* **2**, 14773 (2014).
25. Behl, M., Razzaq, M. Y. & Lendlein, A. Multifunctional Shape-Memory Polymers. *Advanced Materials* **22**, 3388 (2010).
26. Fratzl, P. Biomimetic materials research: what can we really learn from nature's structural materials? *Journal of The Royal Society Interface* **4**, 637 (2007).
27. Meyers, M. A., Chen, P. Y., Lin, A. & Seki, Y. Biological materials: structure and mechanical properties. *Progress in Materials Science* **53**, 1 (2008).

28. Williams, D. F. On the mechanisms of biocompatibility. *Biomaterials* **29**, 2941 (2008).
29. Wang, Y. X., Robertson, J. L., Spillman, W. B., & Claus, R. O. Effects of the chemical structure and the surface properties of polymeric biomaterials on their biocompatibility. *Pharmaceutical research* **21**, 1362 (2004).
30. Ramakrishna, S., Mayer, J., Wintermantel, E., & Leong, K. W. Biomedical applications of polymer-composite materials: a review. *Composites science and technology* **61**, 1189 (2001).
31. Roach, P., Eglin, D., Rohde, K. & Perry, C. C. Modern biomaterials: a review—bulk properties and implications of surface modifications. *Journal of Materials Science: Materials in Medicine* **18**, 1263 (2007).
32. Williams, D. F. On the nature of biomaterials. *Biomaterials* **30**, 5897 (2009).
33. Wang, X., Li, Y., Wei, J. & De Groot, K. Development of biomimetic nano-hydroxyapatite/poly (hexamethylene adipamide) composites. *Biomaterials* **23**, 4787 (2002).
34. Crapo, P. M. & Wang, Y. Physiologic compliance in engineered small-diameter arterial constructs based on an elastomeric substrate. *Biomaterials* **31**, 1626 (2010).
35. Barnes, C. P., Sell, S. A., Boland, E. D., Simpson, D. G., & Bowlin, G. L. Nanofiber technology: designing the next generation of tissue engineering scaffolds. *Advanced drug delivery reviews* **59**, 1413 (2007).
36. Chen, Q., Liang, S. & Thouas, G. A. Elastomeric biomaterials for tissue engineering. *Progress in polymer science* **38**, 584 (2013).
37. Pillai, O. & Panchagnula, R. Polymers in drug delivery. *Current opinion in chemical biology* **5**, 447 (2001).
38. Tamada, J. A. & Langer, R. Erosion kinetics of hydrolytically degradable polymers. *Proceedings of the National Academy of Sciences* **90**, 552 (1993).
39. Nair, L. S. & Laurencin, C. T. Biodegradable polymers as biomaterials. *Advances in Polymeric Biomaterials* **32**, 762 (2007).
40. Griffith, L. G. Emerging design principles in biomaterials and scaffolds for tissue engineering. *Annals of the New York Academy of Sciences* **961**, 83 (2002).
41. Saltzman, W. M. (2001). *Drug delivery: engineering principles for drug therapy*. Oxford University Press.

42. Bajpai, A., Shukla, S., Saini, R., & Tiwari, A. (2010). *Stimuli responsive drug delivery systems: from introduction to application*. Smithers Rapra Technology Limited.
43. Jain, K. K. (2008). Drug delivery systems-an overview. In *Drug delivery systems*. Humana Press.
44. Bader, R. A., & Putnam, D. A. (2014). *Engineering polymer systems for improved drug delivery*. John Wiley & Sons..
45. Hoare, T. R. & Kohane, D. S. Hydrogels in drug delivery: Progress and challenges. *Polymer* **49**, 1993 (2008).
46. Huang, X. & Brazel, C. S. On the importance and mechanisms of burst release in matrix-controlled drug delivery systems. *Journal of controlled release* **73**, 121 (2001).
47. Behl, M. & Lendlein, A. Shape-memory polymers. *Materials today* **10**, 20 (2007).
48. Cho, J. W., Kim, J. W., Jung, Y. C., & Goo, N. S. Electroactive shape-memory polyurethane composites incorporating carbon nanotubes. *Macromolecular Rapid Communications* **26**, 412 (2005).
49. Han, J., Fei, G., Li, G. & Xia, H. High intensity focused ultrasound triggered shape memory and drug release from biodegradable polyurethane. *Macromolecular Chemistry and Physics* **214**, 1195 (2013).
50. Quitmann, D., Gushterov, N., Sadowski, G., Katzenberg, F., & Tiller, J. C. Solvent-sensitive reversible stress-response of shape memory natural rubber. *ACS applied materials & interfaces* **5**, 3504 (2013).
51. Gu, X. & Mather, P. T. Water-triggered shape memory of multiblock thermoplastic polyurethanes (TPUs). *RSC Advances* **3**, 15783 (2013).
52. Lendlein, A., Jiang, H., Jünger, O. & Langer, R. Light-induced shape-memory polymers. *Nature* **434**, 879 (2005).
53. Liu, C., Qin, H. & Mather, P. T. Review of progress in shape-memory polymers. *Journal of Materials Chemistry* **17**, 1543 (2007).
54. Wischke, C., Neffe, A. T., Steuer, S., & Lendlein, A. Evaluation of a degradable shape-memory polymer network as matrix for controlled drug release. *Journal of Controlled Release* **138**, 243 (2009).
55. Mather, P. T., Luo, X., & Rousseau, I. A. Shape Memory Polymer Research. *Annual Review of Materials Research* **39**, 445 (2009).

56. Yang, P., Baker, R. M., Henderson, J. H., & Mather, P. T. In vitro wrinkle formation via shape memory dynamically aligns adherent cells. *Soft Matter* **9**, 4705 (2013).
57. Lendlein, A. & Langer, R. Biodegradable, Elastic Shape-Memory Polymers for Potential Biomedical Applications. *Science* **296**, 1673 (2002).
58. Xie, T., Xiao, X., Li, J. & Wang, R. Encoding localized strain history through wrinkle based structural colors. *Advanced Materials* **22**, 4390 (2010).
59. Lee, E., Zhang, M., Cho, Y., Cui, Y., Van der Spiegel, J., Engheta, N., & Yang, S. Tilted pillars on wrinkled elastomers as a reversibly tunable optical window. *Advanced Materials* **26**, 4127 (2014).
60. Castano, L. M. & Flatau, A. B. Smart fabric sensors and e-textile technologies: a review. *Smart Materials and Structures* **23**, 053001 (2014).
61. Hu, J. & Chen, S. A review of actively moving polymers in textile applications. *Journal of Materials Chemistry* **20**, 3346 (2010).
62. Eisenhaure, J. D., Xie, T., Varghese, S., & Kim, S. Eisenhaure, J. D., Xie, T., Varghese, S., & Kim, S. (2013). Microstructured shape memory polymer surfaces with reversible dry adhesion. *ACS applied materials & interfaces* **5**, 7714 (2013).
63. Liu, C., Qin, H., & Mather, P. T. Review of progress in shape-memory polymers. *Journal of Materials Chemistry* **17**, 1543 (2007).
64. Rodriguez, E. D. & Weed, D. C. Anisotropic Shape-Memory Elastomeric Composites: Fabrication and Testing. *Macromolecular Chemistry and Physics* **214**, 1247 (2013).
65. Onyejekwe, I. U. Nitric Oxide Releasing Polymers For Vascular Graft Applications. Doctoral Dissertation. *Syracuse University* (2012).
66. Serrano, M. C., Carbajal, L., & Ameer, G. A. Shape-Memory Polymers: Novel Biodegradable Shape-Memory Elastomers with Drug-Releasing Capabilities *Advanced Materials* **23**, 2211 (2011).
67. Kashif, M., Yun, B. M., Lee, K. S., & Chang, Y. W. Biodegradable shape-memory poly (ϵ -caprolactone)/polyhedral oligomeric silsesquioxane nanocomposites: Sustained drug release and hydrolytic degradation. *Materials Letters* **166**, 125 (2016).
68. Wang, C. C., Huang, W. M., Ding, Z., Zhao, Y. & Purnawali, H., Zheng, L. X., Fan, H. & He, C. B. Rubber-like shape memory polymeric materials with repeatable thermal-assisted healing function. *Smart Materials and Structures* **21**, 115010 (2012).

69. Lawton, M. I., Tillman, K. R., Mohammed, H. S., Shipp, D. A & Mather, P. T. Anhydride-based reconfigurable shape memory elastomers. *ACS Macro Letters* **5**, 203 (2016).

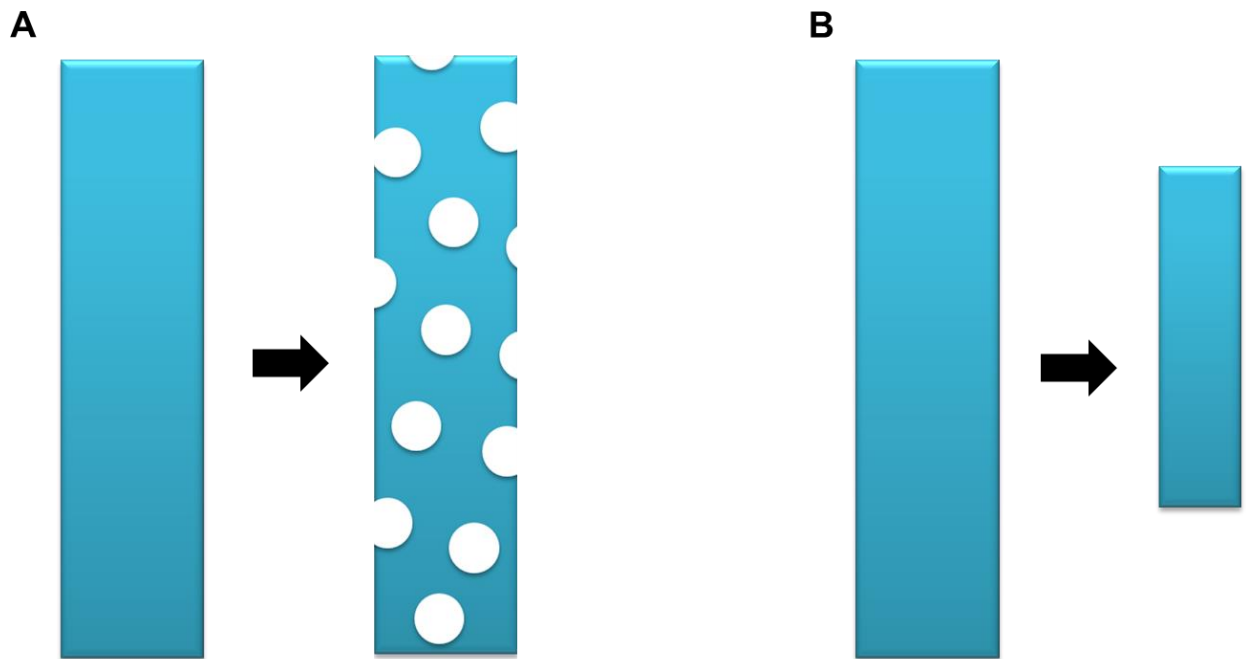


Figure 1-1. Example of erosion mechanisms in degradable polymers where (A) bulk (homogenous) erosion occurs throughout the polymer and (B) surface (heterogeneous) erosion degrades at the surface, while the sample maintains its shape and properties but decreases in size.

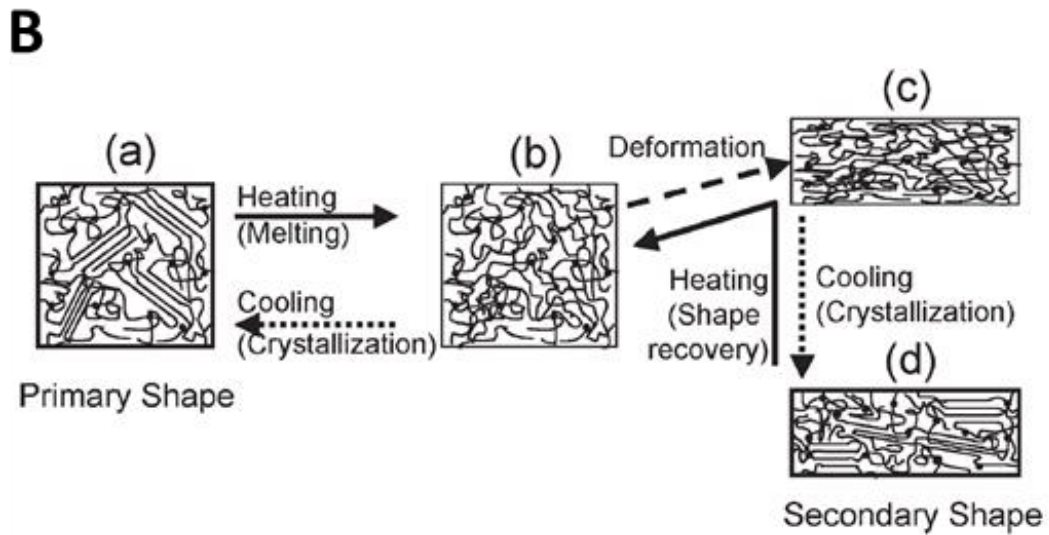
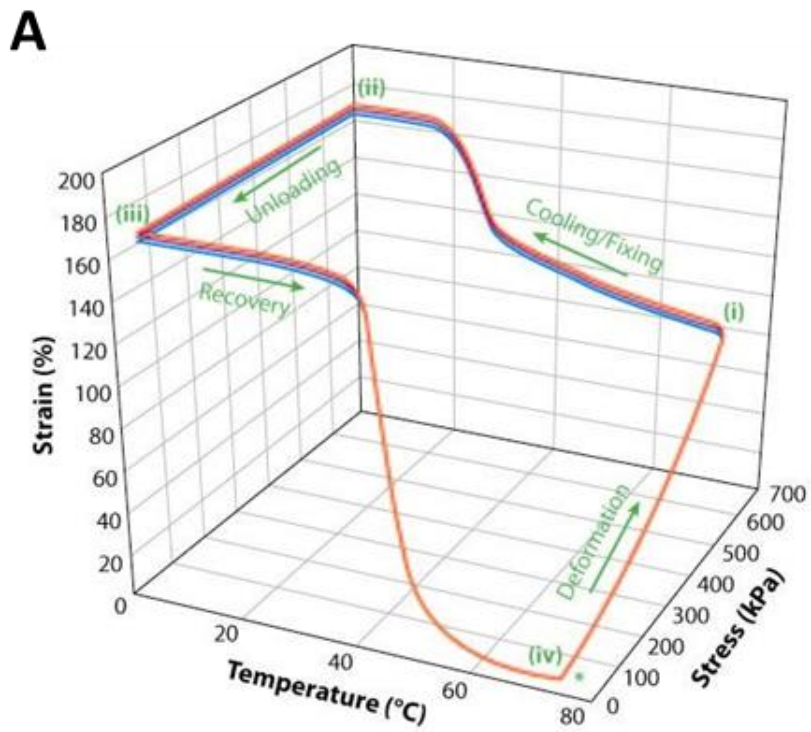


Figure 1-2. One way shape memory depicted (A) quantitatively and (B) morphologically.^{53,55}

Chapter 2

Shape Memory Elastomeric Composite with Controlled Drug Release of a Hydrophilic Drug Model

2.1 Synopsis

In this chapter the fabrication and characterization of an elastomeric polymeric construction with inherent shape memory properties capable of localized, long-term tunable drug release of a hydrophilic drug model is described. This assemblage was fabricated using an electrospinning process to produce a micro-fibrous framework. The fibers were doped with a hydrophilic drug model, Rhodamine B, and embedded within a siloxane based elastomeric matrix to form a composite, which is critical to regulating water transport from the environment to the fibers to release the drug. *In vitro* drug release studies were conducted in PBS under physiological conditions to evaluate the effect of drug concentration, fiber size, fiber crystallinity, drug loading and the addition of the siloxane. We found that the integration of this elastomer can control the initial burst release commonly observed in many drug delivery devices and extend drug release. The effect of the microstructural properties of the fibrous phase on drug release were explored and tuned through thermal treatment of the composite.

2.2 Introduction

The requirements for prosthetic implants are becoming increasingly more complex in order to meet the clinical demand of providing biomimetic materials. One approach has been the development of smart materials such as shape memory polymers (SMPs), which have been studied to address these needs by providing self-anchoring stents, minimally invasive surgery,

and even surfaces that can direct cellular traffic.^{1,2} SMPs are a category of materials that can memorize a temporary strain and return to its pre-programmed shape in response to external stimuli such as heat, electricity, ionic strength, and irradiation.³⁻⁶ While several groups have developed SMPs that can also provide drug delivery capabilities, only very few exhibit soft and elastomeric properties with a long-term, stable degradation profile. For example, a SMP was developed by Wischke et al. to deliver a variety of model drugs that released over several months, however the Young's modulus was greater than that required for soft tissue applications such as vascular grafts.^{7,8} Another drug-releasing SMP was developed by Serrano et al., which exhibited soft, elastomeric properties comparable to native arterial tissue, however its biodegradation profile falls short of that required for certain vascular applications such as arteriovenous access grafts, where mechanical stability is required over years.⁹

We have studied poly(ϵ -caprolactone) (PCL) as a candidate for a drug carrier while imparting mechanical support and shape memory switching. PCL is a semicrystalline polyester currently approved by the Food and Drug Administration (FDA) for biomedical devices, with long term biodegradation of over two years.¹⁰ PCL is an attractive option for biomedical applications, particularly those requiring drug delivery,¹¹ and many groups have studied PCL-based fibers as a drug delivery vehicle; however typical release times are on the order of hours to a few days.¹²⁻¹⁴ Consequently, many efforts have been made to blend or chemically modify PCL with other components in an effort to improve the sustained drug release outcome, though these materials are limited to drug delivery only and do not also exhibit shape memory functionality.¹⁵⁻

Our group has previously studied PCL and its mechanisms in formulating SMPs. We have been able to fabricate soft elastomeric composites with shape memory abilities by pairing PCL electrospun fibers with a crosslinked vinyl-terminated polydimethylsiloxane (PDMS) matrix.¹⁹ In this composite, the fibers serve as the shape fixing phase via crystallization while the elastomeric matrix memorizes the permanent shape through its crosslinks, while imparting elasticity. The shape memory properties were previously studied in our group and are exploited for surgical applications in **Chapter 3**; however, this composite's ability to store and release a hydrophilic model drug has not been previously studied.

We conceived that this PCL/PDMS composite can be useful for soft tissue biomedical applications requiring controlled drug release of a hydrophilic drug, such as vascular prosthetics, considering that these polymers are stable in aqueous media and no short term degradation is expected.²⁰ By incorporating a drug in the fibrous phase and then adding an elastomeric barrier, we hypothesized that the elastomer will regulate water transport to the drug-loaded fibers and control burst release while extending the overall drug release. Rhodamine B (RhB) was selected as the hydrophilic model drug to study this drug delivery system since it was easily soluble in water and cost-effective to model hydrophilic drug release. In this chapter, the effects of drug loading, morphology, polymer matrix, on drug release properties were investigated.

2.3 Materials and Methods

2.3.1 Materials

Poly(ϵ -caprolactone) (70,000 – 90,000 g·mol⁻¹), Rhodamine B (RhB), chloroform, tetrahydrofuran (THF), dimethylformamide (DMF) and dibutyltin dilaurate were purchased

from Sigma Aldrich and used as received. Silanol-terminated polydimethylsiloxane (PDMS) (2000 cSt) and poly(diethoxysilane) were purchased from Gelest, Inc.

2.3.2 Fabrication of RhB-Loaded Electrospun Fibers

Fibers were electrospun from PCL solutions ranging in concentration from 10 w/v % - 20 w/v % homogeneously mixed with RhB model drug, where higher concentrations of PCL were used to create larger fiber diameters. The RhB/PCL solutions were prepared by first adding 0.5 – 1.5 wt % RhB relative to the total mass of PCL to a clean glass vial, followed by complete dissolution in a 4:1 THF:DMF solvent mixture. No RhB precipitation was observed in the polymer solution. The RhB/PCL solution was then transferred to a 10 ml syringe fitted with a blunt 22G needle tip. A syringe pump was used to supply a steady flow rate of $1.0 \text{ ml} \cdot \text{h}^{-1}$ which was electrospun onto a grounded 50 mm diameter aluminum drum rotating at 400 rpm, at a distance of 7 cm from the needle tip to a negatively charged drum (-500 V) and an applied voltage of 11.5 kV. Following electrospinning, all fiber mats were dried at room temperature under vacuum (-30 mm Hg) for 48 h to remove any residual solvents prior to further use.

2.3.3 Preparation of RhB-Loaded Fibrous Elastomeric Composite

A pre-polymer elastomer was prepared by mixing silanol-terminated polydimethylsiloxane (PDMS) with 3 wt% polydiethoxysilane (crosslinker) and 0.5 wt% dibutyltin dilaurate (catalyst). The electrospun RhB loaded PCL fiber mats were then coated by the PDMS mixture, followed by exposure to vacuum at room temperature for 15 minutes to enable thorough infiltration of PDMS within the fiber mat. Excess PDMS was removed from the surface using a spatula followed by a 72 h cure at room temperature in a desiccator. The

chemical structures of the composite components and PDMS crosslinking scheme are shown in **Scheme 2-1**.

2.3.4 Morphological Characterization

A JEOL JSM-5600 scanning electron microscope (SEM) was used to visualize the samples with an accelerating voltage of 4 – 6 kV. Prior to imaging, samples were sputtered coated with gold for 45 s. Fiber diameter measurements were determined by taking a minimum of 50 measurements at five different locations using an image analysis software (version 1.46, National Institutes of Health). The average diameter and standard deviation were calculated using a minimum of 250 total measurements. Statistical significance was determined using a one-way analysis of variance (ANOVA) with a significance criterion of $p < 0.05$, using the Minitab software package.

An Olympus BX51 optical microscope equipped with a hot-stage and temperature controller (Instec HCS402) was used to visualize the phase distribution of RhB in the PCL fibers. A RhB/PCL fiber mat sample was sandwiched between two glass slides and then placed on the hot stage maintained isothermally at 80 °C to melt the fibers.

The porosity (P), of the electrospun fiber mats was calculated according to **Eqn. 2-1** below, where ρ_f is the measured density of the sample and ρ_0 is the known density of pure PCL, which has a value in the literature of $1.145 \text{ g}\cdot\text{cm}^{-3}$.²¹ The density of the fiber mat samples was determined by dividing the mass of the sample by its volume. A TA Instruments AR-G2 rheometer fitted with parallel plates was used to measure the thickness of each sample for improved accuracy, given the compressible nature of the samples, where the slightest change in force can be readily detected to avoid deforming the sample during the measurement.

$$P (\%) = 1 - \frac{\rho_f}{\rho_0} \times 100 \% \quad (2-1)$$

2.3 5 Thermal Characterization

Differential Scanning Calorimetry (DSC) was performed using a Q200 manufactured by TA Instruments, Inc. Samples weighing 2.5 – 4.0 mg were sealed in Tzero aluminum pans and heated from -60°C to 120°C at 10°C · min⁻¹. The melting enthalpy was calculated from the first heating cycle by integrating the melting peak, and was used to determine the crystallinity of PCL in the elastomeric composite in their as-manufactured state according to:

$$\chi_c (\%) = \frac{\Delta H_m}{\Delta H_f^0} \times 100 \% \quad (2-2)$$

where χ_c is the degree of crystallinity, ΔH_f is the heat of fusion measured by DSC and ΔH_f^0 is the heat of fusion of crystalline PCL, with a literature value of 139 J · g⁻¹.²² The melting enthalpy was calculated from the second heating cycle by integrating the melting peak, and was used to determine the fraction of PCL (W_{PCL}) in the elastomeric composite by comparing the degree of crystallinity according to:

$$W_{PCL} (\%) = \frac{\Delta H_m}{\Delta H_{m,0}} \times 100 \% \quad (2-3)$$

where ΔH_m is the melting enthalpy of the composite measured by DSC and $\Delta H_{m,0}$ is the melting enthalpy of pure electrospun PCL, as determined by DSC.

For completeness of materials characterization, the thermogravimetric analysis (TGA) was conducted by loading samples weighing 5 – 10 mg into a TA Instruments Q500 thermogravimetric analyzer. The samples were heated to 600 °C at 20 °C min⁻¹ under nitrogen purge.

2.3.6 In Vitro RhB Release

Rectangular samples of 1 cm x 2 cm were placed in a known volume (4 – 10 ml) of phosphate buffered saline (PBS, pH 7.4) in sealed glass vials. The vials were placed in a thermal shaker at 37°C to simulate physiological conditions. At different time intervals, a 150 uL aliquot of the PBS media was sampled from the vial and the RhB concentration was measured in a 96-well plate using spectrophotometry (Biotek® Synergy 2 Microplate Reader) at a wavelength of 553 nm (peak absorbance for Rhodamine B). The concentration of RhB was determined using a standard curve. After each time point, the PBS media was completely replaced with fresh PBS of a known volume to simulate *in vivo* “sink” conditions. Three replicates at each time point were used and an average and standard deviation is reported. The cumulative amount of RhB released was calculated and plotted as a function of time.

The theoretical total encapsulated moles of RhB in the fibers, n_T , was calculated for each sample according to **Eqn. 2-4** below:

$$n_T = \frac{x_i m_i}{M_{RhB}} \quad (2-4)$$

where x_i is the fraction the RhB mass relative to the PCL mass for sample i , m_i is the mass of the electrospun fibers containing both PCL and RhB, and M_{RhB} is the molecular weight of RhB, which is 479.01 g · mol⁻¹. The cumulative percent of RhB released (D) was calculated according to **Eqn. 2-5** below:

$$D_{RhB}(\%) = \frac{\sum_{i=1}^t C_i V_i}{n_T} \times 100 \% \quad (2-5)$$

where C_i is the molar concentration of RhB at time point i , V_i the volume of the release media relative at each time point, up to time t .

2.3.7 Thermal Treatment to Induce Crystallization

Fibrous samples were thermally treated prior to drug release by placing “webs” (non-woven films) of them in an isothermal oven at 45 °C for 10 days. These conditions were selected to remain below the melting transition of PCL to preserve the fibrous morphology. Prior testing indicated that this longer annealing time enabled considerable changes in the crystalline content. The composite samples were subjected to a stepped thermal treatment in an isothermal oven by first exposing to 90 °C for 20 min, immediately followed by placing in another oven at 50 °C for 1 h.

2.3.8 Mechanical Properties

Tensile mechanical properties were studied by punching samples into a dog bone geometry (ASTM Standard D638-03 Type IV, scaled down by a factor of 4), and loading onto a Test Resources Model 100P Universal Testing Machine equipped with a 24 N load cell. The samples were stretched at a rate of 33 $\mu\text{m s}^{-1}$, and engineering stress-strain curves were used to determine Young’s modulus, strain-to-failure, and tensile strength. Five samples of each type were tested and an average and standard deviation are reported for each sample type.

2.4 Results

2.4.1 Fiber Characterization and Composite Morphology

The SEM micrographs in **Figure 2-1** reveal that a range of increasing fiber diameters was produced by electrospinning with an increasing concentration of PCL in the solvent, as was expected. The surface of the fibers appeared smooth and did not appear altered by the presence of RhB. The resulting fiber diameters ranged from $0.23 \mu\text{m} \pm 0.13 \mu\text{m}$ to $1.29 \mu\text{m} \pm 0.63 \mu\text{m}$. All

fiber diameter populations shown in **Figure 2-1** were statistically significantly different at the 95 % confidence interval. The porosity of the fiber mats generally increased with increased fiber diameter, as was anticipated (not shown). Generally, an optimum porosity is necessary for controlled drug release, where if the samples are too porous, too much drug may be released too quickly.²³ No obvious RhB crystals were observed on the surface for any of the fiber samples. **Figure 2-2** shows that the RhB distribution in the fibers is heterogeneous, as evidenced by regions of light and dark pink, indicative of the immiscibility of RhB in PCL. The air bubbles in **Figure 2-2** formed during melting of the fibers and originated from the empty voids originally between the fibers. **Figure 2-3(A)** shows the SEM micrographs of the surface of PCL fibers containing 0.5% RhB and post-infiltration of the PDMS elastomer. The cross-section of the composite, as seen in **Figure 2-3(B)**, reveals that the PDMS completely encapsulated the fibers, while occupying the voids within the fiber mat. Similar results were found for a higher concentration of RhB (not reported).

2.4.2 In Vitro RhB Release from PCL fibers

Figure 2-4A summarizes the RhB release from various fiber diameters of electrospun PCL. Surprisingly, there was no observed correlation between the size of the fiber and burst release, duration of release, and drug entrapment (unreleased drug), indicating that another factor influenced the drug release characteristics. The total amount of RhB released at 48 h relative to fiber diameter and sample porosity is compared in **Figure 2-4B**, where neither variable demonstrated an impact on RhB release. All samples showed a similar release pattern, with an initial burst release within the first 3 h, followed by a plateau of either no or very slow release. Only the smallest diameter sample of $0.23 \mu\text{m} \pm 0.13 \mu\text{m}$ exhibited near complete release of

RhB, with the highest burst release of 93 % at 48 h, whereas the largest diameter of $1.29 \mu\text{m} \pm 0.63 \mu\text{m}$ showed the slowest and least amount of release at 45 % at 48 h; however, the correlation did not continue with the intermediate fiber diameters.

2.4.3 Thermal Characterization and RhB Release

A clear melting transition was observed for all RhB/PCL electrospun samples as was expected due to the semicrystalline nature of PCL as seen in **Figure 2-5A**. When compared with the results of **Figure 2-4**, described above, it was observed that the amount of RhB released increased with increasing melting temperature and enthalpy, as shown in **Figure 2-5B** and tabulated in **Table 2-1**. The relative degree of crystallinity based on the first heating cycle, showed a positive correlation with the amount of RhB release and no clear trend with fiber diameter. The variation seen here may be due to the differences in time on the bench at room temperature (aging time) before testing, which was not controlled in this study. This is particularly possible since PCL features a subambient glass transition temperature ($T_g \sim -60 \text{ }^\circ\text{C}$). The melting transition for RhB was not visible since it occurs at $\sim 211 \text{ }^\circ\text{C}$, which is also its decomposition temperature and therefore its crystalline state in the fibers could not be determined thermally.

2.4.4 RhB Release from Thermally Treated Fiber Mats

A separate series of experiments was conducted to promote crystallization, purposefully, and study the RhB release from PCL fibers at two drug concentrations, 0.5 % and 2.0 % RhB in PCL. In this study, the fiber diameters of the two samples were not significantly different, in order to isolate the PCL crystallization effect on drug release. The resulting fiber diameters were

1.3 $\mu\text{m} \pm 0.9 \mu\text{m}$ and 1.2 $\mu\text{m} \pm 0.4 \mu\text{m}$ for the 0.5 % RhB/PCL and 2.0 % RhB/PCL samples, respectively. Here, the electrospun fibers were placed in an isothermal oven for 10 days at 45 °C to promote increasing completion of PCL crystallization while preventing melting of the fibers. The results in **Figure 2-6** show that applying an annealing treatment to the fibers caused a decreasing shift in RhB release, which was more pronounced at the higher RhB concentration, where a total of only 25 % of RhB was released following annealing, compared to the 51% level for the as-electrospun case. In comparison, the low concentration samples showed only a ~10 % reduction of RhB release following crystallization. The DSC thermograms in **Figure 2-6B** verified that the thermal treatment did, indeed, increase crystallinity. It is further interesting to note that while the changes were slight, the influence on drug release was significant and opposite compared to the trend for as-electrospun samples where differences in crystallinity were accompanied by other sample variations.

2.4.5 RhB Release from PCL/PDMS Composites

The RhB release from the PCL/PDMS composite is shown in **Figure 2-7** for a concentration of 0.5 % RhB and compared to drug release from the parent fiber mat (no PDMS), as-electrospun. The PDMS matrix greatly extended the RhB release compared to the quick burst release detected for the fiber mats. By 24 h, the fibrous samples had completed release of 66 % of the total theoretical RhB concentration. While the fibrous samples contained, apparently, a significant amount of entrapped RhB, most of the observed release occurred within the initial two hours (60 %). In contrast, the 0.5 % RhB/PCL/PDMS composite extended the burst release from 2 h to 48 h and appeared to liberate more RhB from the fibers such that approximately 95 % of the RhB was released after seven days with near completion at 14 days. We attributed this

behavior to the full wetting of the fibers by the PDMS, which created additional pathways for diffusion otherwise blocked by trapped air between the fibers. The release of RhB from the fiber mats can be followed visually over time by witnessing the color change, which begins a dark pink and gradually becomes white as the RhB is leached into the media that in turn absorb the pink color (**Figure 2-8**).

2.4.6 RhB Release from Thermally Treated PCL/PDMS Composites

Following the results in the sections above, a separate series of experiments was conducted to investigate the effect of the crystalline properties of PCL on the release of RhB from the PCL/PDMS composite. Unlike the fibrous samples, complete melting of the PCL phase could be performed in the composite samples since the fibrous morphology would be preserved by the surrounding crosslinked PDMS matrix. Thus, a stepped thermal treatment of 90 °C / 20 min followed by 50 °C / 1 h – melting the fibers – then cooling to room temperature for 15 min was implemented to induce complete recrystallization of the 0.5 % RhB/PCL/PDMS fibrous phase; for this experiment, the fiber diameter and fiber content were verified to be constant between samples. The resulting RhB release in **Figure 2-9A** shows that a 0.7 J/g increase (~18% increase) in first heat enthalpy of fusion produced a significant decrease in the RhB release from the more crystalline composite. In particular, 22 % less RhB was released at 48 h and this difference was generally maintained for the remaining four days of the testing period. These results are consistent with the thermally treated RhB/PCL fiber mats in *Section 2.4.4*, where a small increase in PCL crystallinity led to a marked decrease in RhB release. The DSC first heat thermograms in **Figure 2-9B** verify the increase in enthalpy of fusion for the melting peak following PCL stepped recrystallization. Interestingly, however, the melting point was lowered.

This decrease in the melting transition temperature may be due to the formation of more homogeneously sized distribution of crystallites, and likely smaller average size, following recrystallization from the PCL melt, which is further evidenced by the narrower melting peak. Detailed x-ray scattering analysis is needed to verify this explanation.

2.4.7 Mechanical Properties

The tensile mechanical properties for the composite are shown in **Figure 2-10** and summarized in **Table 2-2** and compared to its individual components. The addition of the RhB did not affect the mechanical properties in any significant manner (tensile data of samples with RhB not shown). The Young's moduli and strain-to-failure of the composite samples ranged from $2.7 \text{ MPa} \pm 0.6 \text{ MPa}$ to $5.0 \text{ MPa} \pm 0.6 \text{ MPa}$, and $460 \% \pm 60 \%$ to $640 \% \pm 120 \%$, respectively, across varying weight fractions of PCL in the composite ranging from 5.9 wt% to 15.6 wt% (**Table 2-2**). No correlation was observed between PCL fiber content in the composite and the Young's modulus or strain-to-failure, where both features were between that of the cross-linked PDMS film and electrospun PCL, as was expected from a biphasic composite. Only the Young's moduli for the composites containing 7.9 % and 8.5 % fibers showed a statistically significant difference ($\sim 1 - 2.3 \text{ MPa}$) from the rest of the groups. The composites containing 6.6 % and 15.6 % were not statistically different from each other, but statistically different from the 5.9 % and 11.4 % groups. The composite samples containing 5.9 % fibers showed a statistical increase in strain-to-failure from those groups containing 6.6 % and 7.9 % fibers, which were not statistically different from each other; this difference was by approximately 160 – 180 % strain. We observed that the shape of the stress-strain curves of the composite appeared to evolve from one that is more linear (**Figure 2-10A**) to containing a toe region (**Figure 2-10D-F**).

Although the appearance of a toe region became more prominent with increasing PCL fiber content, the Young's moduli and % elongation values did not appear to approach that of PCL during this growth.

2.5 Discussion

The motivation of this study was to investigate the controlled release of a hydrophilic drug from a soft, elastomeric shape memory composite. Rhodamine B (RhB), was selected as the model drug since its hydrophilic character (solubility of ~ 8 mg/ml)²⁴ is akin to another drug molecule we are also interested in studying. More specifically, the controlled release from a hydrophilic nitric oxide donor molecule incorporated into this composite is later examined in **Chapter 3**. The challenge with any nitric oxide donor is that drug release is typically indirectly measured and the nitric oxide itself is highly reactive; therefore the use of a model drug provides a low cost alternative to develop this material as a candidate for controlled release of nitric oxide as well as other hydrophilic drugs. The ease with which RhB release can be directly quantified and visually verified (**Figure 2-8**) is of great advantage for investigating the impact of different processing factors on the hydrophilic drug release from this composite, resulting in translatable findings. As such, we aimed to systematically study the effect of drug loading, fiber size, and crystallinity on drug release from our composite material.

It has been demonstrated that drug release can be extended by increasing the diameter of electrospun fibers,²⁵ though for semicrystalline drug carriers, the dependence of drug release on vehicle size becomes more complex.²⁴ In our investigation, the RhB release did not strongly correlate with fiber size (**Figure 2-4**), but showed a strong dependence on PCL crystallinity. For untreated electrospun fibrous samples, we observed an emerging trend where more RhB was

recovered for those samples exhibiting greater PCL crystallinity (**Figure 2-5**). We noted that the sample with the fastest drug release rate exhibited a double endothermic peak, indicating that in addition to greater crystallinity, the crystalline microstructure likely contained various lamellar thickness populations, though additional testing is required to determine the impact of crystallite polydispersity on drug release.^{26,27} The crystallinity of a polymeric vehicle is an important factor in drug delivery as it can limit the diffusion of water transport into the polymer bulk and hence, the drug release and drug retention within the fibers.²⁸ Specifically, water transport through PCL occurs through the amorphous regions of the polymer, thus circumventing the crystalline areas, which has been used by others as a strategic advantage for controlled release.¹³ Nonetheless, the crystallinity of PCL is an important feature for the shape memory polymer feature of this composite.¹⁹ In light of these observations, we postulated that the growing crystalline front during electrospinning expelled the RhB toward the fiber surface during fiber formation, thereby enabling faster and more complete leaching of RhB. We did not directly observe RhB crystals on the fiber surface. This may be due to small crystal size, unresolved by light microscopy, or due to the drug being buried just beneath the surface and therefore easily accessible to the diffusing external aqueous media.

Polymer fibers have been shown to exhibit distinct morphological differences across the fiber cross-section, such that a “skin-core” structure is formed.^{29,30} In this configuration, the microstructure of electrospun semicrystalline fibers, such as PCL, tend to organize such that the amorphous phase is contained within the fiber core enveloped by a crystalline “skin” or sheath. Here, decreasing the fiber diameter results in increasing the crystallinity.³¹ We hypothesized that the addition of a hydrophilic molecule, such as RhB, to the PCL fiber would result in phase

separation, and drive the dispersion of RhB beneath this crystalline sheath toward an amorphous core, as depicted schematically in **Figure 2-11**. We further theorized that increasing this sheath thickness, such as by a post-electrospinning heat treatment, would reduce the rate and completeness of RhB release. Additionally, we postulated that the presence of trapped air between the fibers limited the diffusive pathways that promoted drug entrapment.

To test this hypothesis, we conjectured that by annealing the fiber mats, to just below the melting transition (to maintain the fibrous structure), the RhB release could be controlled by altering the PCL crystalline microstructure. Following heat treatment, the fiber mats showed an increase in the melting enthalpy for two different RhB concentrations. Consistent with our hypothesis, we observed that increasing the crystallinity of the RhB doped fibers substantially decreased both the immediate burst and overall drug release. This effect was more pronounced in the fibers containing a greater concentration of RhB, where not only was the total amount of RhB released halved, the increase in crystallinity following annealing was also greater, despite exhibiting a lower initial melting enthalpy. These results suggest that the fiber crystallinity is potentially a much greater influence on hydrophilic drug release from PCL than fiber diameter. Furthermore these results indicate that there must be a critical RhB concentration in the fibers below which the influence of thermally induced crystallization becomes negligible, and a high recovery of drug can be expected, similar to the effect of decreasing fiber diameter. A separate study would be required to determine this critical concentration by testing drug release from a series of RhB concentration in electrospun PCL. Considering that the polymer/drug solution is supplied as a single, homogeneous phase during electrospinning, we assumed the differences in the surface energy of hydrophilic (higher surface energy in air) RhB would likely position the

drug in the more amorphous core of the hydrophobic PCL fibers during phase separation. We suspected that the dispersion of RhB in the fiber core is more uniform at lower concentrations, as enhanced molecular dispersions between the drug and polymer tend to occur in the amorphous regions.³² We also note that any entrapped drug would be liberated long term (over two years) due to the hydrolysis and enzymatic degradation of the PCL chains *in vivo*, although partial release does not necessarily indicate inadequate bioactivity.^{33,34}

The addition of the PDMS elastomeric matrix to the PCL fibers served to prolong and increase the totality of RhB release. Comparing the drug release of the composite to that of the bare fibers, sustained drug release was extended by approximately 16 days, where most of the RhB discharge occurred within approximately two hours. The PDMS matrix provided a diffusion-limited water transport from the external aqueous environment to the drug loaded fibers, thus preventing immediate dissolution of RhB to the aqueous media. Although PDMS is hydrophobic, it is also permeable to water.³⁵ When compared to the fibrous samples, the PDMS-based composite did not exhibit a quick, spontaneous release; rather a sustained initial release which was steadily extended from 2 h to 48 h. We observed that the final cumulative total RhB released was greater in the composite than in the fibrous samples. We hypothesized that the wetting of the fibers by PDMS displaced air that may otherwise block RhB release thus enabling further release of any RhB buried within the PCL fibers, though further investigation is merited.

Taking into account the large effect of the PCL microstructure on RhB release, we contemplated complete recrystallization of PCL within the PCL/PDMS composite. This was possible since the crosslinked PDMS would retain the percolating channels of the electrospun fibers following melting of PCL, which is one of the central principles of imparting shape

memory behavior to this material. We observed that following slow recrystallization after complete melting of PCL, the RhB release was significantly less for the more crystalline samples, which was consistent with what we observed for the annealed fibrous study described above (**Figure 2-6**), consequently providing another strategy in addition to fiber diameter to control RhB release, and further supporting our skin-core microstructural assumption.

As has been studied in previously in our group, the combination of PCL and PDMS provide unique properties not present in either constituent alone. The percolating PCL fibers impart significant strength not present in the PDMS elastomer, which is ideal for load bearing applications, while the PDMS imparts elasticity, allowing for the ability to match the Young's modulus of soft tissues such as skin, blood vessels, muscle and cartilage.³⁶ The emergence of a toe region, which produced “J-shaped” stress-strain curves, is an interesting feature resonant of native soft tissues containing hierarchical components, differing from hard tissues.³⁷ Analogous to our composite material, soft tissues are fiber-reinforced, composed primarily of collagen and elastin, which are the load-bearing and elastic components of soft tissues such as tendons, ligaments, arteries.^{38,39} Considering that the fibrous PCL phase is also load bearing, we postulate that at low strains the stress corresponds to macroscopic stretching of the PDMS crosslinks and slippage of the PCL fibers past each other in the toe region. Upon additional stress, the fibers begin to orient in the tensile direction and elongate, until plastic deformation sets in at higher strains and rupturing of the PDMS crosslinks, leading to ultimate failure. We observed that the toe region became more apparent with an increase in percentage of the PCL phase, where samples featuring 8 % or more of PCL exhibited this exponentially shaped curve.

2.6 Conclusions

An elastomeric shape memory composite containing a hydrophilic model drug was successfully prepared by embedding drug loaded semicrystalline PCL fibers within a crosslinked PDMS elastomer. Controlled drug releasing properties were demonstrated, where it was determined that the crystallinity of the fibrous phase had a greater effect on drug release than did fiber diameter. The crystallization mechanism determined whether the microstructural properties increased or decreased drug release. We postulated that growing crystalline front during fiber pushed the drug toward the fiber surface leading to quicker and total release, whereas post-fiber formation crystallization was distinct and served to drive the hydrophilic drug toward more amorphous fiber core, away from the growing crystalline sheath. This migratory behavior of the hydrophilic drug within the hydrophobic semicrystalline PCL fibers was explained to be a result of phase separation. Moreover, the tensile mechanical properties demonstrated that this composite was an excellent candidate for soft tissue applications due to its elasticity, low modulus, and biomimetic multi-stage load bearing response typically associated with native soft tissues.

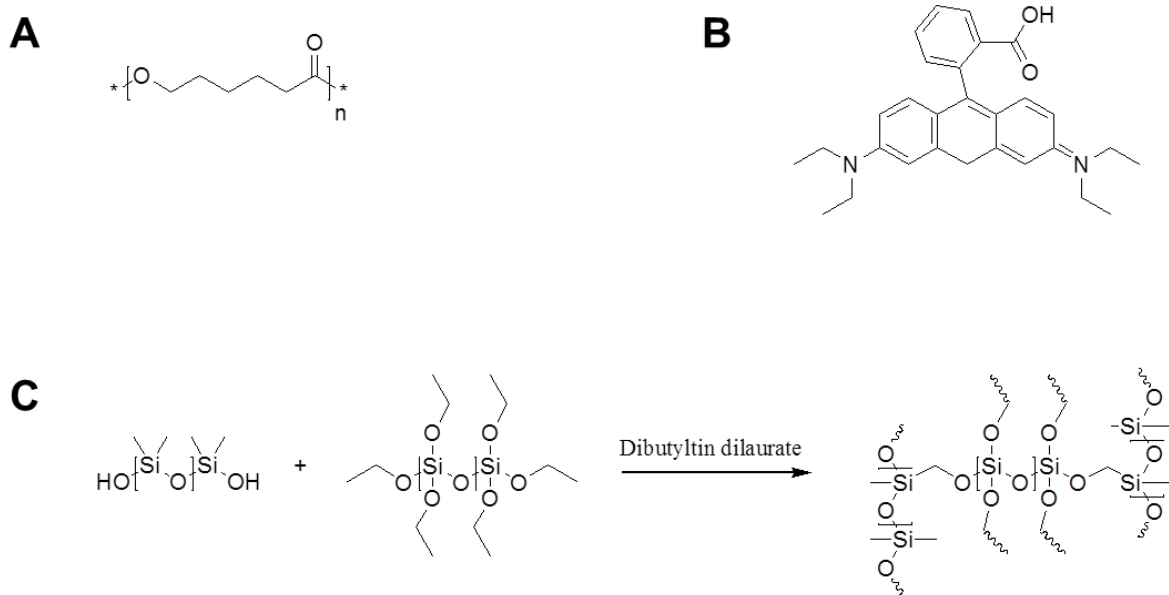
2.7 References

1. Yang, P., Baker, R. M., Henderson, J. H. & Mather, P. T. In vitro wrinkle formation via shape memory dynamically aligns adherent cells. *Soft Matter* **9**, 4705 (2013).
2. Lendlein, A. & Langer, R. Biodegradable, Elastic Shape-Memory Polymers for Potential Biomedical Applications. *Science* **31**, 1673 (2002)
3. Luo, X. & Mather, P. T. Shape Memory Assisted Self-Healing Coating. *ACS Macro Letters* **2**, 152 (2013).
4. Liu, C., Qin, H. & Mather, P. T. Review of progress in shape-memory polymers. *Journal of Materials Chemistry* **17**, 1543 (2007).

5. Mather, P. T., Luo, X. & Rousseau, I. A. Shape Memory Polymer Research. *Annual Review of Materials Research* **39**, 445 (2009).
6. Lendlein, A., Jiang, H., Jünger, O. & Langer, R. Light-induced shape-memory polymers. *Nature* **434**, 879 (2005).
7. Wischke, C., Neffe, A. T., Steuer, S. & Lendlein, A. Evaluation of a degradable shape-memory polymer network as matrix for controlled drug release. *Journal of Controlled Release* **138**, 243 (2009).
8. Koens, M. J. W, Faraj, K. A., Wismans, R. G., van der Vliet, J. A., Krasznai, A. G., Cuijpers, V. M. J. I., Jansen, J. A., Daamen, W. F. & van Kuppevelt, T. H. Controlled fabrication of triple layered and molecularly defined collagen/elastin vascular grafts resembling the native blood vessel. *Acta Biomaterialia* **6**, 4666 (2010).
9. Serrano, M. C., Carbajal, L & Ameer, G. A. Shape-Memory Polymers: Novel Biodegradable Shape-Memory Elastomers with Drug-Releasing Capabilities. *Advanced Materials* **23**, 2210 (2011).
10. Sun, H., Mei, L., Song, C., Cui, X. & Wang, P. The in vivo degradation, absorption and excretion of PCL-based implant. *Biomaterials* **27**, 1735 (2006).
11. Dash, T. K. & Konkimalla, V. B. Polymeric Modification and Its Implication in Drug Delivery: Poly- ϵ -caprolactone (PCL) as a Model Polymer. *Molecular Pharmaceutics* **9**, 2365 (2012).
12. Seif, S., Franzen, L. & Windbergs, M. Overcoming drug crystallization in electrospun fibers – Elucidating key parameters and developing strategies for drug delivery. *International Journal of Pharmaceutics* **478**, 390 (2015).
13. Jeong, J. C., Lee, J. & Cho, K. Effects of crystalline microstructure on drug release behavior of poly(ϵ -caprolactone) microspheres. *Journal of Controlled Release* **92**, 249 (2003).
14. Mary, L. A., Senthilram, T., Suganya, S., Nagarajan, L, Venugopal, J., Ramakrishna, S. & Giri Dev, V. R. Centrifugal spun ultrafine fibrous web as a potential drug delivery vehicle. *Express Polymer Letters* **7**, 238 (2013).
15. Han, J., Chen, T. X., Branford-White, C. J. & Zhu, L. M. Electrospun shikonin-loaded PCL/PTMC composite fiber mats with potential biomedical applications. *International Journal of Pharmaceutics* **382**, 215 (2009).
16. Tiwari, S. K., Tzezana, R., Zussman, E. & Venkatraman, S. S. Optimizing partition-controlled drug release from electrospun core-shell fibers. *International Journal of Pharmaceutics* **392**, 209 (2010).

17. Wang, Y., Wang, B., Qiao, W. & Yin, T. A Novel Controlled Release Drug Delivery System for Multiple Drugs Based on Electrospun Nanofibers Containing Nanoparticles. *Journal of Pharmaceutical Sciences* **99**, 4805 (2010).
18. Yu, H., Jia, Y., Yao, C. & Lu, Y. PCL/PEG core/sheath fibers with controlled drug release rate fabricated on the basis of a novel combined technique. *International Journal of Pharmaceutics* **469**, 17 (2014).
19. Luo, X. & Mather, P. T. Preparation and characterization of shape memory elastomeric composites. *Macromolecules* **42**, 7251 (2009).
20. Mather, P.T., Onyejekwe, I.U. & Ishida, K. System and method for the release of nitric oxide using nanoscale media. U.S. Patent 8,394,393 (2013).
21. Vaz, C. M., Van Tuijl, S., Bouten, C. & Baaijens, F. Design of scaffolds for blood vessel tissue engineering using a multi-layering electrospinning technique. *Acta Biomaterialia* **1**, 575 (2005).
22. Crescenzi, V., Manzini, G., Calzolari, G. & Borri, C. Thermodynamics of fusion of poly- β -propiolactone and poly- ϵ -caprolactone. comparative analysis of the melting of aliphatic polylactone and polyester chains. *European Polymer Journal* **8**, 449 (1972).
23. Karuppuswamy, P., Venugopal, J. R., Navaneethan, B., Laiva, A. L, Ramakrishna, S. Polycaprolactone nanofibers for the controlled release of tetracycline hydrochloride. *Materials Letters* **141**, 180 (2015).
24. Berkland, C., Kipper, M. J., Narasimhan, B., Kim, K. & Pack, D. W. Microsphere size, precipitation kinetics and drug distribution control drug release from biodegradable polyanhydride microspheres. *Journal of Controlled Release* **94**, 129 (2004).
25. Cui, W., Li, X., Zhu, X., Yu, G., Zhou, S. & Weng, J. Investigation of Drug Release and Matrix Degradation of Electrospun Poly(dl-lactide) Fibers with Paracetamol Inoculation. *Biomacromolecules* **7**, 1623 (2006).
26. Wei, C. L., Chen, M. & Yu, F. E. Temperature modulated DSC and DSC studies on the origin of double melting peaks in poly(ether ether ketone). *Polymer* **44**, 8185 (2003).
27. Rim, P. B. & Runt, J. P. Melting behavior of crystalline/compatible polymer blends: poly(ϵ -caprolactone)/poly(styrene-co-acrylonitrile). *Macromolecules* **16**, 762 (1983).
28. Perez, M. H., Zinutti, C., Lamprecht, A., Ubrich, N., Astier, A., Hoffman, M., Bodmeier, R. & Maincent, P. The preparation and evaluation of poly(ϵ -caprolactone) microparticles containing both a lipophilic and a hydrophilic drug. *Journal of Controlled Release* **65**, 420 (2000).

29. Johnson, D. J. Structure-property relationships in carbon fibres. *Journal of Physics D: Applied Physics* **20**, 286 (1987).
30. Baji, A., Mai, Y. W., Wong, S. C., Abtahi, M. & Chen, P. Electrospinning of polymer nanofibers: Effects on oriented morphology, structures and tensile properties. *Composites Science and Technology* **70**, 703 (2010).
31. Lim, C. T., Tan, E. & Ng, S. Y. Effects of crystalline morphology on the tensile properties of electrospun polymer nanofibers. *Applied Physics Letters* **92**, 141908 (2008).
32. Izumikawa, S., Yoshioka, S., Aso, Y. & Takeda, Y. Preparation of poly(l-lactide) microspheres of different crystalline morphology and effect of crystalline morphology on drug release rate. *Journal of Controlled Release* **15**, 133 (1991).
33. Chen, D. R., Bei, J. Z. & Wang, S. G. Polycaprolactone microparticles and their biodegradation. *Polymer Degradation and Stability* **67**, 455 (2000).
34. Woodruff, M. A. & Hutmacher, D. W. The return of a forgotten polymer—Polycaprolactone in the 21st century. *Progress in Polymer Science* **35**, 1217 (2010).
35. Randall, G. C. & Doyle, P. S. Permeation-driven flow in poly(dimethylsiloxane) microfluidic devices. *Proceedings of the National Academy of Sciences*, **102**, 10813 (2005).
36. Ramakrishna, S., Mayer, J. & Wintermantel, E. Biomedical applications of polymer-composite materials: a review. *Composites Science and Technology* **61**, 1189 (2001).
37. Holzapfel, G.A. Biomechanics of soft tissue. *The Handbook of Materials Behavior Models, Vol. 3—Multiphysics Behaviors*, 1049–1063. Academic Press, Boston (2001).
38. Fratzl, P., Misof, K., Zizak, I., Rapp, G., Amenitsch, H., Bernstorff, S. Fibrillar Structure and Mechanical Properties of Collagen. *Journal of Structural Biology* **122**, 119 (1998).
39. Surrao, D. C., Hayami, J., Waldman, S. D. & Amsden, B. G. Self-Crimping, Biodegradable, Electrospun Polymer Microfibers *Biomacromolecules* **11**, 3624 (2010).



Scheme 2-1. Chemical structures of (A) poly(ϵ -caprolactone) and (B) Rhodamine B, and (C) synthesis of cross-linked silanol-terminated PDMS.

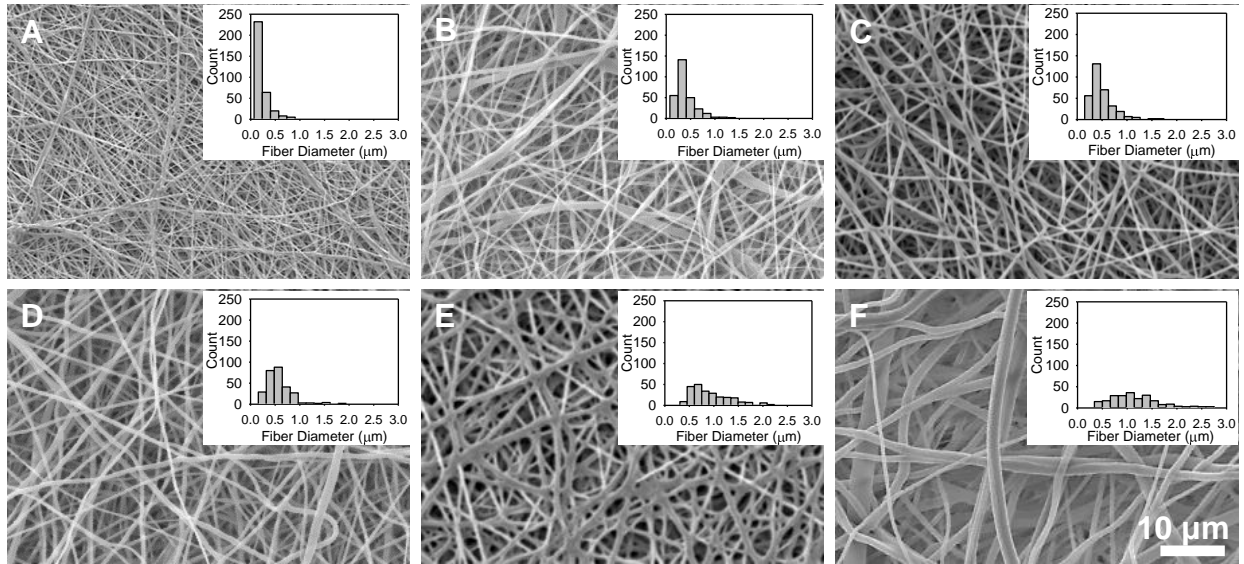


Figure 2-1. Scanning electron microscopy micrographs of PCL fibers containing 0.5 wt % RhB with an average fiber diameter of A) $0.23 \mu\text{m} \pm 0.13 \mu\text{m}$, B) $0.41 \mu\text{m} \pm 0.23 \mu\text{m}$, C) $0.50 \mu\text{m} \pm 0.24 \mu\text{m}$, D) $0.61 \mu\text{m} \pm 0.34 \mu\text{m}$, E) $0.91 \mu\text{m} \pm 0.40 \mu\text{m}$, and F) $1.29 \mu\text{m} \pm 0.63 \mu\text{m}$. Fiber diameter are reported as mean \pm standard deviation for $n > 250$ fibers ($p < 0.05$).

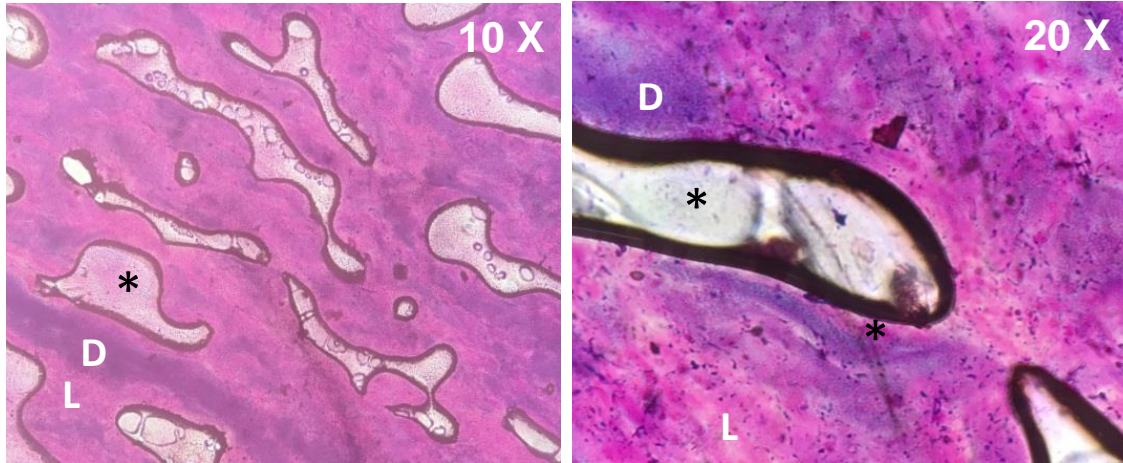


Figure 2-2. Optical microscopy at two magnifications of 2 % RhB/PCL fibers melted at 80 °C. Letters denote areas of light (L) and dark (D) pink regions indicating low and high concentrations of RhB. White regions are air pockets formed during melting, as marked by an asterisk.

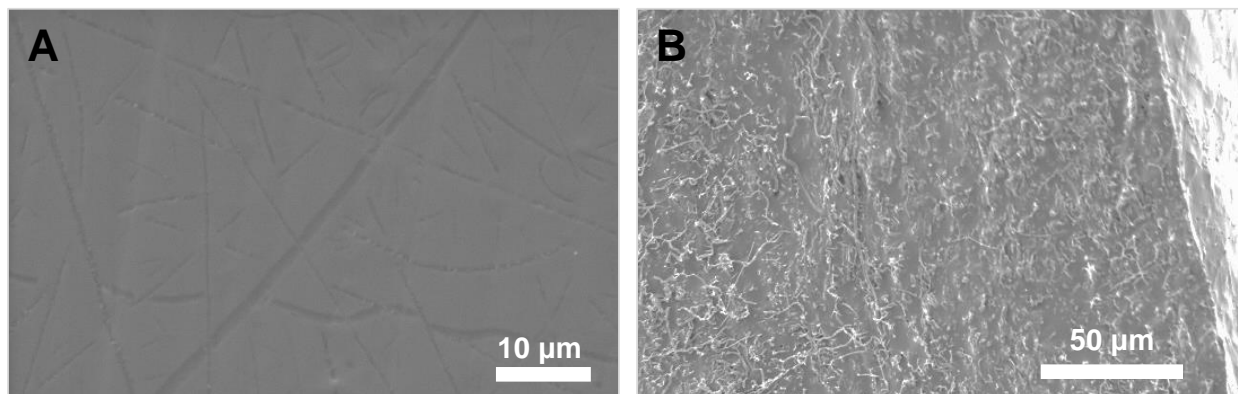


Figure 2-3. Representative scanning electron microscopy micrographs of RhB/PCL-PDMS composite showing the (A) surface and (B) cross-section.

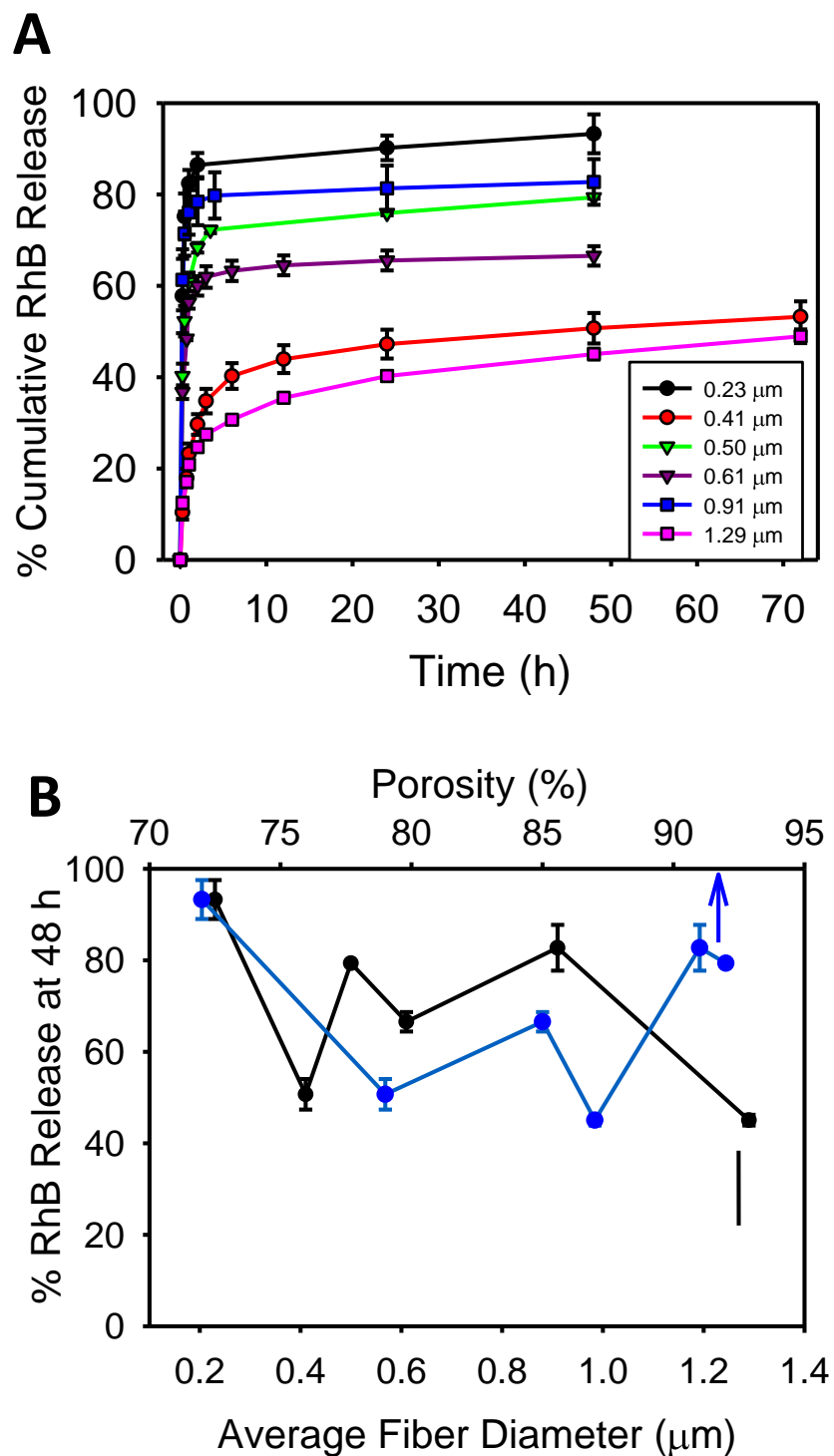


Figure 2-4. (A) Cumulative RhB release from electrospun 0.5 % RhB/PCL fibers of various diameters and (B) a comparison of the cumulative RhB release at 48 h with fiber morphology.

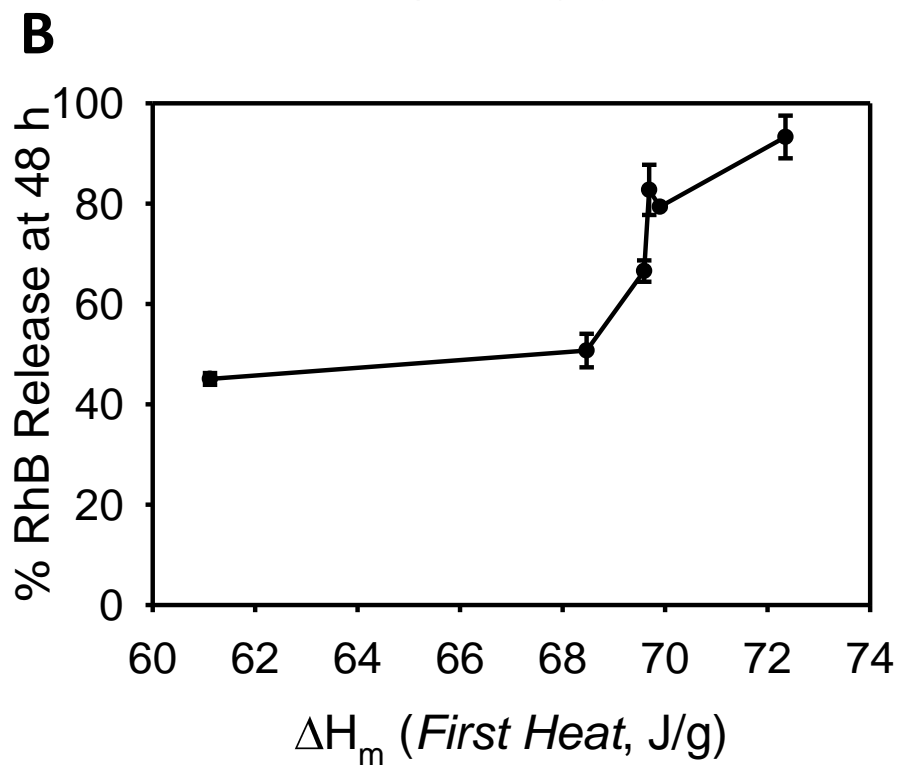
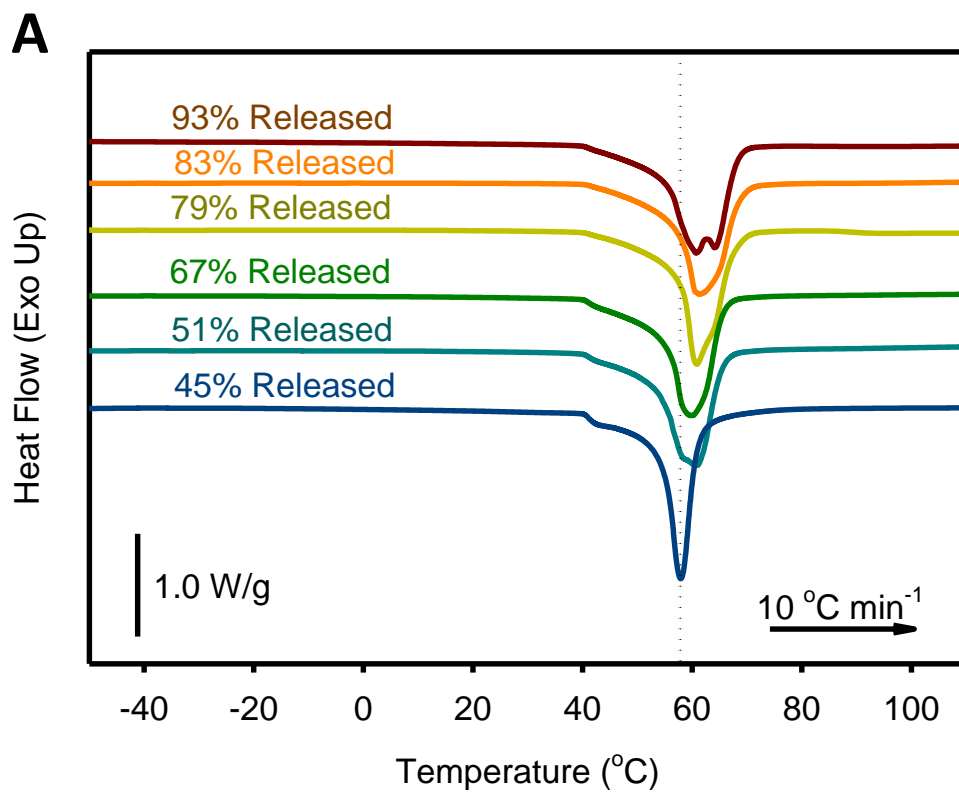


Figure 2-5. First heat DSC thermograms of various fiber diameters of electrospun PCL containing 0.5% RhB in comparison to amount of RhB released at 48 h.

Table 2-1. DSC thermograms of various fiber diameters of electrospun PCL with 0.5 wt % RhB.

Fiber Diameter (μm)	RhB Release at 48 h (%)	$\Delta H_{m,1}^a$ (J/g)	$\Delta H_{m,2}^b$ (J/g)	$T_{m,1}^a$ ($^{\circ}\text{C}$)	$T_{m,2}^b$ ($^{\circ}\text{C}$)	$\Delta H_{c,1}^a$ (J/g)	$T_{c,1}^a$ ($^{\circ}\text{C}$)	χ_1^a (%)
1.29	45.3	61.1	51.4	58.0	56.5	48.7	33.1	44.0
0.41	50.7	68.5	52.9	60.8	57.7	50.3	32.2	49.3
0.61	66.5	69.6	54.6	60.0	59.8	50.1	32.0	50.1
0.50	79.4	69.9	50.2	60.9	57.7	51.2	32.3	50.3
0.91	82.7	69.7	46.3	61.2	58.9	48.6	32.0	50.1
0.23	93.3	72.4	54.3	60.7	58.6	52.5	31.7	52.1

^aDetermined from the first heating cycle.

^bDetermined from the second heating cycle.

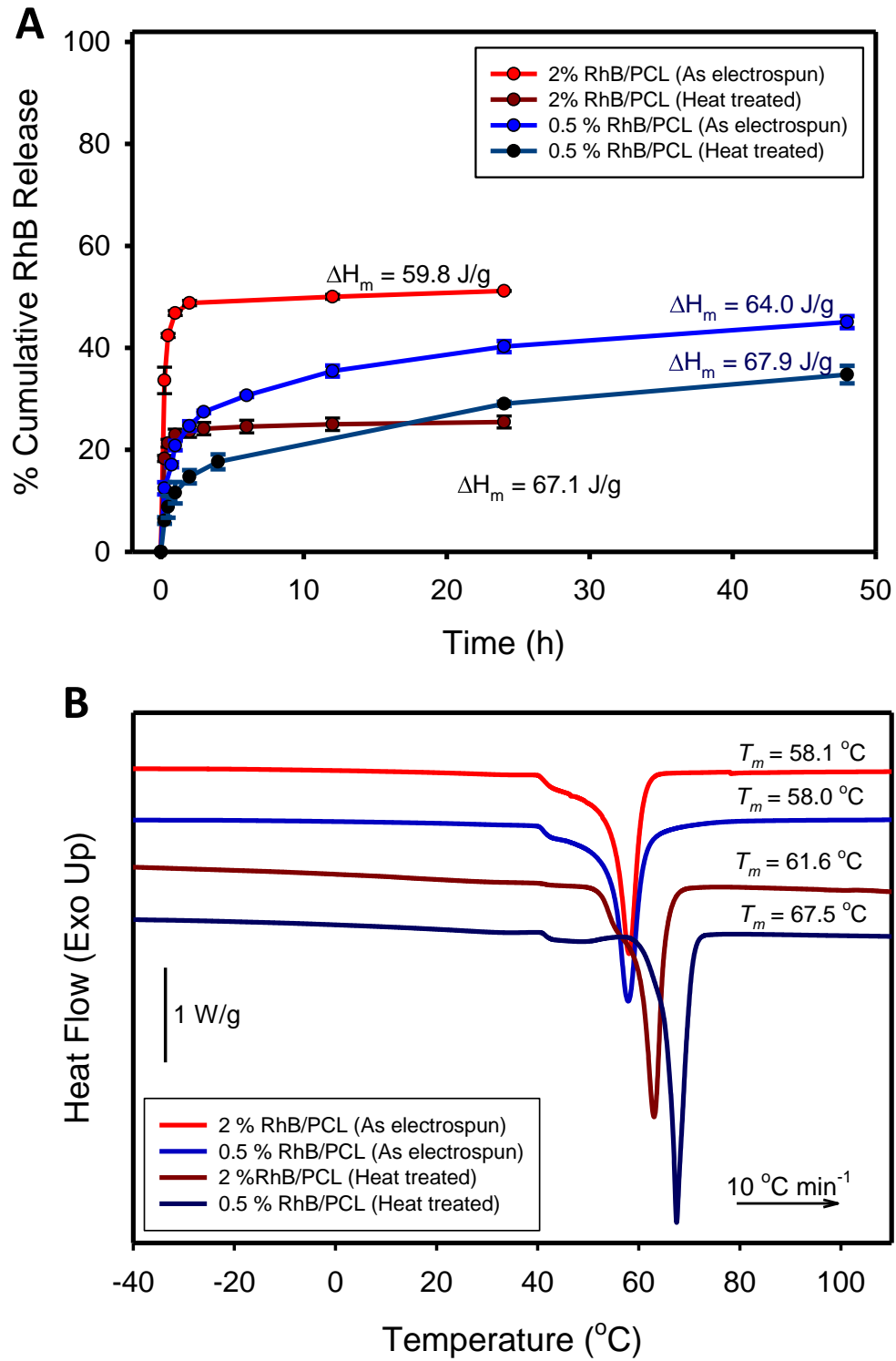


Figure 2-6. (A) Controlled RhB release results and (B) thermal characterization comparing drug release performance following annealing of two concentrations of RhB electrospun in PCL fibers.

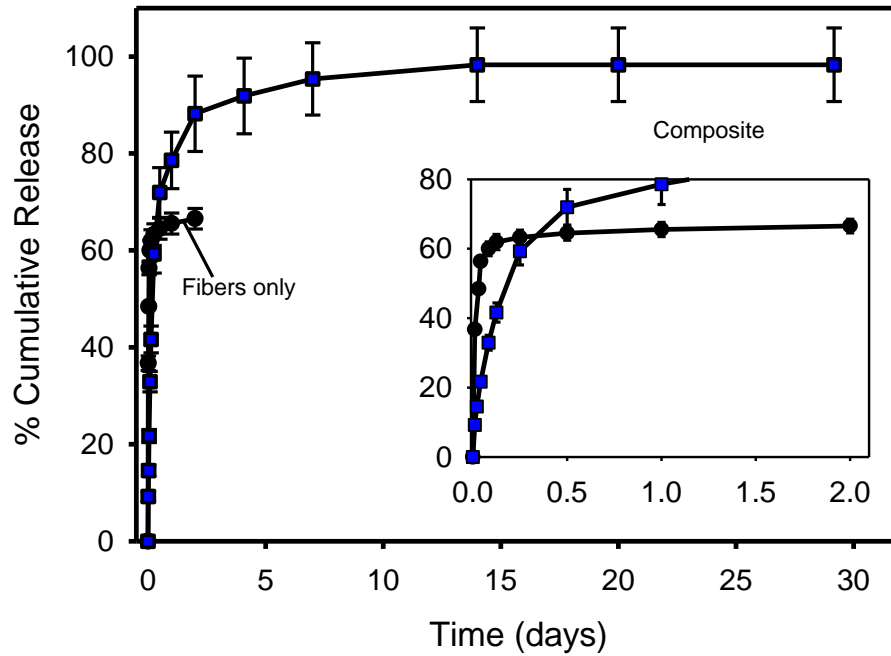


Figure 2-7. Comparison of RhB release from 0.5 % RhB/PCL (fibers only) and 0.5 % RhB/PCL/PDMS (composite) in PBS at 37 °C for samples fabricated from the same parent fiber mat.

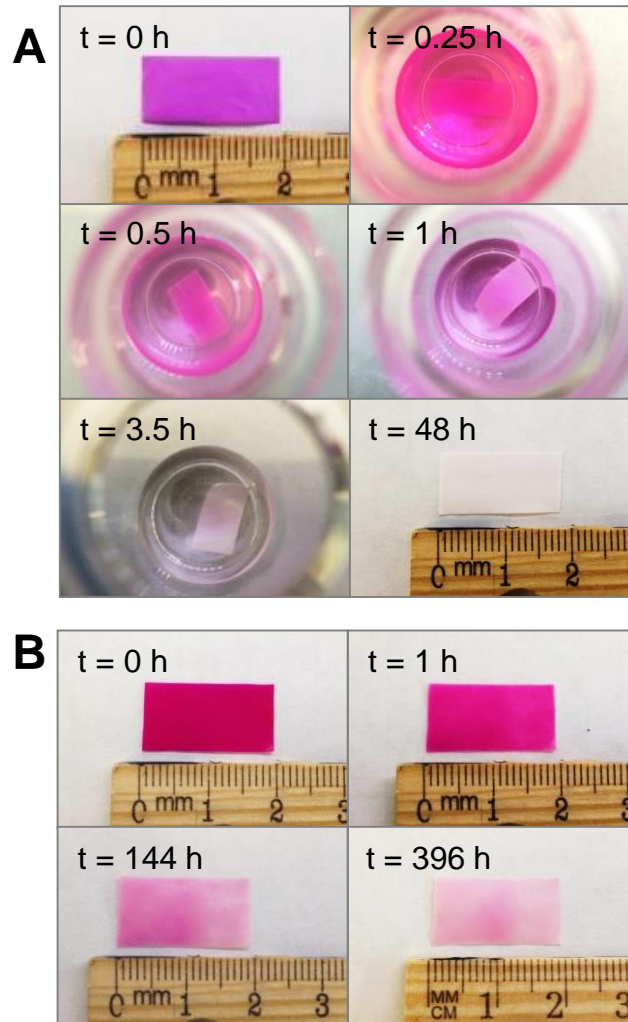


Figure 2-8. Representative samples of (A) 1.5 % RhB/PCL fiber mat and (B) 1.5 % RhB/PCL/PDMS composite after several time points of drug release in PBS at 37 °C. Color loss is due to the release of RhB from the fibers into the surrounding media.

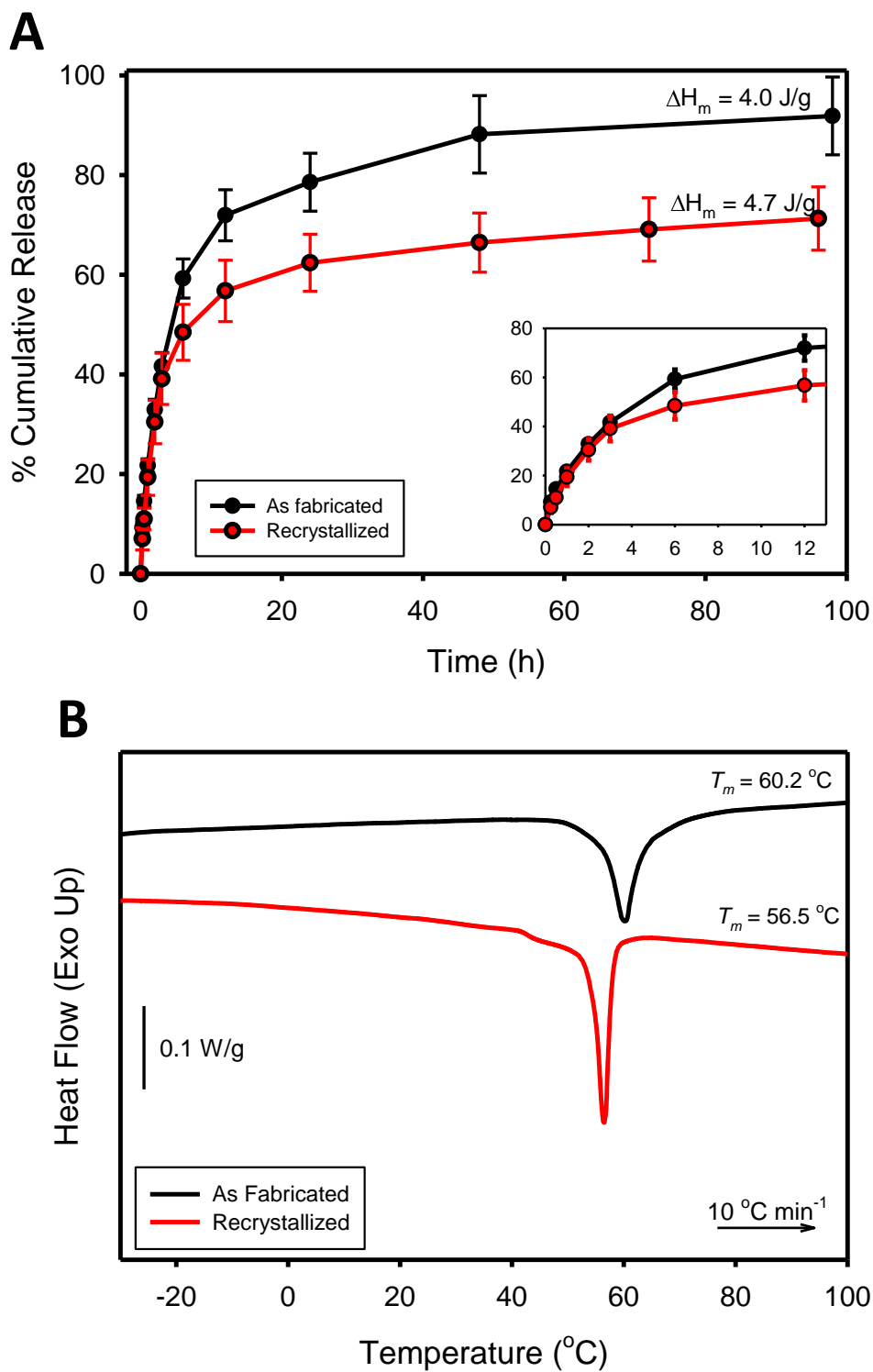
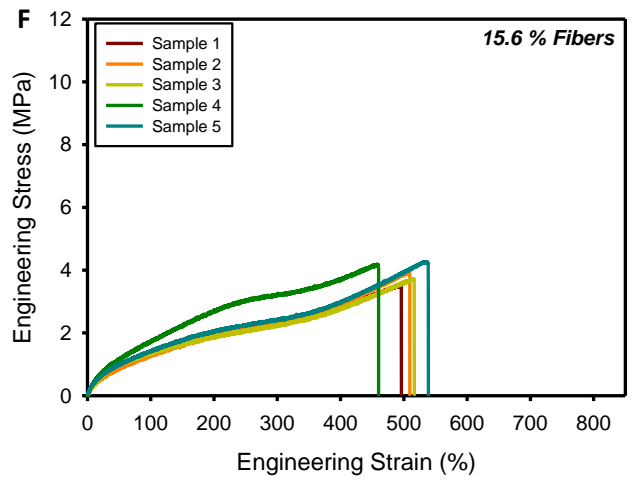
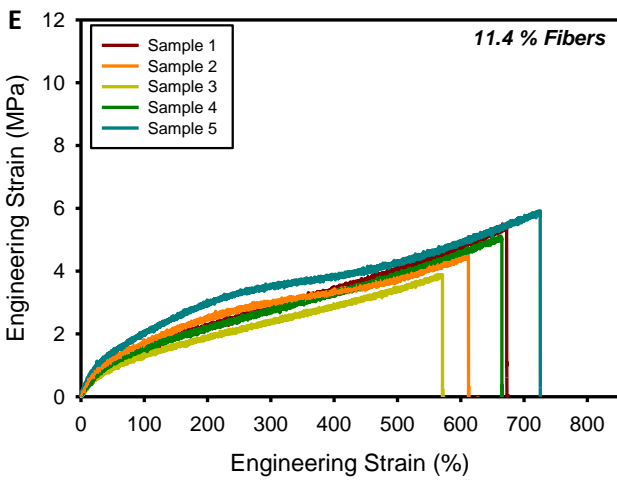
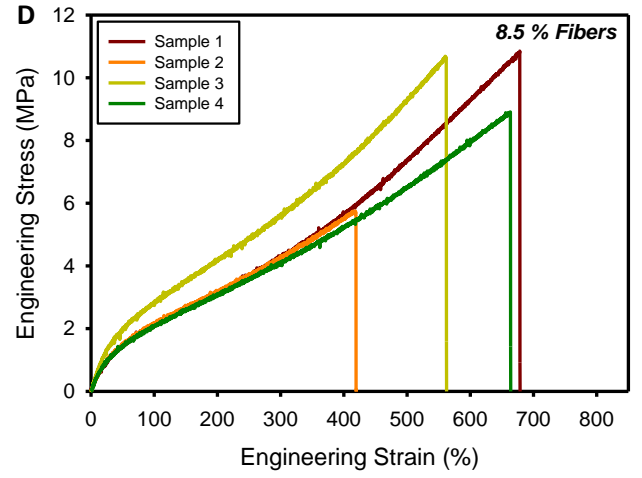
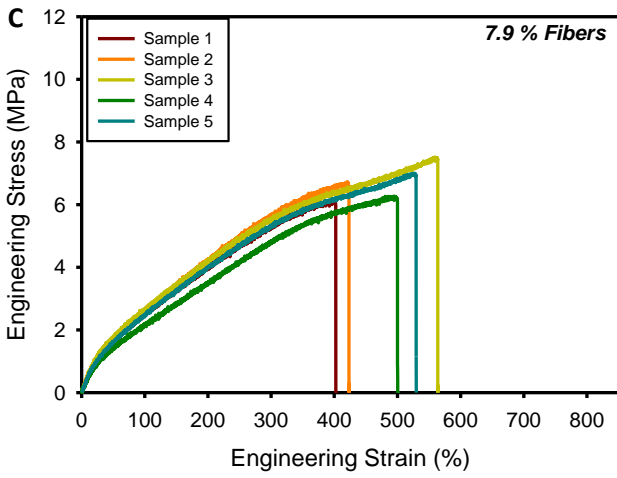
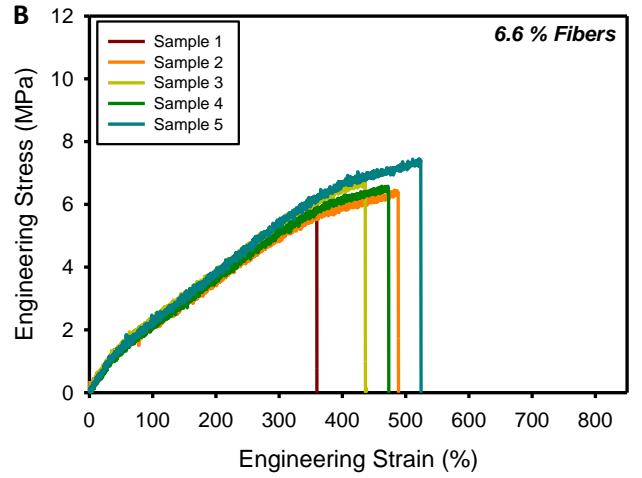
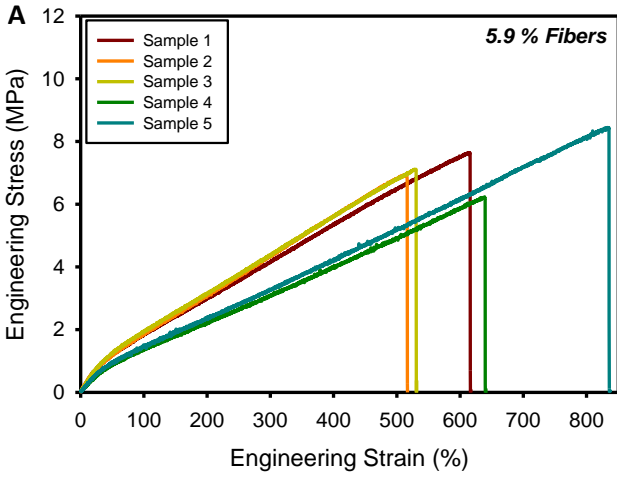


Figure 2-9. (A) Controlled RhB release results and the (B) corresponding thermal characterizations comparing drug release performance following thermal treatment of the PCL/PDMS composite.



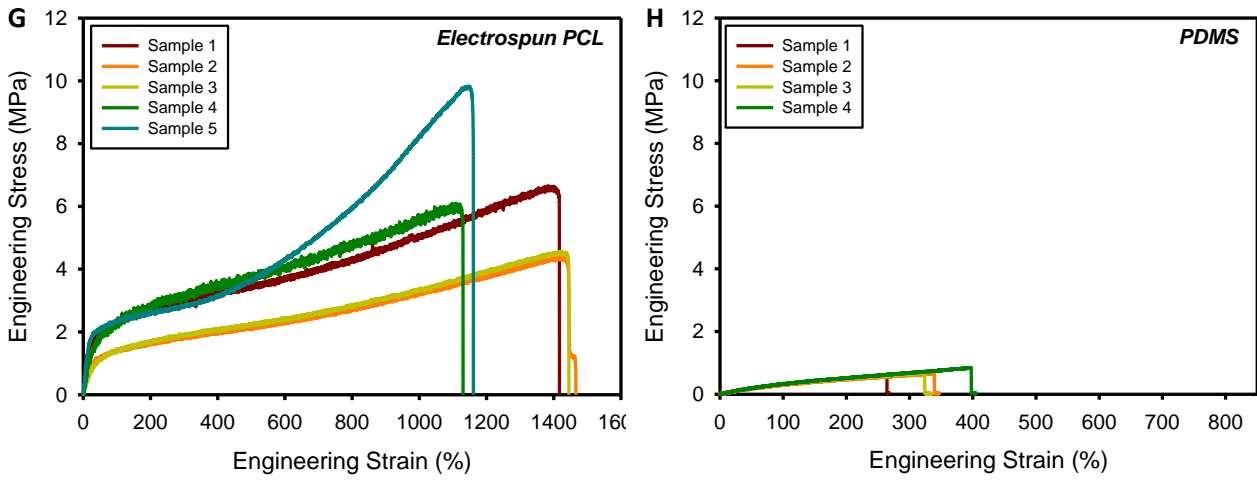


Figure 2-10. Tensile stress-strain curves for the PCL/PDMS composite at various fiber fraction values.

Table 2-2. Summary of tensile mechanical properties of the PCL/PDMS composite.

Sample	Fiber Content (%)^a	Young's Modulus (MPa)	Elongation (%)
PCL/PDMS	5.9	2.7 ± 0.6	640 ± 120
	6.6	3.8 ± 0.9	460 ± 60
	7.9	5.0 ± 0.3	480 ± 70
	8.5	5.0 ± 0.6	580 ± 120
	11.4	3.4 ± 0.9	610 ± 110
	15.6	4.2 ± 0.6	500 ± 30
Electrospun PCL	100	7.1 ± 2.9	1300 ± 140
PDMS	N/A	0.4 ± 0.01	330 ± 50

^aDetermined by DSC

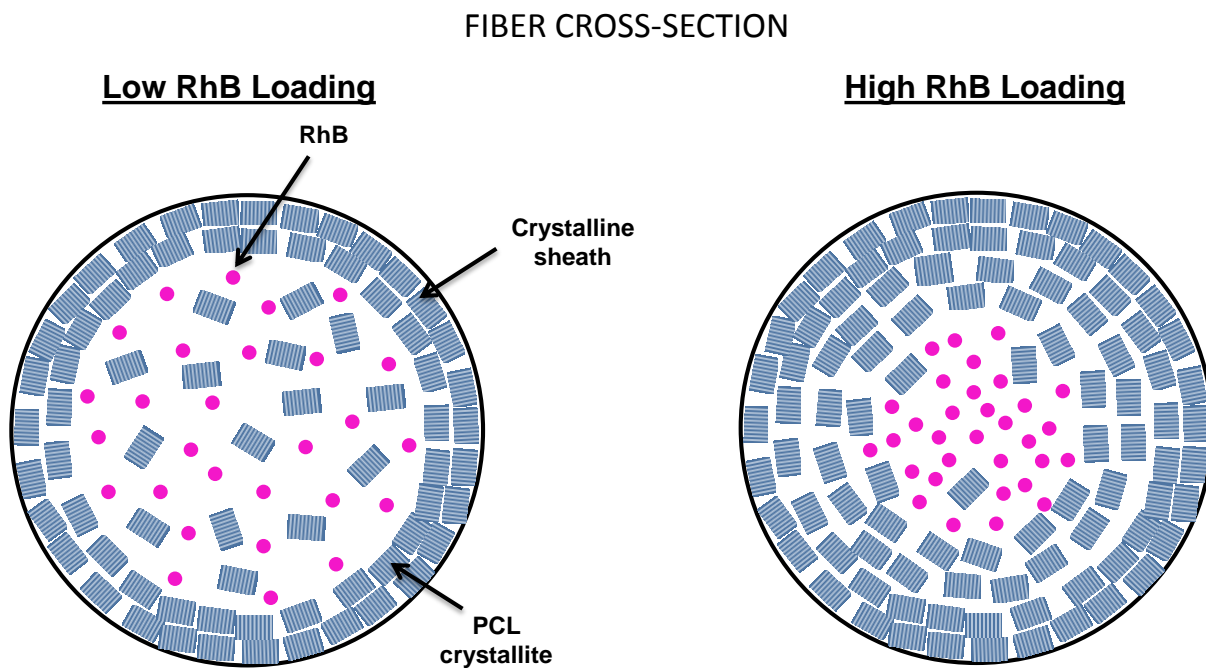


Figure 2-11. Phase separation between hydrophilic model drug Rhodamine B within the PCL fiber.

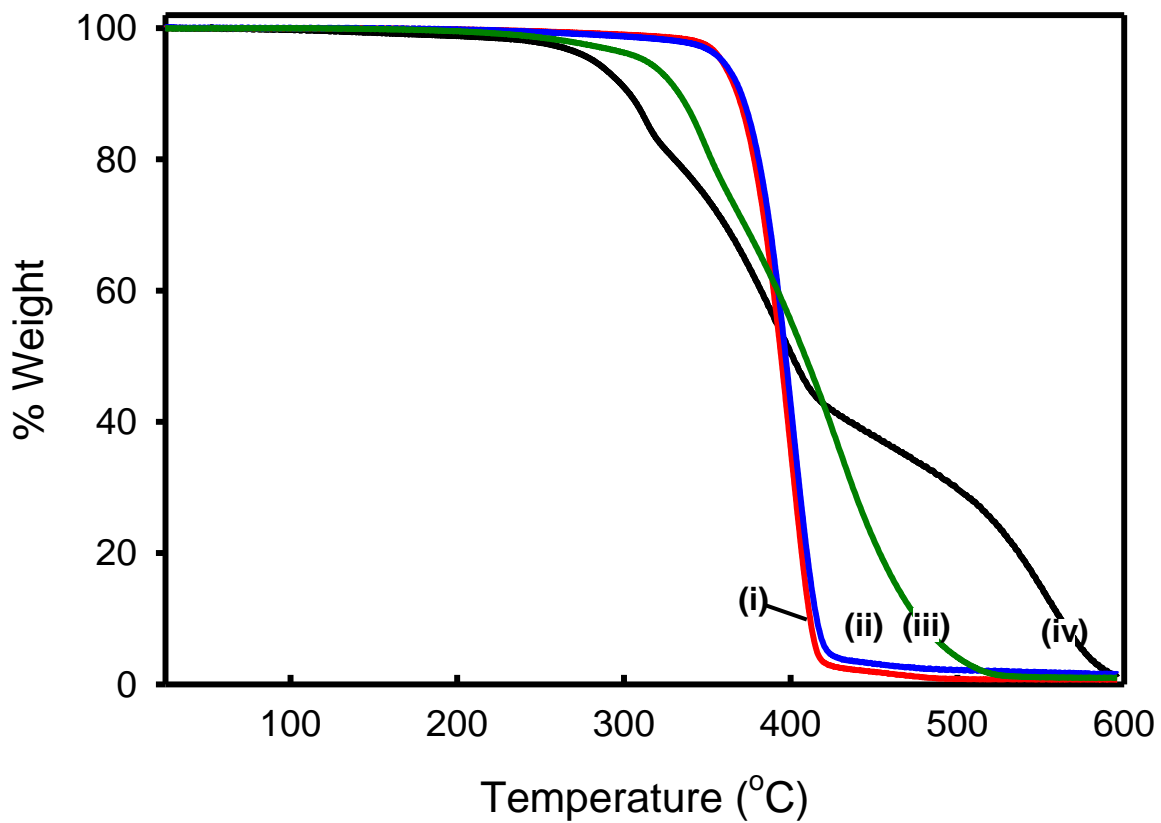


Figure 2-12. Thermogravimetric characterizations of the (i) 0.5 % RhB/PCL, (ii) 1.5 % RhB/PCL, (iii) PDMS, and (iv) 1.5 % RhB/PCL/PDMS composite.

Chapter 3

Nitric Oxide Releasing Shape Memory Elastomeric Composite for Vascular Graft Applications

3.1 Synopsis

The development and characterization of a soft, elastomeric composite with controlled and sustained nitric oxide (NO) releasing capabilities for the prevention of restenosis is presented in this chapter. To avoid the unwanted systemic side effects associated with a free radical such as NO, our approach delivers NO locally to the injured site by supplying it from the vascular graft material. Under *in vitro* physiological conditions, the production of NO from the composite was studied for several weeks, demonstrating that the addition of elastomeric matrix PDMS and adjusting the drug content served to best produce controlled and sustained release. The composite material exhibited suture retention strength comparable to native human arterial tissue and sustained elevated internal pressures in excess of physiological levels. The performance of a vascular graft implant is also dependent on its biocompatibility. Accordingly, a cytocompatibility study was conducted on the NO-releasing composite materials developed in **Chapter 2**, revealing that reducing the tin catalyst used in crosslinking PDMS significantly improved cell viability; however, the NO interacted with the catalytic activity, influencing the silicone crosslinking reaction. The NO-releasing composite was a strong chemottractant to endothelial cells. This material is a good candidate for vascular prosthetics.

3.2 Introduction

End-stage renal disease affected approximately 350 million people in 2013 in the United States alone.¹ Given the limited availability of kidney transplants, hemodialysis is the most

common treatment for kidney failure in order to support the affected patient's life. During hemodialysis, blood is drawn from and returned to the patient through a vascular access site typically formed in the patient's non-dominant upper extremity such as between the radial artery and cephalic vein in the wrist, where an arteriovenous (AV) graft is surgically implanted.² The clinical gold standard for an AV access is to use an AV fistula, a surgically created direct connection between an artery and a vein; however, over 20% of hemodialysis patients, such as those who are diabetic or elderly, are not suitable candidates for AV fistulas due to inadequate diseased veins, and therefore synthetic grafts are the best option in these cases.^{1,3}

Current commercially available prosthetic AV grafts are typically composed of polyethylene terephthalate (Dacron®), or expanded polytetrafluoroethylene (PTFE) (Gore-Tex®) and have a high rate of low patency for small diameter grafts (defined as sized at or below 6 mm in diameter) due to the progression of thrombosis and neointimal hyperplasia. These complications result in a diminished average device lifespan of about two to three years for these devices.⁴⁻⁷ In turn, additional surgical interventions are required and associated treatments total in excess of \$1 billion per year.¹ More specifically, over 70% of AV graft failures are due to stenosis that evolve into thrombosis at or within 3 cm of the vein to graft anastomosis.⁸ The current clinical approach to mitigate these risks includes administration of anti-platelet and anticoagulation drug regimens such as dipyridamole, sulfinpyrazone, ticlopidina, combined aspirin and heparin, which have their own side effects and are not able to maintain full patency long-term, thus simply delaying graft failure.⁹⁻¹¹

Consequently, a great deal of research has been conducted to improve the performance of synthetic vascular grafts. For example, efforts have been made to immobilize heparin, a

commonly used anticoagulant, by such mechanisms as covalent bonding or surface adsorption, either as a polymeric surface coating or within the bulk of PTFE-based grafts; however, the results are a modest improvement at best.^{12,13} Other strategies include controlled release of anti-proliferative agents from the graft material to limit smooth muscle cell migration and proliferation growth on the graft luminal surface that cultivates intimal hyperplasia. For example, Owen et al. developed an injectable thermosensitive degradable polymer gel that can be loaded with paclitaxel, dipyridamole, and/or sirolimus.¹⁴ While the advantage of this approach is that the drug can be replenished, it would require administering ultrasound-guided injections on a weekly basis, with a risk of the gel migrating from the targeted location. Furthermore, the results of this research did not show that neointimal hyperplasia *in vivo* was significantly reduced in the porcine model studied. Following a similar approach, Baek and coworkers found that dip coating ePTFE grafts with sirolimus still resulted in neointimal hyperplasia formation following implantation in pigs, though at a slower rate than the untreated control group.¹⁵ Others have tried directly seeding endothelial cells onto ePTFE grafts for enhanced performance, as yet another approach.¹⁶⁻¹⁸ While these modifications to PTFE show some potential, the long term clinical performance is unknown and expediently obtaining these cells on demand remains a challenge. In addition, these strategies do not address incompatible mechanical properties that also often plague synthetic AV grafts.

Compliance mismatch is a physical problem that also needs to be addressed concurrently with material thromboresistance for an artificial AV graft to successfully function long term. Current synthetic grafts are poorly matched to the native blood vessel, where the Young's modulus of PTFE and Dacron® polyester grafts has been reported to be as high as approximately

0.5 GPa and 14 GPa, respectively, making them significantly stiffer than that of 0.12 – 3.7 MPa reported for native blood vessels.¹⁹⁻²³ As a result, this critical compliance mismatch enables intimal hyperplasia and the ensuing turbulent flow, adding to the reduced graft patency.^{24,25}

Controlled delivery of nitric oxide (NO) from a synthetic graft can potentially resolve the issue of thrombogenicity of prosthetic vascular implants biomimetically. NO is a diatomic molecule naturally produced by endothelial cells (ECs) that is vital to maintaining vascular homeostasis and thromboresistance of the endothelium.²⁶ Integration of NO into the vascular graft material has the added benefit of actively recruiting ECs, suppressing smooth muscle cell (SMC) proliferation and migration, and even inhibiting leukocyte chemotaxis, all which harmoniously work to impede thrombosis and neointimal hyperplasia.^{9,27}

Exogenous NO production can be replicated by incorporating NO donors into vascular graft materials; these donors are synthetic compounds that are capable of decomposing into NO under specific conditions.²⁸ There are several classes of NO donors; however, the most studied are *N*-diazoniumdiolates and *S*-nitrosothiols due their ease of releasing NO under physiological conditions.^{29,30} *N*-diazoniumdiolates are synthesized by reacting primary, secondary amines, or polyamines with NO under high pressure, yielding two moles of NO per amine functional group.⁹ These types of donors dissociate into NO and its corresponding amine in the presence of water, as shown in **Scheme 3-1**, with its decomposition decreasing with increasing pH.³¹ The structure of an amine-functionalized NO donor molecule influences the half-life of the donor at physiological conditions, ranging from a few seconds to 20 h for diethylenetriamine nitric oxide adduct (DETA-NO).³² The other major class of NO donors, *S*-nitrosothiols, are synthesized by reacting a thiol with NO or nitrogen oxides^{28,33} which then release NO following exposure to

UV, heat, oxides, and transition metal ions.³⁴ In light of the nature of the triggers for these types of NO donors, these substances are more useful for applications such as topical patches for wound healing or antimicrobial medical tubing, where external switching is advantageous³⁵ rather than as implants under aqueous flow conditions, unless further modification is done to incorporate the NO release trigger within the delivery vehicle.³⁶

In general, use of any type of NO donor by itself does not provide long term efficacy due to its high reactivity in blood,³⁷ and also does not provide targeted therapy. Given these limiting conditions, many researchers have studied incorporating these molecules into a polymeric vehicle to control the drug release properties. For example, Zhang et al. studied covalently bound NO donor to silicone rubber and demonstrated tunable release by altering the NO donor loading and polymer formulation.³⁸ This silicone rubber exhibited *in vitro* NO release up to 20 d and had some improved thromboresistance in rabbit models, though these results still fall short of the long term patency goals of years. Another group investigated fabricating core-shell fibers where the outer “shell” layer of the polymer fibers was composed of either poly(ϵ -caprolactone) (PCL) or heparin and the inner “core” layer of the fibers were composed of a PCL/NO donor mixture, allowing for NO donor encapsulation and controlled NO release.³⁹ The investigators showed that the NO release profile for the core shell samples exhibited a steadier release than the control groups containing only solid fibers. Additionally, it was found that NO release sustained for just 55 h and involved a significant burst release, which is too short for significant therapeutic effect. Considering that near complete endothelialization of prosthetic surfaces has been reported to vary between a period of 4 – 12 weeks, this time frame is too short to provide adequate therapy.⁴⁰⁻⁴⁴ Although that material demonstrated enhanced mouse fibroblast (3T3) proliferation

after several days, it would have been more significant to the intended application to study the NO release on human aortic endothelial cells (HAECs) proliferation and migration. Other researchers turned to making coatings for cardiovascular devices that would provide the same NO releasing benefit, with sustained release even up to 30 d⁴⁵; however, these strategies didn't address the physical/mechanical limitations of current implants that can also result in thrombosis and NO release is typically up until 24 h.⁴⁶

Composite materials with drug releasing capabilities, such as the drug releasing PCL/PDMS composite introduced in **Chapter 2**, have the potential to meet these multifaceted demands for developing vascular grafts. In the Mather research group, controlled NO release was previously investigated by incorporating donor molecule DETA-NO into a composite composed of a commercially available polydimethylsiloxane (PDMS) (Sylgard 184) and polyvinylacetate (PVAc).^{47,48} This combination of materials exhibited controlled NO release over several weeks; however the effect of NO donor loading in the composite was not studied. Furthermore, the focus of that research was the use of amorphous poly(vinyl acetate) as the fibrous phase, which led to significant shrinkage of the composite dimensions by up to 50% when hydrated, thus not making it an ideal candidate for use as vascular graft.⁴⁹ In **Chapter 2**, a custom cross-linked PDMS chemistry was developed and combined with electrospun PCL fibers to form a composite that demonstrated mechanical properties suitable for vascular graft applications and controlled release of a hydrophilic model drug, which can mitigate these challenges. Therefore, the goal of this work was to investigate the ability of that PCL/PDMS composite to controllably release NO from a hydrophilic donor molecule. We further assessed the suitability of this composite's mechanical properties in an application specific relevant manner by evaluating the suture

retention and burst pressure strengths. The cytocompatibility of the composite was studied with systematic improvements by altering the PDMS crosslinking chemistry. Lastly, the *in vitro* migratory responsiveness of endothelial and smooth muscle cells in the presence of the NO releasing composite was evaluated.

3.3 Methods

3.3.1 Materials

Poly(ϵ -caprolactone) (70,000 – 90,000 g·mol⁻¹), tetrahydrofuran (THF), anhydrous dimethylformamide, and dibutyl tin dilaurate were purchased from Sigma Aldrich and used as received. Diethylenetriamine NONOate (DETA-NO) was purchased from Cayman Chemicals. Silanol-terminated polydimethylsiloxane (2000 cSt) and poly(diethoxysilane) were purchased from Gelest, Inc.

3.3.2 Fabrication of NO-Loaded Electrospun Fibers

NO-loaded fibers were prepared by first dissolving 13 w/v% PCL in 4:1 THF:DMF solvent mixture. NO donor compound DETA-NO was separately mixed with 0.2 ml anhydrous methanol per 10 mg DETA-NO until a homogenous suspension was observed. The DETA-NO suspension was then added to the PCL solution under constant stirring conditions, such that the targeted concentration of DETA-NO was obtained relative to the mass of PCL in the final solution. The DETA-NO/PCL solution was then transferred to a 10 ml syringe fitted with a blunt 22 gauge needle tip. A syringe pump was used to supply a steady flow rate of 1.0 ml · h⁻¹. The solution was electrospun onto a grounded 3 mm – 50 mm diameter aluminum drum rotating at

400 rpm, at a distance of 7 cm from the needle tip and an applied voltage of 11.5 kV. Following electrospinning, all fiber mats were dried at room temperature under vacuum (-30 mm Hg) for 48 h to remove any residual solvents prior to further use and stored at -18 °C in a desiccated container.

3.3.3 Preparation of NO-Loaded Fibrous Elastomeric Composite

A pre-polymer elastomer was prepared by mixing silanol-terminated polydimethylsiloxane (ST-PDMS) with 3 wt% polydiethoxysiloxane (crosslinker) and 0.5 wt% dibutyl tin dilaurate (catalyst) similar to what was previously done by others.⁵⁰ The electrospun drug-loaded PCL fiber mats were then coated by the PDMS mixture, followed by exposure to vacuum at room temperature for 15 min to enable thorough infiltration of PDMS within the fiber mat. Excess PDMS was removed from the surface using a spatula followed by a 72 h cure at room temperature in a desiccator.

3.3.4 Morphology

A JEOL JSM-5600 scanning electron microscope (SEM) was used with an accelerating voltage of 4 – 6 kV. Samples were sputter-coated with gold 45 s prior to imaging. Fiber diameter measurements were determined by taking a minimum of 50 measurements at five different locations using ImageJ software (version 1.46, National Institutes of Health). The average diameter and standard deviation were calculated using a minimum of 250 total measurements. Statistical significance was determined using a one-way analysis of variance (ANOVA) with a significance criterion of $p < 0.05$, using the Minitab software package.

3.3.5 Thermal Characterization

Differential scanning calorimetry (DSC) was performed using a Q200 manufactured by TA Instruments, Inc. Samples weighing 2.5 – 4.0 mg were sealed in Tzero aluminum pans and heated from -60°C to 120°C at 10°C · min⁻¹. The melting enthalpy was calculated from the first heating cycle by integrating the melting peak, and was used to determine the crystallinity of PCL in the elastomeric composite according to:

$$\chi_c(\%) = \frac{\Delta H_m}{\Delta H_f^0} \times 100 \% \quad (3-1)$$

where χ_c is the degree of crystallinity, ΔH_f is the heat of fusion measured by DSC and ΔH_f^0 is the heat of fusion of crystalline PCL, with a literature value of 139 J · g⁻¹.⁵¹

The melting enthalpy was calculated from the second heating cycle by integrating the melting peak, and was used to determine the fraction of PCL (W_{PCL}) in the elastomeric composite by comparing the melting enthalpies according to:

$$W_{PCL}(\%) = \frac{\Delta H_m}{\Delta H_{m,0}} \times 100 \% \quad (3-2)$$

where ΔH_m is the melting enthalpy of the composite measured by DSC and $\Delta H_{m,0}$ is the melting enthalpy of pure electrospun PCL, as determined by DSC.

3.3.6 In Vitro NO Release

Samples of 1 cm x 2 cm were placed in a known volume (4 – 10 ml) of phosphate buffered saline (PBS, pH 7.4) in sealed glass vials and placed in a thermal shaker at 37 °C to simulate physiological conditions. Nitric oxide was indirectly measured using a commercially available Griess reagent assay (Promega Corp.), a widely used technique that

spectrophotometrically measures the concentration of nitrite in the media.⁵² Since NO reacts with oxygen in water to produce nitrite, a stable, non-volatile compound, the total nitrite in PBS was assumed to be due to NO decomposition from the donor compound, where one mole of DETA-NO can release two moles of NO (**Figure 3-1**). The Griess reagent assay process entails first diazotizing the nitrite in the sample buffer with 1% sulfanilamide in 5% phosphoric acid (SA) followed by azo coupling with aqueous 0.1% *N*-1-naphthylethylenediamine dihydrochloride (NED). The resulting chromophore formed by the reaction with NED has an absorbance maximum at 540 nm, which using a plate reader (Biotek® Synergy 2 Microplate Reader). The detection limit for the Griess assay is 125 pmol, which is well below the target NO (nitrite) release concentration. A calibration curve was first prepared for all measurements using known concentrations of nitrite. The NO flux from the samples was determined by converting the measured concentration value to into mass (moles) and dividing by the surface area of the sample and plotting versus time (min). The slope of a linear regression revealed the flux ($\text{mol cm}^{-2} \text{ min}^{-1}$). All testing was conducted in triplicate at each time point, and an average and standard deviation are reported.

3.3.7 Suture Retention Strength

Suture retention strength of the composite was conducted in accordance with ANSI/AAMI/ISO 7198: 1998/2004 “Cardiovascular implants – Tubular vascular prostheses” standard using a tensile tester (Test Resources, Model 100P).⁵³ Samples were cut into rectangles of 2.0 cm by 1.2 cm. One end was secured using a single throw of a commercially available monofilament polypropylene suture of size 5-0 looped once (5-0 Prolene, Ethicon, Piscataway, NJ) into a single loop at 2 mm from the edge and knotted a minimum of five times. The

unsutured end was fastened by the stage clamp while the opposing clamp mounted to transducer was gripped onto the knotted end of the suture. The suture was pulled from the sample at a rate of $50 - 120 \text{ mm} \cdot \text{min}^{-1}$ until the suture completely ripped through the sample wall resulted in failure. The peak force required to pull the suture through the sample is reported as the suture retention strength (N). An average and standard deviation are reported for a total of five samples.

3.3.8 Burst Pressure

Burst pressure testing was performed on tubular graft samples with an inner diameter of 6 mm consistent with other studies.⁵³⁻⁵⁵ The graft tubes were each cut to a minimum length of 3 cm, in accordance with ANSI/AAMI/ISO 7198,⁵³ and were fitted over a custom testing platform that allowed both ends to be secured, as shown in **Figure 3-8A**. The sample was pressurized with water and air bubbles expelled at room temperature using a syringe pump to supply water at 20 mL min^{-1} until failure, as has been reported by others.^{56,57} The internal hydrostatic pressure was measured over time using an in-line pressure gage while the graft diameter was actively measured using a linear laser positioned at a fixed distance and projected onto a screen. The gap or shadow in the projected laser line due to the graft was used to determine the diameter (**Figure 3-8A**). Prior to testing, a standard curve was constructed using known diameter measurements from which the actual external diameter calculated with an accuracy of 0.5 mm. All captured images were calibrated using reference lines of known dimension and analyzed using ImageJ software. The pressure at which the sample bursts was reported as the burst pressure. A sample size of three was used and an average and standard deviation are reported. The hoop stress (σ_H) for a thin-walled tube was calculated using **Eqn. 3-3** below, where P , d , and t refer to the internal

pressure, tube diameter, and tube wall thickness, respectively. A thin wall assumption was used since the ratio of the radius to tube thickness was greater than ten.

$$\sigma_H = \frac{Pd}{2t} \quad (3-3)$$

The compliance (C) was calculated using the burst pressure data and according to **Eqn. 3-4** below, where d_0 refers to the initial, unpressurized diameter.

$$C = \frac{\Delta d}{d\Delta P} \quad (3-4)$$

3.3.9 Kink Resistance

A tubular PCL/PDMS sample was fitted over a flexible, kink-free wire support of diameter 5.9 mm. Shape fixing was conducted by heating the sample above the melting transition of PCL at 60 °C and then deforming the sample into a bend of radius of 0.8 cm or until just before a kink formed, followed by quenching in a freezer at -18 °C to recrystallize the PCL fibers. The sample was then removed from the wire support and a fixed shape was observed and the fixed bend radius was measured. Shape recovery was then triggered by placing the sample in an oven at 60 °C to melt PCL, and enabling the PDMS crosslinks to recover the previously permanently memorized, strain-free shape. The radius of curvature of the recovered shape was then measured. A kink in the tube was defined visually as a large scale buckling in the outer surface of the tube wall at the point of bending.⁵⁸ The radius of curvature of the fixed sample measured using ImageJ image analysis software and compared to the deformed sample before removal from the bent wire support. The fixing ratio, R_f , was calculated using **Eqn. 3-5** below,

where r_d is the radius of curvature of the targeted deformed shape (while on the wire support) and r_f is the radius of curvature of the resulting fixed shape.

$$R_f(\%) = \frac{r_d}{r_f} \times 100\% \quad (3-5)$$

The recovery of the straight tube was assessed according to the recovery ratio below:

$$R_r(\%) = \left(\frac{r_f - r_r}{r_f - L_0} \right) \times 100\% \quad (3-6)$$

where L_0 is the original length, and r_r is the recovered length following heating. The reciprocal value of the radius of curvature was used to describe the curvature of the sample. The critical curvature is the curvature value limit before a kink will occur with increased bending. The critical curvature, shape fixing ratio and standard deviation of three samples per test group was reported.

3.3.10 Cytotoxicity

Sample preparation was conducted according to ISO 10993-5 and ISO 10993-12, where a non-contact extraction-based method was used to determine cytocompatibility.^{59,60} Samples were cut into pieces in order to maintain an extraction ratio of $3 \text{ cm}^2 \cdot \text{ml}^{-1}$ of sample surface area to extract media. All samples were sterilized by ultraviolet light for 1 h per side. Sterilized samples were then incubated in media for a specified sample extraction time (24 – 72 h). Following extraction, the sample media was used to incubate L929 cells for 24 h at 37 °C in 95% humidified air containing 5% CO₂. Cytotoxicity was quantified using the CCK-8 assay to colorimetrically measure mitochondrial activity, an indicator of cell viability. The cell culture media was replaced with 100 uL of 10% (v/v) CCK-8 solution in media was incubated for 4 h.

The absorbance of the samples was measured at 450 nm using a plate reader (Biotek® Synergy 2 Microplate Reader). Cell viability was calculated by dividing the absorbance values of the sample by the absorbance value of the positive control and reported as a percentage of the positive control. A minimum cell viability of 70% or greater was used to determine cytocompatibility.⁵⁸ All testing was conducted in triplicate and a mean and a standard deviation are reported.

3.3.11 Mechanical Characterization

Tensile mechanical properties was studied by punching samples into a dog bone geometry (ASTM Standard D638-03 Type IV, scaled down by a factor of 4), and loading onto a Test Resources Model 100P Universal Testing Machine equipped with a 24 N load cell. The samples were stretched at a rate of $33 \mu\text{m s}^{-1}$, and engineering stress-strain curves were used to determine Young's modulus, strain-to-failure, and tensile strength. Five samples of each type were tested and an average and standard deviation are reported.

3.3.12 Cell Migration Assay

The cell migration was performed in a modified Boyden chamber⁶¹ using 24-well Transwell plates (Corning™ Transwell, 8 μm pore size). All samples were sterilized by ultraviolet light for 1 h per side. Samples punched into 6.5 mm diameter discs were placed in the bottom compartment and allowed to soak in media for 48 h prior to cell seeding to ensure full water uptake through the sample and initiation of NO release. Bovine aortic endothelial cells (BAECs) or bovine smooth muscle cells (BSMCs) from passages 5 and 6, respectively, were cultured for 72 h prior to cell seeding. The cells were suspended in media containing 10% fetal

bovine serum (FBS), 1% GlutaMAX, and 1% penicillin/streptomycin and Dulbecco's modified Eagle's medium (DMEM). The Transwells were then seeded with 10,000 cells in the upper compartment and placing the sample in the bottom compartment with 600 uL of cell culture media. Both the cell culture media and a solution containing 10 μ M of DETA-NO in media were used separately as positive controls. The DETA-NO control was prepared just prior to cell seeding due to its high reactivity and sterilized by filtration (0.20 μ m, Corning®). Serum-reduced media containing 1% FBS was used as the negative control. The assembled migration chambers were incubated for 48 h in a humidified incubator at 37 °C with 5% CO₂ to allow cells to migrate through the Transwell filter. After the migration period, the cells were fixed using 4% formaldehyde in PBS and stained with Alexa Fluor 647 conjugated phalloidin (1:40 dilution, Life Technologies) for actin cytoskeleton visualization and Sytox Green (1:10000 dilution in PBS, Life Technologies) for nucleus staining. Non-migrated cells in the seeding (upper) chamber were removed using a cotton swab, leaving only the migrated cells on the obverse filter surface for analysis. The stained cells were imaged using a Leica DMI 4000B inverted fluorescence microscope equipped with a Leica DFC 340FX camera using a 10X/0.22 NA objective. Pseudocoloring was applied to the images using ImageJ software. The total number of migrated cells from three representative areas per well were quantified using Automated Contour-based Tracking for In Vitro Environments (ACTIVE) software.^{62,63} Each assay test condition was conducted in triplicate wells, and an average and standard deviation are reported.

3.4 Results

3.4.1 Fabrication

PCL fiber mats containing DETA-NO were prepared by electrospinning with an average fiber diameter of $0.91 \mu\text{m} \pm 0.51 \mu\text{m}$ and $0.46 \mu\text{m} \pm 0.24 \mu\text{m}$ for fiber mats loaded with 0.5% and 1.5% DETA-NO, respectively. No drug crystals or particle aggregation were observed on the fiber surfaces, though it may be too small for the SEM resolution limit of the equipment used (**Figure 3-1A-B**). The fiber mats were then successfully imbibed with PDMS, which occupied the interstitial space between the PCL fibers, as shown in **Figure 3-1C-D**. Tubular composite samples (**Figure 3-1E**) were also fabricated by electrospinning the fibers onto a smaller diameter mandrel and were used for burst pressure and shape memory kink testing.

3.4.2 Thermal Characterization

The thermal properties of the NO releasing PCL/PDMS composites are presented in **Figure 3-2** and **Table 3-1**, and compared with their respective components. Both composites are composed of mostly PDMS, comprising approximately 8 – 10% based on a comparison of the melting enthalpies between the fibers and the composites in the second heating cycle. Some variation in the local composition of the composite was expected given that the PDMS deposition and infiltration process is manually performed. The melting endotherm of DETA-NO was not visible in the thermograms.

3.4.3 NO Release

The *in vitro* cumulative drug release profiles of the PCL/PDMS composites doped with two NO donor concentrations were compared to NO release from the non-encapsulated fibers and presented in **Figure 3-3**. Consistent with the drug delivery results in **Chapter 2**, the addition of the crosslinked PDMS elastomeric matrix to the PCL fibers served as a water-regulating composite that suppressed the initial burst release for 0.5% DETA-NO/PCL/PDMS composite, which was reduced from approximately 12% to 9% drug release within the first 3 h. The burst release was not substantially different between the 1.5% DETA-NO/PCL/PDMS composite and its corresponding fiber mat, since both exhibited a 4 % cumulative release by 3 h. Notwithstanding quantitative differences attributed to DETA-NO loading, both composites continued releasing NO long after the fibrous samples stopped and with greater total NO released, also consistent with the drug delivery results in **Chapter 2**.

In general, increasing the concentration of the NO donor in the samples resulted in decreased total NO released over time on a percentage basis, by approximately 16% of theoretical stored NO between composites, and 11% for the fiber mats. After 72 d, the 0.5% DETA-NO/PCL/PDMS composite had released approximately 27% of the theoretical NO, whereas the 1.5% DETA-NO/PCL/PDMS composite had released approximately 12%. Both composites also showed drastically reduced release rates at that time point. In contrast, both fiber mat samples no longer released significant amount of drug after approximately 2 – 3 d, with total concentrations well below their respective composite analogs, totaling to 86% and 94% unreleased drug remaining for the 0.5% DETA-NO/PCL and 1.5% DETA-NO/PCL samples,

respectively. These trends are consistent with what was observed for Rhodamine B release from the same materials discussed in **Chapter 2**.

To assess the physiological relevance of these NO release results, the profile values were converted into flux values by plotting the NO release ($\text{mol} \cdot \text{cm}^{-2}$), normalized by the sample surface area, alongside the release time (in minutes), and divided into four stages, each composed of a linear trend. The slope of best-fit linear regression of each stage revealed the flux in **Figures 3-4** and **3-5**. The flux values both NO concentrations in the composite were observed to progressively decrease over time, as tabulated in **Table 3-2**, however, both composites exhibited sustained NO release for over eight weeks.

3.4.4 Suture Retention

The suture retention strength of the DETA/NO-PCL-PDMS composite was quantified according to ANSI/AAMI/ISO 7198⁶⁴ using a single throw of 5-0 Prolene sutures using a tensile tester as shown in **Figure 3-6**. The suture retention strength was $2.0 \text{ N} \pm 0.4 \text{ N}$ for the composite when tested at $50 \text{ mm} \cdot \text{min}^{-1}$. This average value reduced slightly when tested at faster speeds, resulting in suture retention strengths of $1.6 \text{ N} \pm 0.4 \text{ N}$ and $1.7 \text{ N} \pm 0.4 \text{ N}$ for pull speeds of $100 \text{ mm} \cdot \text{min}^{-1}$ and $120 \text{ mm} \cdot \text{min}^{-1}$, respectively (**Figure 3-7** and **Table 3-3**). These differences due to pull speed were not statistically significantly different at the 95% confidence interval.

3.4.5 Burst Pressure

The burst pressure of the PCL/PDMS composite was tested using a custom testing platform shown in **Figure 3-8**. The average burst strength was $1508 \text{ mm Hg} \pm 284 \text{ mm Hg}$, which was over 12 times greater than the physiological pressure of human arteries of 120 mmHg

which was specified by ANSI 7198.⁴¹ The estimated hoop stress (**Eqn. 3-3**) based on the burst pressure value was 11,310 mm Hg (1.5 MPa), which was slightly lower than average tensile strength of the PCL/PDMS composite of approximately 7 MPa reported in **Chapter 2**. The resulting compliance, based on the burst pressure data was determined to be approximately 0.028 % mm Hg⁻¹ ± 0.005 % mm Hg⁻¹, which was lower than the value of approximately 0.44 % mm Hg⁻¹ reported for the saphenous vein.⁶⁵ Since compliance is dependent on sample thickness, a reverse calculation (assuming a Young's modulus of 3.85 MPa reported in **Chapter 2**) estimated that decreasing the sample thickness to between 0.1 to 0.2 mm would achieve the literature reported value for saphenous veins. The failure of the composite sample under high hydrostatic pressure progressed as localized plastic deformation, where whitening (akin to crazing of amorphous polymers undergoing fracture) of the composite was observed at the site where water leaked from the graft sample, as shown in **Figures 3-8B** and **3-9B**. A linear relationship was observed between the internal pressure and diameter expansion until the diameter expansion was approximately 130 – 150% of its original diameter, at which point continued inflation did not substantially increase the internal pressure before failure occurred.

3.4.6 Kink Resistance

The results of fixing tubular samples of the composite into a kink-free, looped shape of varying tube diameters and wall thickness are presented in **Figures 3-10** and **3-11**. The two wall thicknesses tested for 3 mm graft samples were: 0.19 mm ± 0.05 mm (“thin”) and 0.34 mm ± 0.07 mm (“thick”). The two wall thicknesses for the 6 mm graft samples were: 0.17 mm ± 0.09 mm (“thin”) and 0.47 mm ± 0.01 mm (“thick”). The permanent (original) shape of this sample was a straight tube, which was then deformed into a kink-free bend as described in Section 3.3.9.

All samples exhibited full shape recovery within seconds of stress-free exposure to 60 °C in an isothermal oven, as can be seen in **Figure 3-10**. For two graft sizes, the critical curvature increased when the wall thickness was increased, particularly for the 6 mm graft, as shown in **Figure 3-11A**. The 6 mm graft displayed some wrinkling on the surface when the wall thickness was decreased. Reducing the clearance between the fixing wire support and the sample aided in limiting wrinkle formation; however some wrinkle formation occurred for the 3 mm grafts with thicker walls. These wrinkles were local surface features much smaller than the tube diameter, unlike a kink, which is a large-scale occlusion of the tube lumen, caused by mechanical buckling during tube flexure. The shape fixing ratio, presented in **Figure 3-11B**, increased for both the 3 mm and 6 mm samples when the wall thickness decreased.

3.4.7 Cytotoxicity

The cell viability results of the NO releasing composite and its individual components shown in **Figure 3-12(A)**. The electrospun PCL, both with and without DETA-NO, demonstrated cytocompatibility at $125\% \pm 20\%$ and $124\% \pm 11\%$, respectively, with no significant difference due to the addition of DETA-NO after 24 h of material extraction. Additional extraction time in media slightly decreased viability to $96\% \pm 0.2\%$ for electrospun PCL and $92\% \pm 0.1\%$ electrospun PCL with DETA-NO, which was well above the 70% threshold for cytocompatibility. When PCL was combined with PDMS to form the composite, the resulting cell viability was $22\% \pm 3\%$ cell at 24 h, which was not significantly different than cast PDMS films, which had a cell viability of $23\% \pm 3$.

Based on the above results, it was hypothesized that the source of toxicity was residual tin catalyst (DBTDL) used to synthesize crosslinked PDMS. To test this hypothesis, PDMS was

then synthesized using different concentrations of DBTDL. The resulting cell viability in **Figure 3-12(B)** showed that increasing the DBTDL concentration from 0.25% up to 1% resulted in poor cell viability ranging from $25\% \pm 7\%$ to $39\% \pm 6\%$, with slightly greater viability at lower catalyst concentration. Cell viability significantly improved to $98\% \pm 9\%$ when PDMS was synthesized using 0.1% DBTDL. These findings were then used to improve the cytocompatibility of the NO-releasing composite by crosslinking PDMS using a lower DBTDL level; however, it was discovered that while the SMEC containing 0.1% DBTDL had no issues curing, the addition of DETA-NO prevented complete cure of the PDMS, even after 14 d at 50 °C, which is more than sufficient to crosslink PDMS (data not shown). **Figure 3-12(C)** shows the cell viability results of drug-loaded and neat composite at different DBTDL concentrations. Consistent with the cell viability results for PDMS in **Figure 3-12(B)**, only the composite containing 0.1% catalyst was similarly cytocompatible with a cell viability of $94\% \pm 11\%$. Since the DETA-NO containing composite could not be tested using a DBTDL concentration of 0.1% due to poor cure, only the cell viability results for DBTDL concentrations of 0.25% and 0.5% are shown. The cell viability significantly improved when DETA-NO was added to the composite by up to 60% for the composite containing 0.25% DBTDL, and 26% for composite containing 0.5% DBTDL. Based on these results, it was postulated that DETA-NO possibly counteracted the catalytic activity of DBTDL, which may explain why at very low levels of DBTDL, the DETA-NO releasing composite was unable to cure even at aggressive conditions. Furthermore, this may explain why these samples exhibited better cytocompatibility at higher concentrations compared to the composite without DETA-NO. The DETA-NO/SMEC containing 0.25% was determined to be cytocompatible based on a cell viability of $73\% \pm 6\%$

relative to the positive control. Given that reducing the catalyst concentration further affected the ability for PDMS to cure, this DBTDL composition (0.25%) was selected for chemotaxis studies described in Section 3.3.10.

Figure 3-12(D) showed that the cell viability for DETA-NO concentrations of 0.1 μM to 100 μM in cell media was significantly greater than 70%, with values ranging from $94\% \pm 19\%$ to $117\% \pm 18\%$, indicating cytocompatibility and even cell growth; only a DETA-NO concentration of 1000 μM showed strong cytotoxicity, which was comparable to the negative control. Based on these results, a 10 μM DETA-NO solution was selected to use as a second positive control in the chemotaxis study described in Section 3.4.10. The tensile testing results in **Figure 3-13** and **Table 3-4** showed no significant differences in the mechanical properties of the crosslinked PDMS at catalyst concentrations between 0.1 wt% to 1.0 wt%.

3.4.8 Migration Assay

The *in vitro* migration of BAECs and BSMCs was evaluated in the presence of the 0.5% DETA-NO/PCL/PDMS composite and summarized in **Figure 3-14**. Following 48 h of cell migration, there was significantly greater cell migration toward the NO-releasing PCL/PDMS composite, which was not significantly different than the DETA-NO positive control for both cell types. The BSMCs also migrated in response to NO, independent of NO source, whether from the composite or positive control, though with highly variable results, as indicated by the large error bars for the BSMCs in **Figure 3-14**. The PCL/PDMS composite without drug exhibited significantly less BAEC and BSMC migration than the doped composite. The least overall amount of migration activity was observed for both the media and the serum-reduced media controls, with no significant difference in cell count between the two media conditions. In

general, there was no statistical difference between the cell migration populations of the BAECs and the BSMCs in all the test conditions, as both cell types migrated in similar patterns. The morphology of the migrated BAECs and BSMCs shown in **Figures 3-15** and **3-16** were consistent healthy ECs and SMCs.

3.5 Discussion

PCL and PDMS have each been widely studied for use in medical devices owing to their excellent biocompatibility properties.^{66,67} The combination of these two materials to form a drug-releasing elastomeric composite with controlled release of a hydrophilic model drug was studied in **Chapter 2**. This chapter served to further study this composite material for a vascular graft application, this time incorporating an NO-releasing molecule, considering that the composite also demonstrated good mechanical properties to substitute human blood vessels, as discussed in **Chapter 2**.

In healthy blood vessels, the endothelial lining of the luminal surface of prevents restenosis due to the continuous EC release of NO that provides a non-thrombogenic blood-contacting surface.⁶⁸ To mimic this effect, DETA-NO was selected as the NO donor to integrate into the PCL/PDMS composite due to its relatively long half-life of 20 h in aqueous solution at 37 °C. The addition of the PDMS elastomeric matrix served to sustain NO release due to its water-regulating properties, while although hydrophobic, is semi-permeable to water.⁶⁹ The spontaneous release initially observed within the first few hours is likely due to NO donor readily accessible at the surface and was greatly reduced by the addition of the PDMS matrix, which served to shield the NO donor from instant dissociation in water. We attribute subsequent release of NO donor to diffusion from the bulk of the PCL fibrous framework. We had

hypothesized that increasing the NO donor concentration would increase both the total amount released (on a percentage basis) and the accompanying release rate; however, the opposite trend occurred. This result occurred despite the composite with lower drug loading exhibited slightly more PCL crystallinity and larger fiber diameters, both which may act as a hindrance to drug release as was determined in **Chapter 2**. We surmise that this may be due to added entrapment of drug within the fiber core. This type of indirect correlation between drug loading and release has been observed in other controlled drug release systems, particularly in drug encapsulated micro- and nanospheres, where it was suggested that above a particular concentration the drug dispersion throughout the polymer matrix becomes heterogeneous, thus impeding release.⁷⁰⁻⁷³ In systems where drug has poor miscibility in the polymeric carrier, the drug may be crystalline or appear as aggregates, rather than exist as a molecular dispersion within the matrix, and may require an additional step of first being dissolved by the external aqueous environment prior to beginning diffusion out of the polymer, thus resulting in reduced release at higher loading.⁷⁴ The crystallinity of PCL would also provide domains that would impede water penetration and thus drug diffusion out, which is what we found in **Chapter 2**, where the PCL/PDMS composite also showed less release as the loading of a hydrophilic model drug Rhodamine B increased. Considering that a suspension of DETA-NO in PCL was electrospun, the resulting fibers likely did not contain uniform drug dispersion throughout the cross-section and this is more evident as the concentration is increased. Since the solubility of the DETA-NO solution in the electrospinning solution was limited, it is likely that phase separation between DETA-NO and PCL occurred while the electrospinning solvent evaporated during fiber formation and that the recrystallization of PCL during this stage further encased the drug within the fiber core. This was

supported by the observation that the 0.5% DETA-NO samples were slightly more crystalline than the 1.5% samples and still released more, further supporting the notion that the observed drug release pattern was a result of phase separation. Additionally, the differences in total drug release between the fibrous samples and the composites was consistent with that observed in **Chapter 2**, where the composite samples released more total drug. We postulate that this difference may be due to trapped air in the fiber mats that may block drug diffusion into the aqueous media, which is not present in the composite, where PDMS wets the surfaces of fiber and media, displacing the air that may otherwise block release.

NO release of the native endothelium has been reported to be within $0.05 - 0.1 \text{ nmol cm}^{-2} \text{ min}^{-1}$.⁷⁵ The 0.5% DETA-NO/PCL/PDMS composite was found to release within this order of magnitude during the first 3 d in PBS at 37 °C (**Figure 3-4** and **Table 3-2**). The initial burst and ensuing NO release during this period may be critical to preventing restenosis by SMC migration and proliferation, which can occur approximately 24 h following surgical intervention that triggers vascular injury, with maximum activity at 48 h.⁷⁶ The subsequent long-term sustained NO release is necessary for continued suppression of SMC proliferation while supporting endothelialization for ultimately building confluency, which generally occurs within of 4 – 12 weeks following implantation.⁴⁰⁻⁴⁴ Host body responses to synthetic vascular grafts occur immediately upon contact with blood, beginning with protein adsorption, platelet adhesion within several hours, followed by EC and SMC migration.^{77,78} It has been reported that up to 18% of synthetic vascular grafts for dialysis fail due to thrombosis within the first 3 weeks;⁷⁹ ideally, a vascular graft would last for the life of the patient with no need for additional surgeries to replace with another graft, though such a synthetic option currently does not exist. Compared

to those options, our composite material is an improvement since it has demonstrated the potential for continuous mediation of EC advancement through NO release for over two months. Although the NO flux in the later stages (**Table 3-2**) was found to be below NO release by native endothelial cells, this can potentially be improved by implementing a thermal treatment to the composite to reduce the PCL crystallinity, as determined in **Chapter 2**, and may even be sufficient when combined with the endothelial cell based NO release.

In order to be successful as a vascular graft implant, the material must be able to support sutures under tension during and after surgery. The suture retention strength is an indicator of anastomotic strength, which is can also be affected by suture needle thickness, needle shape, and the material and thickness of the suture; these factors are typically not controlled or standardized.^{80,80} The suture retention strength of human saphenous veins using the same suture has been reported to be $1.92 \text{ N} \pm 0.02 \text{ N}$, which was comparable to that for our composite material.^{81,81} Generally, researchers use an approximate value of 2.0 N as the minimum acceptable strength for prosthetic vascular graft materials, though the testing tensile speeds used are not standardized in the field.⁸²⁻⁸⁵ Since the ANSI procedure calls for a wide range of $50 - 200 \text{ mm} \cdot \text{min}^{-1}$, our composite was tested at three different speeds, with no statistical significant difference in the suture retention strength between the speeds, though the strength decreased slightly with increasing pull speed. We postulated that this strength can be improved by optimizing the volume fraction and crystallinity of PCL fibers in the composite.

Healthy human arteries can withstand systolic blood pressures of approximately 120 mm Hg.⁸⁶ Our PCL/PDMS composite material demonstrated an average burst pressure of $1508 \text{ mm Hg} \pm 284 \text{ mm Hg}$, which was more than twice that of the currently acceptable commercial

options, such as non-elastomeric ePTFE which has a reported burst pressure of ~ 600 mm Hg,²¹ and over 12 times greater than blood pressure. Although the clinical requirement for vascular graft prosthetics is approximately 2000 mm Hg (38.7 psi), this is in order to ensure that it performs beyond any expected physiological thresholds and is based on the incredible burst strength of the human saphenous vein, but is also in great excess of systolic pressure, as has been pointed out by others.^{57,87} Burst pressure strength of graft materials have been shown to be dependent on the rate of inflation, where higher inflation rates lead to lower burst pressure results.⁸⁸ In this study, the PCL/PDMS composite material was tested using an aggressive rate and was still able to achieve a high value, which demonstrated the robustness of this material. The nonlinear behavior of the graft under high pressures was suggestive of irreversible plastic deformation and has been referred to as the aneurysmal point in the vascular graft.⁸⁸ The point of failure of the graft consistently occurred central to the clamped areas and presented as small punctures or slits in the material, surrounded by “crazed” (or whitened) areas (**Figure 3-9B**). Unlike other vascular substitutes, our samples did not exhibit perspiration of water during pressurization,⁸⁸ indicating good adhesion between the fibrous and elastomeric phases during dilation since no pores were formed. It is likely that any minor defect in the fiber/matrix distribution from the manual fabrication process attributed to a compromised region for stresses to concentrate; optimizing the graft fabrication and testing at a lower inflation rate would likely improve the burst strength and reduce the variation in the average values. Burst pressure is also inherently higher for smaller diameters and greater wall thicknesses, and considering that we only tested the largest diameter for a small graft, we anticipate that the strength will only

improve. In any case, our composite greatly exceeded physiological pressures and showed great potential to meet the preferred clinical target and is an adequate substitute for blood vessels.

Kink resistance of the composites was studied to assess the potential to form a loop for precision surgical placement as is typical of many arteriovenous procedures.⁸⁹ Failure to prevent kinking of the graft during surgical placement can impede blood flow and lead to graft failure. In this work, the shape memory properties of the PCL/PDMS composite were exploited to provide tailorable loop configurations, which were quantified by measuring the bend radius before a kink appeared with additional applied stress. The larger graft size was prone to surface wrinkling as the wall thickness decreased. For both sizes, increasing the wall thickness improved kink resistance by enabling tighter loops to be formed without kink development. It is likely that the thicker tube walls resisted the wall thinning associated with tube bending that predisposes it to wrinkling and kinking.⁹⁰ Reducing the clearance between the fixing wire support and the sample aided in limiting wrinkle formation; however some wrinkle formation occurred for the smaller grafts with thicker walls. These particular wrinkle formations (**Figure 3-10H**) were local surface features on the outer surface of the bend, much smaller than the diameter, and unlike a kink, which is a large-scale occlusion of the tube lumen caused by mechanical buckling during tube flexure. This wrinkling behavior dependence on thickness and diameter are consistent with what has been reported for bending hollow aluminum alloy tubes.⁹⁰ We also observed that the fixing ratio for tube bending was improved for samples with thinner walls, regardless of diameter. We postulate that this may be due to an imbalance of contributing forces between the fixing fibrous and elastomeric phases, and that future optimization of these volume fractions can improve this result. Unlike other biomedical materials, this graft material will maintain its looped

configuration upon release of the load due to its inherent shape memory effect, thereby being more likely to maintain its shape during the desired application. The looped formation can be reformed by simply heating the sample above 60 °C to recover its original straight shape, and the shape programming cycle can be reactivated as needed. The programming temperatures are well above physiological temperatures and accidental recovery of the shape will not occur post-implantation.

Many polymers commonly used for biomedical applications, such as polyurethanes and silicones, rely on the use of heavy metal catalysts such as DBTDL or stannous octoate in their syntheses or crosslinking reactions.⁹¹ Given that these organotin catalysts are known to be cytotoxic, some researchers have sought to avoid employing these types of catalysts^{92,93} while others have demonstrated cytocompatibility of their materials.⁹⁴ More specifically, the polycondensation or room temperature vulcanization of siloxanes frequently utilize organotin catalysts such as DBTDL.^{50,95,96} In this study, we identified that the cytotoxicity of the tin catalyst could be mitigated by reducing the concentration of the catalyst in the cross-linking reaction of PDMS, as demonstrated in **Figure 3-12(B)**; this approach has been similarly employed by others. For example, Zhang and coworkers developed an NO-releasing silicone rubber that employed comparable polycondensation chemistry to crosslink PDMS, using DBTDL as the catalyst.³⁸ While they determined that catalyst levels of 0.03% to 0.5% was sufficient to cure PDMS, no cytotoxicity was reported in this study. It is also unlikely that they would have observed any NO interference with PDMS curing since the films were cured prior to diazeniumdiolation of the pendant amine groups. In another study, Pretti and coworkers studied the ecotoxicology of PDMS coatings, also synthesized using similar chemistry.⁹⁷ Here, they

compared a tin catalyst (dibutyltin diacetate) to a bismuth-based one (bismuth neodecanoate) and found that after 14 d of leaching in seawater, only the tin-based crosslinked PDMS exhibited toxicity to the marine organisms studied using a concentration of 0.1%. In contrast, Zhu et al. developed a PDMS-based polyurethane copolymer membrane that showed good cell viability using 0.1 wt% DBTDL as the catalyst concentration, which was consistent with our results.⁹⁴ In our study, we also observed that the addition of NO donor DETA-NO to the composite appeared to interfere with the PDMS crosslinking reaction at a very low catalyst concentration, such that only those composites fabricated without the NO donor were able to cure at this concentration. We hypothesized that the NO donor may be poisoning enough of tin catalyst to prevent the crosslinking reaction at low catalyst concentrations. Furthermore, since the NO-releasing composite became more cytocompatible with the addition of DETA-NO, we also postulated that the NO possibly counteracts the catalytic activity of DBTDL. In light of this, a catalyst concentration of 0.25 wt% was selected for further cell culture testing of the NO releasing composite due to the favorable cytocompatible results and ability to cure. Additionally, the mechanical properties of PDMS at varying catalyst concentrations showed no compromise in strength or elasticity.

The ability of the NO-releasing composite material to attract endothelial cells and deter smooth muscle cell migration was evaluated *in vitro* using a modified Boyden chamber migration assay. Following vascular surgery, SMCs migrate from the cut edges of the adjacent artery and are available to participate in the neointima formation along the luminal surface of a synthetic graft, whereas in native vessels, the ECs are already present to repair the endothelium, thus preventing undesired SMC luminal proliferation.⁹⁸ We separately tested the migration of

BAECs and BSMEs in the presence of the NO releasing PCL/PDMS composite, using a 48 h migration period as had been done by others.⁹⁹ The strikingly strong endothelial cell chemotactic response to the NO releasing PCL/PDMS compared to the undoped PCL/PDMS composite and control groups demonstrated the ability of the composite to provoke a positive biological response and thus the potential to generate new endothelial lining on the synthetic surface *in vivo*. To our surprise, the BSME responded similarly to the BAECs, where BSME migration was also promoted by the NO releasing PCL/PDMS composite. This effect has been observed before by others, where vascular smooth muscle cell (VSMC) chemotaxis was found to be highly dependent on NO donor concentration. In that study, Seymour et al. had hypothesized that the combination of DETA-NO with a statin would provide an additive inhibitory effect on vascular VSMC migration.¹⁰⁰ Instead, they observed that the NO donor counteracted the statin activity and VSMC chemotaxis was increased at high concentrations of DETA-NO. Their findings confirmed a previous study, where the same authors had observed VSMC stimulation at high concentrations of DETA-NO over long term exposure (> 18 h).¹⁰¹ Interestingly, our selected DETA-NO concentration was well below what Seymour et al. had observed to stimulate VSMC migration; however, the duration of exposure to DETA-NO in our study was considerably longer than what the authors examined (48 h versus 20 h) and may have also contributed to SMC stimulation. An improvement on this assay would be to co-culture the ECs and SMCs into a single migration assay to better simulate physiological conditions, as the presence of ECs may aid in preventing or considerably reducing SMC proliferation.⁷⁶ The graft produces a favorable environment for endothelialization. Overall, the results of this migration study demonstrated that the NO release from the composite (**Figure 3-4**) sufficed to stimulate the endothelial cell

migration necessary for luminal surface remodeling and may even be too high given that smooth muscle cells were negatively stimulated. Since this was conducted *in vitro*, it is also possible that the required concentration of exogenous NO may be different to induce a similar *in vivo* biological reaction.⁹⁹

3.6 Conclusions

An elastomeric shape memory composite comprised of electrospun PCL embedded within a crosslinked PDMS elastomer and doped with an NO donor drug was successfully prepared and demonstrated controlled release of NO for over ten weeks. Increasing the DETA-NO concentration escalated the phase separation effect between the DETA-NO drug and the PCL fibers and resulted in reduced drug release as more drug molecule was trapped within fiber interior. This composite exhibited good suture retention comparable to native blood vessels and a burst pressure strength that exceeded commercially available options. The NO-releasing composite demonstrated good cytotoxicity when using a reduced concentration of the tin catalyst used to crosslink the PDMS matrix, with no impact on the tensile mechanical properties. The addition of the NO donor compound counteracted both the catalytic activity and cell toxicity caused by the catalyst. Lastly, the NO-releasing composite promoted significant endothelial cell migration. We expect that this composite material is a good candidate for blood vessel prosthetics such as AV or bypass grafts where long term mechanical and anti-thrombogenic properties are desired.

3.7 Acknowledgements

Dr. Ariel Ash-Shakoor performed all cytotoxicity testing in this study. The cell migration assays were performed by Dr. Ariel Ash-Shakoor and Tackla S. Winston.

3.8 References

1. United States Renal Data System, 2015 USRDS Annual Data Report, *NIH*, 2015
2. Fan, P.Y. & Schwab, S.J. Vascular access: concepts for the 1990s. *Journal of the American Society of Nephrology* **3**, 1 (1992).
3. Akoh, J.A. Prosthetic arteriovenous grafts for hemodialysis. *Journal of Vascular Access* **10**, 137 (2009).
4. Bozof, R., Kats, M., Barker, J. & Allon, M. Time to symptomatic vascular stenosis at different locations in patients with arteriovenous grafts. *Seminars in Dialysis* **21**, 285 (2008).
5. Hentschel, D.M., Reynolds, T. & Tammewar, G. Biological Grafts for Hemodialysis Access: Historical Lessons, State-of-the-Art and Future Directions. *Seminars in Dialysis* **26**, 233 (2013).
6. Troisi, N., Chisci, E., Frosini, P., Romano, E., Setti, M. & Mingardi, G. Hybrid simultaneous treatment of thrombosed prosthetic grafts for hemodialysis. *Journal of Vascular Access* **15**, 396 (2014).
7. Gibson, K.D., Caps, M.T., Kohler, T.R., Hatsukami, T.S., Gillen, D.L., Aldassy, M., Sherrard, D.J. & Stehman-Breen, C.O. Assessment of a policy to reduce placement of prosthetic hemodialysis access. *Kidney International* **59**, 2335 (2001).
8. Schwab, S.J. Vascular access for hemodialysis. *Kidney International* **55**, 2078 (1999).
9. Frost, M.C., Reynolds, M.M. & Meyerhoff, M.E. Polymers incorporating nitric oxide releasing/generating substances for improved biocompatibility of blood-contacting medical devices. *Biomaterials* **26**, 1685 (2005).
10. Varu, V.N., Tsihlis, N.D. & Kibbe, M.R. Basic science review: nitric oxide—releasing prosthetic materials. *Vascular and Endovascular Surgery* **43**, 121 (2009).
11. Santoro, D., Benedetto, F. & Mondello, P. Vascular access for hemodialysis: current perspectives. *Journal of Nephrology* **7**, 281 (2014).

12. Hoshi, R.A., Van Lith, R., Jen, M.C., Allen, J.B., Lapidos, K.A. & Ameer, G. The blood and vascular cell compatibility of heparin-modified ePTFE vascular grafts. *Biomaterials* **34**, 30 (2013).
13. Zea, N., Menard, G., Le, L., Luo, Q., Bazan, H.A., Sternbergh, W.C. & Smith, T.A. Heparin-bonded polytetrafluoroethylene does not improve hemodialysis arteriovenous graft function. *Annals of Vascular Surgery* **30**, 28 (2016).
14. Owen, S.C., Li H, Sanders, W.G. & Cheung, A.K. Correlation of tissue drug concentrations with in vivo magnetic resonance images of polymer drug depot around arteriovenous graft. *Journal of Controlled Release* **146**, 23 (2010).
15. Baek, I., Bai, C.Z., Hwang, J. & Park, J.H. Suppression of neointimal hyperplasia by sirolimus-eluting expanded polytetrafluoroethylene (ePTFE) haemodialysis grafts in comparison with paclitaxel-coated grafts *Nephrology Dialysis Transplantation* **27**, 1997 (2011).
16. Laube, H.R., Duwe, J., Rutsch, W. & Konertz, W. Clinical experience with autologous endothelial cell-seeded polytetrafluoroethylene coronary artery bypass grafts. *The Journal of Thoracic and Cardiovascular Surgery* (2000).
17. Dudash, L.A., Kligman, F., Sarett, S.M., Kottke-Marchant, K & Marchant, R.E. Endothelial cell attachment and shear response on biomimetic polymer-coated vascular grafts. *Journal of Biomedical Materials Research Part A* **100A**, 2204 (2012).
18. Sreerekha, P.R. & Krishnan LK. Cultivation of Endothelial Progenitor Cells on Fibrin Matrix and Layering on Dacron/Polytetrafluoroethylene Vascular Grafts. *Artificial Organs* **30**, 242 (2006).
19. Greenwald, S.E. & Berry, C.L. Improving vascular grafts: the importance of mechanical and haemodynamic properties. *The Journal of Pathology* **190**, 292 (2000).
20. Chaouet, M., Le Visage, C., Baille, W.E., Escoubet, B., Chaubet, F., Mateescu, M.A. & Letourneur, D. A novel cross-linked poly (vinyl alcohol)(PVA) for vascular grafts. *Advanced Functional Materials* **19**, 18 (2008).
21. Roeder, R., Wolfe, J., Lianakis, N., Hinson, T., Geddes, L.A., & Obermiller, J. Compliance, elastic modulus, and burst pressure of small-intestine submucosa (SIS), small-diameter vascular grafts. *Journal of Biomedical Materials Research Part A* **47**, 65 (1999).
22. Kannan, R.Y., Salacinski, H.J. & Butler, P.E. Current status of prosthetic bypass grafts: a review. *Journal of Biomedical Materials Research Part B* **74B**, 570 (2005).

23. Soletti, L., Hong, Y., Guan, J., Stankus, J.J., El-Kurdi, M.S., Wagner, W.R. & Vorp, D.A. A bilayered elastomeric scaffold for tissue engineering of small diameter vascular grafts. *Acta Biomaterialia* **6**, 110 (2010).
24. Roy-Chaudhury, P., Kelly, B.S., Miller, M.A., Reaves, A., Armstrong, J., Nanayakkara, N. & Heffelfinger, S.C. Venous neointimal hyperplasia in polytetrafluoroethylene dialysis grafts. *Kidney International* **58**, 2325 (2001).
25. Perktold, K., Leuprecht, A., Prosi, M., Berk, T., Czerny, M., Trubel, W. & Schima, H. Fluid dynamics, wall mechanics, and oxygen transfer in peripheral bypass anastomoses. *Annals of Biomedical Engineering* **30**, 447 (2002).
26. Ravi, S. & Chaikof, E.L. Biomaterials for vascular tissue engineering. *Regenerative Medicine* **5**, 107 (2010).
27. Lord, M.S., Yu, W., Cheng, B., Simmons, A., Poole-Warren, L. & Whitelock, J.M. The modulation of platelet and endothelial cell adhesion to vascular graft materials by perlecan. *Biomaterials* **30**, 4898 (2009).
28. Wang, P.G., Xian, M., Tang, X., Wu, X., Wen, Z., Cai, T. & Janczuk, A.J. Nitric oxide donors: chemical activities and biological applications. *Chemical Reviews* **102**, 1091(2002).
29. Riccio, D.A. & Schoenfish, M.H. Nitric oxide release: Part I. Macromolecular scaffolds. *Chemical Society Reviews*. **41**, 3731, (2012).
30. Wang, P.G., Xian, M., Tang, X., Wu, X., Wen, Z., Cai, T. & Janczuk, A.J. Nitric oxide donors: chemical activities and biological applications. *Chemical Reviews* **102**, 1091(2002).
31. Hou, Y.C., Janczuk, A. & Wang, P.G. Current trends in the development of nitric oxide donors. *Current Pharmaceutical Design*. **5**, 417 (1999).
32. Hrabie, J.A. & Keefer, L.K. Chemistry of the nitric oxide-releasing diazeniumdiolate (“nitrosohydroxylamine”) functional group and its oxygen-substituted derivatives. *Chemical Reviews*. **102**, 1135 (2002).
33. Bohl, K.S. & West, J.L. Nitric oxide-generating polymers reduce platelet adhesion and smooth muscle cell proliferation. *Biomaterials* **21**, 2273 (2000).
34. Singh, R.J., Hogg, N., Joseph, J. & Kalyanaraman, B. Mechanism of nitric oxide release from S-nitrosothiols. *Journal of Biological Chemistry* **271**, 18596 (1996).
35. Colletta, A., Wu, J., Wo, Y., Kappler, M., Chen, H., Xi, C. & Meyerhoff, M.E. S-Nitroso-N-acetylpenicillamine (SNAP) Impregnated Silicone Foley Catheters: A Potential

Biomaterial/Device To Prevent Catheter-Associated Urinary Tract Infections *ACS Biomaterials Science and Engineering* **1**, 416 (2015).

36. Oh, B.K. & Meyerhoff, M.E. Spontaneous Catalytic Generation of Nitric Oxide from S-Nitrosothiols at the Surface of Polymer Films Doped with Lipophilic Copper(II) Complex. *Journal of the American Chemical Society*. **125**, 9552 (2003).

37. Palmer, R., Ferrige, A.G. & Moncada, S. Nitric oxide release accounts for the biological activity of endothelium-derived relaxing factor. *Nature*. **327**, 524 (1987).

38. Zhang, H., Annich, G.M., Miskulin, J., Osterholzer, K., Merz, S.I., Bartlett, R.H. & Meyerhoff, M.E. Nitric oxide releasing silicone rubbers with improved blood compatibility: preparation, characterization, and in vivo evaluation. *Biomaterials* **23**, 1485 (2002).

39. Zhang, L., Wang, K., Zhao, Q., Zheng, W.T., Wang, Z.H., Wang, S. & Kong, D. Core-shell fibrous vascular grafts with the nitric oxide releasing property. *Science China Chemistry* **53**, 528 (2010).

40. de Valence, S., Tille, J.C., Giliberto, J.P., Mrowczynski, W., Gurny, R., Walpoth, B.H., & Möller, M. Advantages of bilayered vascular grafts for surgical applicability and tissue regeneration. *Acta Biomaterialia* **8**, 3914 (2012).

41. Singha, K. & Singha, M. Cardio Vascular Grafts: Existing Problems and Proposed Solutions. *International Journal of Biological Engineering* **2**, 1 (2012).

42. Zhang Z, Wang Z, Liu S, Kodama M. Pore size, tissue ingrowth, and endothelialization of small-diameter microporous polyurethane vascular prostheses. *Biomaterials* **25**, 177 (2004).

43. Zheng, W., Wang, Z., Song, L., Zhao, Q., Zhang, J., Li, D., Wang, S., Han, J., Zheng, X., Yang, Z. & Kong, D. Endothelialization and patency of RGD-functionalized vascular grafts in a rabbit carotid artery model. *Biomaterials* **33**, 2880 (2012).

44. de Valence, S., Tille, J.C., Mugnai, D., Mrowczynski, W., Gurny, R., Möller, M. & Walpoth, B.H. Long term performance of polycaprolactone vascular grafts in a rat abdominal aorta replacement model. *Biomaterials* **33**, 38 (2012).

45. Kushwaha, M., Anderson, J.M., Bosworth, C.A., Andukuri, A., Minor, W.P., Lancaster, J.R., Anderson, P.G., Brott, B.C. & Jun, H. A nitric oxide releasing, self assembled peptide amphiphile matrix that mimics native endothelium for coating implantable cardiovascular devices. *Biomaterials* **31**, 1502 (2010).

46. Yang, J., Welby, J.L. & Meyerhoff, M.E. Generic nitric oxide (NO) generating surface by immobilizing organoselenium species via layer-by-layer assembly. *Langmuir* **24**, 10265 (2008).

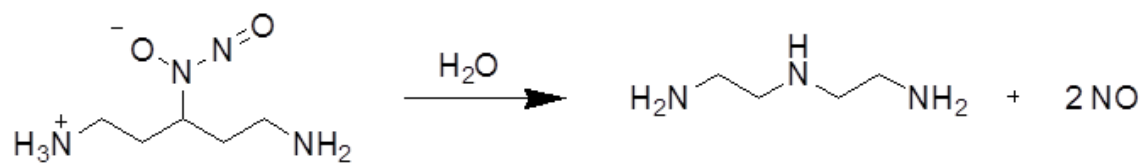
47. Mather, P., Onyejekwe, I. & Ishida, K. System and method for the release of nitric oxide using nanoscale media. U.S. Patent No. 8,394,393 (2013).
48. Onyejekwe, I. U. Nitric Oxide Releasing Polymers For Vascular Graft Applications. Doctoral Dissertation. *Syracuse University* (2012).
49. Lawton, M.I. & Mather, P.T. Controlled Drug Delivery of a Hydrophilic Drug Model from a Fibrous Elastomeric Composite with Shape Memory Properties. *Proceedings of the Annual Technical Conference & Exhibition Society of Plastics Engineers* 2370 (2015) ISBN: 978-0-9850112-7-7.
50. Beiermann, B.A., Keller, M.W. & Sottos, N.R. Self-healing flexible laminates for resealing of puncture damage. *Smart Materials and Structures* **18**, 085001 (2009).
51. Crescenzi, V., Manzini, G., Calzolari, G. & Borri, C. Thermodynamics of fusion of poly- β -propiolactone and poly- ϵ -caprolactone. comparative analysis of the melting of aliphatic polylactone and polyester chains. *European Polymer Journal* **8**, 449 (1972).
52. Sun, J., Zhang, X., Broderick, M. & Fein, H. Measurement of nitric oxide production in biological systems by using Griess reaction assay. *Sensors* **3**, 276 (2003).
53. ANSI/AAMI, Cardiovascular implants-vascular prostheses. Association for the Advancement of Medical Instrumentation-VP20. In (*Revision of ANSI/AAMI VP20-2001*), Association for the Advancement of Medical Instrumentation: Arlington, VA, 2004.
54. McClure, M.J., Sell, S.A., Simpson, D.G, Walpoth, B.H. & Bowlin, G.L. A three-layered electrospun matrix to mimic native arterial architecture using polycaprolactone, elastin, and collagen: a preliminary study. *Acta Biomaterialia* **6**, 2422 (2010).
55. Spadaccio, C., Rainer, A., Centola, M., Trombetta, M. & Chello, M. Heparin-releasing scaffold for stem cells: a differentiating device for vascular aims. *Regenerative Medicine* **5**, 645 (2010).
56. Wise, S.G., Byrom, M.J., Waterhouse, A., Bannon, P.G. & Ng, M.K. A multilayered synthetic human elastin/polycaprolactone hybrid vascular graft with tailored mechanical properties. *Acta Biomaterialia* **7**, 295 (2011).
57. Drilling, S., Gaumer, J. & Lannutti, J. Fabrication of burst pressure competent vascular grafts via electrospinning: effects of microstructure. *Journal of Biomaterials Research Part A* **88**, 923 (2009).
58. Clements, B.A., Bushman, J., Murthy, N.S., Ezra, M., Pastore, C.M. & Kohn, J. Design of barrier coatings on kink-resistant peripheral nerve conduits. *Journal of Tissue Engineering* **7**, 1 (2016).

59. ISO 0993-12: 2008–Biological Evaluation of Medical devices–Part 12: Sample Preparation and Reference Materials (2008).
60. ISO 10993-5. Biological Evaluation of Medical Devices. Part 5: Tests for in Vitro Cytotoxicity (2009).
61. Chen, H. C. Boyden chamber assay. *Cell migration*. Humana Press 15 (2005).
62. Wang, J., Brasch, M.E., Baker, R.M., Tseng, L.F. Peña, A.N. & Henderson, J.H. Shape memory activation can affect cell seeding of shape memory polymer scaffolds designed for tissue engineering and regenerative medicine. *Journal of Materials Science: Materials in Medicine* **28**, 151 (2017).
63. Baker, R.M., Brasch, M.E., Manning, M.L. & Henderson, J.H. Automated, contour-based tracking and analysis of cell behaviour over long time scales in environments of varying complexity and cell density. *Journal of the Royal Society Interface* **11**, 20140386 (2014).
64. ANSI/AAMI, Cardiovascular implants-vascular prostheses. Association for the Advancement of Medical Instrumentation-VP20. In (*Revision of ANSI/AAMI VP20-2001*), Association for the Advancement of Medical Instrumentation: Arlington, VA, 2004.
65. Nezarati, R. M., Eifert, M. B., Dempsey, D. K., & Cosgriff-Hernandez, E. Electrospun vascular grafts with improved compliance matching to native vessels. Nezarati, Roya M., Michelle B. Eifert, David K. Dempsey, and Elizabeth Cosgriff-Hernandez. "Electrospun vascular grafts with improved compliance matching to native vessels." *Journal of Biomedical Materials Research Part B: Applied Biomaterials* **103**, 313 (2015).
66. Abbasi, F., Mirzadeh, H. & Katbab, A.A. Modification of polysiloxane polymers for biomedical applications: a review. *Polymer Internatioal* **50**, 1279 (2001).
67. Malikmammadov, E., Tanir, T.E., Kiziltay, A., Hasirci, V. & Hasirci, N. PCL and PCL-based materials in biomedical applications. *Journal of Biomaterials Science, Polymer Edition* **29**, 863 (2017).
68. Wu, K.K. & Thiagarajan, P. Role of endothelium in thrombosis and hemostasis. *Annual Review of Medicine* **47**, 315 (1996).
69. Randall, G.C.& Doyle, P.S. Permeation-driven flow in poly (dimethylsiloxane) microfluidic devices. *Proceedings of the National Academy of Sciences* **102**, 10813 (2005).
70. Kakish, H.F., Tashtoush, B., Ibrahim, H.G. & Najib, N.M. A novel approach for the preparation of highly loaded polymeric controlled release dosage forms of diltiazem HCl and diclofenac sodium. *European Journal of Pharmaceutics and Biopharmaceutics* **54**, 75 (2002).

71. Kim, S.Y., Shin, I., Lee, Y.M., Cho, C.S. & Sung, Y.K. Methoxy poly (ethylene glycol) and ϵ -caprolactone amphiphilic block copolymeric micelle containing indomethacin.: II. Micelle formation and drug release behaviours. *Journal of Controlled Release* **51**, 13 (1998).
72. Mu, L. & Feng, S.S. PLGA/TPGS nanoparticles for controlled release of paclitaxel: effects of the emulsifier and drug loading ratio. *Pharmaceutical Research* **20**, 1864 (2003).
73. Wischke C, Schwendeman SP. Principles of encapsulating hydrophobic drugs in PLA/PLGA microparticles. *Elsevier*. 2008.
74. Mao, S., Shi, Y., Li, L., Xu, J., Schaper, A. & Kissel T. Effects of process and formulation parameters on characteristics and internal morphology of poly (d, l-lactide-co-glycolide) microspheres formed by the solvent evaporation method. *European Journal of Pharmaceutics and Biopharmaceutics* **68**, 214 (2008).
75. Reynolds, M.M., Frost, M.C. & Meyerhoff, M.E. Nitric oxide-releasing hydrophobic polymers: preparation, characterization, and potential biomedical applications. *Free Radical Biology and Medicine* **37**, 926 (2004).
76. Clowes, A.W., Gown, A.M., Hanson, S.R. & Reidy, M.A. Mechanisms of arterial graft failure. 1. Role of cellular proliferation in early healing of PTFE prostheses. *The American Journal of Pathology* **118**, 43 (1985).
77. Smith, D.J., Chakravarthy, D., Pulfer, S., Simmons, M.L., Hrabie, J.A., Citro, M.L., Saavedra, J.E., Davies, K.M., Hutsell, T.C., ooradian, D.L., Hanson, S.R. & Keefer, L.K. Nitric Oxide-Releasing Polymers Containing the [N(O)NO]- Group. *Journal of Medicinal Chemistry* **39**, 1148 (1996).
78. Xue, L. & Greisler, H.P. Biomaterials in the development and future of vascular grafts. *Journal of Vascular Surgery* **37**, 472 (2003).
79. Miller, P.E., Carlton, D., Deierhoi, M.H., Redden, D.T. & Allon, M. Natural history of arteriovenous grafts in hemodialysis patients. *American Journal of Kidney Diseases* **36**, 68 (2000).
80. Mine, Y., Mitsui, H., Oshima, Y., Noishiki, Y., Nakai, M. & Sano, S. Suture Retention Strength of Expanded Polytetrafluoroethylene (ePTFE) Graft. *Acta Medica Okayama* **64**, 121 (2010).
81. L'Heureux, N., Dusserre, N., Konig, G., Victor, B., Keire, Pl, Wight, T.N., Chronis, N.A.F., Kyles, A.E., Gregory, C.R., Hoyt, G., Robbins, R.C. & McAllister, T.N. Human tissue-engineered blood vessels for adult arterial revascularization. *Nature Medicine* **12**, 361 (2006).

82. Billiar, K., Murray, J., Laude, D., Abraham, G. & Bachrach, N. Effects of carbodiimide crosslinking conditions on the physical properties of laminated intestinal submucosa. *Journal of Biomedicl Matrials Research* **56**, 101 (2001).
83. Nieponice, A., Soletti, L., Guan, J., Deasy, B.M., Huard, J., Wagner, W.R. & Vorp, D.A. Development of a tissue-engineered vascular graft combining a biodegradable scaffold, muscle-derived stem cells and a rotational vacuum seeding technique. *Biomaterials* **29**, 825 (2008).
84. Lee, S.J., Oh, S.H., Liu, J., Soker, S., Atala A. & Yoo, J.J. The use of thermal treatments to enhance the mechanical properties of electrospun poly (ϵ -caprolactone) scaffolds. *Biomaterials* **29**, 1442 (2008).
85. Mine, Y., Mitsui, H., Oshima, Y., Noishiki, Y., Nakai, M. & Sano, S. Suture Retention Strength of Expanded Polytetrafluoroethylene (ePTFE) Graft. *Acta Medica Okayama* **64**, 121 (2010).
86. L'Heureux, N., Germain, L., Labbé ,R. & Auger, F.A. In vitro construction of a human blood vessel from cultured vascular cells: a morphologic study. *Journal of Vascular Surgery* **17**, 499 (1993).
87. Konig, G., McAllister, T.N., Dusserre, N., Garrido, S.A., Iyaican, C., Marini, A., Fiorillo, A., Avila, H., Wystrychowski, W., Zagalski, K., Maruszewski, M., Jones, A.L., Cierpka, L., de la Fuente, L. & L'Heureux, N. Mechanical properties of completely autologous human tissue engineered blood vessels compared to human saphenous vein and mammary artery. *Biomaterials* **30**, 1542 (2009).
88. Sarkar, S., Hillery, C., Seifalian, A. & Hamilton, G. Critical Parameter of Burst Pressure Measurement in Development of Bypass Grafts Is Highly Dependent on Methodology Used. *Journal of Vascular Surgery* **44**, 846 (2006).
89. Fillinger, M.F., Reinitz, E.R., Schwartz, R.A. Resetarits, D.E., Paskanik, A.M., Bruch, D. & Bredenberg, C.E. Graft geometry and venous intimal-medial hyperplasia in arteriovenous loop grafts. *Journal of Vascular Surgery* **11**, 556 (1990)
90. Heng, L., He, Y., Zhiyong, Z. & Zekang, W. 'Size effect' related bending formability of thin-walled aluminum alloy tube. *Chinese Journal of Aeronautics* **26**, 230 (2013).
91. Tanzi, M.C., Verderio, P., Lampugnani, M.G., Dejana, E. & Sturani, E. Cytotoxicity of some catalysts commonly used in the synthesis of copolymers for biomedical use. *Journal of Materials Science: Materials in Medicine* **5**, 393 (1994).
92. Gao, Z., Nahrup, J.S., Mark, J.E. & Sakr, A. Poly (dimethylsiloxane) coatings for controlled drug release. I. Preparation and characterization of pharmaceutically acceptable materials. *Journal of Applied Polymer Science* **90**, 658 (2003).

93. Xue, L., Zhang, Y., Zuo, Y., Diao, S., Zhang, J. & Feng, S. Preparation and characterization of novel UV-curing silicone rubber via thiol-ene reaction. *Materials Letters* **106**, 425 (2013).
94. Zhu, R., Wang, X., Yang, J., Zhang, Z., Hou, Y. & Lin, F. Influence of hydroxyl-terminated polydimethylsiloxane on high-strength biocompatible polycarbonate urethane films. *Biomedical Materials* **12**, 015011 (2017).
95. Meera, K.S., Sankar, R.M., Jaisankar, S.N. & Mandal, A.B. Physicochemical studies on polyurethane/siloxane cross-linked films for hydrophobic surfaces by the sol-gel process. *The Journal of Physical Chemistry B* **117**, 2682 (2013).
96. Kasprzyk, W., Krzywda, P., Bednarz, S. & Bogdał, D. Fluorescent citric acid-modified silicone materials. *RSC Advances* **5**, 90473 (2015).
97. Pretti, C., Oliva, M., Mennillo, E., Barbaglia, M., Funel, M. Yasani, B.R. Martinelli, E. & Galli, G. An ecotoxicological study on tin- and bismuth-catalysed PDMS based coatings containing a surface-active polymer. **98**, 250 (2013).
98. Clowes, A.W., Kirkman, T.R. & Clowes, M.M. Mechanisms of arterial graft failure. II. Chronic endothelial and smooth muscle cell proliferation in healing polytetrafluoroethylene prostheses. *Journal of Vascular Surgery* **3**, 877 (1986).
99. Sarkar, R., Meinberg, E.G., Stanley, J.C. & Gordon, D. Nitric oxide reversibly inhibits the migration of cultured vascular smooth muscle cells. *Am Heart Assoc.* **78**, 225 (1996).
100. Seymour, K., Stein, J., Han, X., Maier, K.G. & Gahtan, V. Statins and nitric oxide donors affect thrombospondin 1-induced chemotaxis. *Vascular and Endovascular Surgery* **48**, 470 (2014).
101. Seymour, K., Stein, J., Han, X., Maier, K.G. & Gahtan, V. Statins and nitric oxide donors affect thrombospondin 1-induced chemotaxis. *Vascular and Endovascular Surgery* **48**, 470 (2014).



Scheme 3-1. The decomposition of diethylenetriamine nitric oxide donor (DETA-NO) upon exposure to water.

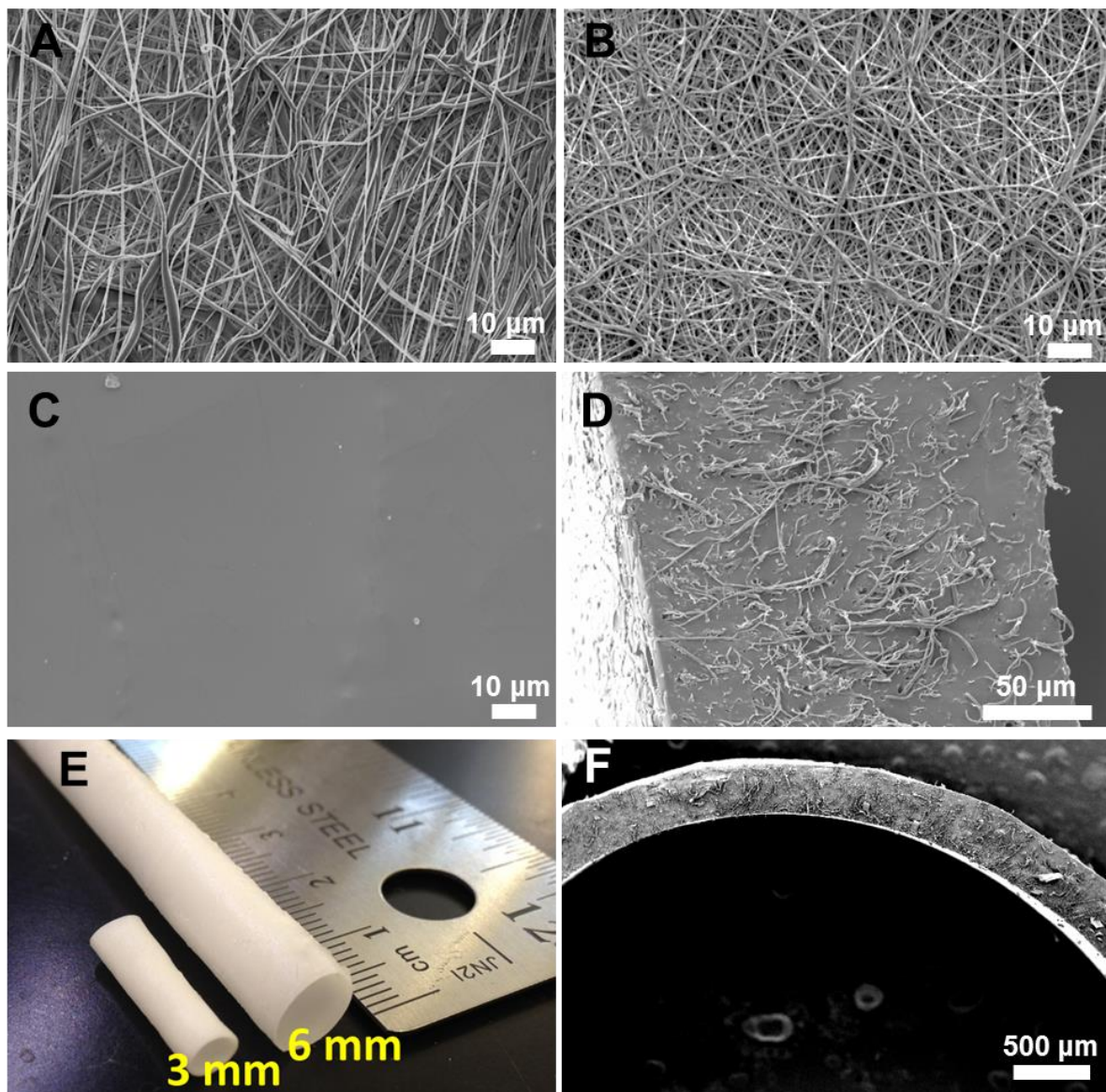


Figure 3-1. SEM micrographs of electrospun DETA-NO loaded PCL fibers showing the (A) 0.5 % DETA-NO/PCL fiber mat, (B) the 1.5 % DETA-NO/PCL fiber mat, (C) the fiber mat surface following following PDMS infiltration, (D) the cross-section of the DETA-NO/PCL/PDMS composite, (E) the composite in tubular form, and (F) the cross-section of the tubular composite. The micrographs in C - D are shown for 0.5% DETA-NO donor concentration.

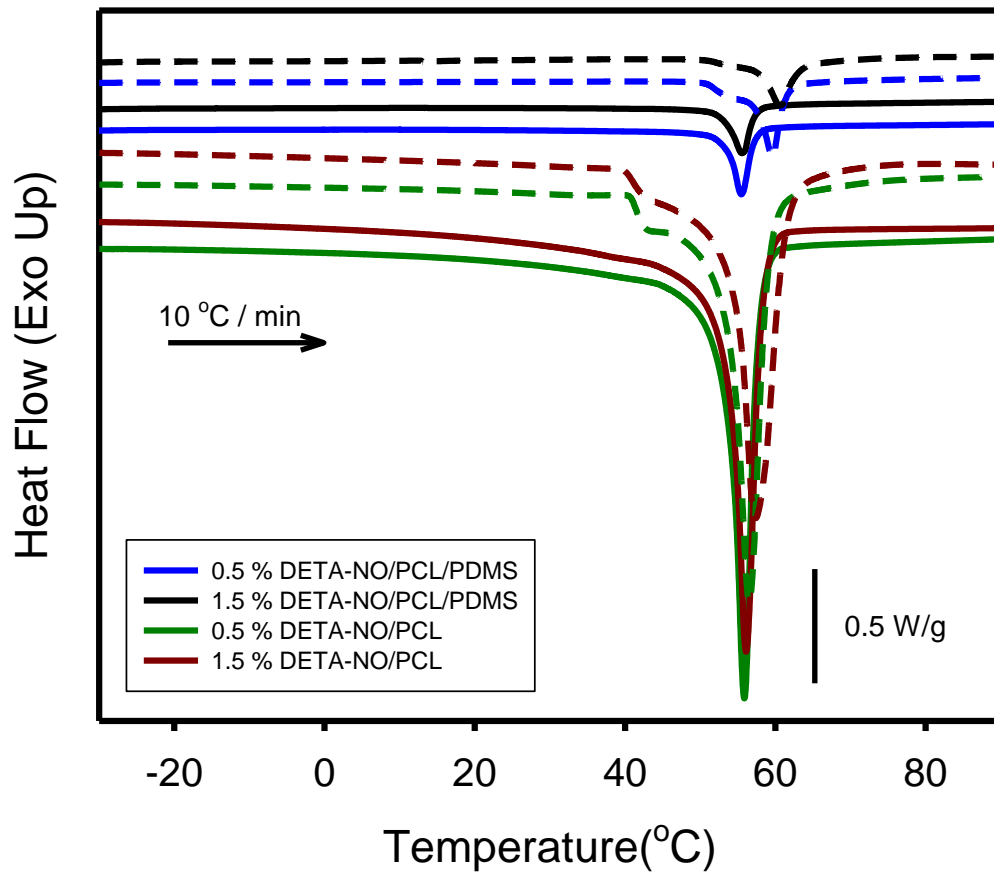


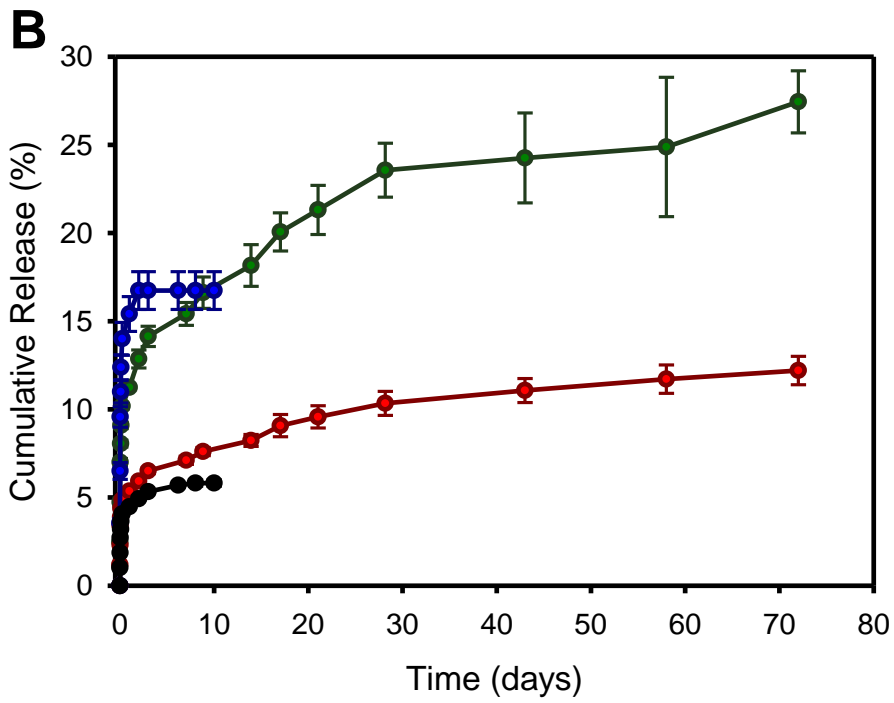
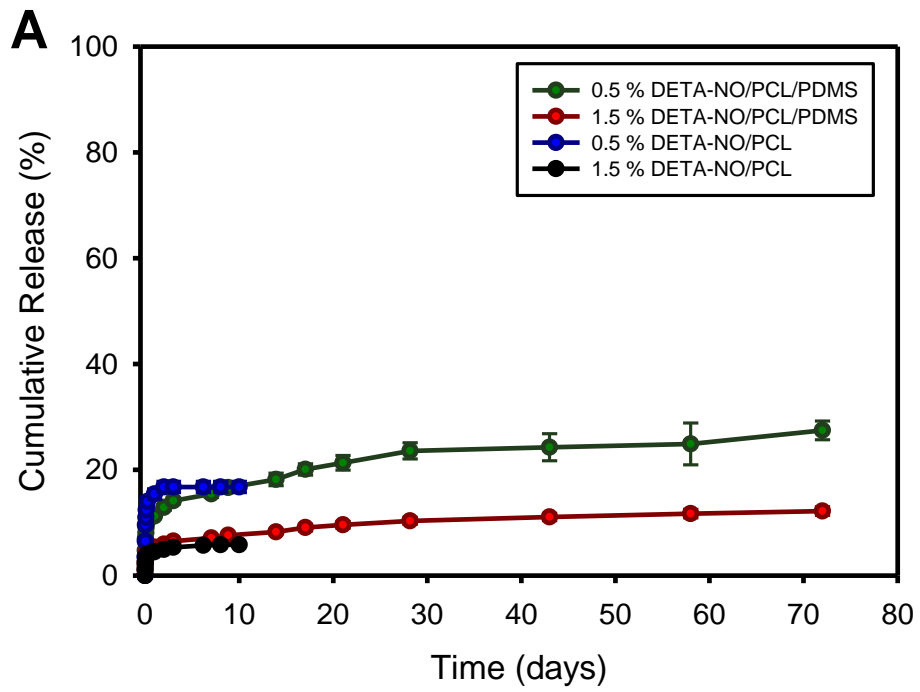
Figure 3-2. DSC thermograms comparing melting transitions of NO releasing PCL/PDMS composite and fibrous components at two NO donor concentrations. Solid lines denote second heating cycle and dashed lines denote first heating cycle.

Table 3-1. Thermal properties of the NO releasing PCL/PDMS composite and fibrous components at two NO donor concentrations.

	$\Delta H_{m,1}$ ^a (J/g)	$\Delta H_{m,2}$ ^b (J/g)	$T_{m,1}$ ^a (°C)	$T_{m,2}$ ^b (°C)	χ_1 ^a (%)	PCL Content ^b (%)
0.5 % DETA-NO/PCL/PDMS	7.9	5.0	59.7	55.5	5.7	10.0
1.5 % DETA-NO/PCL/PDMS	6.1	4.0	60.7	55.6	4.4	7.9
0.5 % DETA-NO/PCL	57.9	50.0	56.5	55.9	N/A	N/A
1.5 % DETA-NO/PCL	62.2	56.6	57.4	56.1	N/A	N/A

^aDetermined from the first heating cycle.

^bDetermined from the second heating cycle.



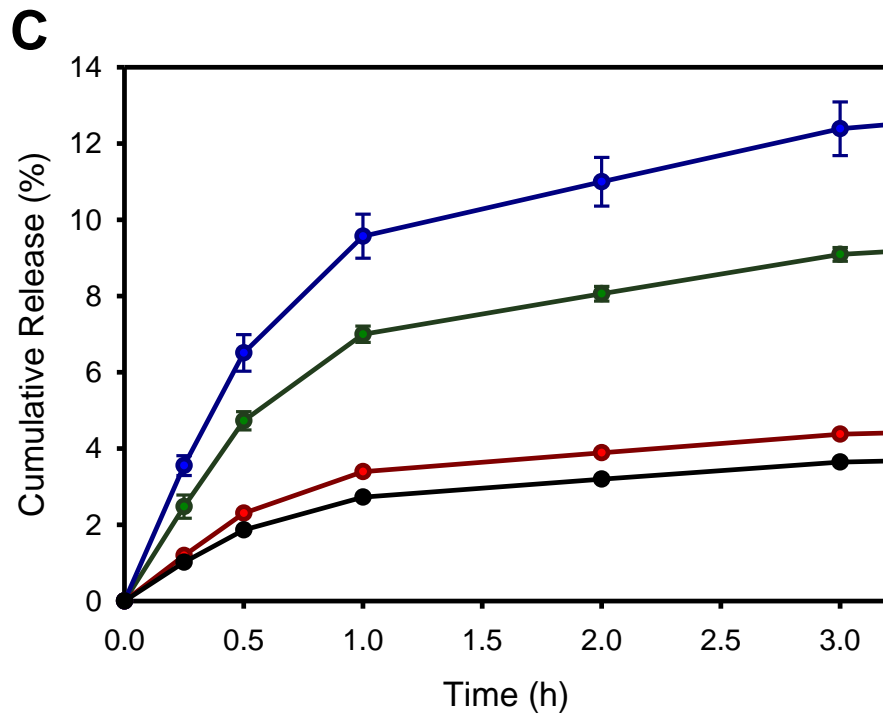


Figure 3-3. (A) Overall cumulative NO profiles comparing electrospun fibers and as fibers embedded in the PDMS matrix for two NO donor concentrations. The plots in (B) and (C) are magnified views of (A).

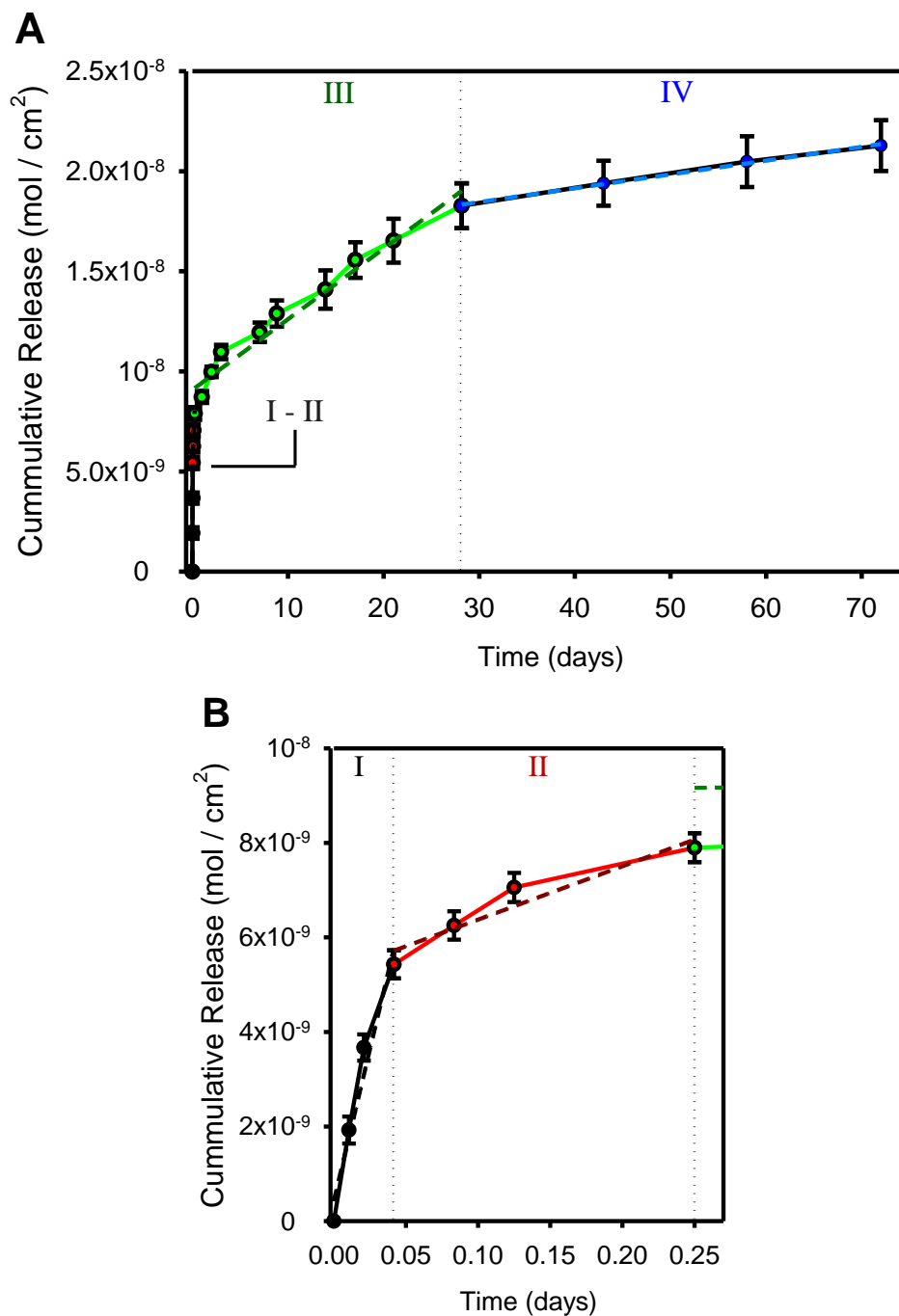


Figure 3-4. (A) Cumulative NO release of 0.5% DETA-NO/PCL/PDMS composite divided into five stages. A magnified view of the release pattern in stages I and II are shown in (B). A linear regression (dashed line) was used to calculate the flux in each of NO release phase.

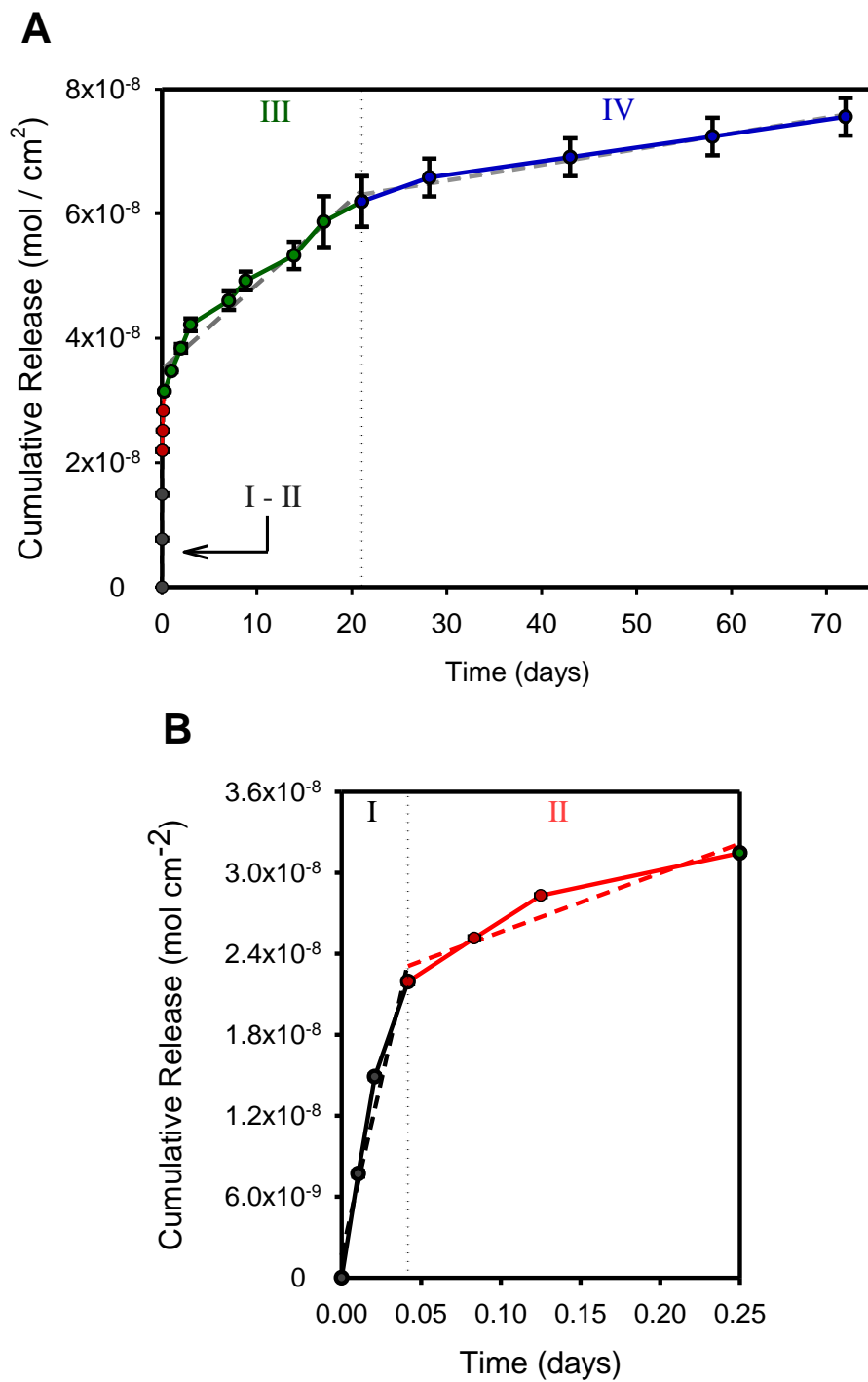


Figure 3-5. (A) Cumulative NO release of 1.5% DETA-NO/PCL/PDMS composite divided into five stages. A magnified view of the release pattern in stages I and II are shown in (B). A linear regression (dashed line) was used to calculate the flux in each of NO release phase.

Table 3-2. Linear regression parameters of NO release profiles used to calculate the flux.

Sample		Slope of Cumulative Release vs. Time (mol · cm ⁻² · min ⁻¹)	Y-Intercept ₂ (mol · cm ⁻²)	R-squared (%)
0.5% DETA-NO/PCL/PDMS	Stage I	10 ⁻¹⁰	0	94.2
	Stage II	8 x 10 ⁻¹²	5 x 10 ⁻⁹	91.9
	Stage III	8 x 10 ⁻¹³	9 x 10 ⁻⁹	95.9
	Stage IV	5 x 10 ⁻¹⁴	2 x 10 ⁻⁸	99.6
1.5% DETA-NO/PCL/PDMS	Stage I	4 x 10 ⁻¹⁰	0	94.2
	Stage II	3 x 10 ⁻¹¹	2 x 10 ⁻⁸	91.2
	Stage III	9 x 10 ⁻¹³	3 x 10 ⁻⁸	95.7
	Stage IV	2 x 10 ⁻¹³	6 x 10 ⁻⁸	97.8

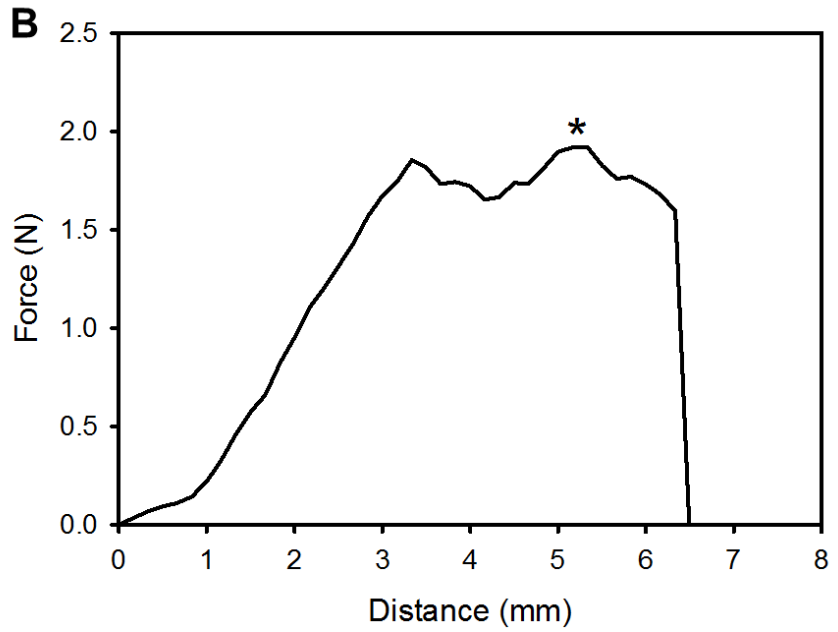


Figure 3-6 (A) Suture retention testing set-up and (B) representative force-displacement plot for the composite using a tensile speed of $50 \text{ mm} \cdot \text{min}^{-1}$. The suture retention strength is denoted by an asterisk.

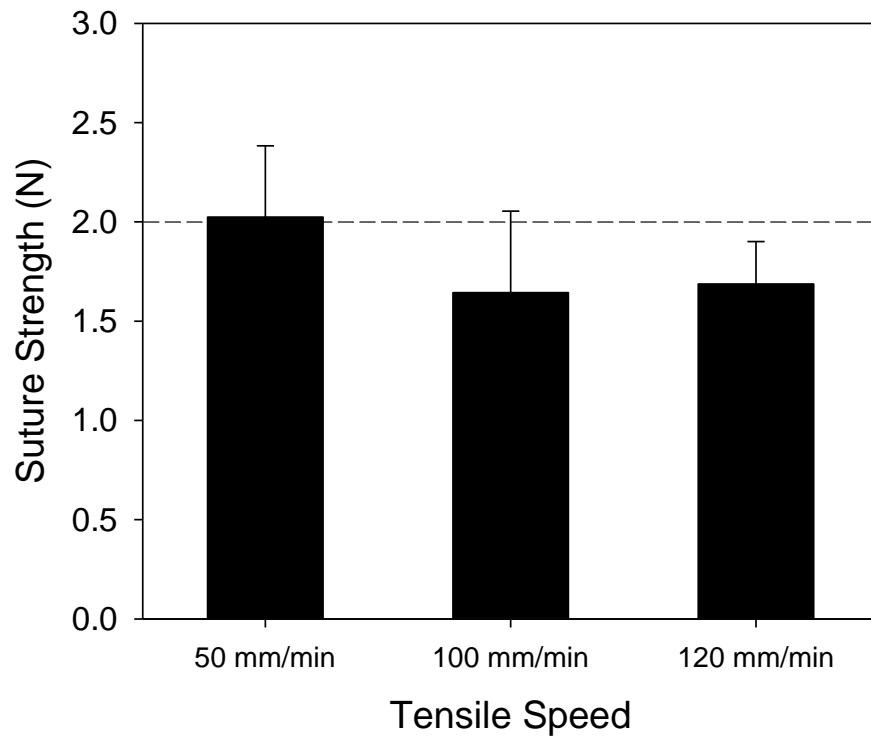


Figure 3-7 Average suture retention strength for the composite at three different tensile speeds.

Table 3-3 Average suture retention strength for the composite at three different tensile speeds.

# Samples	Tensile Speed (mm/min)	Peak Strength (N)
17	50	2.0 ± 0.4
6	100	1.6 ± 0.4
8	120	1.7 ± 0.2

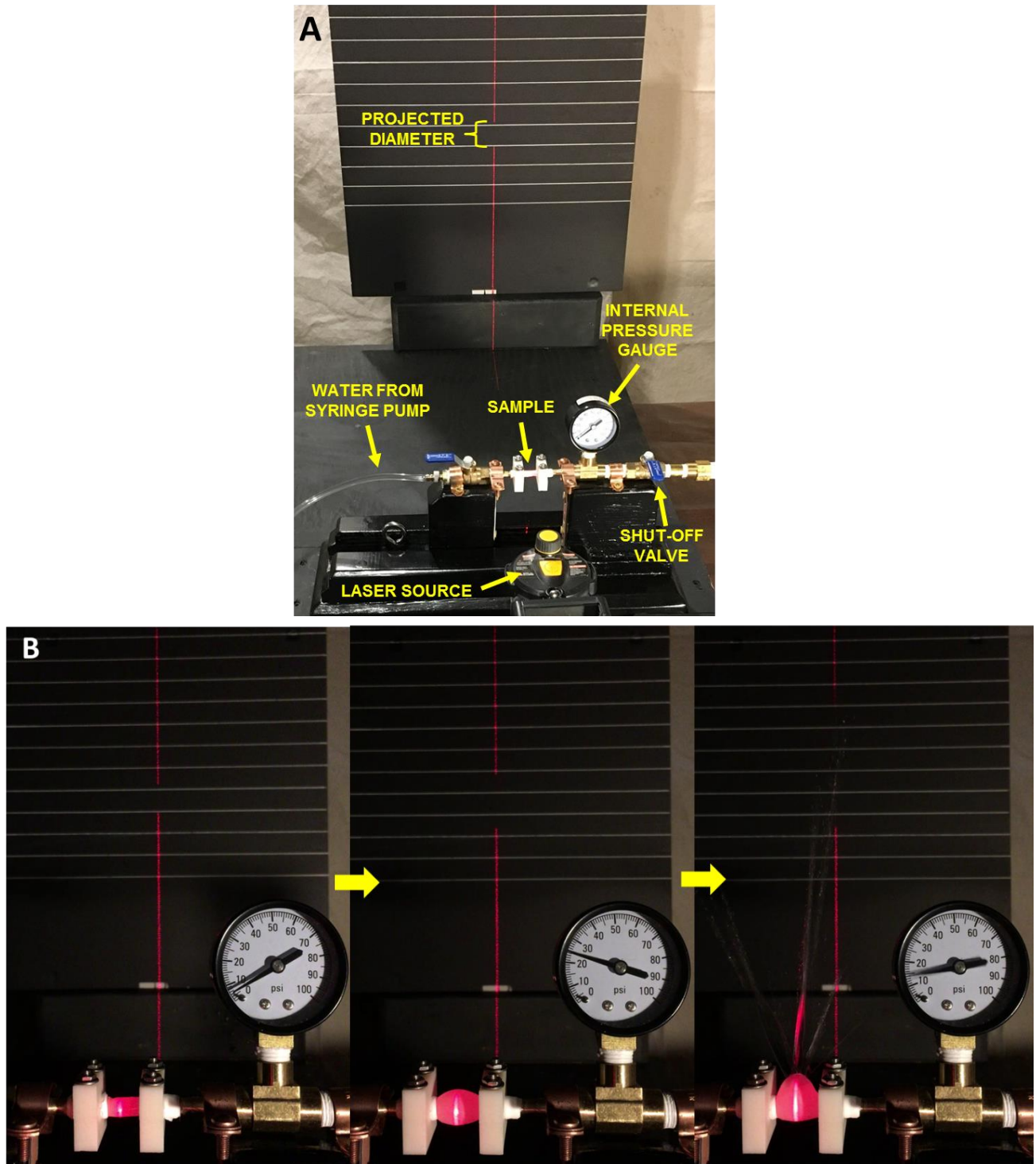


Figure 3-8 (A) Burst pressure testing set-up and (B) representative images of sample dilation and failure.

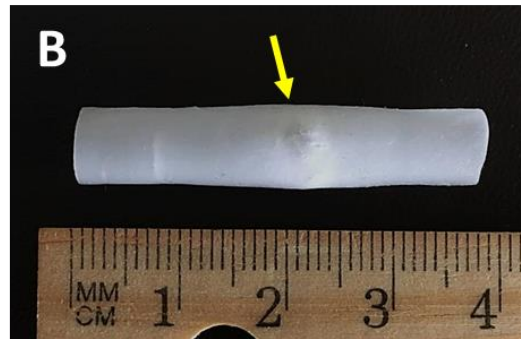
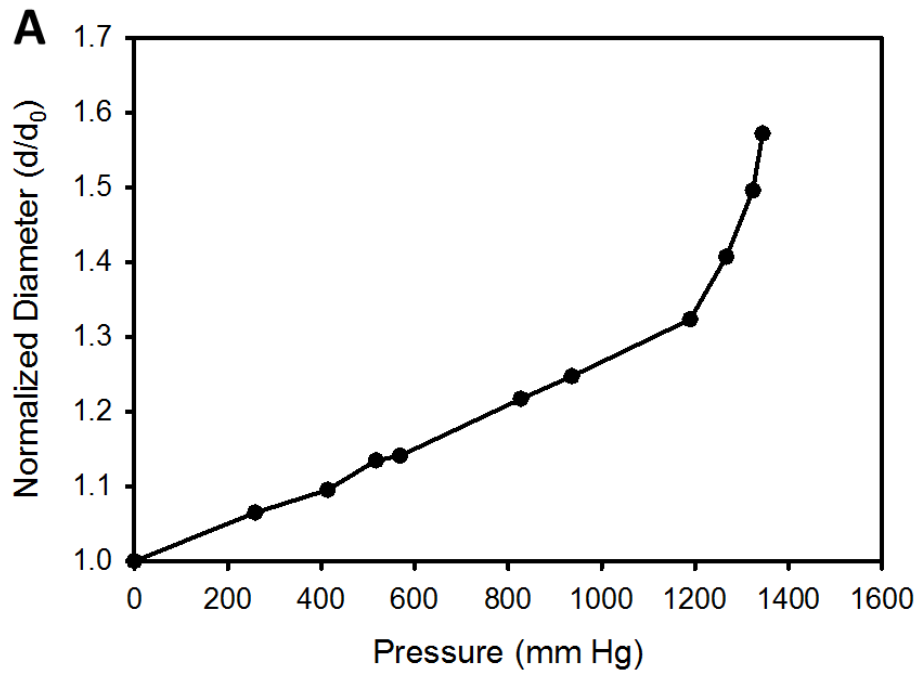


Figure 3-9 Results of burst pressure testing showing (A) representative pressure-diameter and hoop stress displacement curves and (B) representative sample following high pressure burst failure. The arrow indicates the area where point of failure occurred.

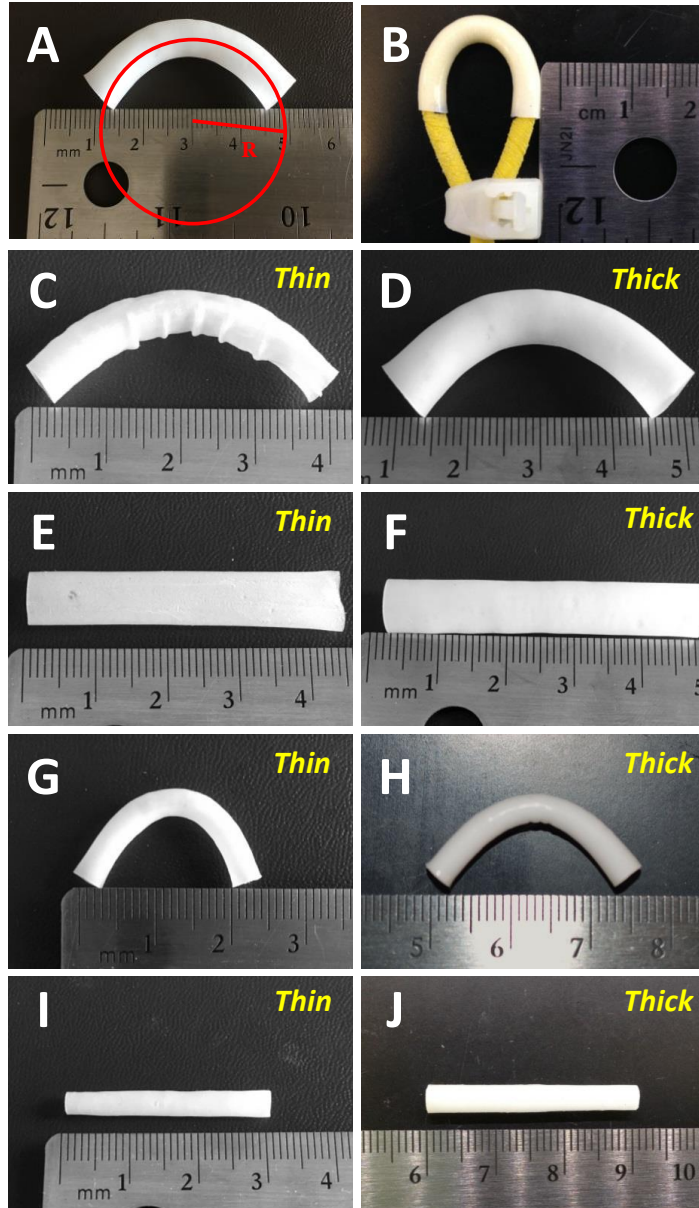


Figure 3-10 Kink-free bends for surgical placement using thermal shape programming feature showing (A) the radius measurement and the (B) supporting substrate used to fix a looped shape. Representative fixed shapes are shown for the 6 mm graft in (C) and (D), with respective recovered shapes in (E) and (F). Representative fixed shapes for the 3 mm graft are shown in (G) and (H), with respective recovered shapes in (I) and (J). The wall thickness classification is denoted on the photos.

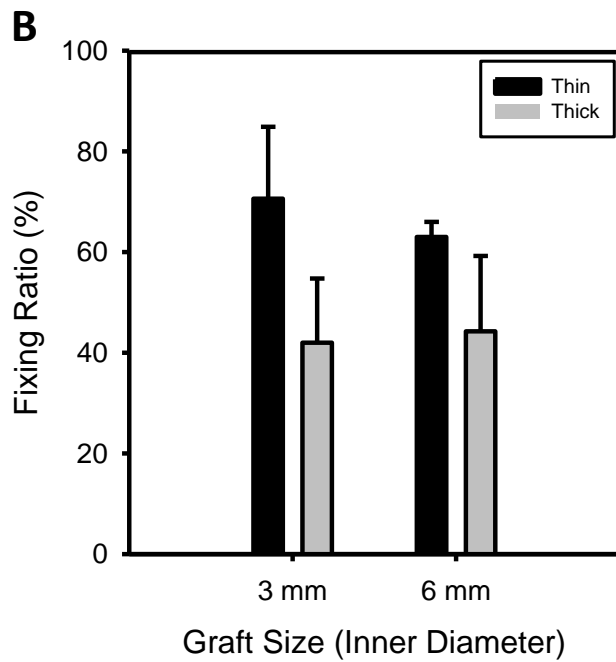
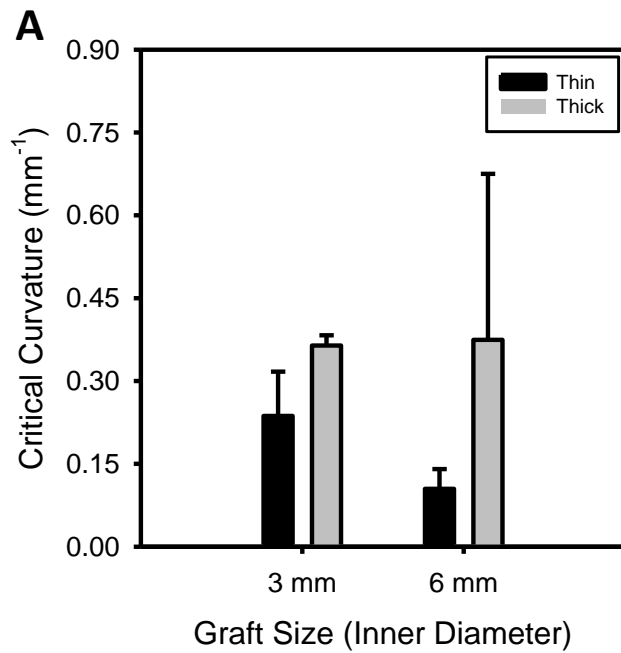
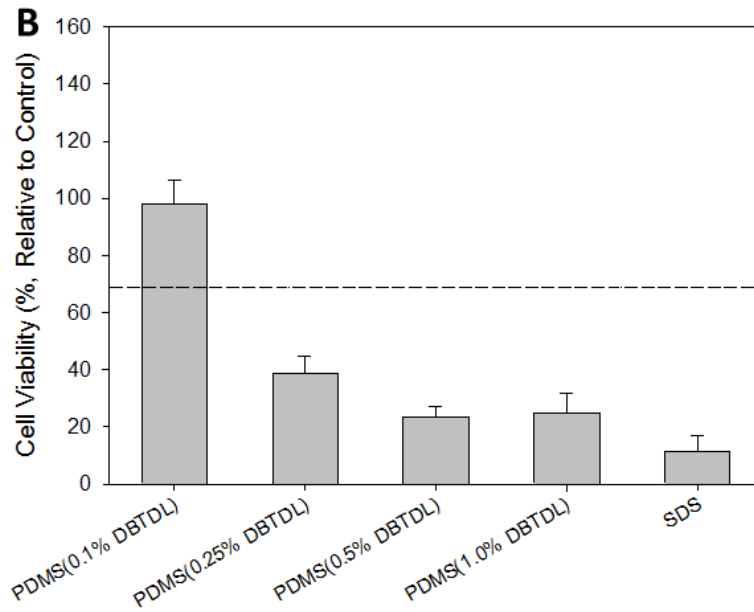
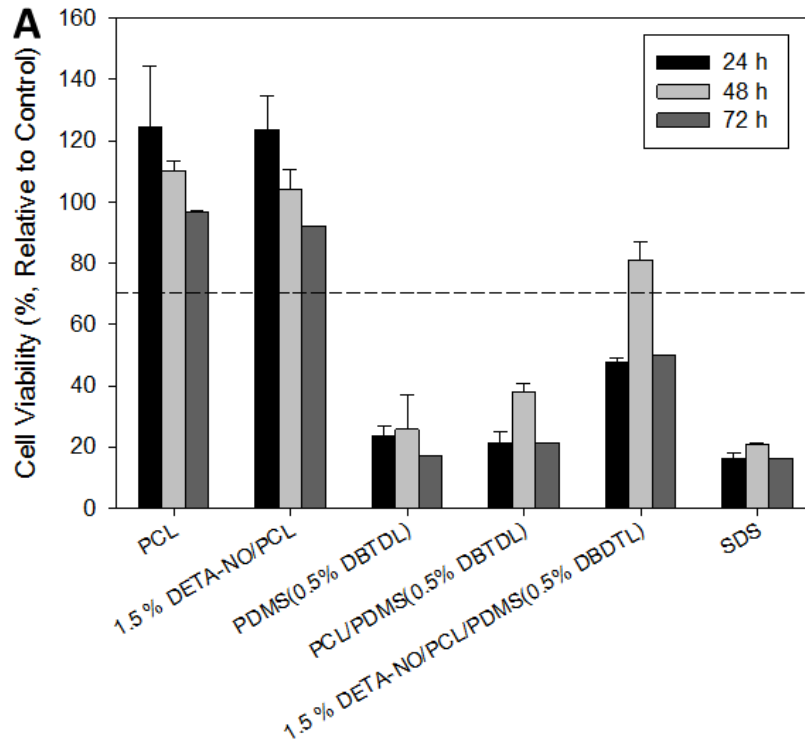


Figure 3-11 Results of kink resistance testing demonstrating (A) the critical curvature, which was the curvature value limit before a kink will occur with increased bending, and (B) shape fixing ratio dependence on graft tube wall thickness and diameter.



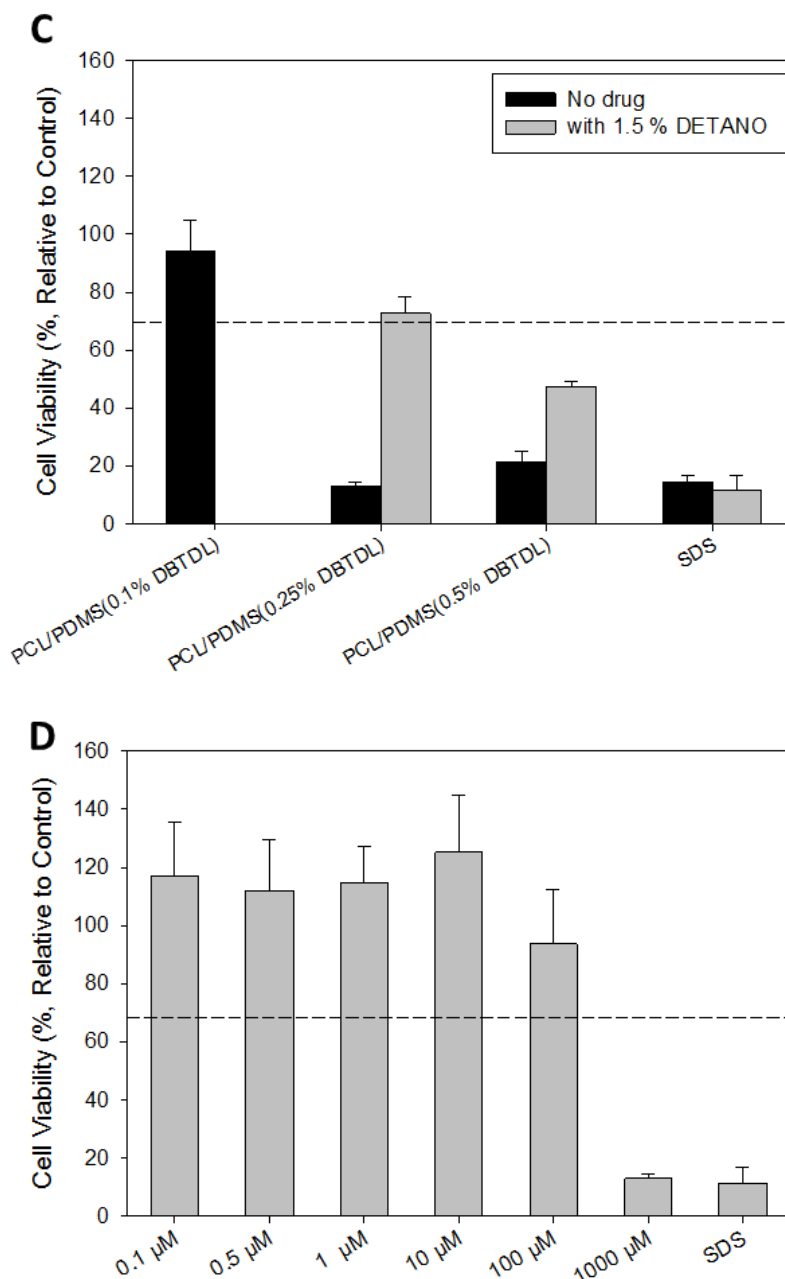


Figure 3-12. Cell viability of L929 fibroblast cells cultured in extracts from (A) the NO releasing PCL/PDMS composite and its components at different extraction times, (B) the PDMS elastomer with various catalyst concentrations, (C) the composite, both with and without NO donor, fabricated using different PDMS catalyst concentrations (% w/w), and (D) varying concentrations of the NO donor DETA-NO in cell culture media. The results for (B) – (D) were measured following 24 h of incubation in media. The results of the doped composite in (C) containing 0.1 % DBTDL could not be tested due to NO donor interference with PDMS crosslinking. All testing was conducted in triplicate. Dashed line indicates acceptable cytocompatibility level of 70 %.

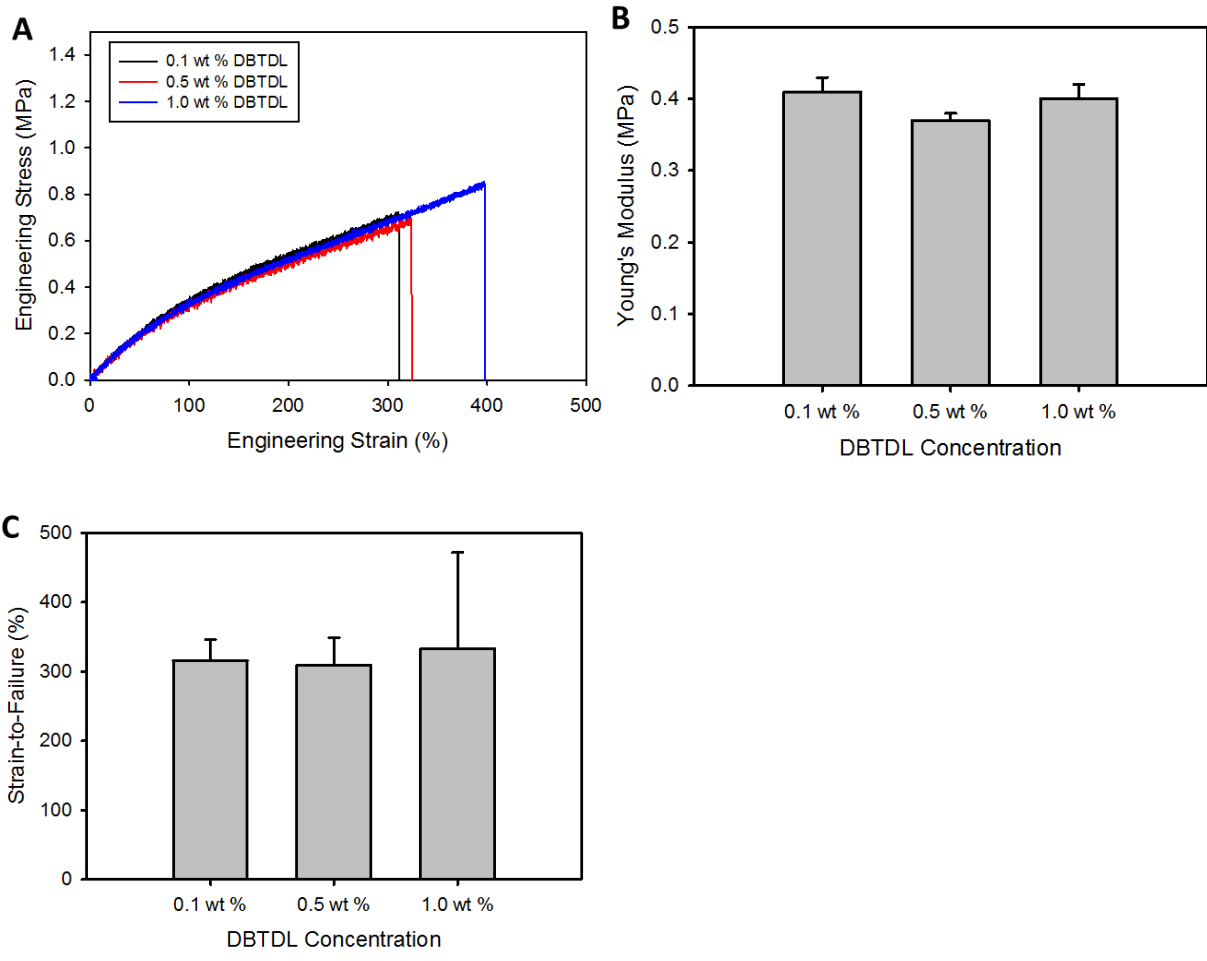


Figure 3-13. Mechanical properties of crosslinked PDMS using different concentrations of DBTDL catalyst showing (A) representative engineering tensile stress-strain curves, (B) Young's moduli, and (C) strain-to-failure.

Table 3-4. Summary of mechanical properties of PDMS crosslinked using different DBTDL concentrations.

DBTDL Concentration (wt %)	Young's Modulus (MPa)	Strain-to-Failure (%)
0.1	0.41 ± 0.02	316 ± 30
0.5	0.37 ± 0.01	309 ± 40
1.0	0.40 ± 0.02	333 ± 139

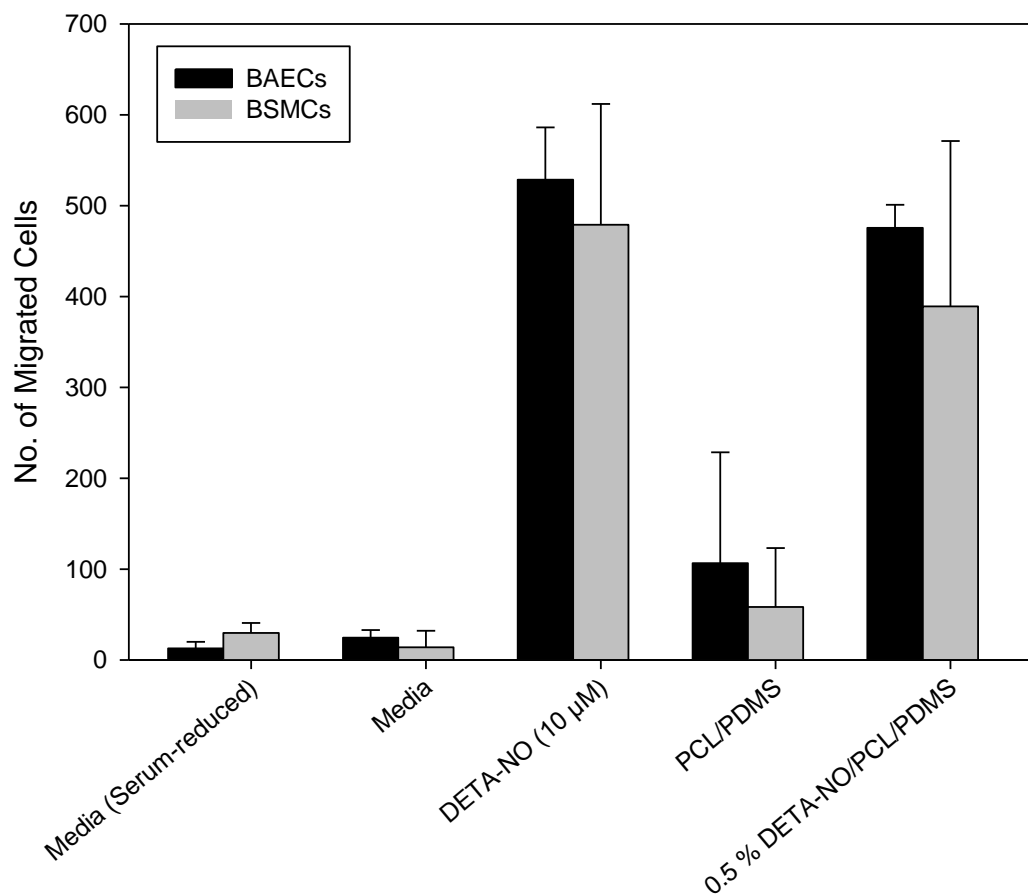


Figure 3-14. Effect of NO release from the 0.5 % DETA-NO/PCL/PDMS composite on BAEC and BSMC migration. Comparisons were made to the positive controls (media and DETA-NO in media) and negative control (serum-reduce media). The data shown are the mean and standard deviation of three experiments.

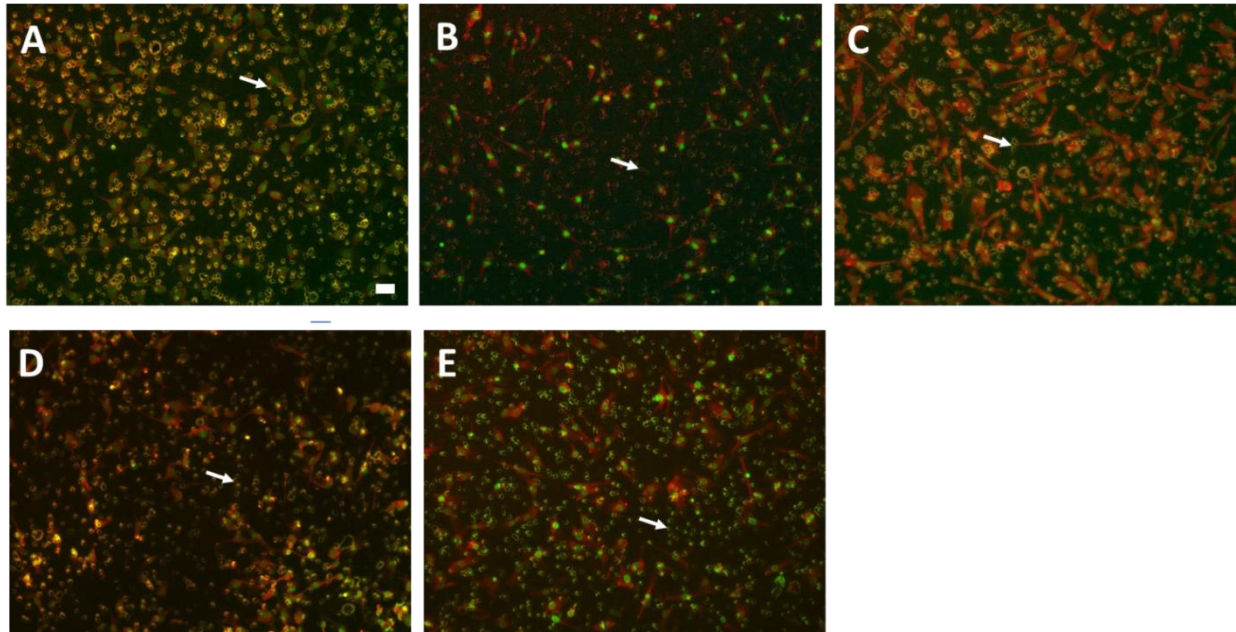


Figure 3-15. Representative micrographs of stained BAECs on the lower surface of the Transwell membrane taken with fluorescence microscope (10 X magnification). The cells visible on this surface are a result of migration over 48 h. The various conditions are (A) serum-reduced media, (B) media only, (C) 10 μ M DETA-NO in media, (D) PCL/PDMS, and (E) 0.5 % DETA-NO/PCL/PDMS composite. The cells were stained for nuclei (green) and cytoskeleton (red), and the arrow points to the open pores on the Transwell membrane. The scale bar represents 50 μ m.

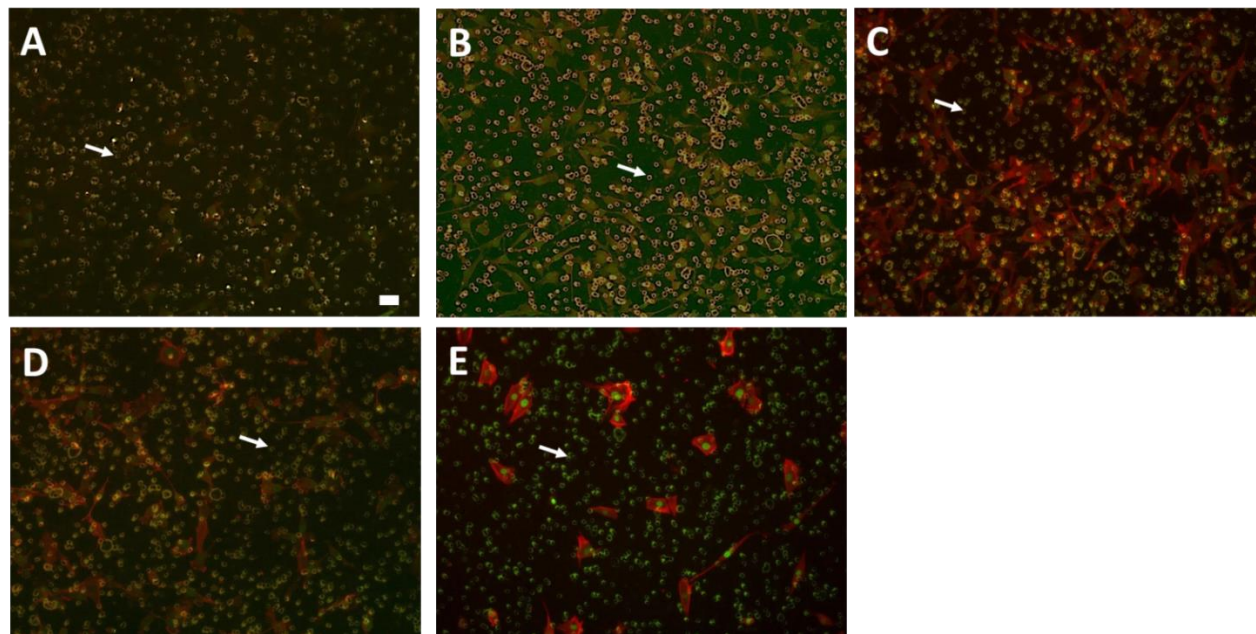


Figure 3-16. Representative micrographs of stained BSMCs on the lower surface of the Transwell membrane taken with fluorescence microscope (10 X magnification). The cells visible on this surface are a result of migration over 48 h. The various conditions are (A) serum-reduced media, (B) media only, (C) DETA-NO in media, (D) PCL/PDMS, and (E) DETA-NO/PCL/PDMS composite. The cells were stained for nuclei (green) and cytoskeleton (red), and the arrow points to the open pores on the Transwell membrane. The scale bar represents 50 μm .

Chapter 4

Anhydride-Based Reconfigurable Shape Memory Elastomeric Composite¹

4.1 Synopsis

Soft shape memory polymers typically embody a permanently memorized geometry that cannot be altered, and therefore a new sample must be fabricated each time a new structure is required. In this chapter, a shape memory elastomeric composite featuring thermoplastic fibers as a fixing phase and a polyanhydride-based elastomer as the permanent, elastic phase is developed and characterized. It was discovered that the elastomer is capable of dynamic covalent exchange reactions at elevated temperatures ($T > 50\text{ }^{\circ}\text{C}$) among the network chains that allowed near-complete reconfiguration of the permanent shape in the solid state. Together, these features were combined to create a shape memory elastomer capable of arbitrary programming of both temporary and permanent shapes.

4.2 Introduction

Shape memory polymers (SMPs) are mechanically active materials featuring at least two primary attributes: “memory” of a stress-free permanent configuration (or shape) and “programming” of a temporary shape through a combination of heating and molding.¹ Deployment from the programmed to permanent shapes is triggered by heat, light, solvent-exposure, or other means. At the molecular and nanoscale levels, memory is afforded by crosslinks (covalent or physical) established at a stress-free state during processing, while

¹ The work in this chapter was originally published in Lawton, M. I., Tillman, K. R. & Mohammed, H. S. Anhydride-based reconfigurable shape memory elastomers. *ACS Macro Letters* **5**, 203 (2016).

programming (or “fixing”) is accomplished by kinetic trapping of a deformed and stressed shape by means of crystallization, vitrification, secondary crosslinking, or even plastic deformation. These physical transformations act to immobilize the constituent network chains, translating to macroscopic shape fixing. There are four (4) major classifications of such SMPs were identified and the interested reader is referred to that paper² and other recent reviews³⁻⁷ for more details.

The systems described above achieve shape fixing in a manner that engenders high macroscopic stiffness due to the positive impact of either vitrification or crystallization on modulus. Soft shape memory with lower tensile modulus even in the fixed state is needed for SMPs to be useful as seals, gaskets, stamps, and some surgical devices. Addressing this need, many have reported on liquid crystalline elastomers,^{8,9} POSS-grafted biopolymers,^{10,11} PEO-based epoxy networks,¹² and hydrogen-bonded networks¹³ that have both softness and shape memory. Alternatively, soft shape memory polymers, or SM elastomers, can be achieved by an elastomeric composite approach wherein an elastomer is reinforced with a percolating fixing phase.¹⁴ Such shape memory elastomeric composites (SMECs) can be achieved by imbibing an electrospun fixing phase with an elastomeric matrix precursor, followed by crosslinking of the matrix,¹⁵ or by dual-electrospinning of a fixing polymer and a thermoplastic elastomer.¹⁶ This SMEC approach to soft shape memory is applied in the present work.

Reports of soft shape memory polymers to date have all featured a permanent, memorized shape whose geometry either cannot be altered (covalent networks) or cannot be altered without traversing a fluid state by remolding (thermoplastic SMPs). As a practical matter, this leads to shapes that are usually limited to flat films – a natural geometry for casting and molding processes. To prepare an SMP article with a new configuration or with a non-flat

shape, a new sample must be made and this is both time-consuming and inefficient. Thus, we were motivated for the present work to design a covalently bonded elastomeric matrix for use in a SMEC configuration capable of permanent shape reconfiguration by facile thermomechanical means. Such a matrix composition would allow for fine-tuning of sample geometry, prototyping of devices, recycling, versatility in shape memory “target” shape, and possibly self-healing.

In contemplating the dynamic covalent chemistry needed for the envisioned soft reconfigurable SMP, we considered the recent advances in the fields of self-healing polymers^{17,18} and photo-responsive polymers.¹⁹ In one class of self-healing polymers, reversible covalent bonds have been exploited to reform bonds following crack-induced damage to the materials. Wudl and colleagues pioneered use of Diels-Alder chemistry in this manner, utilizing diene/dienophile pairs; e.g., furan/maleimide, that proved to be very effective in allowing bond reconfiguration and crack-rebonding by application of heat during external crack closure. Meanwhile, Bowman and colleagues have reported on photoactive “covalent adaptive networks” that undergo interchange reactions during exposure to light, reconfiguring the deformed networks toward a stress free state apparently without macroscopic fluidization. This general concept was appealing to us for our purposes, but the requirement of light illumination during processing was deemed to be cumbersome and limiting.

In separate studies, Shipp et al. introduced biodegradable elastomers utilizing thiol-ene “click” chemistry and incorporating hydrolytically labile anhydride groups.²⁰ For our present study, we postulated that the anhydride groups of the elastomeric matrix might enable desired exchange reactions for thermal reconfiguration based on limited (and often old) literature that indicated such exchange reactions occur in solution, though no prior report testing this notion in

solid or rubbery materials could be found to support our conjecture.²¹⁻²⁵ In this report, we present the synthesis and characterization of a new soft, shape memory elastomer that is thermally reconfigurable, termed Re-SMEC.

4.3 Methods

4.3.1 Materials

4-Pentenoic anhydride (PNA), pentaerythritol tetrakis(3-mercaptopropionate) (PETMP), azobisisobutyronitrile (AIBN), chloroform, N,N-dimethylformamide (DMF), trimethylolpropane diallyl ether (TMPDAE), 1,6-hexanedithiol (HDT), 1-hydroxycyclohexyl phenyl ketone (99%), anhydrous dichloromethane (DCM), anhydrous diethyl ether ($\geq 99\%$, DEE), and tetrahydrofuran (HPLC-grade, $\geq 99.9\%$, THF) were purchased from Sigma-Aldrich and used as received. Thermoplastic polyurethane PCL (PCL PU) was synthesized using 3,4-dihydroxy-1-butene (DHB), hexamethylene diisocyanate (HDI), toluene and poly(ϵ -caprolactone) diol ($M_n \sim 2000 \text{ g mol}^{-1}$), which were purchased from Sigma-Aldrich and dried prior to synthesis. Tin-POMS was used as a catalyst and purchased from Hybrid Plastics and dried prior to use.

4.3.2 Thiol-ene Elastomer Syntheses

PAH was synthesized by reacting PNA with PETMP using a stoichiometry of one allyl per thiol functional group, and 1 wt% AIBN, and cast on glass slides with a 0.25 mm Teflon spacer, followed by UV cure for 30 min. Similarly, TMPDAE-based elastomer was reacted with PETMP using the same stoichiometry and concentration of AIBN. Poly(TMPDAE) was UV cured for 1 h followed by a thermal post-cure at 70 °C for 1 h to be consistent with the conditions to cure the PAH/PCL PU composite.

4.3.3 Polycaprolactone Polyurethane Synthesis

PCL-based polyurethane (PCL PU) was synthesized by Wenbin Kuang, a graduate student in the Mather Research Group. PCL diol was combined with HDI as the urethane linker and small molecule DHB (molar ratio of 3:6:2.1) with 1 wt% tin POMS catalyst and was reacted in toluene under nitrogen at 100 °C for 12 h. The polymer was then precipitated in excess hexane and washed with DI water several times and vacuum dried at room temperature prior to use.

4.3.4 Electrospinning

The PCL PU of Section 4.3.3 was electrospun from a 20% (w/v) solution prepared by dissolving 2 g PCL PU in chloroform/DMF (volume ratio = 2:1). PCL PU fibers were produced using a flow rate of 1 mL h⁻¹, a voltage of 16 kV, and a needle to collector distance of 12 cm onto a rotating and translating cylindrical collector with a diameter of 5 cm.

4.3.5 PAH/PCL PU Composite Fabrication

The polyanhydride monomer was applied onto the surface of the electrospun PCL PU fiber mat and vacuum was utilized at room temperature for complete infiltration of the monomer into the PCL PU fiber mat, followed by removal of excess monomer on the surface. PAH/PCL PU was photocured for 30 min exposed on both surfaces using a 365 nm (2.5 W) ultraviolet light source at a distance of 15 cm from the sample to the light source. This irradiation cure step was followed by a thermal post-cure at 70 °C for 1 h to complete cure of the PAH matrix, as the PCL PU fibers can prevent the absorption of UV below the surface.

4.3.6 Morphology

A JEOL JSM-5600 scanning electron microscope (SEM) was used with an accelerating voltage of 4 – 6 kV. Samples were either sputtered with gold or gold palladium for 9 – 45 s prior to imaging.

4.3.7 Differential Scanning Calorimetry

A TA Instruments Q200 differential scanning calorimeter (DSC) was used to study the melting and glass transitions and enthalpies. All samples were first cooled to -60 °C, followed by heating at 10 °C min⁻¹ to 100 °C. Only the second heating cycles are reported to remove any effect from variable thermal histories. The glass transition was selected from the inflection point of the step transition, and the maxima were taken as the melting transition point. The melting enthalpy was calculated from the second heating cycle by integrating the melting peak, and used to determine the fraction of PCL in the elastomeric composite by comparing the degree of crystallinity according to:

$$\chi_c(\%) = \frac{\Delta H_f}{\Delta H_{f0}} \times 100 \% \quad (4-1)$$

where χ_c is the degree of crystallinity, ΔH_f is the heat of fusion measured by DSC and ΔH_{f0} is the heat of fusion of pure electrospun PCL, as determined by DSC.

4.3.8 Thermomechanical Characterization

A TA Instruments Q800 dynamic mechanical analyzer (DMA) was used in multifrequency strain mode to measure the storage and loss moduli and tan delta. All samples

were first cooled to -60 °C, followed by heating at 10 °C min⁻¹ to 90 °C. Samples were cut into rectangular strips, maintaining a ratio of length to width of 5:1.

4.3.9 Tensile Testing

A Test Resources mechanical tester equipped with a 24 N (5.6 lb_f) load cell was used in the tensile mode to generate stress-strain curves. Samples were punched by a dog bone cutter (ASTM D63 Type IV, scaled down by a factor of 4) and were stretched at a rate of 33 μm s⁻¹ until failure, at room temperature.

4.3.10 Stress Relaxation

A TA Instruments Q800 dynamic mechanical analyzer (DMA) was used in stress relaxation mode to measure the iso-strain, time dependent response at a constant temperature. The stress relaxation time reported was zeroed to when the stress is applied. Strain values of 1 – 5% were used. The data was fit to a conventional Arrhenius equation to describe the temperature dependence of stress relaxation is expressed in **Eq 4-2** below, where τ is the stress relaxation time, τ_0 is the reference time, E_a is the activation energy of the reaction, A is the reaction factor, R is the gas constant, and T is the absolute temperature (K).²⁶ **Eq 4-2** was rearranged to calculate the activation energy from the slope, as shown in **Eq 4-3**.

$$\tau(T) = Ae^{-E_a/RT} \quad (4-2)$$

$$\ln \tau = \ln \tau_0 + \frac{E_a}{RT} \quad (4-3)$$

4.3.11 Qualitative Shape Memory and Reconfiguration Testing

A rectangular strip was deformed by wrapping in foil and arbitrarily molding the foil into a wave pattern then placing in water heated to 40 °C to melt the PCL PU fibers; the sample was held submerged for 1 min, followed by immediate quenching in an ice bath for several seconds to recrystallize PCL PU to set the temporary, fixed shape. This fixed shape was then placed back in the warm water to examine recovery, qualitatively. In a separate experiment designed to mechanically program the permanent shape, the permanent shape of a Re-SMEC was reprogrammed by deforming and fastening the sample around a cylindrical rod and placed in an oven at a higher temperature of 80 °C for 20 min followed by cooling to RT. The reconfigured shape was tested for permanency by placing in the warm water bath for 20 min and observing whether any shape change occurs. A new shape memory cycle was conducted again using same methods described here, using a different temporary shape. The cumulative exposure of the sample to the water bath was kept to less than 1.5 h, to prevent significant degradation of the samples.²⁷

4.3.12 Quantitative Shape Memory and Reconfiguration Testing

The shape memory and permanent shape reconfiguration of the composite were quantified using the DMA. The DMA was used in controlled force mode to stretch a dog bone sample at 40 °C to a 15% strain by ramping the force at 0.05 N min⁻¹. The temperature was then decreased at 3 °C min⁻¹ to -40 °C and held isothermal for 10 min to fix the temporary shape. The force was then unloaded at 0.25 N min⁻¹ until it reached the preload force of 10⁻³ N. The permanent shape was recovered by heating at 2 °C min⁻¹ to 40 °C, and holding isothermal for 10

min. The permanent shape was then reprogrammed by changing the DMA mode to stress relaxation and holding a strain of 5.0 % and an isothermal temperature of 90 °C for 5 min followed by a recovery time of 20 min. To run a second shape memory cycle, the DMA was immediately switched back to controlled force mode and a new shape memory cycle was executed using the parameters described above. To test consecutive shape memory cycles without shape reconfiguration, the DMA was set to the controlled force mode and the shape memory cycle described above was repeated three times. The degree of shape fixing (R_f) and the degree of shape recovery (R_r) were quantified for each cycle using the following equations:

$$R_f(\%) = \left(\frac{\varepsilon_{fixed}}{\varepsilon_{deformed}} \right) \times 100 \% \quad (4-1)$$

$$R_r(\%) = \left(\frac{\varepsilon_{fixed} - \varepsilon_{recovered}}{\varepsilon_{fixed} - \varepsilon_0} \right) \times 100 \% \quad (4-2)$$

where ε_0 is the original strain (at the beginning of each cycle), $\varepsilon_{deformed}$ is the deformed strain that occurs after cooling while still under a load, ε_{fixed} is the fixed strain that results following unloading, and $\varepsilon_{recovered}$ is the recovered strain following heating.

4.4 Results

4.4.1 Thiol-ene Elastomer Synthesis

Similar to a previous report, the polyanhydride elastomer (PAH) was synthesized using commercially available materials to yield a crosslinked, degradable polyanhydride (**Scheme 4-1A**).²⁸ Using the same materials and methods, another diene monomer, trimethylolpropane diallyl ether (TMPDAE), was substituted to yield a non-anhydride elastomer for comparison of shape reconfiguration performance (**Scheme 4-1B**).

4.4.2 PAH/PCL-PU Composite Fabrication and Morphology

Poly(ϵ -caprolactone)-based polyurethane (PCL PU) was synthesized as shown in **Scheme 4-1B** to serve as the shape fixing phase via crystallization with a resulting molecular weight of 157,000 g mol⁻¹, as determined by gel permeation chromatography (data not shown). This PCL PU was electrospun to create a nonwoven fiber mat and the reactive PAH monomer mixture was then imbibed into the PCL fiber mat and cured as shown in **Scheme 4-1C**. The morphology of the PAH/PCL composite was observed using scanning electron microscopy (SEM), where the electrospun PCL exhibited a fibrous morphology (**Scheme 4-1D**) that was completely infiltrated by PAH, as indicated by the absence of cavities (**Scheme 4-1E**).

4.4.3 Thermal Properties

The thermal properties of the composite were characterized using differential scanning calorimetry (DSC). A comparison of the second heating and first cooling cycles of electrospun PCL PU and neat PAH shows that the thermal transitions of both components are also detected in the composite at the same temperatures as in the individual components, with electrospun PCL PU exhibiting a relatively low melting transition at 30.3 °C (**Figure 4-1A,B**). By dividing the enthalpy of fusion of the composite by the enthalpy of fusion of electrospun PCL PU, it was estimated that the composite contained 23% PCL. The thermal properties of the PAH and pTMPDAE elastomers are shown in **Figure 4-1** and **Figure 4-3A**, respectively. Based on these data, the glass transition temperatures for PAH and pTMPDAE were determined to be -31.5 °C and -21.0 °C, respectively.

4.4.4 Thermomechanical Properties

The thermomechanical properties of the composite were characterized using dynamic mechanical analysis (DMA). Consistent with DSC results, the tensile storage modulus of the composite exhibited transitions corresponding to its individual components (**Figure 4-1A**). Specifically, the composite exhibited a drop in storage modulus around $-30\text{ }^{\circ}\text{C}$ that can be attributed to the glass transition of PAH, as can be seen from the loss modulus maximum in **Figure 4-2B**, and a second storage modulus drop around $30\text{ }^{\circ}\text{C}$ attributed to the melting of PCL PU, which was used for exploiting shape memory. The storage modulus of the PAH/PCL PU samples was observed to be between that of its components, PCL and PAH, for $T < T_m$.

4.4.5 Mechanical Properties

Uniaxial tensile mechanical properties at room temperature were determined by performing tensile testing on dog bone samples. The resulting engineering stress-strain curves shown in **Figure 4-4** and summarized in **Table 4-1** reveal that the composite mechanical properties are between that of the individual components. The Young's modulus of the PAH/PCL PU composite was $5.6\text{ MPa} \pm 1.4\text{ MPa}$ and was not significantly different from that of the PAH elastomer, at $4.5\text{ MPa} \pm 0.5\text{ MPa}$. The strain-to-failure of $160\% \pm 40\%$ and tensile strength of $4.2\text{ MPa} \pm 0.9\text{ MPa}$ of the composite increased dramatically, compared to PAH alone, which was $25\% \pm 5\%$ and $1.1\text{ MPa} \pm 0.1\text{ MPa}$, respectively.

4.4.6 Stress Relaxation

The shape reconfiguration potential of the polyanhydride elastomer component prior to the addition of PCL was investigated by studying its stress relaxation response for a range of

temperatures. **Figure 4-5** shows that only the PAH elastomer exhibited stress relaxation, whereas the elastomer lacking anhydride groups, such as when substituting PAH with pTMPDAE (**Scheme 4-1A**), it featured no time-dependent reduction in stress. Stress relaxation testing was also conducted at increasing temperatures for the same sample of PAH, which revealed that stress relaxation occurred a meaningful (and increasing) rate for temperatures above 40 °C, with stress decaying exponentially for all temperatures (**Figure 4-5B**). Increasing the temperature enabled faster completion of shape reconfiguration, from approximately 9 min at 90 °C to greater than 4 h at 50 °C.

4.4.7 Qualitative Shape Reconfiguration

To examine the shape reconfiguration of the PAH elastomer qualitatively, samples of the PAH- and TMPDAE-based elastomers were heated and deformed around a cylindrical rod and the resulting shape was observed. As shown in **Figure 4-6**, only the anhydride-based (PAH) elastomer maintained the newly configured curved shape, whereas the TMPDAE-based elastomer returned immediately to its original, flat shape upon removal of the load.

4.4.8 Qualitative Shape Memory and Reconfiguration

The top row of **Figure 4-7A** demonstrates that the composite can exhibit basic one way shape memory behavior, beginning as a flat strip programmed into a serpentine form at 40 °C, which then recovers back to its original flat form upon being thermally trigger. The ability of this composite to *reconfigure* its shape is demonstrated in the bottom row of **Figure 4-7A**, where the composite is heated to 80 °C while deformed into a circular bend, that does not recover to its as-cured flat shape under the same conditions used to trigger shape recovery (**Figure 4-7A iii – iv**).

The newly reconfigured permanent shape can undergo additional shape memory cycles, which are demonstrated by again heating to 40 °C and deforming indiscriminately into a coil that is then recovered to the reconfigured permanent, circular shape.

4.4.9 Quantitative Shape Memory and Reconfiguration

The shape memory and reconfiguration cycles were quantified and shown in **Figures 4-7B** and **Figure 4-8**. **Figure 4-7B** first demonstrates one way shape memory by programming a temporary elongated shape and recovering to its as-fabricated length. The permanent shape was then reconfigured to a new length by implementing a stress relaxation cycle (between time markers 105 min and 125 min); this was followed by another one way shape memory cycle, which was recovered to the reconfigured length. The results in **Figure 4-8** verify that the composite is capable of traditional one-way shape memory, repeatable for three consecutive cycles. Based on this, the shape fixing ratios were determined to be 87 %, 86 %, and 86 % for cycles 1, 2, and 3, respectively, and did not significantly diminish with each additional cycle. The additional elongation of the sample upon cooling during the fixing cycle is likely due to PCL crystallization.²⁹ The shape recovery ratios were calculated to be 84 %, 93 %, and 78 % for cycles 1, 2, and 3, respectively. While these recovery ratios are modest in quality, the results indicate, collectively, significant and reproducible shape memory behavior in addition to the new reconfigurability.

4.5 Discussion

In this chapter, we identified the dynamic covalent bond exchange properties of a cross-linked polyanhydride elastomer and its temperature dependence, and subsequently used these features to develop a reconfigurable shape memory elastomeric composite (Re-SMEC).

Embedding the PCL PU fibers within a cross-linked PAH elastomeric matrix resulted in a composite with thermal and mechanical properties between its individual components, as expected, with the exception of Young's modulus, which was similar to that of the PAH elastomer. This is not surprising, given that the composite was determined to be composed of approximately 87% PAH. The PAH elastomer has a lower strain-to-failure than would be expected from other soft elastomers such as PDMS (see Chapter 3); however, the addition of the PCL PU fibers significantly improved these properties six-fold, expanding this material's potential applications.

The time- and temperature-dependent relaxation properties of the polyanhydride elastomer component, prior to combining with PCL to form a composite, were studied and compared with pTMPDAE, a similarly structured cross-linked thiol-ene elastomer lacking the anhydride bridging group needed for bond reconfiguration reactions. As shown in **Figure 4-5A**, only the PAH elastomer exhibited stress relaxation, whereas pTMPDAE featured no time dependent reduction in stress. This supports our hypothesis that the bond reconfiguration in the solid state of the PAH elastomer is due to dynamic covalent exchange reactions involving the anhydride groups, as depicted by following the color-coded elements in **Scheme 4-2**. We postulate that this mechanism may be concerted or involve a free acid group. To our knowledge, exchange reactions of anhydride groups have been reported to occur for small molecules in the

liquid state.²¹⁻²⁵ About six decades ago, Hurd et al. studied using a ketene agent to prevent mixed anhydrides from exchanging during purification, thus simplifying the process.²⁵ More recently, Tarcha et al. found that sebacic anhydride had a tendency to disproportionate into methacrylic anhydride and oligomers of poly(sebacic acid) during storage, while in the liquid state, and this reaction can be stabilized by decreasing the temperature.²² These studies all involved anhydride monomers in liquid form and not polymerized anhydride in the solid state.

As seen in **Figure 4-5B**, the temperature dependence of the PAH tensile stress relaxation was found to enable faster completion of shape reconfiguration at higher temperatures, as is evidenced by the significant change in relaxation time from 4 h to 9 min. Arrhenius' law is often used to provide insight into the temperature dependence of chemical reactions such as polymerizations, diffusion of molecules and degradation, to name a few. We observed that the temperature dependence of the associated relaxation time of the PAH elastomer followed an Arrhenius behavior, with an activation energy of 7.7 kcal/mol (**Figure 4-9**). This activation energy is lower than what has been observed in other exchange reaction systems, allowing for more efficiency and responsiveness in the design of a smart material. For transesterification-based exchange reactions, others have reported activation energies within the range of 19 – 33 kcal/mol.³⁰⁻³² Denissen et al. reported a relatively low activation energy of 14 kcal/mol for their vinylogous polyurethane vitrimers, with quick stress relaxation times of 550 s to 85 s, though these were at high temperatures of 130 °C to 170 °C.³³ At temperatures of 180 – 210 °C, Aden et al. observed activation energies of 11 kcal/mol of the ester-ester exchange of poly(ethylene terephthalate) using a ethyl benzoate catalyst³⁴ It was also observed that the initial modulus of PAH increased slightly with temperature (**Figure 4-10**). While a theory for elasticity of

thermally reconfigurable networks has not yet been developed, to our knowledge, we attribute this observation to the prediction from conventional rubber (entropy) elasticity theory that the elastic modulus increases proportionally with temperature as $E \sim nkT$, where n is the crosslink density.

To visually demonstrate the shape reconfiguration of the PAH elastomer, a qualitative shape reconfiguration test was conducted and compared with similarly synthesized pTMPDAE elastomer. The deformed shape following thermally activated stress and strain around a cylindrical rod is shown in **Figure 4-6**. Interestingly, only the anhydride-based (PAH) elastomer maintained the newly configured curved shape, whereas the TMPDAE-based elastomer returned immediately to its original, flat shape upon removal of the load, as expected of an elastomer. Moreover, when the deformed PAH was heated back to 80 °C in the stress-free state, it did not return to its original shape, but remains deformed (not shown), further supporting that this new shape is permanent, as a result of the rearrangement of the anhydride bonds.

In light of these thermally reconfigurable properties, a shape memory system was then designed with thermal triggers below 50 °C as this would prevent overlap of operating regimes with the PAH shape reconfiguration that was shown to occur above this temperature. To fabricate a shape memory composite capable of permanently changing its original shape, a low-melting poly(ϵ -caprolactone)-based polyurethane (PCL PU) was synthesized to serve as the shape fixing phase via crystallization (**Scheme 4-1B**). A shape reconfiguration temperature of 80 °C was selected due to the reasonably short time requirement. The top row of **Figure 4-7A** demonstrates that the composite can exhibit basic one way shape memory behavior, and the

ability of this composite to *reconfigure* its shape is demonstrated in the bottom row of **Figure 4-7A**, and was demonstrated to undergo additional shape memory cycles.

This shape memory observation was also quantified (**Figure 4-7B**) where a stress relaxation cycle was implemented to produce a reconfigured shape between shape memory cycles. Like other shape memory systems, the permanent shape for this composite is established by the polyanhydride crosslinks, which served to recall the permanent shape, and is governed by the geometry under which it was polymerized.³⁵ Unlike other systems, this original shape can be reprogrammed by rearrangement of these crosslinks so that the shape memory performs relative to this newly reconfigured permanent shape. While others have developed reconfigurable shape memory systems, few are biocompatible and to our knowledge, none are fully biodegradable which can be used to tailor geometry-specific implantable medical devices capable of controlled drug delivery.³⁶⁻³⁸ Additionally, this composite enables shape recovery to occur at physiological temperatures, which can potentially be used for designing medical devices that require this action in the body and with timed degradation.

4.6 Conclusions

In conclusion, a new shape memory composite with the ability to reconfigure its permanent shape was developed. This biocompatible and fully degradable composite provides benefits over other reconfigurable systems in that this material can also provide temporary shape programming and recovery without interference with its permanent reconfiguration encoding. Additionally, since shape memory occurs at physiological temperatures, the potential exists for many biomedical applications such as degradable implants with deploying mechanisms, self-healing applications, and dynamic surfaces for tissue engineering.

4.7 Acknowledgements

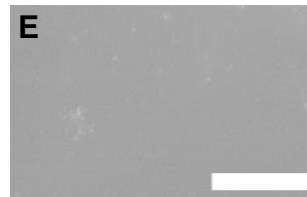
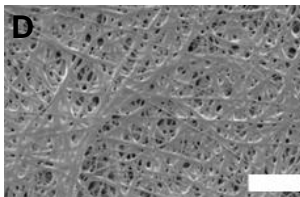
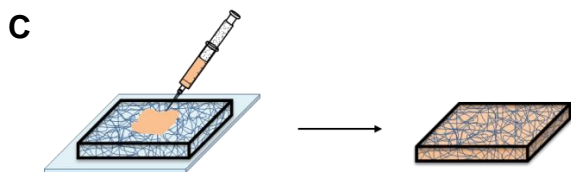
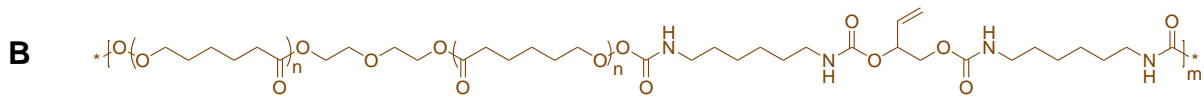
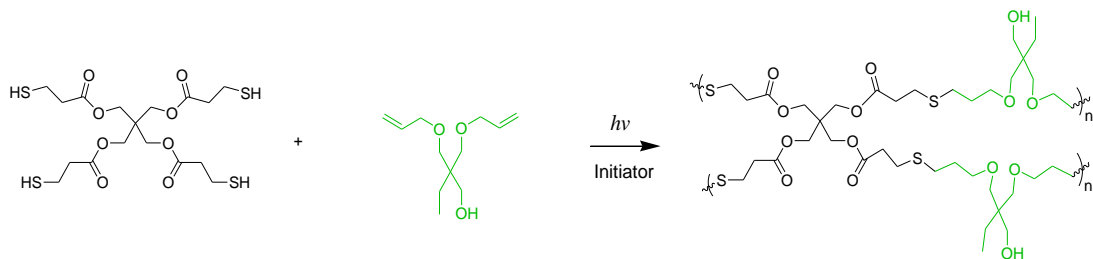
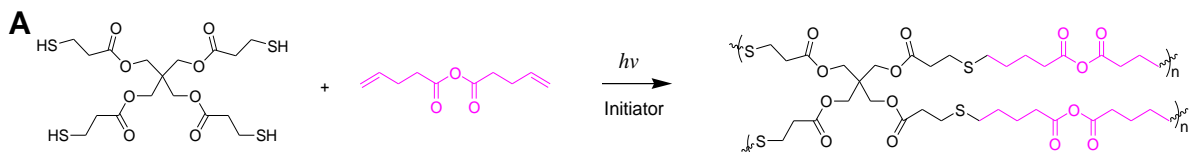
This work was performed in collaboration with Prof. Devon A. Shipp at Clarkson University in Potsdam, NY. The PCL PU in this chapter was synthesized and characterized for molecular weight by Wenbin Kuang, a graduate student in the Mather Research Group.

4.8 References

1. Lendlein, A. & Kelch, S. Shape-memory polymers. *Angewandte Chemie International* **41**, 2034 (2002).
2. Wischke, C. Neffe, A.T., Steuer, S. & Lendlein, A. Evaluation of a degradable shape-memory polymer network as matrix for controlled drug release. *Journal of Controlled Release* **138**, 243 (2009).
3. Xie, T. Recent advances in polymer shape memory. *Polymer* **52**, 4985 (2011).
4. Yackacki, C. Shape-Memory and Shape-Changing Polymers. *Polymer Reviews* **53**, 1 (2013).
5. Mauldin, T. C. & Kessler, M. R. Self-healing polymers and composites. *International Materials Reviews* **55**, 317 (2010).
6. Behl, M., Razzaq, M. Y. & Lendlein, A. Multifunctional Shape-Memory Polymers. *Advanced Materials* **22**, 3388 (2010)7.Yackacki, C. M. Shape-memory and shape-changing polymers. *Taylor & Francis* (2013).
8. Burke, K. A. & Mather, P. T. Soft shape memory in main-chain liquid crystalline elastomers. *Journal of Materials Chemistry* **20**, 3449 (2010).
9. Ahir, S. V. & Tajbakhsh, A. R. Self-assembled shape-memory fibers of triblock liquid-crystal polymers. *Advanced Functional Materials* **16**, 556 (2006).
10. Knight, P. T., Lee, K. M., Chung, T. & Mather, P. T. PLGA– POSS End-Linked Networks with Tailored Degradation and Shape Memory Behavior. *Macromolecules* **42**, 6596 (2009).
11. J Jung, Y. C., So, H. H. & Cho, J. W. Water-responsive shape memory polyurethane block copolymer modified with polyhedral oligometric silsesquioxane. *Journal of Macromolecular Science, Part B* **45**, 453 (2006).
12. Torbati, A. H., Nejad, H. B., Ponce, M., Sutton, J. P. & Mather, P. T. Properties of triple shape memory composites prepared via polymerization-induced phase separation. *Soft Matter* **10**, 3112 (2014).
13. Cao, Y., Guan, Y., Du, J., Peng, Y., Yip, C.W. & Chan, A.S. Hydrogen-bonded polymer network—poly (ethylene glycol) complexes with shape memory effect. *Journal of Materials Chemistry* **12**, 2957 (2002).

14. Zhang, H., Wang, H., Zhong, W. & Du, Q. A novel type of shape memory polymer blend and the shape memory mechanism. *Polymer* **50**, 1596 (2009).
15. Luo, X. & Mather, P. T. Preparation and characterization of shape memory elastomeric composites. *Macromolecules* **42**, 7251 (2009).
16. Robertson, J. M., Nejad, H. B. & Mather, P. T. Dual-spun shape memory elastomeric composites. *ACS Macro Letters* **4**, 436 (2015).
17. Montarnal, D., Capelot, M., Tournilhac, F. & Leibler, L. Silica-like malleable materials from permanent organic networks. *Science* **334**, 965 (2011).
18. Chen, X., Dam, M.A., Ono, K., Mal, A., Shen, H., Nutt, S.R., Sheran, K & Wudl, F.. A thermally re-mendable cross-linked polymeric material. *Science* **295**, 1698 (2002).
19. Kloxin, C. J. & Bowman, C. N. Covalent adaptable networks: smart, reconfigurable and responsive network systems. *Chemical Society Reviews* **42**, 7161 (2013).
20. Shipp, D. A., McQuinn, C. W. & Rutherglen, B. G. Elastomeric and degradable polyanhydride network polymers by step-growth thiol-ene photopolymerization. *Chemical Communications* 6415 (2009).
21. Tarbell, D. S. Carboxylic carbonic anhydrides and related compounds. *Accounts of Chemical Research* **2**, 296 (1969).
22. Tarcha, P. J., Su, L., Baker, T. & Langridge, D. Stability of photocurable anhydrides: methacrylic acid mixed anhydrides of nontoxic diacids. *Journal of Polymer Science Part A: Polymer Chemistry* **39**, 4189 (2001).
23. Benoiton, N. L., Lee, Y. C. & Chen, F. M. Studies on the disproportionation of mixed anhydrides of N-alkoxycarbonylamino acids. *International Journal of Peptide and Protein Research* **41**, 338 (1993).
24. Ponticorvo, L. & Rittenberg, D. O18 Exchange Reactions between Anhydrides and Carboxylic Acids. *Journal of the American Chemical Society* **40**, 1705 (1954).
25. Hurd, C. D. & Dull, M. F. The use of ketene in the preparation of simple and mixed acid anhydrides. *Journal of the American Chemical Society* **54**, 3427 (1932).
26. Rodriguez, F., Cohen, C., Ober, C. K. & Archer, L. *Principles of Polymer Systems*. 5th Edition. Taylor & Francis, London (2014).

27. Poetz, K. L., Mohammed, H. S., Snyder, B. L. & Liddil, G. Photopolymerized Cross-Linked Thiol–Ene Polyhydrides: Erosion, Release, and Toxicity Studies. *Biomacromolecules* **15**, 2573 (2014).
28. Rutherglen, B. G., McBath, R. A. & Huang, Y. L. Polyhydride networks from thiol–ene polymerizations. *Macromolecules* **43**, 10297 (2010).
29. Chung, T., Romo, A. & Mather, P.T. Two-way reversible shape memory in a semicrystalline network. *Macromolecules* **41**, 184 (2008).
30. Kuang, X., Liu, G., Dong, X. & Wang, D. Correlation between stress relaxation dynamics and thermochemistry for covalent adaptive networks polymers. *Materials Chemistry Frontiers* **1**, 2052 (2017).
31. Brutman, J. P., Delgado, P. A. & Hillmyer, M. A. Polylactide vitrimers. *ACS Macro Letters* **3**, 607 (2014).
32. Fortman, D. J., Brutman, J. P. & Cramer, C. J. Mechanically Activated, Catalyst-Free Polyhydroxyurethane Vitrimers *Journal of the American Chemical Society* **137**, 14019 (2015).
33. Denissen, W., Rivero, G., Nicolay, R., Leibler, L., Winne, J.M. & Du Prez, F.E. Vinylogous Urethane Vitrimers. *Advanced Functional Materials* **25**, 2451 (2015).
34. A Aden, M. & Gilmer, J.W. Transesterification of poly (ethylene terephthalate). *ACS Division of Polymer Chemistry Meeting* **28**, 304 (1987).
35. Liu, C., Qin, H. & Mather, P.T. Review of progress in shape-memory polymers. *Journal of Materials Chemistry* **17**, 1743 (2007).
36. Michal, B. T., Jaye, C. A., Spencer, E. J. & Rowan, S. J. Inherently photohealable and thermal shape-memory polydisulfide networks. *ACS Macro Letters* **2**, 694 (2013).
37. Zhao, Q., Zou, W., Luo, Y. & Xie, T. Shape memory polymer network with thermally distinct elasticity and plasticity. *Science Advances* **2**, e1501297 (2016).
38. Li, J., Lewis, C. L., Chen, D. L. & Anthamatten, M. Dynamic mechanical behavior of photo-cross-linked shape-memory elastomers. *Macromolecules* **44**, 5336 (2011).



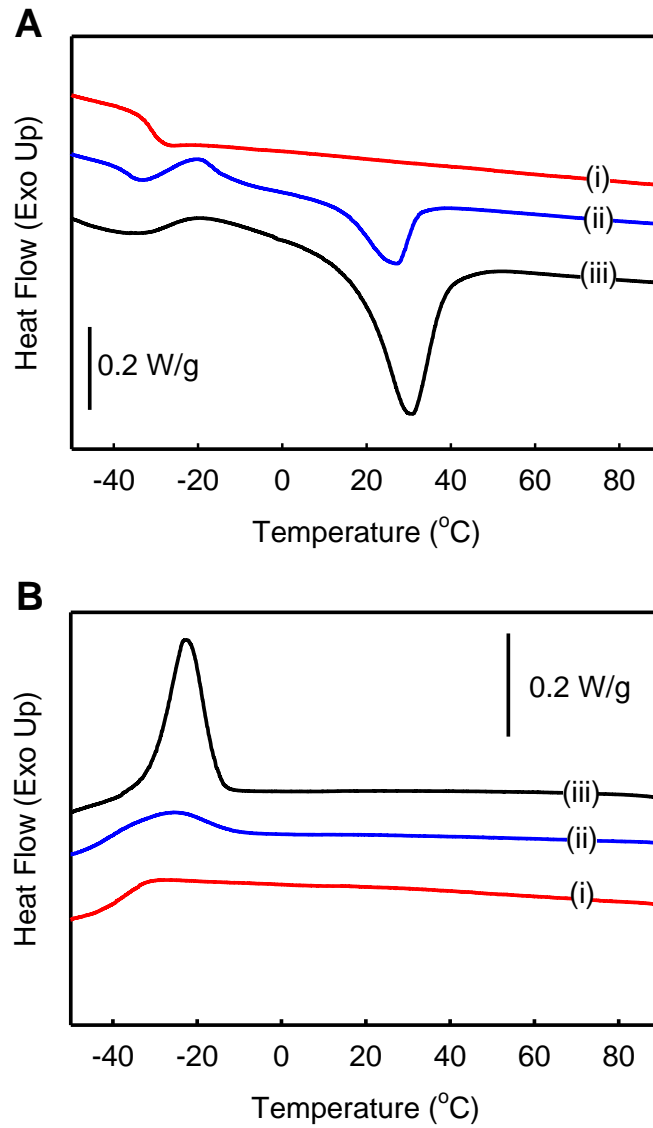


Figure 4-1. (A) Differential scanning calorimetry (DSC) second heating curves, and (B) first cooling curves of (i) neat PAH elastomer, (ii) PAH/PCL PU composite, and (iii) electrospun PCL PU.

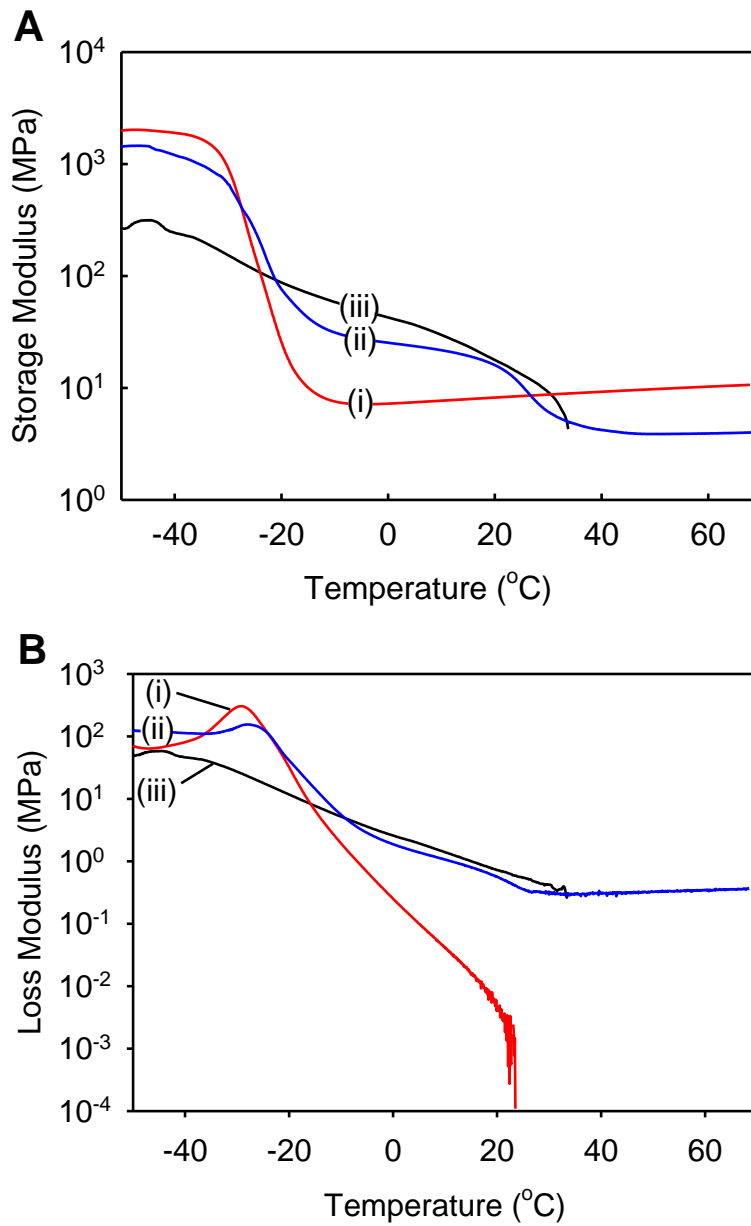


Figure 4-2. Dynamic mechanical analysis (DMA) (A) storage modulus curves and (B) loss modulus curves of (i) neat PAH elastomer, (ii) PAH/PCL PU composite, and (iii) electrospun PCL PU.

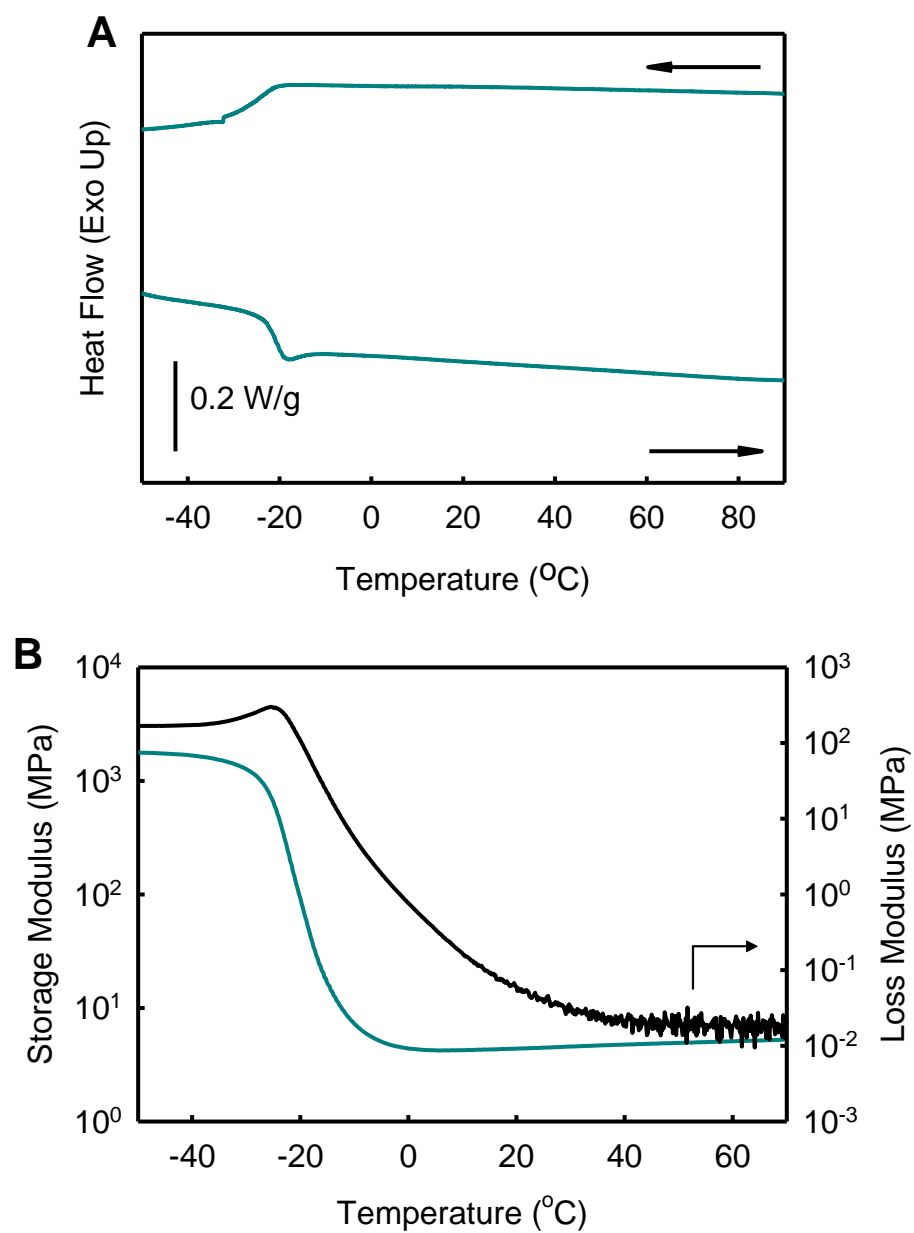


Figure 4-3. (A) Differential scanning calorimetry first cooling and second heating results and (B) dynamic mechanical analysis of pTMPDAE-based elastomer.

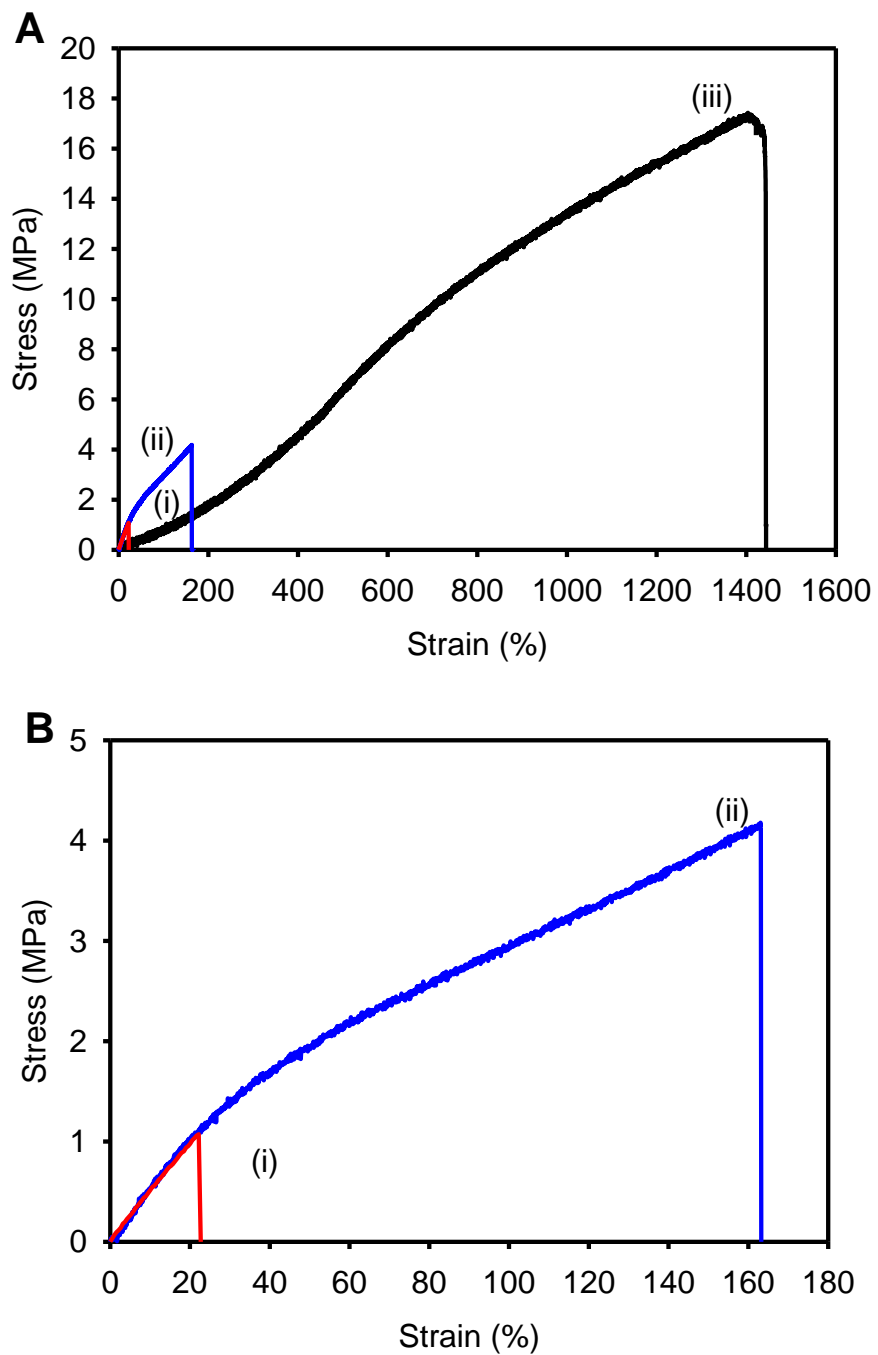


Figure 4-4. Representative engineering stress-strain curves of (i) PAH elastomer, (ii) the PAH-PCL PU composite, and (iii) electrospun PCL PU, where the composite and its components are shown in (A). More details of the PAH elastomer and the composite are shown in (B).

Table 4-1. Summary of mechanical properties for the PAH/PCL PU elastomeric composite.

Sample	Young's Modulus (MPa)	Strain-to-Failure (%)	Tensile Strength (MPa)
PAH	4.6 ± 0.5	26 ± 5	1.1 ± 0.1
PCL PU	1.1 ± 0.4	1400 ± 70	17.6 ± 1.7
Composite	5.6 ± 1.4	160 ± 40	4.2 ± 0.9

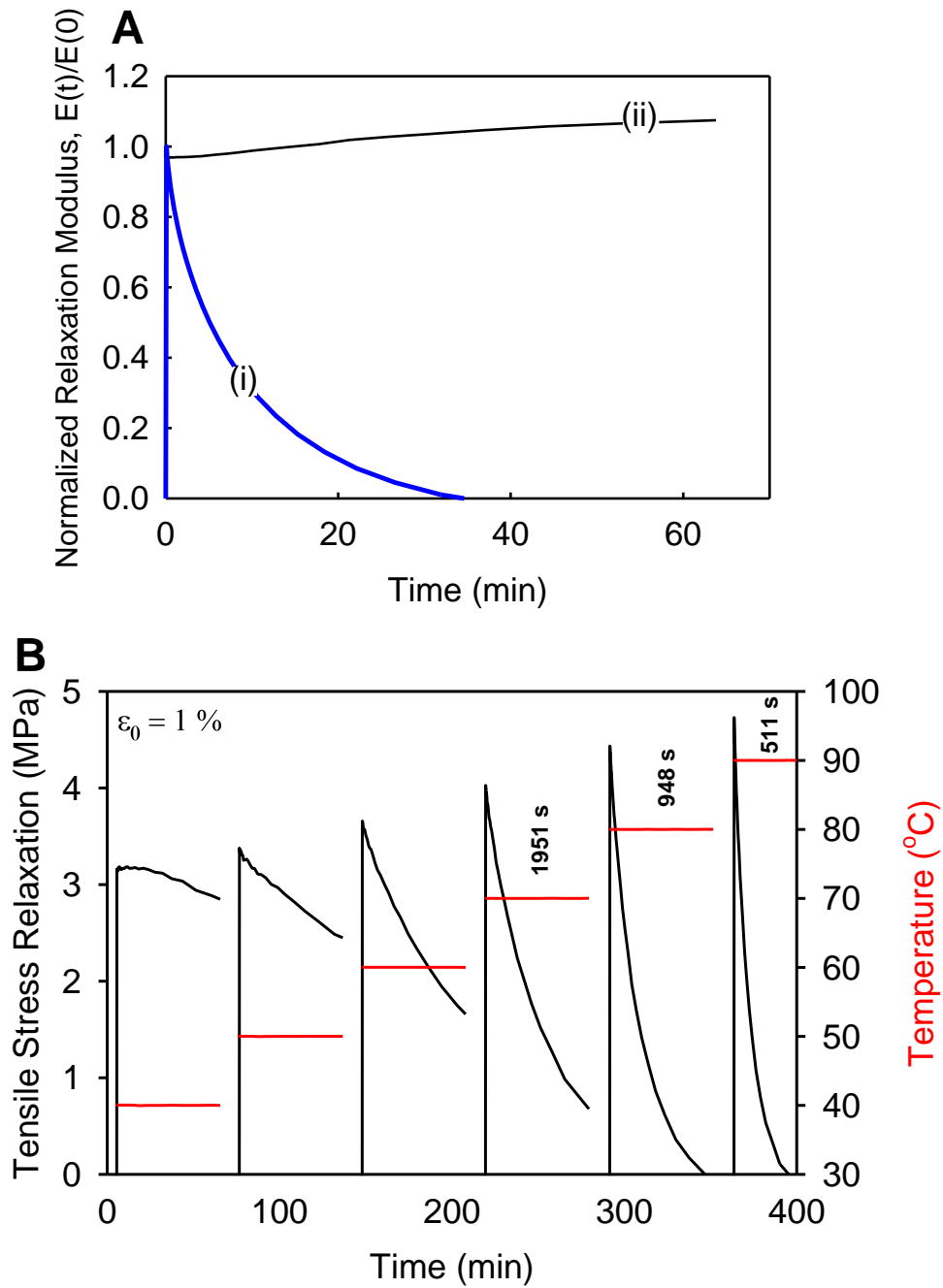


Figure 4-5. Shape reconfiguration as measured by stress relaxation. The relaxation modulus versus time are shown for: (A) varying the network composition at 80 $^{\circ}\text{C}$ for (i) PAH and (ii) TMPDAE, and (B) varying reconfiguration temperatures for the PAH elastomer.

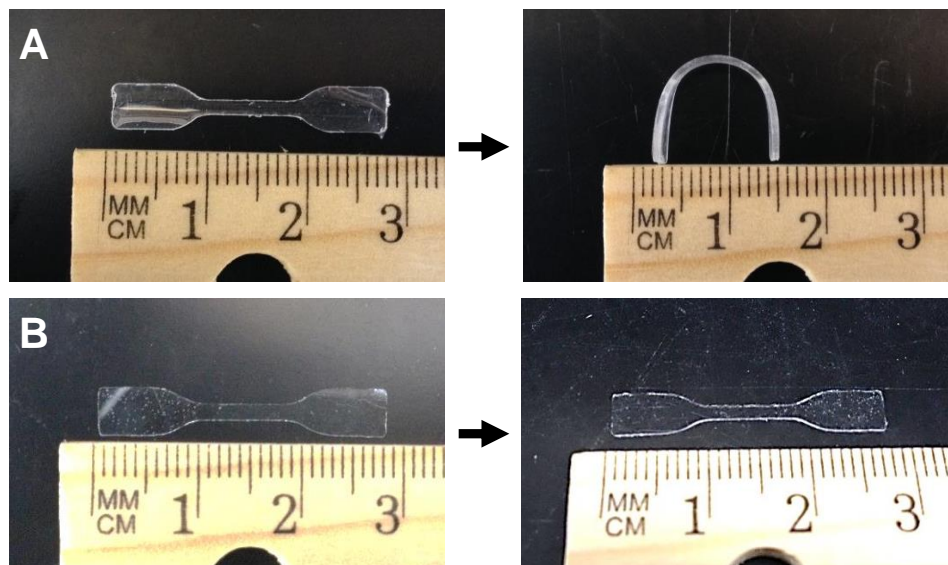


Figure 4-6. Shape reconfiguration response of elastomers synthesized using: (a) anhydride (PAH) and (b) TMPDAE diene monomers, in the flat configuration (left) and resulting shape following shape reconfiguration at 80 °C (right).

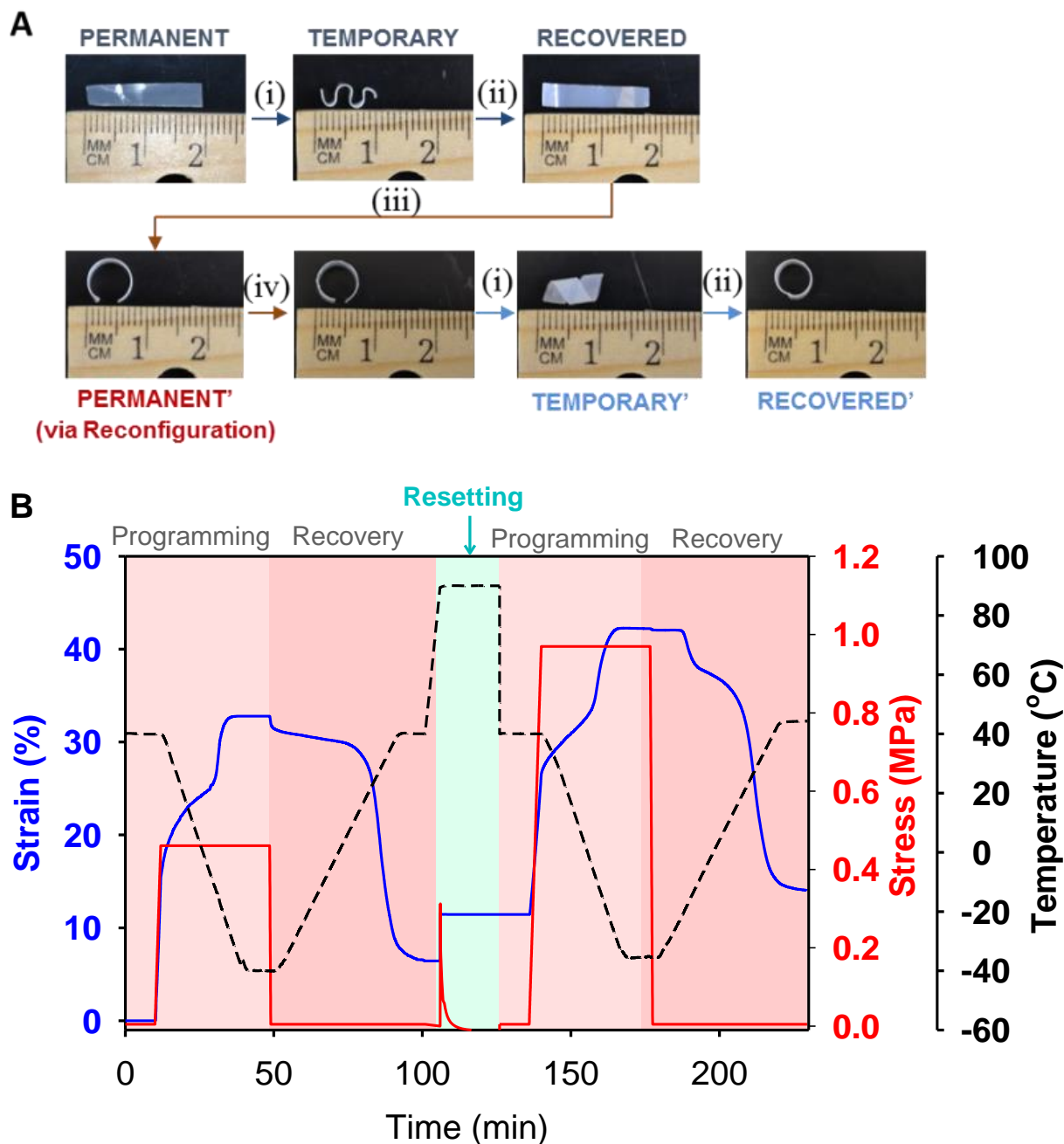


Figure 4-7. Shape memory and reconfiguration behavior of PAH/PCL PU polyurethane composite. (A) Images of qualitative study demonstrating one way shape memory where (i) a temporary shape is fixed and then (ii) recovered to the original shape, followed by (iii) reconfiguration of the permanent shape; (iv) the reconfigured shape does not recover to the original geometry. (B) Quantitative shape memory and shape reconfiguration cycles for the PAH/PCL PU composite.

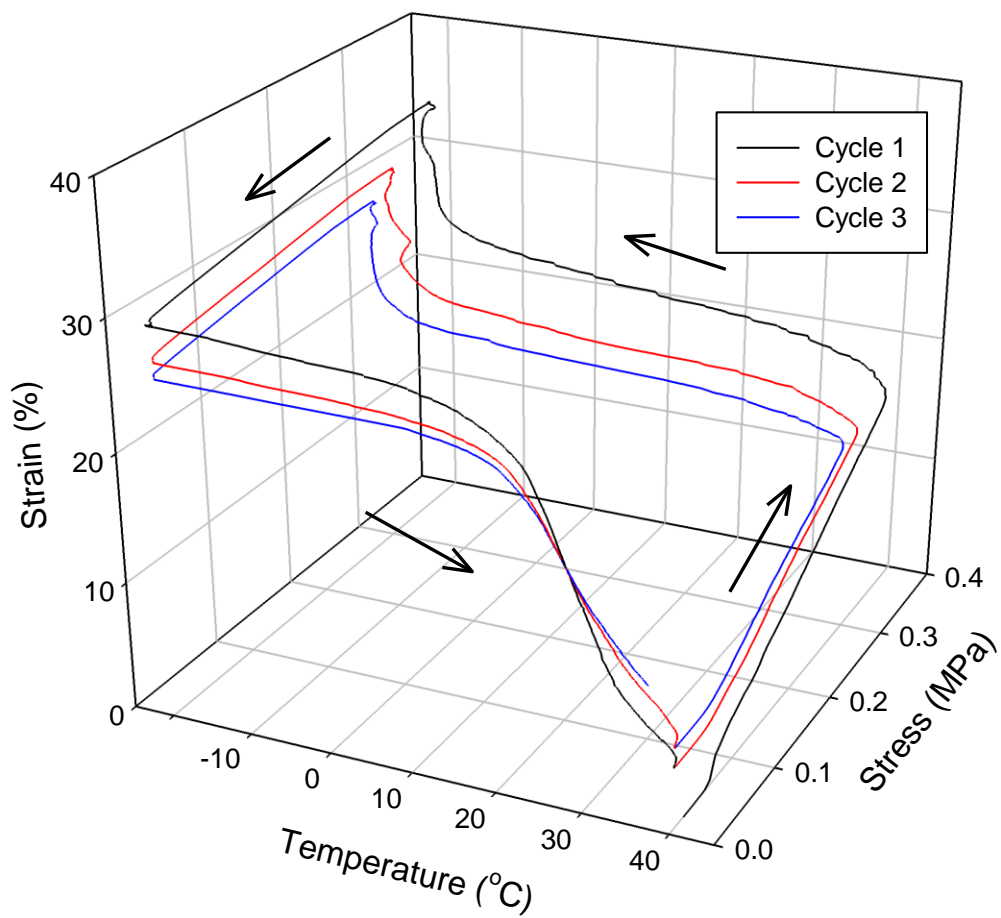
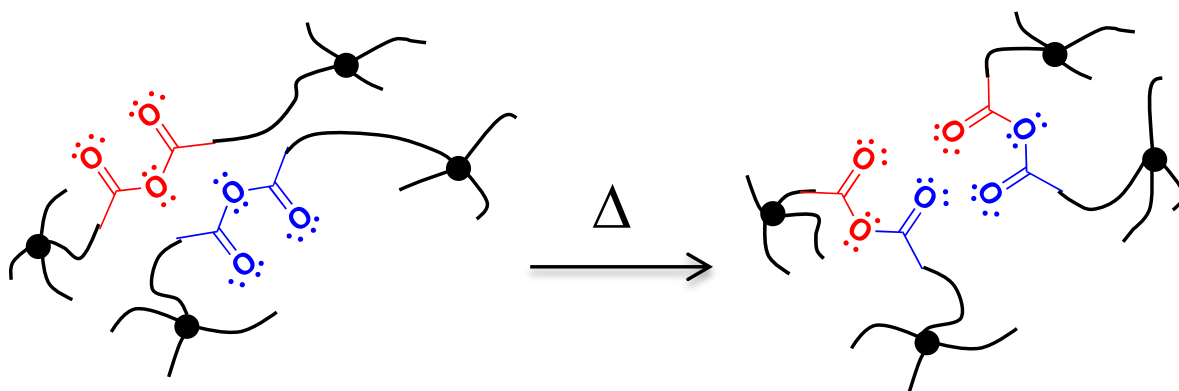
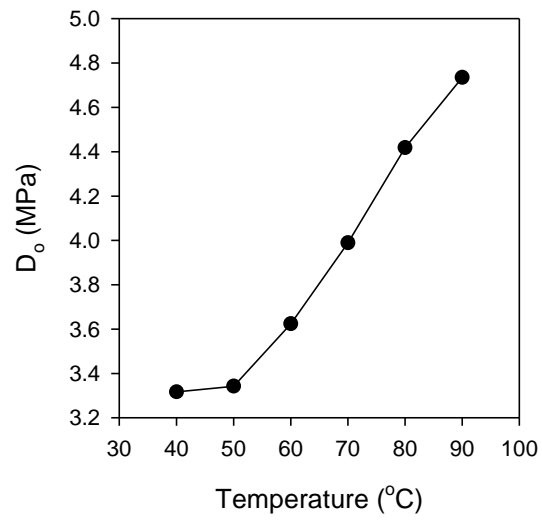
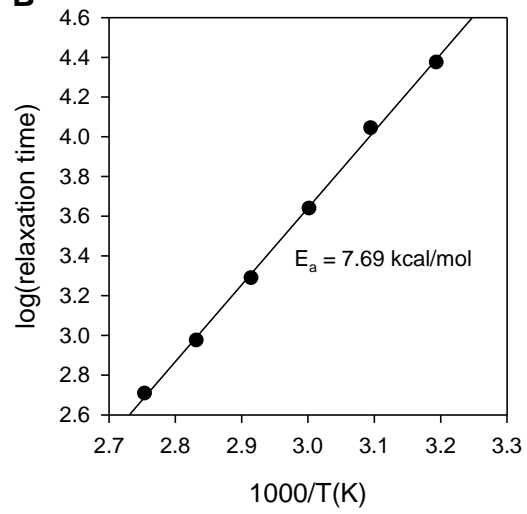


Figure 4-8. Shape memory stress-temperature-strain plot for PAH/PCL PU composite.



Scheme 4-2. Dynamic covalent exchange activated thermally and involving rearrangement of adjacent anhydride groups.

A**B**

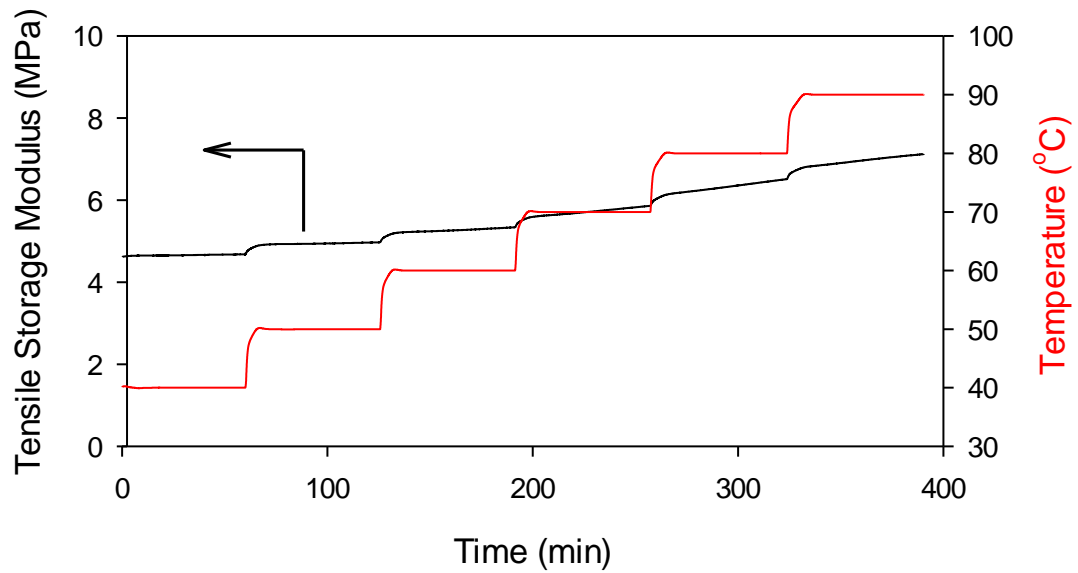


Figure 4-10. Isothermal tensile storage modulus of the PAH elastomer as temperature is increased in a stepwise manner.

Chapter 5

Biodegradable Shape Memory Elastomeric Composites with Controlled Release of a Model Drug

5.1. Synopsis

The degradation and drug release properties of polyanhydride (PAH) based elastomeric shape memory composites developed in **Chapter 4** were studied. Under *in vitro* physiological conditions, the degradation rate of the PAH matrix was strongly influenced by the selection of the polymeric fibrous phase. Based on the gravimetric, thermal and morphological properties, degradation was significantly faster for the composite containing poly(ϵ -caprolactone) (PCL) fibers compared to composites with poly(vinyl acetate) (PVAc) fibers. An erosion mechanism was found to occur as a modified surface to bulk degradation in the composite, although the PAH by itself erodes heterogeneously. A hydrophilic model drug was incorporated in the fibrous phases and used to study the *in vitro* controlled release properties of these composites. For the PCL-based composite, drug release correlated with PAH matrix degradation. In contrast, the drug release for the PVAc-based composite proceeded more steadily and slowly increased over time, which was attributed to plasticization by PAH degradation products and water. Lastly, the shape memory properties were examined for both composites. The PCL/PAH composite was capable of preserving arbitrary fixed shapes during and for months after matrix degradation. While the PVAc/PAH composite could not maintain a fixed shape in aqueous media due to significant shrinkage, it proved capable of one way shape memory independent of the reconfiguration properties of the PAH matrix.

5.2. Introduction

Degradable materials generally have two major applications: (1) ecological, where a biodegradable packaging can minimize the environmental impact of consumer products, and (2)

biomedical, where, for example, a resorbable prosthesis eliminates the need for retrieval surgeries and circumvents long-term foreign responses.^{1,2} These multifaceted, broad range of applications for degradable materials translates to complex requirements for device development, ranging from rapid degradation for short-term use to long-term maintenance of mechanical integrity, among other prerequisites. In the biomedical domain, degradable materials are required to subsist in the relatively aggressive environment of the human body, while also providing organ function, or substituting for or repairing a specific tissue. Biodegradation is required to occur in such a manner that degradation matches the material replacement by native cells.³ Ideally, the material should promote cell attachment and proliferation, with means for cellular nutrient and waste transport that facilitates tissue regeneration, and the degradation rate of a material must be engineered to accommodate this.⁴ Aside from tailoring the degradation rate, other factors must be considered when designing biodegradable materials such as material processability, mechanical properties, shelf life, biocompatibility during degradation with safe elimination from the body, as well as material properties during degradation.⁵ The challenges with developing degradable biomaterials are that degradation is also dependent on morphology, hydrophilicity, crystallinity, additives (such as drugs, salts or plasticizers) molecular weight, size, shape, and whether degradation was studied *in vivo* or *in vitro*.⁶⁻⁸ Consequently, the advancement of degradable materials is dependent on multiple research fronts and disciplines.

Degradation of a polymeric material proceeds according to two main mechanisms: surface/heterogeneous or bulk/homogenous degradation. The mechanisms of degradation are generally either hydrolytic, enzymatic, or oxidative in nature. These materials are discernable by their hydrolyzable bonds, with the chemical interaction between the labile bond and water

dictating the hydrolysis rate.⁹ Polymers that undergo surface erosion maintain their geometry during degradation while the material loss occurs at the surface, where it is exposed to its environment; the material loss generally proceeds at a constant rate. A bulk eroding polymer loses material through its matrix as water penetrates through its volume, and its erosion rate depends on the amount of available material at a given time point.¹⁰ Typical degradable biomaterials are based on homopolymers or copolymers of poly(glycolic acid), poly(lactic acid), polyesters, and polydioxanones, bacterial-derived polymers, polyanhydrides, or natural polymers.^{11,12}

As mentioned earlier, biomaterials are tasked with meeting complex, application-driven requirements for placement in dynamic environments. As such, it is not adequate for a material to solely possess tunable degradability, since this will still fall short of meeting other constraints. Supplementing these materials with additional functionality such as mechanical toughness, shape memory for minimally invasive surgery, and controlled drug release for infection management, can greatly extend its scope to numerous applications, which is why many researchers endeavored to achieve these goals, as revealed by several review articles.¹³⁻¹⁴ Neffe et al. recognized this technological gap, and sought to combine three functions into one material by cross-linking drug-loaded oligo[(ϵ -hydroxycaproate)-*co*-glycolate]dimethacrylates.¹⁵ By varying the glycolate and *n*-butylacrylate content, the degradation rate of this copolymer was greatly varied. Serrano et al. developed a degradable shape memory elastomer capable of both controlled release and tunable degradation by synthesizing cross-linked polydiolcitrate polyesters.¹⁶ Through alteration of the molar ratio of hydroxyl to carboxyl groups in the synthesis reaction, as well as by the addition of a hydrophilic monomer, the authors were able to shift the degradation

from approximately 90% to 40% degraded at 8 w, and show good shape memory with drug release of a model molecule up to approximately 20 d. Nagahama et al. synthesized custom cross-linked branched oligo(caprolactone) networks also capable of one way shape memory and controlled drug release.¹⁷ The polymer degradation was tuned by the addition of ϵ -caprolactone monomer during synthesis to influence crystallinity in the sample. The degradation of these materials was slow, with the samples retaining over 96% of its initial weight for 120 d, at which point the different degradation profiles became apparent. The authors demonstrated controlled drug release; however the release rate was not different between differing samples. These studies, like others,¹⁸⁻¹⁹ achieved multifunctional degradable materials that rely on customized chemical synthesis methods, which are time-consuming, specific, and more expensive for scale-up and manufacturing. Zhang et al. observed this challenge and aimed to address the need for a more cost-effective multifunctional material by combining commercially available materials to create a shape memory composite with tunable degradation.²⁰ The authors showed that a combination of poly(lactic acid) fibers and a cross-linked poly(trimethylene carbonate) matrix exhibited good shape memory and a high mechanical moduli, which is not suitable for tissue engineering of soft tissues. Moreover, this study did not examine or verify the claim of tunable degradation of these materials and therefore it is unclear how it performs as a multifunctional biomaterial. As such, there remains an opportunity to develop a more cost-effective, manufacturing-friendly multifunctional material with tailorable degradation, particularly with low moduli.

Another approach to meet the challenging requirement of multifunctionality is to blend existing materials to form composites. Polymeric composites offer versatility of material

properties and hold the potential of designing materials that meet multiple requirements. Composites have an added commercial benefit in that the simple regulation of the ratio of its individual components, such as homopolymers, results in a diversity of material properties. The blending of polymers to form a composite is scalable and cost-effective, particularly when using commercially available materials, and even more so if the material has been previously used in FDA-approved devices. On the other hand, composite materials introduce challenges of reproducibility of microstructure and often a large impact of the fiber/matrix interface on macroscopic properties. Our research strategy in this chapter was based on the integration of commercially available biocompatible materials to form multifunctional, degradable composites.

One polymer of interest to us was poly(ϵ -caprolactone) (PCL), a degradable, semicrystalline polyester with proven biocompatibility that has been widely studied as a platform for new products due to its ease of manufacture, and long-term degradability. PCL has been studied extensively *in vivo* and is FDA approved for use in a number of biomedical devices including sutures and drug delivery vehicles^{21,22} PCL is commercially available in a range of molecular weights, and easy to manufacture given its ability to dissolve in many common organic solvents and its relatively low melting transition of approximately 54 – 60 °C for melt processing. Degradation of PCL occurs after about 2 - 4 y via hydrolysis of the ester groups and occurs in two main stages beginning with a reduction in molecular weight, which is likely dominated by bulk erosion that can be accelerated in the presence of lipase.^{4,23,24} PCL by itself, however, does not meet many biomedical needs beyond biocompatibility. To extend its range of application, many have combined it with another polymer or material.²⁵⁻²⁶

In **Chapter 4** we presented a study of the shape memory and shape reconfiguration properties of a new elastomeric composite that combined PCL with cross-linked polyanhydride (PAH). However, the degradation properties of this new composite had not been investigated. PAH is a hydrophobic polymer that undergoes surface erosion by hydrolysis of the anhydride groups. Further, it is distinguished from other materials undergoing hydrolytic reactions, such as esters and amides, in that it has a much shorter half-life due to the relative instability of the anhydride linkage in many types of aqueous environments.²⁷ PAH has been demonstrated to be biocompatible and has been approved in some forms by the FDA in devices to treat brain cancer.^{28,29} Due to these properties, PAH-based materials are primarily studied for drug delivery applications given their predictable degradation profile. The PAH used in this study was developed by Shipp et al., where a thiol-ene chemistry was used to create cross-linked, elastomeric polyanhydrides with tailorable properties and was shown to undergo *in vitro* surface degradation over a period of approximately three days.³⁰

Prior work in the Mather research group focused on developing soft, elastomeric shape memory composites using electrospun fibers with a distinct thermal transition embedded in an elastomeric matrix. Both Luo et al. and Robertson et al. developed shape memory composites combining electrospun PCL embedded in a non-degradable matrix such as polydimethylsiloxane or a polyurethane, each termed a shape-memory elastomeric composite (SMEC).^{31,32} These composites were limited to shape memory and the drug-releasing properties of these composite configurations were not studied. In the present work, we utilized a degradable elastomeric matrix, where we sought to understand the influence of the fiber hydrophobicity on matrix degradation. We hypothesized that embedding a semicrystalline, hydrophobic percolating fibrous

phase, such as PCL, will increase the degradation rate of the surrounding PAH matrix relative to using another polymer, such as polyvinyl acetate (PVAc), due to the decreased water interaction with PCL relative to PVAc, therefore enabling greater aqueous availability for PAH degradation. We anticipated that by substituting the fibrous phase with another polymer in the composite, the degradation rate and drug release from the fibers could be modulated. We also examined the mechanical and shape memory properties during degradation.

5.3. Materials and Methods

5.3.1 Materials

Poly(ϵ -caprolactone) (PCL) ($M_n \sim 80,000 \text{ g mol}^{-1}$), 4-Pentenoic anhydride (PNA), pentaerythritol tetrakis(3-mercaptopropionate) (PETMP), azobisisobutyronitrile (AIBN), chloroform, N,N-dimethylformamide (DMF), phosphate buffered saline (pH of 7.4), and tetrahydrofuran (HPLC-grade, $\geq 99.9\%$, THF) were purchased from Sigma-Aldrich and used as received. Poly(vinyl acetate) (PVAc, $M_n \sim 350,000 \text{ g mol}^{-1}$) was purchased from Scientific Polymer Products and was used as received.

5.3.2 Electrospinning of PCL

Poly(ϵ -caprolactone) (PCL) was electrospun from a 20% (w/v) solution prepared by dissolving 2 g PCL in THF/DMF (volume ratio = 2:1). PCL fibers were produced using a flow rate of 1 mL h^{-1} , a voltage of 11 kV, and a needle to collector distance of 7 cm onto a grounded rotating and translating collector. Following electrospinning, the PCL fiber mat was vacuum dried at room temperature for 24 h.

5.3.3 Electrospinning and Thermal Treatment of PVAc

Poly(vinyl acetate) (PVAc) was electrospun from a 20% (w/v) solution prepared by dissolving 2 g of PVAc in methanol/DMF (volume ratio = 7:3). PVAc fibers were produced using a flow rate of 1.0 mL h⁻¹, a voltage of 11 kV, and a needle to collector distance of 7 cm onto a grounded rotating and translating collector. Following electrospinning, the PVAc fiber mat was vacuum dried at room temperature for a minimum of 24 h. The PVAc fiber mat was maintained secured on the aluminum foil substrate used in electrospinning, which was used to aid in anchoring the fibers during thermal treatment to relieve residual stresses incurred during electrospinning. A post-electrospinning thermal treatment of 50 °C for 24 h, while the fiber mat remained constrained on the aluminum foil used to deposit fibers during electrospinning, was implemented to minimize fiber shrinkage.

5.3.4 PAH Monomer Preparation

The polyanhydride (PAH) monomer preparation and synthesis conditions are the same as those used in **Chapter 4** of this thesis and described in Section 4.3.2.

5.3.5 PCL/PAH Composite Fabrication

The methods of vacuum infiltration of electrospun PCL with PAH monomer and curing are the same as those used in **Chapter 4** of this thesis and detailed in Chapter 4.3.5.

5.3.6 PVAc/PAH Composite Fabrication

To minimize shrinkage of the PVAc fibers upon contact with the PAH monomer or water, as a result of residual stresses accrued during the electrospinning process, the PAH

monomer was allowed to slowly pre-cure for 19 h – 20 h at 1.6 °C (in a standard refrigerator) prior to vacuum infiltration of the PAH monomer into the PVAc fiber mat. It was determined that slowly pre-curing the PAH monomer under refrigeration combined with thermally treating the PVAc fibers enabled reproducible fabrication of the PVAc/PAH composite. The PVAc/PAH was photocured for 30 min exposed on both surfaces using a 365 nm (2.0 mW cm^{-2}) ultraviolet light source at a distance of 15 cm from the sample to the light source. Although the former step led to complete matrix cure, the irradiation cure step was followed by a thermal post-cure at 70 °C for 1 h to be consistent with PCL/PAH curing conditions.

5.3.7 Thermal Characterization

Differential scanning calorimetry (DSC) was performed using a TA Instruments Q200 apparatus. Samples weighing 2 – 5 mg were sealed in Tzero aluminum pans and were from -60 °C to 120 °C at 10 °C min^{-1} . The characteristic thermal transitions for all samples were determined using the second heat for glass transition or first heat for crystallization. The glass transition was selected from the inflection point of the step transition, and the maxima were taken as the crystallization transition point.

For the PCL/PAH composite, the crystallization enthalpy (ΔH_c) was used to determine PCL content of the composite, as it is directly related to crystallinity. The crystallization enthalpy was calculated from the first heating cycle by integrating the crystallization peak, and used to determine the fraction of PCL in the elastomeric composite by comparing the degree of crystallinity according to:

$$W_{PCL}(\%) = \frac{\Delta H_c}{\Delta H_{c,0}} \times 100 \% \quad (5-1)$$

where χ_c is the degree of crystallinity, ΔH_c is the heat of crystallization of the composite measured by DSC and $\Delta H_{c,0}$ is the heat of crystallization of pure electrospun PCL, which was determined by DSC to be 60.6 J g^{-1} .

For the PVAc/PAH composite, the change in heat capacity at T_g (ΔC_p) was used to determine the PVAc content of the composite, as it is directly related to its glass transition. The heat capacity was calculated from the step change using the TA Instruments Universal Analysis software (version 4.5A) during the second heating cycle, and used to determine the fraction of PVAc in the elastomeric composite by comparing the degree of amorphousness according to:

$$\alpha_A(\%) = \frac{\Delta C_p}{\Delta C_{p,0}} \times 100 \% \quad (5-2)$$

where α_A is the percentage of material (PVAc) having the T_g under isolated analysis, ΔC_p is the change in heat capacity of the composite measured by DSC, and $\Delta C_{p,0}$ is the heat capacity change of the corresponding pure electrospun PVAc, which was determined by DSC to be $0.62 \text{ J g}^{-1}\text{°C}^{-1}$.

5.3.8 *In Vitro Degradation*

The *in vitro* degradation of the PAH-based composites was carried out by cutting samples into 1 cm x 1 cm squares and immersing separately in phosphate buffered saline (PBS, pH of 7.4). All samples were placed in an isothermal shaker (New Brunswick Scientific, Model C24) under a constant temperature of 37 °C and agitating at 60 rpm for up to 14 days. A minimum ratio of 2 mg of sample per mL of PBS was used and the acidity of the dissolution media was monitored daily and changed every few days to maintain a pH of 7.4. At a scheduled time point,

three samples were removed from PBS, rinsed with DI water and dried at room temperature *in vacuo*. The mass loss was calculated by comparing the mass at a given time point (M_t) with the initial mass (M_0) prior to degradation, as shown in **Eqn. 5-3** below. Each mass loss determination was conducted in triplicate and an average and standard deviation are reported.

$$M (\%) = 100 \% \times \left(1 - \frac{M_0 - M_t}{M_0} \right) \quad (5-3)$$

The thermal, morphological, and mechanical properties of the samples were also evaluated at different degradation times using DSC, SEM, and tensile testing. The composition of the samples during degradation was analyzed by comparing the DSC thermograms of the degraded samples to that of its individual, unaltered components, as detailed in Section 5.3.7.

5.3.9 Mechanical Properties

Tensile mechanical properties was studied by punching samples into a dog bone geometry (ASTM Standard D638-03 Type IV, scaled down by a factor of 4), and loading onto a Test Resources Model 100P Universal Testing Machine equipped with a 24 N load cell. The samples were stretched at a rate of $33 \mu\text{m s}^{-1}$, and engineering stress-strain curves were used to determine Young's modulus, strain-to-failure, and tensile strength. Five samples of each type were tested and an average and standard deviation are reported.

5.3.10 Morphology

The surface features of the samples were microscopically visualized using a JEOL JSM 5600 scanning electron microscope (SEM) and an accelerating voltage of 5 kV. The samples were sputter coated with gold for 45 s prior to imaging.

5.3.11 Qualitative Shape Memory

Shape memory was performed for the PVAc/PAH composite only, as the glass transition temperature of the composite (~ 30 °C) enabled one way shape memory without activation of the PAH reconfiguration, unlike the PCL/PAH composite ($T_m \sim 60$ °C), as discussed in **Chapter 4**. A rectangular strip was deformed into a temporary shape by wrapping around a Teflon rod of known diameter and securing in place by wrapping in foil. The sample was then placed in an isothermal oven at 45 °C for 10 min followed by immediate placement in a freezer (-18 °C) for 10 min; the sample was then removed from the rod to observe the fixed shape. Shape recovery was triggered by placing the sample in the isothermal oven at 45 °C in the stress-free state.

5.3.12 Quantitative Shape Memory

The shape memory of was quantified using the DMA based on a four-step sequence.³³ The DMA was used in controlled force mode to stretch a dog bone sample at 40 °C to a 15% strain by ramping the force at 0.02 N min^{-1} . The temperature was then decreased at 3 °C min^{-1} to 0 °C and held isothermal for 5 min to fix a temporary shape. The force was then unloaded at 0.05 N min^{-1} until it reached the preload force of 10^{-3} N . The permanent shape was recovered by heating at 10 °C min^{-1} to 40 °C, and holding isothermal for 5 min. The shape memory loop described above was repeated three times. The degree of shape fixing (R_f) and the degree of shape recovery (R_r) were quantified for each cycle using the **Eqns. 5-4 and 5-5** below, where ϵ_0 is the original strain (at the beginning of each cycle), $\epsilon_{deformed}$ is the deformed strain that occurs after cooling while still under a load, ϵ_{fixed} is the fixed strain that results following unloading, and $\epsilon_{recovered}$ is the recovered strain following heating.

$$R_f(\%) = \left(\frac{\varepsilon_{fixed}}{\varepsilon_{deformed}} \right) \times 100 \% \quad (5-4)$$

$$R_r(\%) = \left(\frac{\varepsilon_{fixed} - \varepsilon_{recovered}}{\varepsilon_{fixed} - \varepsilon_0} \right) \times 100 \% \quad (5-5)$$

5.3.13 Fixed Shape during Degradation

Here, we sought to measure the ability of the composites to retain a fixed shape during degradation. For that, samples were prepared by arbitrarily deforming a rectangular strip into a spiral, a curve or a wave pattern. The samples thus deformed were placed in an isothermal oven at 70 °C and held there for 10 min, melting the constituent PCL crystals, followed by transferring to freezer maintained at -18 °C for 10 min, recrystallizing the PCL to fix the temporary shape. The newly fixed shape was then placed buffered PBS at 37 °C, agitated at 60 rpm, as described in Section 5.3.8, to begin *in vitro* degradation and photographed at different time points for visual assessment and comparison to the original fixed shape and equilibrium (flat) shape. Shape fixing during degradation was not performed on the PVAc/PAH samples since the PVAc shrinks considerably upon PAH degradation and subsequent exposure to water and therefore cannot maintain a fixed shape while immersed in water.

5.3.14 In Vitro RhB Release

Controlled drug release of hydrophilic model drug Rhodamine B (RhB) from the PAH-based samples was conducted using the methods established in **Chapter 2** (Section 2.3.6).

5.4. Results

5.4.1 Fabrication of PAH-based composites

The fabrication process of PAH-based composites followed a similar method used for the fabrication of the PCL-PU/PAH composite discussed in **Chapter 4**, using either commercially available PCL or PVAc electrospun into fibers. **Scheme 5-1** summarizes the chemical structures for the PAH, PCL, and PVAc components. The cross-linking of the PAH elastomer proceeded using same scheme as in **Chapter 4**, using the vacuum infiltration process previously described to combine the fibers with the monomer to form a composite; only the PVAc-based composite required an additional thermal treatment to prevent significant shrinkage during the PAH curing step, as a result of residual stresses accrued during the electrospinning process. **Figure 5-1** summarizes the effect of applying a thermal treatment to electrospun PVAc, where significant shrinkage occurs without heat treatment following exposure to water (**Figure 5-1C**), and dissolution of the PVAc fibers occurs when combined with PAH monomer (**Figure 5-1A**). It was determined that slowly pre-curing the PAH monomer under refrigeration combined with thermally treating the PVAc fibers enabled reproducible fabrication of the PVAc/PAH composite with visually distinct phases.

The thermal and thermomechanical properties of PAH-based composites are presented in **Figure 5-2**, and compared with their respective individual components. **Figure 5-2A** shows that both composites display two distinct thermal transitions corresponding with their individual components. The PCL/PAH composite shows a melting transition at 54.3 °C and a glass transition temperature of -21.4 °C; the melting temperature of electrospun PCL, itself was 54.8

°C, and the glass transition of neat PAH was -21.2 °C. Using **Eqn. 5-1**, the PCL/PAH composite contained approximately 18% PCL. The PVAc/PAH exhibited glass transition temperatures of -31.3 °C and 30.1 °C; the glass transition temperature of neat electrospun PVAc was 44.7 °C. Using **Eqn. 5-2**, the PVAc/PAH composite comprised of approximately 16% PVAc. Given, however, the evident plasticization of PVAc by PAH monomers, this estimate of PVAc incorporation level is dubious. **Figure 5-2B** shows that at 25 °C, the PCL/PAH and PVAc/PAH had a storage moduli of 14.9 MPa and 304.1 MPa, respectively. The storage modulus for electrospun PVAc decreased from 491 MPa to 408 MPa at 25 °C following heat treatment, which we attributed to a lower of the molecular orientation in the constituent fibers. Both composites showed the presence of a rubbery plateau between 50 °C and 80 °C, which is due to the presence of PAH.

The morphologies of both the surface and cross-sections are shown in **Figure 5-3**, which verified complete infiltration of the PAH through the thickness of both samples, as presented in **Figures 5-3B** and **5-3E**, where the surfaces are smooth, likely due to film formation of PAH. The cross-sections of both composites, as shown in **Figures 5-3C** and **5-3F**, reveal an absence of voids due to the PAH occupying the space between the fibers. In addition, the electrospun PVAc maintained a fibrous morphology following thermal treatment (**Figure 5-3D**).

The mechanical properties of the PAH-based composites are summarized as engineering stress-strain curves in **Figure 5-4** and **Table 5-1**. The average Young's modulus for the PCL/PAH composite was 7.5 MPa ± 0.9 MPa, which is slighter greater than that of PAH of 4.5 MPa ± 0.4 MPa and not significantly different than that of electrospun PCL at 7.1 MPa ± 3.0 MPa. The strain-to-failure of the composite was determined to be 80% ± 40% and was

significantly less than that of electrospun PCL of $1300\% \pm 140\%$ and much closer to that of PAH at $30\% \pm 5\%$ indicating that the crosslinked PAH dominated the mechanical properties and limited the composite elongation before failure, as it comprised approximately 83% of the composite and testing was conducted above the PVAc glass transition temperature.

Applying a thermal treatment to the electrospun PVAc fibers resulted in a significant increase in Young's modulus for the PAH composite, from $63.5 \text{ MPa} \pm 11.3 \text{ MPa}$ to $157.1 \text{ MPa} \pm 15.2$, with no significant difference in strain-to-failure. This increase in elastic modulus was discernible when handling the sample. The PVAc/PAH composite exhibited a Young's modulus of $2.9 \text{ MPa} \pm 0.5 \text{ MPa}$, which was significantly less than each of the PAH and PVAc individual components, indicating a potential interaction between the two components. The strain-to-failure of PVAc/PAH was $60\% \pm 7\%$ and was slightly greater than that of PAH and PVAc, although these were not statistically significantly different ($p > 0.05$).

5.4.2 In Vitro Degradation Mass Loss

The mass loss profiles of the PAH-based composites in PBS at 37°C are shown in **Figure 5-5**. The composites exhibited distinct degradation rates. The PCL-based composite showed the greatest mass loss within the shortest time period. Specifically, within the first 10 h, PCL/PAH rapidly lost about 55% of its original mass, whereas the PVAc/PAH lost only 13% of its original mass during this time. The mass loss for PCL/PAH ceased at about 24 h, with no significant decrease in mass from 24 h to 14 d and remaining at $29.0\% \pm 1.4\%$. The mass remaining for PCL/PAH at time points 24 h, 48 h, 72 h, 4 d, and 14 d were not significantly different. In contrast, the PVAc/PAH composite lost mass more steadily, reaching about 50%

mass loss between 48 h and 72 h. The PVAc/PAH mass loss rate followed a decreasing exponential pattern, and approached a % mass remaining of $25.6\% \pm 3.7\%$ at 20 d.

5.4.3 Morphology

The surfaces and cross-sections of the composites were examined following different degradation times using scanning electron microscopy. As shown in **Figure 5-6A**, after 5 h of degradation, the smoothness of the surface manifested into wrinkled features, which appear consistent with the surface topology of the underlying PCL fibers. The formation of craters and pores appeared after approximately 24 h of degradation and progressed into connected channels by 48 h. The cross-sections shown in **Figure 5-6B** revealed that degradation initially occurred at the surface and that by 24 h, channels formed on the surface, and traveled through the cross-section. By 72 h, the PCL fibers became exposed at both the surface and cross-section, with small, random regions of PAH matrix becoming visible on the fibers. The PAH matrix was no longer visually evident past 96 h. The dense horizontal linear artifact noticeable in both the 72 h and 96 h micrographs was an artifact from the sectioning process of the samples with a razor blade. Visually, the PCL/PAH samples maintained their macroscopic size and shape throughout degradation with no notable swelling or other geometrical changes.

As shown in **Figure 5-7**, the PVAc/PAH composite degraded at a slower rate than the PCL/PAH composite. No significant changes to the surface are visualized within the first 10 h of degradation, where the surface appeared smooth. The micrograph shown in **Figure 5-7A** at 10 h reveals a crater consistent with a bubble formed at the surface during the cross-linking of PAH. At 24 h, cracks and wrinkles began to form on the surface, and by 48 h, pores were formed that became interconnected channels by 72 h of degradation. Like the PCL-based composite, the

PVAc fibers became noticeable at 72 h, as seen on the both the surface and cross-sections (**Figure 5-7A,B**); however, unlike PCL/PAH, a predominantly fibrous morphology does not occur until 8 d instead of 72 h. The change in fiber morphology when compared to the original (as electrospun) may be due shrinkage that occurred – driven by the PVAc fibers undergoing hydration-triggered contraction³⁴ as the PAH degraded and no longer provided mechanical support. In contrast to the PCL/PAH composite, the PVAc/PAH samples began to visibly shrink and lose their rectangular geometry during degradation, folding onto itself after 24 h of degradation; it was also observed that at this degradation time, the samples became tacky. Interestingly, the PVAc/PAH composites continued to contain PAH, even after 14 d of immersion in an aqueous solution, as indicated by the DSC data in **Table 5-3**, and discussed further in the next section.

5.4.4 Thermal Properties

Differential scanning calorimetry was used to determine the changes in thermal properties, and by inference composition, the PAH-based composites during degradation. **Figures 5-8** and **5-9**, and **Table 5-2** summarize the changes in crystallization enthalpy for the PCL/PAH composite at various degradation times. Over the course of the degradation period, the peak area corresponding to PCL crystallization increased, indicating an increase in crystallinity due to the increasing fraction of PCL in the composite, as the PAH degradation products receded into the buffered media. A rapid growth in the crystallization enthalpy is apparent at 10 h and 48 h, where the PCL fraction quadruples. The glass transition of PAH is no longer evident after 24 h, and the PCL T_c shifts by about 2 °C and became aligned with that of electrospun PCL ($T_c \sim 32$ °C). After 48 h, the increase in melting enthalpy became significantly slower, particularly

between 4 and 14 d, when there was less than a 4% increase in PCL content. By the 14 d, the sample had become composed of approximately 96% PCL, indicating the presence of a small amount of residual PAH. Using DSC to determine the thermal transitions may be more sensitive to compositional changes than by calculating the mass loss. Although mass loss data in **Figure 5-5** showed no significant degradation beyond 24 h, the micrographs in **Figure 5-6** and the thermograms in **Figure 5-8** both support that this is closer to 4 d.

A comparison of the heat capacity changes at T_g of the PVAc component was used to calculate the fraction of PVAc in the composite using **Eqn. 5-2**, and the results are summarized in **Figure 5-10** and **Table 5-3**. **Figure 5-11** plots the time-evolution in glass transition temperature (T_g) corresponding to PVAc phase in the composite, along with mass loss due to PAH degradation. As shown in **Figures 5-10** and **5-11**, the initial T_g of the PVAc component in the composite, prior to degradation, was approximately 30 °C, which is about 15 °C lower than that of pure electrospun PVAc ($T_g \sim 45$ °C), indicating that the PAH may have had a plasticizing effect on the PVAc fibers. During degradation, the PVAc T_g remained stable until about 24 h, when it decreased rapidly from 20.3 °C and continued to rapidly decrease between 24 h and 72 h. After 72 h, the T_g increased from 0.9 °C to 29.5 °C at 96 h, after which it continued to increase, but at a much slower rate from 29.5 °C to 36.7 °C at 14 days. We attributed the T_g recovery to the degradation of the PAH within the PVAc fibers, which would also be limited by diffusion of the degradation products from the fibers. At 14 d, the remaining mass approached 20% PVAc, which was slightly more than the 16% fraction determined by DSC in the composite prior to degradation. Both of these results indicate that at 14 d, some residual PAH remains. A comparison of the rate of increasing fiber content during degradation for both the PCL/PAH and

PVAc/PAH composites are plotted in **Figure 5-12**, showing that the PAH matrix degraded faster for the PCL/PAH composite than the PVAc/PAH composite.

5.4.5 Tensile Mechanical Properties

The tensile mechanical properties were measured at different degradation time points. **Figure 5-13** and **Table 5-4** summarize the mechanical properties for the PCL/PAH composite at various degradation times. During degradation, the Young's modulus steadily decreased, from a starting modulus of $7.5 \text{ MPa} \pm 0.9 \text{ MPa}$ to its lowest at $2.2 \text{ MPa} \pm 0.8 \text{ MPa}$ at 48 h. The modulus did not significantly change between 48 h and 96 h. After 8 d, it began to steadily increase and recover to that of electrospun PCL. By 14 days, the modulus was not significantly different than electrospun PCL, with a modulus of $7.7 \text{ MPa} \pm 3.0$ and $7.1 \text{ MPa} \pm 3.0$, respectively. The strain-to-failure of the composite was initially significantly lower than that of electrospun PCL at $80\% \pm 40\%$ compared to $1300\% \pm 140\%$ and approached this value during degradation. The strain-to-failure was similar to that of PCL after 14 days at around $1200\% \pm 30\%$.

The mechanical properties of the PVAc/PAH composite shown in **Figure 5-14** could not be studied beyond 48 h of degradation due to poor mechanical integrity. The average value calculated for the Young's modulus and strain-to-failure at 48 h reported in **Table 5-5** was based on two samples instead of five since the remaining samples were unable to be tested.

5.4.6 In Vitro Drug Release

The *in vitro* cumulative drug release profiles of both PCL/PAH and PVAc/PAH composites loaded with 0.5% RhB entrapped in the fibers are summarized in **Figure 5-15**. The release profile for the PCL/PAH shown in **Figure 5-15B** did not follow a two stage pattern, with

an initial burst release of approximately 9% within 6 h; this was followed by a period of steady release between 6 h and 5 d, which released another 10%. At this point, a second burst release was observed between 5 d and 8 d, which released the greatest amount of drug at an additional ~50%. This was followed by another period of steady release that liberated an additional 7% drug over the next 7 d. The total drug release was approximately 65% for 15 d, with no significant change after 15 d. In comparison, the RhB-loaded PCL fibers with no matrix (control sample), as shown in **Figure 5-15A**, exhibited a two-step release profile, with a single release at 2 h that released 60% of the drug, and a short, steady release until approximately 48 h, with 67% total released.

Unlike the PCL/PAH composite, the PVAc/PAH sample, as shown in **Figures 5-15A** and **5-15C**, exhibited biphasic drug release with an initial burst release of approximately 20% within 6 h, followed by a steady additional 30% release of RhB over 30 d. As shown in **Figure 5-15C**, RhB release increased with additional degradation of the PAH matrix. In contrast, the RhB-loaded PVAc fibers alone, without the PAH matrix, showed an initial burst release of approximately 18% after 6 h, followed by an additional 12% of RhB released steadily for a period of approximately 7 d, where no significant RhB release was observed between 7 days and 17 days. A total of approximately 31% of RhB was released from the PVAc fiber mat without PAH (control sample), whereas a total of approximately 52% of RhB was released from the PVAc/PAH composite, which appeared to continue to release past 30 days.

5.4.7 Shape Memory

The qualitative and quantitative shape memory properties of the PVAc/PAH composite are shown in **Figures 5-16** and **5-17**, respectively. The fixing and recovery ratios are summarized

in **Table 5-6** and were calculated using **Eqns. 5-4** and **5-5**. The PVAc/PAH exhibited excellent shape fixing for all cycles, with 99% retention of the induced strain following load release. The shape programming temperature was 40 °C, which was above the PVAc/PAH composite temperature and below the reconfiguration temperature for PAH. The shape recovery improved from 74% in the first cycle to 90% for the second cycle. The qualitative shape memory in **Figure 5-16** revealed that the PVAc/PAH composite showed good shape fixing and recovery performance, with a fixing ratio of 92% and a recovery ratio of 100%. The shape memory results are not shown for the PCL/PAH composite, as these samples exhibited poor shape memory since the shape fixing and recovery mechanism is by way of the PCL melting transition of ~55 – 60 °C and overlaps the temperature range at which the PAH crosslinks are rearranged, as discussed in **Chapter 4**. As a result, the composite can only be remolded into new permanent shapes.

5.4.8 Fixed Shape Preservation during Degradation

The PCL/PAH composite demonstrated the ability to retain a temporary shape during degradation, as shown in **Figure 5-18**. The composite was deformed into three different arbitrary shapes and showed excellent shape fixing after four months of immersion in PBS at 37 °C. It was observed that within the first 24 h of *in vitro* degradation, some slight retraction of the shape occurred and no further change in the shape dimensions occurred between 24 h and 4 months. The PCL/PAH composite became more opaque as degradation of the PAH matrix progressed, leaving a solid white sample, which is characteristic of pure PCL.

5.5. Discussion

To compose a biodegradable elastomeric shape memory composite, crosslinked PAH and semicrystalline PCL were combined using commercially available materials. This study examined the degradation of the PCL/PAH composite and the effect of the composition of the fibrous component on degradation and drug release of a model compound by substituting PCL with PVAc.

The mass loss data reveal that changing the fiber composition from PCL to PVAc, both hydrophobic polymers, had influenced the degradation of the surrounding PAH matrix. Although PAH is also hydrophobic, it is composed of moisture-sensitive anhydride linkages that hydrolytically cleave into water-soluble products with a relatively high hydrolysis rate on the time scale of hours-to-days compared to other polyanhydrides.³⁵ By shifting the relative hydrophobicities of the fibers percolating through the PAH matrix, we hypothesized that this would affect PAH degradation due to differences in water accessibility within the internal structure of the composite, where the more hygroscopic PVAc would readily attract water compared to PCL. It is for this reason that PVAc was selected as an alternative material to PCL as the fibrous phase since its relatively polar carboxyl groups impart more moisture-sensitivity than PCL, with the ability to sorb ambient water, which would also impact its T_g and thus chain mobility.^{36,37} PVAc has been reported by others to absorb up to 4 wt% water, whereas PCL is known to absorb less than 0.5 wt% water after 12 days immersed.^{38,39}

Interestingly, the gravimetric data revealed that degradation of the PCL/PAH composite occurred much faster than the PVAc/PAH sample, losing approximately 55% percent of its original mass within 10 h, compared to PVAc/PAH, which took 5 – 6 times longer to attain a

similar result. Overall, the degradation of the PCL-based composite appeared to occur in two main stages, beginning with crater formation at the surface that progressed into pores by 24 h, which coincided with a rapid loss of mass and the majority of the composite erosion. During the second stage, the mass loss rate drastically decreased between 24 h and 14 days, while the pores at the surface appeared to develop into channels through the thickness of the sample, as shown in **Figure 5-6**; these channels continued to enlarge and evolve into the free space between the PCL fibers during this secondary stage of erosion. Here, a drastic increase in the strain-to-failure of the composite also occurred, which is consistent with removal of a substantial mass of the PAH matrix to liberate PCL fiber mobility. This type of degradation is an alteration from the surface erosion that is characteristic of the PAH matrix, which then advanced to bulk degradation. The crater morphology during the first stage enabled direct contact and thus concentration of the buffer solution into the volume of the composite, establishing a route for the degradation front to advance through the sample bulk. As the degradation of PAH proceeded, the crystallization endotherm of PCL became more prominent in the DSC thermograms shown in **Figure 5-8**. Between the mass loss and morphological micrographs, it appeared that degradation of PCL/PAH was complete and matrix-free by 4 days; however, an evaluation of the relative crystallization enthalpies of PCL revealed that residual PAH remained in the composite, with approximately 4% remaining after 14 days. This extended degradation suggests that there may be regions of PAH that begin to degrade later and are likely in the form of a sheath surrounding the PCL fibers, which would be consistent with the fibrous morphology at this stage. The tensile Young's modulus and strain-to-failure do not fully recover before 14 days of degradation, further indicating the presence of PAH within the composite not detected gravimetrically or visually by

SEM, as it is continuing to restrict PCL fiber mobility. There is no contribution from PCL erosion since it degrades considerably slower.⁴

Unlike the PCL/PAH composite, we contemplated that the PVAc fibers were plasticized by PAH based on macroscopic observations during fabrication, where a thermal treatment was necessary to relieve residual stresses incurred during electrospinning to prevent shrinkage, coupled with the observed apparent dissolution of the non-heat treated PVAc fibers into the PAH monomer (**Figure 5-1**). The thermal characterization at different degradation times further supported this postulation, showing that the glass transition (T_g) of PVAc in the composite was significantly decreased by almost 15 °C prior to the degradation study, suggesting a molecular interaction between the heat-treated PVAc fibers and the PAH matrix.

The degradation of the PVAc/PAH composite appeared to proceed in three regimes, and unlike the PCL/PAH composite, the glass transition did not positively correlate with degradation time. Phase I occurred between 0 and 10 h, and degradation was rapid and dominated by the erosion of PAH at the surface, since there was no substantial change in T_g of PVAc or surface morphology. Phase II ensued from 10 h to 72 h, and is marked by a significant drop in T_g and the formation of larger pores and channels. The continued shift in the T_g of PVAc was most likely due to the plasticizing effect of absorbed water as more fibers were exposed to the buffer solution through the growing population of pores and channels during this period. We hypothesized that the PAH as a matrix is severely interrupted, as was the case with PCL/PAH composite at this degradation time; here, the remaining material was likely PVAc fibers containing plasticizing PAH. It is during Phase III that we postulated that the degradation of

PAH continued mostly within the fibers, albeit at a much slower rate and limited by diffusion, which would explain the continuing decrease in mass and the recovery of the PVAc T_g .

Although initially the PVAc/PAH composite showed similar mechanical properties as that of PAH film, the tensile Young's modulus displayed a recovering trend toward that of electrospun PVAc during degradation. Interestingly, the strain-to-failure was substantially increased such that it was approximately six-fold greater than either the PAH or PVAc components individually, which we postulated may be due to rubber toughening by the PAH. As the PVAc/PAH samples degraded, excessive shrinkage occurred, which made it difficult to study the mechanical properties beyond 48 h. This shrinkage was likely caused by additional relaxation of the fibers during plasticization by water, where amorphous PVAc enabled greater access of water through the structure.

The drug release of the PCL/PAH composite did not follow a typical biphasic pattern and instead manifested as two burst release intervals with periods of sustained release following each burst. The small initial burst release was likely due to the liberation of RhB molecules adsorbed previously to the surface that stemmed from migration during composite fabrication, when the PCL fibers were wetted by the PAH monomer. During this early burst release, 15% of the mass of the composite had eroded; however, given that only 9% of drug released, compared to ~60% from the control (PCL fibers without PAH) during the same time frame, we surmised that there was sufficient PAH shielding underlying fibers. The second and final burst release occurred beginning at 4 d and lasted for 3 d; it was at this point that a very high rate of drug release commenced, and during when most of the drug was released. This drug release behavior correlated with the disappearance of the continuous PAH matrix through the structure which led

to near full exposure of the PCL fibers, as visualized by SEM, and signified that the drug release here was primarily erosion-mediated rather than diffusionally controlled. The period of continual, steady RhB release that followed the second burst release, beginning at 8 d, was slow and likely due to diffusion of RhB from the fibers to the media. Since this release was controlled, unlike that of original PCL fiber control, this further suggested that there remained a PAH coating around the fibers. This observation was consistent with the degradation thermal properties (**Table 5-2**) and mechanical data (**Table 5-4**), which indicated that residual PAH remaining after 4 d, as the behavior of the material during this time was not that of pure electrospun PCL. A total of 67% of RhB was released from the PCL/PAH composite and this was likely due to drug trapped in the fibers, as has been previously observed by others.^{40,41}

Amorphous polymers offer an advantage over semicrystalline polymers in that there are no crystallites that can possibly impede drug loading.⁴² Unlike the PCL/PAH composite, the PVAc/PAH sample exhibited biphasic drug release with the initial burst release of 20% of RhB, followed by a slow, steady release at a slower rate, beyond when significant PAH has degraded. The initial burst release was likely due to a combination of eroded PAH (15% mass reduction) and diffusion of surface adsorbed drug. The drug release appeared to continue to steadily release past 30 d, a further indication that residual PAH remained in the composite imparting an additional diffusional barrier to RhB; this is consistent with our hypothesis that additional PAH remained in the fibers beyond 14 d.

One-way shape memory was possible for the PVAc/PAH composite due to the plasticization of the PVAc fibers by the PAH monomer during composite fabrication. This resulted in a decrease in the glass transition temperature to ~ 45 °C and thus enabled the shape

fixing and recovery temperature triggers to occur sufficiently below the shape reconfiguration regime of PAH, which would have inhibited the recovery of the original shape due to the rearrangement of the PAH cross-links during shape fixing.⁴³ It is for this very reason that the one way shape memory performance was poor for the PCL/PAH composite, since the required thermal trigger was above 55 °C and resulted in overlapping permanent and fixed shapes; a modification would be necessary to the PCL thermal transition, which was further discussed in **Chapter 4**. The macroscopic shape memory of the PVAc/PAH composite is demonstrated in **Figure 5-16**, and also showed excellent shape fixing and recovery properties, with 92% of the induced curve retained upon release of the applied load and full recovery of its length upon heating. The shape memory measured thermomechanically in tension revealed consistent R_f values of 99% over three consecutive cycles. The shape recovery ratio of the initial cycle was mediocre at 76%, but improved to 90% after the first cycle. This difference between the first and second cycle may be due to relaxation effects of PVAc. Since the elastomeric component was composed of crosslinked PAH, this composite would also be capable of reprogramming its permanent shape, as discussed in **Chapter 4**. Unlike other fiber reinforced shape memory systems, complex geometries could be fabricated without requiring a new sample to be manufactured each time, as had been proposed by others.²⁰

Finally, the PCL/PAH composite offered a way to maintain a fixed, temporary shape during degradation. This was possible since the fibrous PCL framework was remained following PAH degradation, serving as structural support. This feature may be useful in situation-specific applications where a customized, complex geometry is essential, even after significant degradation. Shape retention during degradation was previously studied by Knight et al., where a

biodegradable copolymer of poly(lactide) and glycolide was synthesized with polyhedral oligosilsesquioxane (POSS) in the backbone.⁴⁴ In their study, it was found that the samples had to be annealed to enable sufficient crystallization for good shape fixing. The samples, however, began recovering slowly during degradation, with approximately 20% recovered length within two weeks and 50% recovered by four weeks. In contrast, by isolating the fixing mechanism to a separate phase with a significantly slower degradation rate, our composite was capable of maintaining a high degree of deformation over a significant period of time; it is likely that this shape retention could extend on the order of two years, when the PCL fibers begin to degrade.

5.6. Conclusions

A fully biodegradable shape memory elastomeric composite was developed using electrospun fibers embedded in a degradable, crosslinked polyanhydride matrix. The degradation of the polyanhydride matrix was dependent on the composition of the fibrous phase, where erosion proceeded more rapidly when the composite contained the more hydrophobic PCL fibers compared to hygroscopic PVAc, since PVAc competed with the degrading PAH for water. The presence of a fibrous structure permeating through the PAH film altered the erosion dynamics from heterogeneous to homogenous. PAH continued to remain on the fibers as a protective sheath for both composite compositions. It was found that the PVAc fibers were plasticized by the PAH, which remained in the fibers, and this resulted in prolonged degradation and enhanced the duration of sustained drug delivery of a hydrophilic model drug. The addition of a drug to a material would be advantageous for infection management following surgical intervention or minimizing thrombosis on the surface of an implant. This composite has the potential to possess these properties in addition to tailorable degradation, reconfigurable shape memory, and long-

term shape retention and can provide an enabling technology with broad biomedical applications such as smart implants and tissue engineering scaffolds.

5.7 Acknowledgements

This work was conducted in collaboration with Tackla S. Winston, an undergraduate student at Syracuse University, in the Mather Research Group. Tackla S. Winston developed, characterized, and performed the studies for the PVAc-based composites in this chapter.

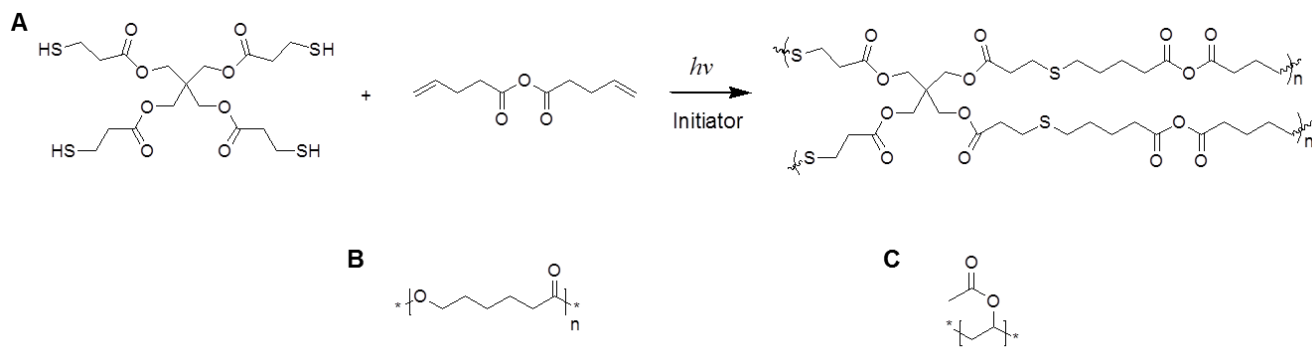
5.8 References

1. Ikada, Y. & Tsuji, H. Biodegradable polyesters for medical and ecological applications. *Macromolecular rapid communications* **21**, 117 (2000).
2. Mohanty, A. K. & Misra, M. Biofibers, biodegradable polymers and biocomposites: an overview. *Folia Microbiol* **48**, 27 (2003).
3. Hutmacher, D. W. Scaffolds in tissue engineering bone and cartilage. *Biomaterials* **21**, 2529 (2000).
4. Hutmacher, D. W., Goh, J. & Teoh, S. H. An introduction to biodegradable materials for tissue engineering applications. *Ann Acad Med Singapore* **30**, 183 (2001).
5. Middleton, J. C. & Tipton, A. J. Synthetic biodegradable polymers as orthopedic devices. *Biomaterials* **21**, 2335 (2000).
6. Alexis, F. Factors affecting the degradation and drug-release mechanism of poly (lactic acid) and poly [(lactic acid)-co-(glycolic acid)]. *Polymer International* **54**, 36 (2005).
7. Panyam, J., Dali, M. M., Sahoo, S. K. & Ma, W. Polymer degradation and in vitro release of a model protein from poly (D, L-lactide-co-glycolide) nano-and microparticles. *Journal of Controlled Release* **92**, 173 (2003).
8. Tracy, M. A., Ward, K. L., Firouzabadian, L., Wang, Y. & Dong, N. Factors affecting the degradation rate of poly (lactide-co-glycolide) microspheres in vivo and in vitro. *Biomaterials* **20**, 1057 (1999).
9. Göpferich, A. Mechanisms of polymer degradation and erosion. *Biomaterials* **17**, 103 (1996).

10. Tamada, J. A. & Langer, R. Erosion kinetics of hydrolytically degradable polymers. *National Acad Sciences* **90**, 552 (1993).
11. Nair, L. S. & Laurencin, C. T. Biodegradable polymers as biomaterials. *Progress in polymer science* **32**, 762 (2007).
12. Griffith, L. G. Emerging design principles in biomaterials and scaffolds for tissue engineering. *Annal of New York Acad of Sci* **961**, 83 (2002).
13. Behl, M., Razzaq, M. Y. & Lendlein, A. Multifunctional Shape-Memory Polymers. *Advanced Materials* **22**, 3388 (2010).
14. Nicole, L., Rozes, L. & Sanchez, C. Integrative approaches to hybrid multifunctional materials: from multidisciplinary research to applied technologies. *Advanced Materials* **22**, 3208 (2010).
15. Neffe, A. T., Hanh, B. D., Steuer, S. & Lendlein, A. Polymer networks combining controlled drug release, biodegradation, and shape memory capability. *Advanced Materials* **21**, 32 (2009).
16. Carbajal, L. Shape-Memory Polymers: Novel Biodegradable Shape-Memory Elastomers with Drug-Releasing Capabilities. *Advanced Materials* **23**, 2210 (2011).
17. Nagahama, K., Ueda, Y., Ouchi, T. & Ohya, Y. Biodegradable Shape-Memory Polymers Exhibiting Sharp Thermal Transitions and Controlled Drug Release. *Biomacromolecules* **10**, 1789 (2009).
18. Kim, K. *et al.* Control of degradation rate and hydrophilicity in electrospun non-woven poly(d,l-lactide) nanofiber scaffolds for biomedical applications. *Biomaterials* **24**, 4977 (2003)
19. Pereira, M., Ouyang, B. & Sundback, C. A. A highly tunable biocompatible and multifunctional biodegradable elastomer. *Advanced Materials* **25**, 1209 (2013).
20. Zhang, X., Geven, M. A., Grijpma, D. W., Peijs, T. & Gautrot, J. E. Tunable and processable shape memory composites based on degradable polymers. *Polymer* **122**, 323 (2017).
21. Bezwada, R. S., Jamiolkowski, D. D., Lee, I. Y. & Agarwal, V. Monocryl® suture, a new ultra-pliable absorbable monofilament suture. *Biomaterials* **16**, 1141 (1995).
22. Mondal, D. & Griffith, M. Polycaprolactone-based biomaterials for tissue engineering and drug delivery: Current scenario and challenges. *International Journal of Polymeric Materials and Polymeric Biomaterials* **65**, 255 (2016).

23. Woodruff, M. A. & Hutmacher, D. W. The return of a forgotten polymer—polycaprolactone in the 21st century. *Progress in Polymer Science* **35**, 1217 (2010).
24. Chen, D. R., Bei, J. Z. & Wang, S. G. Polycaprolactone microparticles and their biodegradation. *Polymer Degradation and Stability* **67**, 455 (2000).
25. Maglio, G., Migliozi, A. & Palumbo, R. Compatibilized poly (ϵ -caprolactone)/poly (L-lactide) blends for biomedical uses. *Macromolecular rapid communications* **20**, 236 (1999).
26. Zhang, Y., Ouyang, H., Lim, C. T., Ramakrishna, S. & Huang, Z.-M. Electrospinning of gelatin fibers and gelatin/PCL composite fibrous scaffolds. *Journal of Biomedical Materials Research* **72B**, 156 (2004).
27. Poetz, K. L. & Shipp, D. A. Polyanhydrides: Synthesis, Properties, and Applications. *Australian Journal of Chemistry* **69**, 1223 (2016).
28. Katti, D. S., Lakshmi, S., Langer, R. & Laurencin, C. T. Toxicity, biodegradation and elimination of polyanhydrides. *Advanced drug delivery reviews* **54**, 933 (2002).
29. Dang, W., Daviau, T., Ying, P., Zhao, Y. & Nowotnik, D. Effects of GLIADEL® wafer initial molecular weight on the erosion of wafer and release of BCNU. *Journal of Controlled Release* **42**, 83 (1996).
30. Shipp, D. A., McQuinn, C. W. & Rutherglen, B. G. Elastomeric and degradable polyanhydride network polymers by step-growth thiol–ene photopolymerization. *Chemical Communications* **42**, 6415 (2009).
31. Luo, X. & Mather, P. T. Preparation and characterization of shape memory elastomeric composites. *Macromolecules* **42**, 7251 (2009).
32. Robertson, J. M., Nejad, H. B. & Mather, P. T. Dual-spun shape memory elastomeric composites. *ACS Macro Letters* **4**, 436 (2015).
33. Rousseau, I. A. & Mather, P. T. Shape memory effect exhibited by smectic-C liquid crystalline elastomers. *Journal of the American Chemical Society* **125**, 15300 (2003).
34. Mather, P. T., Robertson, J. M. & Torbati, A. Water-triggered origami with a polymeric web. U.S. Patent No. 9,556,545 (2017).
35. Poetz, K. L., Mohammed, H. S., Snyder, B. L. & Liddil, G. Photopolymerized cross-linked thiol–ene polyanhydrides: erosion, release, and toxicity studies. *Biomacromolecules* **15**, 2573 (2014).

36. Kenner, V. H. & Knauss, W. G. On the hygrothermomechanical characterization of polyvinyl acetate. *Journal of Applied Physics* **51**, 5131 (1980).
37. Kim, S., Mundra, M. K., Roth, C. B. & Torkelson, J. M. Suppression of the T_g-nanoconfinement effect in thin poly (vinyl acetate) films by sorbed water. *Macromolecules* **43**, 5158 (2010).
38. Ping, Z. H., Nguyen, Q. T., Chen, S. M., Zhou, J. Q., & Ding, Y. D. States of water in different hydrophilic polymers—DSC and FTIR studies. *Polymer* **42**, 8461 (2001).
39. de Campos, A., Klamczynski, A., Wood, D., Williams, T. & Chiou, B.-S. TPS/PCL Composite Reinforced with Treated Sisal Fibers: Property, Biodegradation and Water-Absorption. *Journal of Polymers and the Environment* **21**, 1 (2012).
40. Natu, M. V., de Sousa, H. C. & Gil, M. H. Effects of drug solubility, state and loading on controlled release in bicomponent electrospun fibers. *International journal of pharmaceuticals* **397**, 50 (2010).
41. Luong-Van, E., Grøndahl, L., Chua, K. N. & Nurcombe, V. Controlled release of heparin from poly(ϵ -caprolactone) electrospun fibers. *Biomaterials* **27**, 2042 (2006).
42. L Wischke, C., Neffe, A.T., Steuer, S. and Lendlein, A. Evaluation of a degradable shape-memory polymer network as matrix for controlled drug release. *Journal of Controlled Release* **138**, 243 (2009).
43. Lawton, M. I., Tillman, K. R. & Mohammed, H. S. Shipp, D.A. & Mather, P.T. Anhydride-based reconfigurable shape memory elastomers. *ACS Macro Letters* **5**, 203 (2016).
44. Knight, P. T., Lee, K. M., Chung, T. & Mather, P. T. PLGA– POSS End-Linked Networks with Tailored Degradation and Shape Memory Behavior. *Macromolecules* **42**, 6596 (2009).



Scheme 5-1. (A) Synthesis of polyanhydride elastomer, and chemical structures of (B) poly(ϵ -caprolactone) and (C) poly(vinyl acetate).

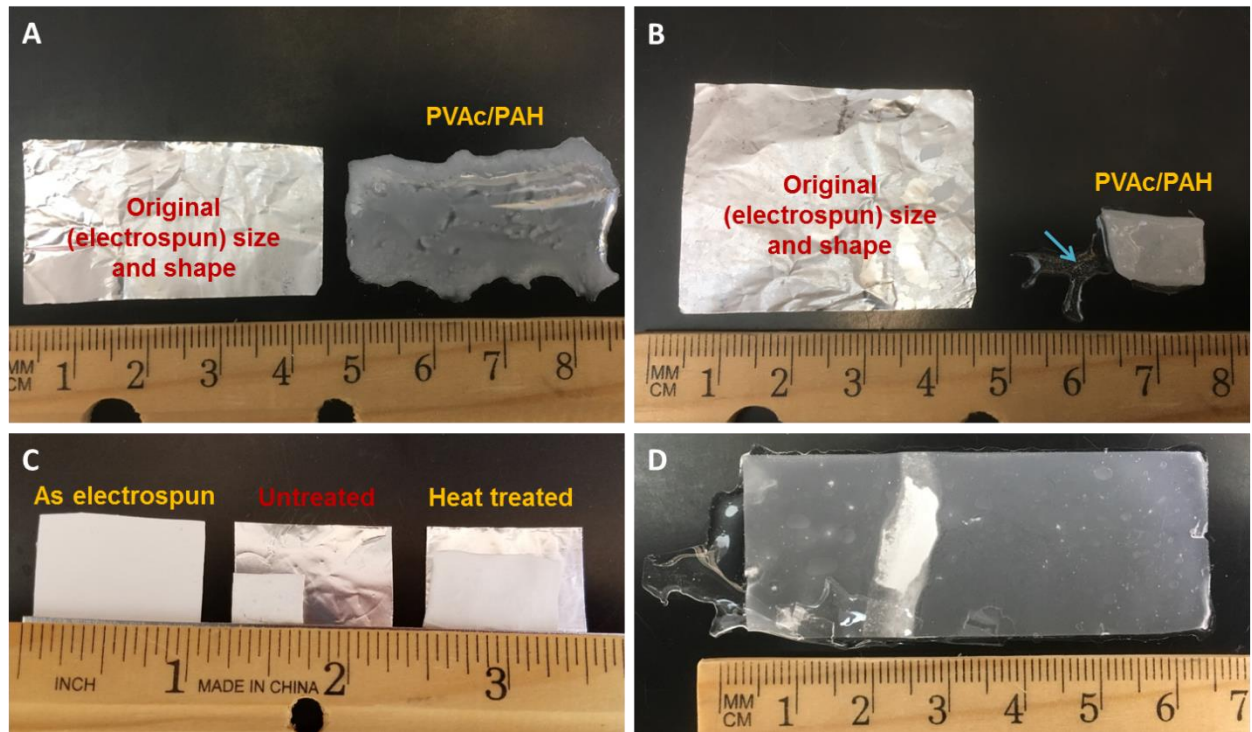


Figure 5-1. Effect of thermal treatment implemented to minimize shrinkage of electrospun PVAc fibers prior to composite fabrication. (A) The resulting composite (right) when no thermal treatment or PAH pre-cure is used in comparison to its original geometry (left) (B) Pre-curing the PAH monomer enabled the PVAc to maintain its fibrous phase within the composite, however significant shrinkage occurred (right). Distinct regions of excess PAH denoted by the blue arrow. (C) Comparison of the effect of heat treatment on electrospun PVAc following hydration in DI water revealed significantly less shrinkage for samples previously treated. The foil substrate shows the original size of the fiber mat. (D) The addition of a heat treatment and pre-cured PAH resulted in a composite with minimal shrinkage and conservation of its original geometry. The excess PAH is trimmed as part of the fabrication process.

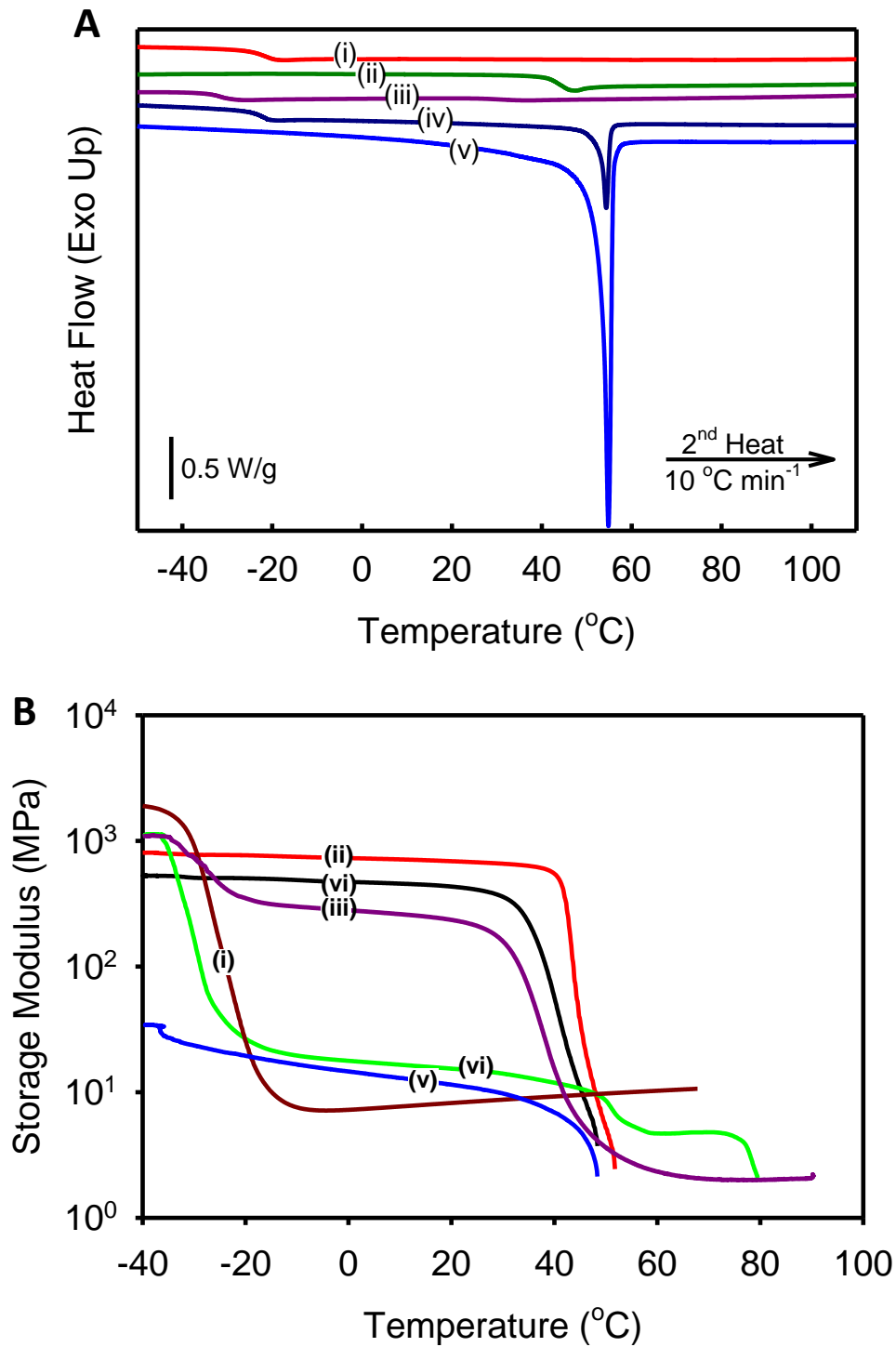


Figure 5-2. (A) Thermal and (B) thermomechanical characterizations of the (i) PAH elastomer, (ii) electrospun PVAc (heat treated), (iii) PVAc/PAH composite (iv) PCL/PAH composite, (v) electrospun PCL, and (vi) electrospun PVAc (untreated).

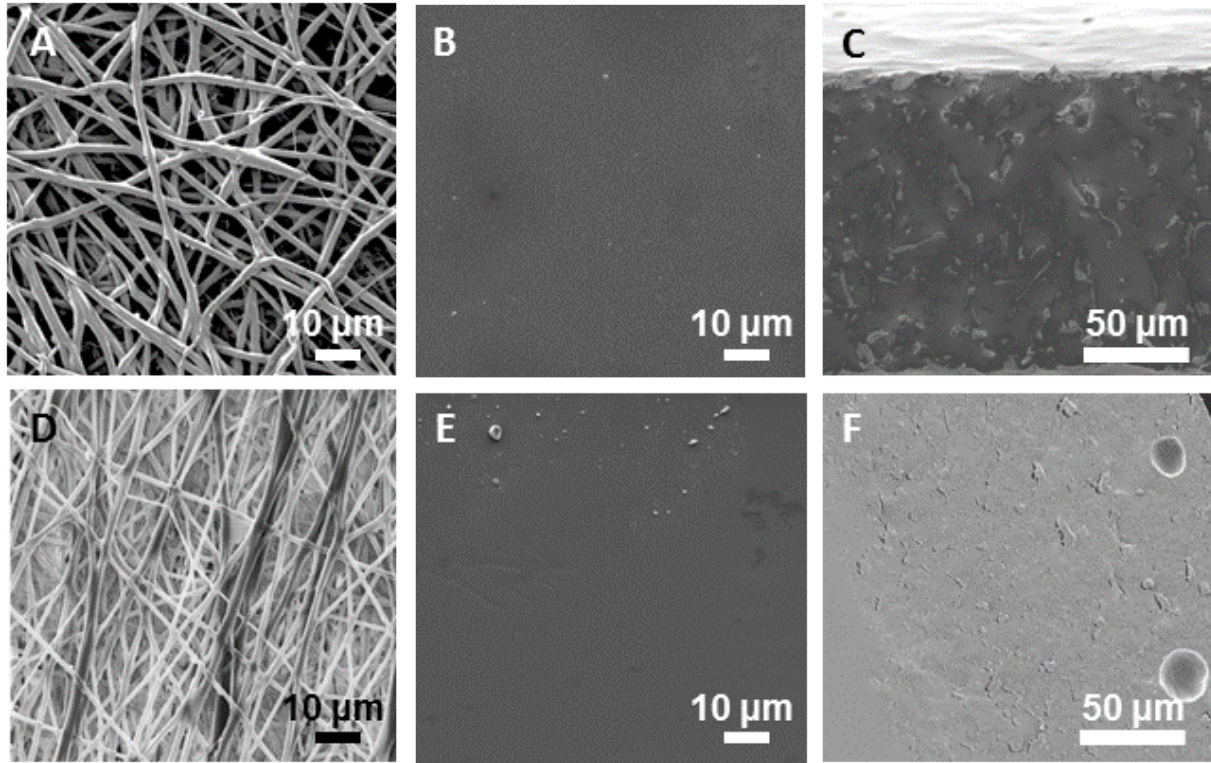


Figure 5-3. Scanning electron microscopy micrographs of (A) electrospun PCL and (B) electrospun PVAc following thermal treatment. The surface and cross-section of PCL/PAH are shown in (C) and (D). The surface and cross-section of PVAc/PAH are shown in (E) and (F).

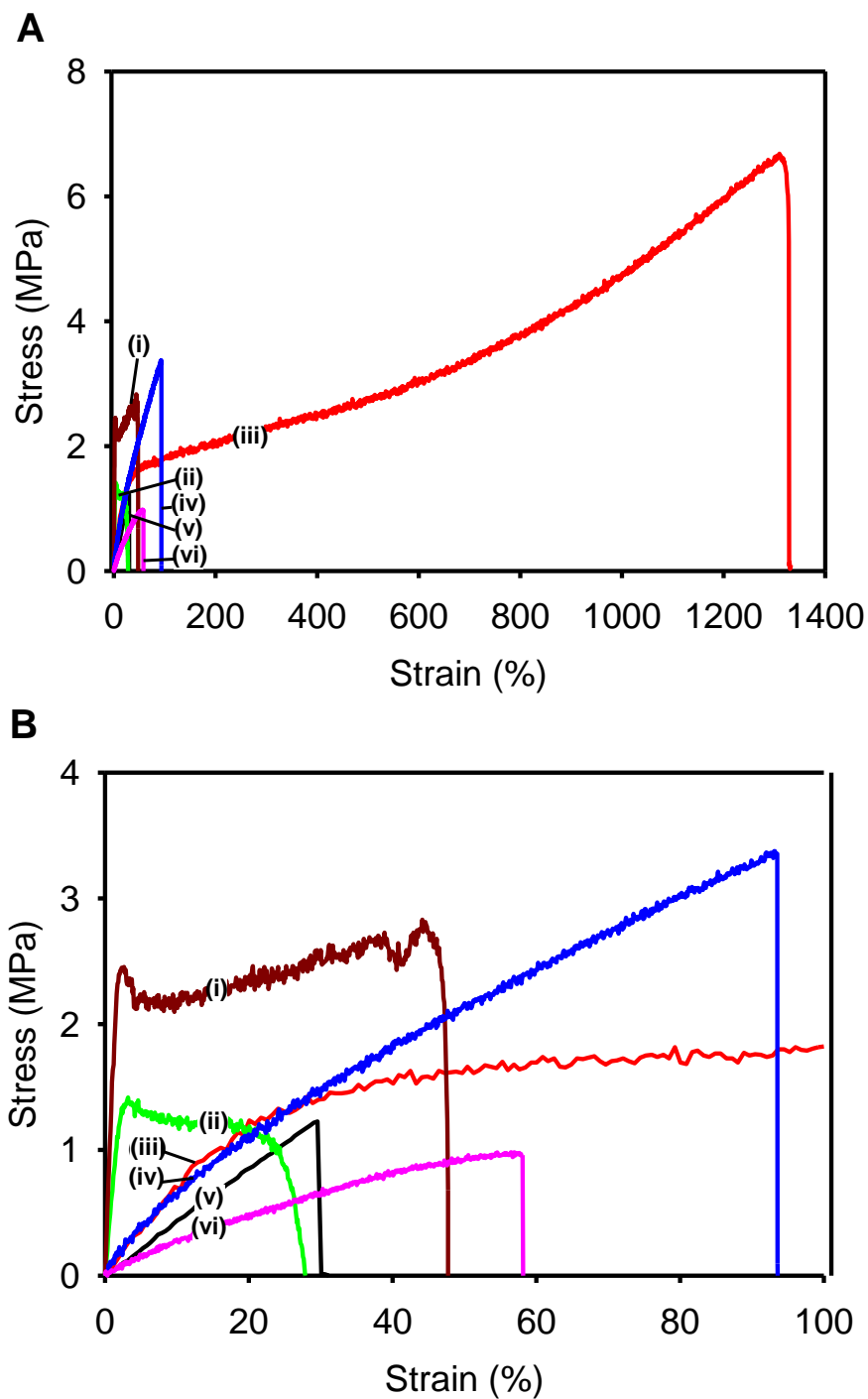


Figure 5-4. Representative tensile engineering stress-strain curves of both the composite and individual components for PCL/PAH and PVAc/PAH composites showing (A) the strain-to-failures and (B) the linear elastic regions for (i) electrospun PVAc (heat treated), (ii) electrospun PVAc (untreated), (iii) electrospun PCL, (iv) PCL/PAH composite, (v) PAH, and (vi) PVAc/PAH composite.

Table 5-1. Summary of tensile engineering stress-strain curves for the PCL/PAH and PVAc/PAH composites and individual components.

	Young's Modulus (MPa)	Strain-to-Failure (%)
PAH	4.5 ± 0.4	30 ± 5
Electrospun PCL	7.1 ± 3.0	1300 ± 140
Electrospun PVAc (Untreated)	63.5 ± 11.3	30 ± 10
Electrospun PVAc (Heat Treated)	157.1 ± 15.2	40 ± 10
PCL/PAH Composite	7.5 ± 0.9	80 ± 40
PVAc/PAH Composite	2.9 ± 0.5	60 ± 7

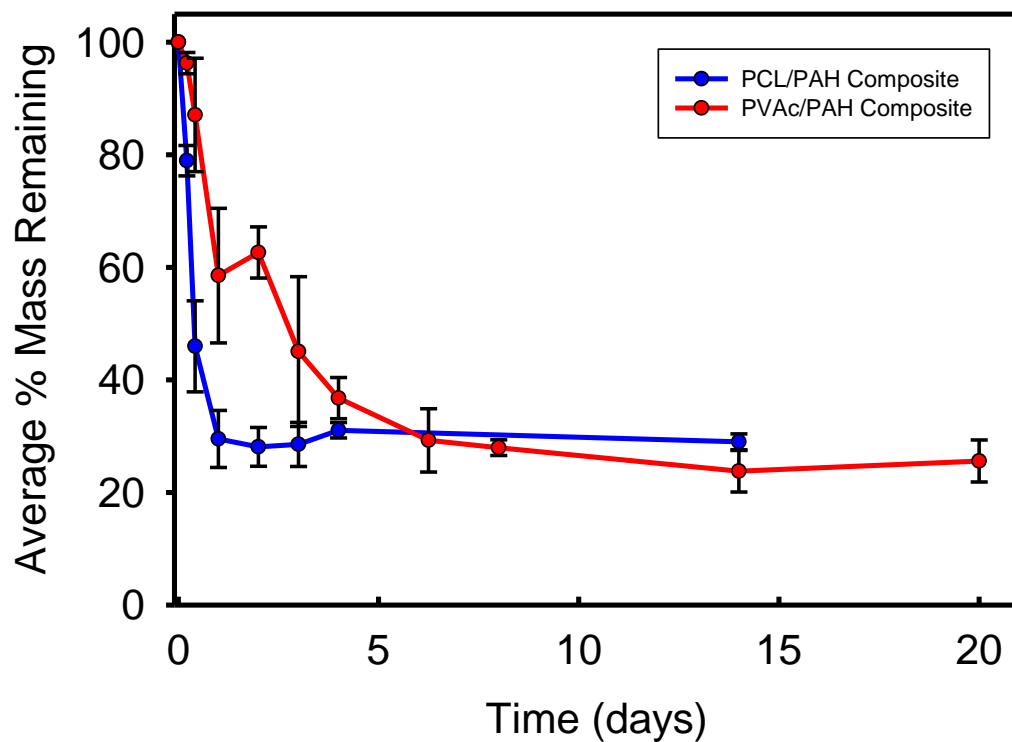


Figure 5-5. Mass loss during *in vitro* degradation in PBS at 37 °C for the PCL/PAH and PVAc/PAH composites.

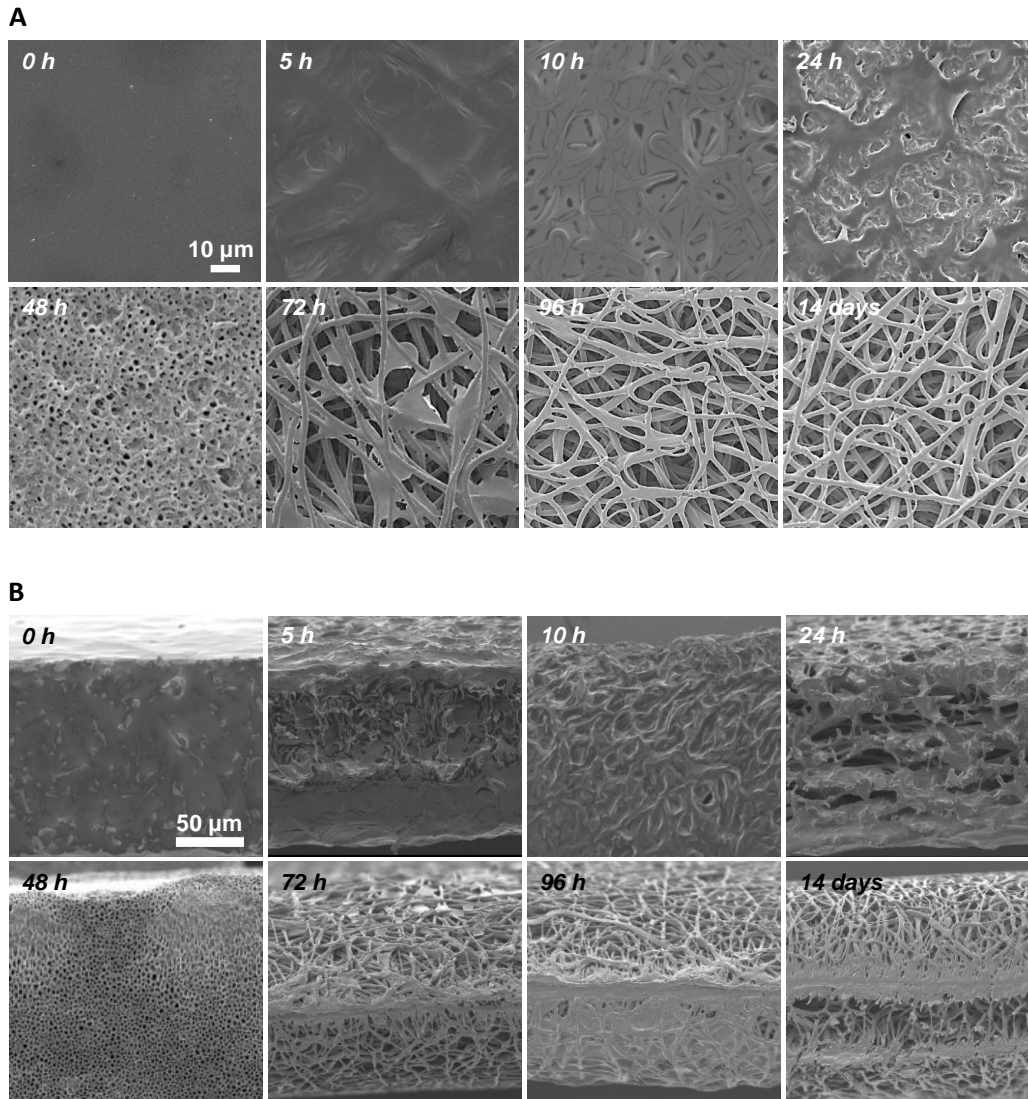


Figure 5-6. Morphological changes during degradation of the PCL/PAH composite in PBS at 37 °C at the A) surface and B) cross-section, revealed using scanning electron microscopy (SEM).

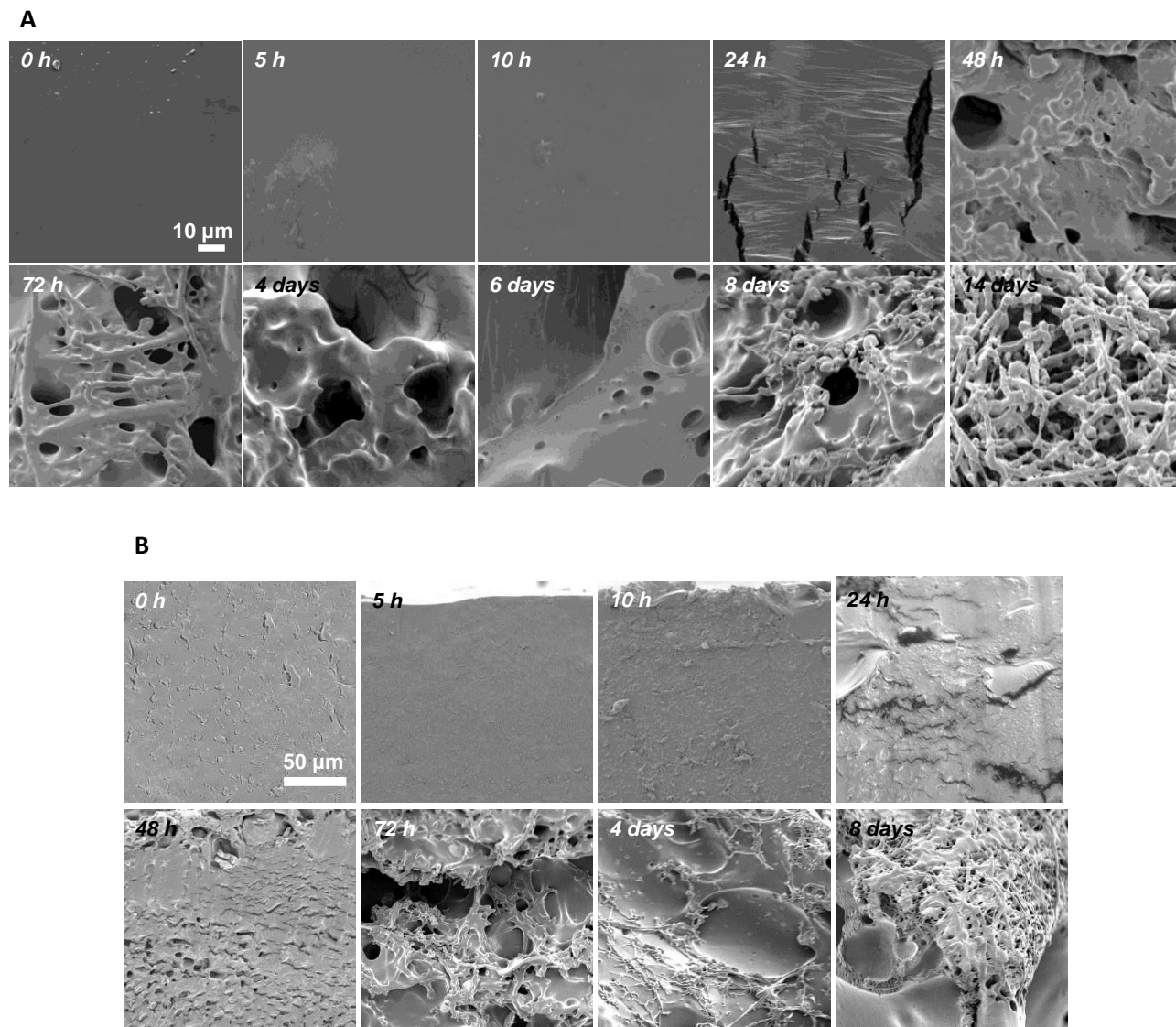


Figure 5-7. Morphological changes during degradation of the PVAc/PAH composite in PBS at 37 °C at the A) surface and B) cross-section, revealed using scanning electron microscopy (SEM).

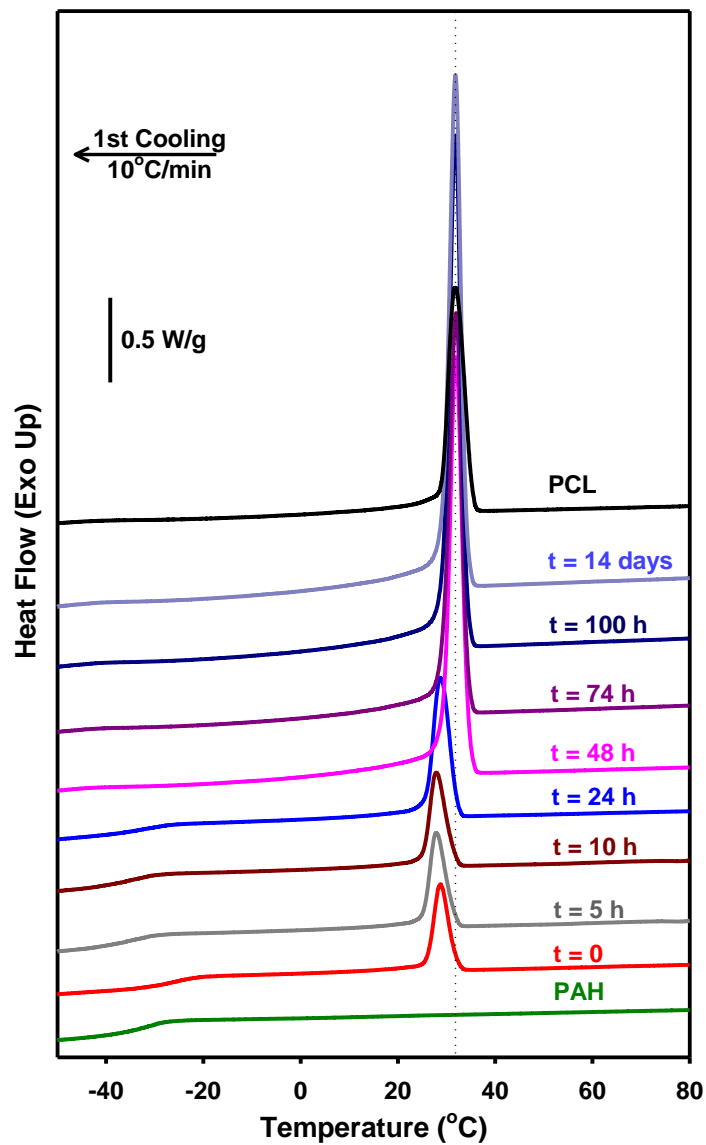


Figure 5-8. Thermal properties of the PCL/PAH composite during degradation. The dotted line indicates the crystallization temperature for electrospun PCL.

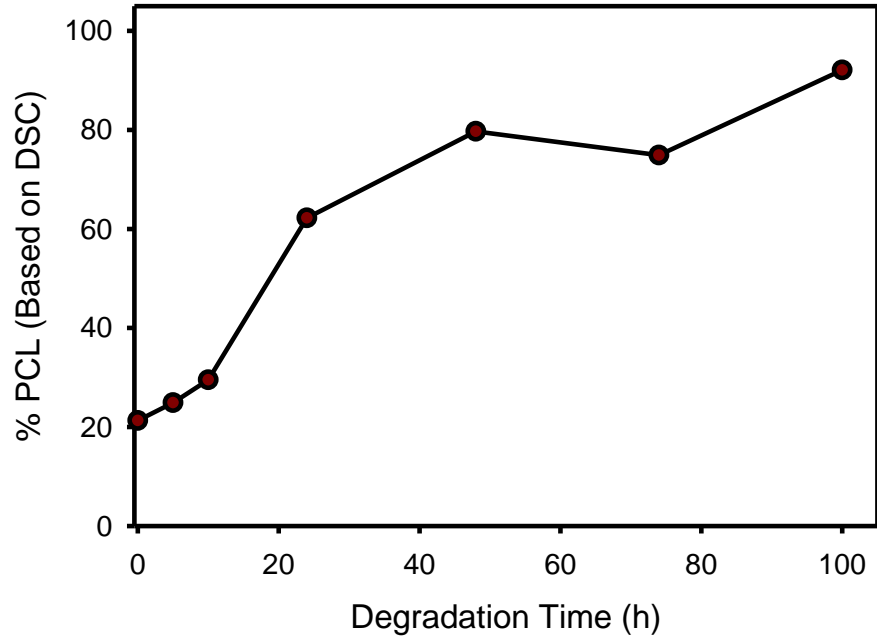


Figure 5-9. Fraction of PCL in the PCL/PAH composite as a function of degradation time.

Table 5-2. Fraction of PCL in the PCL/PAH composite as a function of degradation time.

Degradation Time (h)	ΔH_c (J/g)	T_c (°C)	Amount of PCL(%)
0	9.4	28.8	18.3
5	11.3	27.9	21.9
10	13.7	27.3	26.5
24	32.1	28.7	62.2
48	41.1	31.9	79.7
74	38.7	38.7	74.9
100	47.5	31.8	92.1
336	49.5	32.0	95.8
PCL Fiber Mat	51.6	31.9	100.0

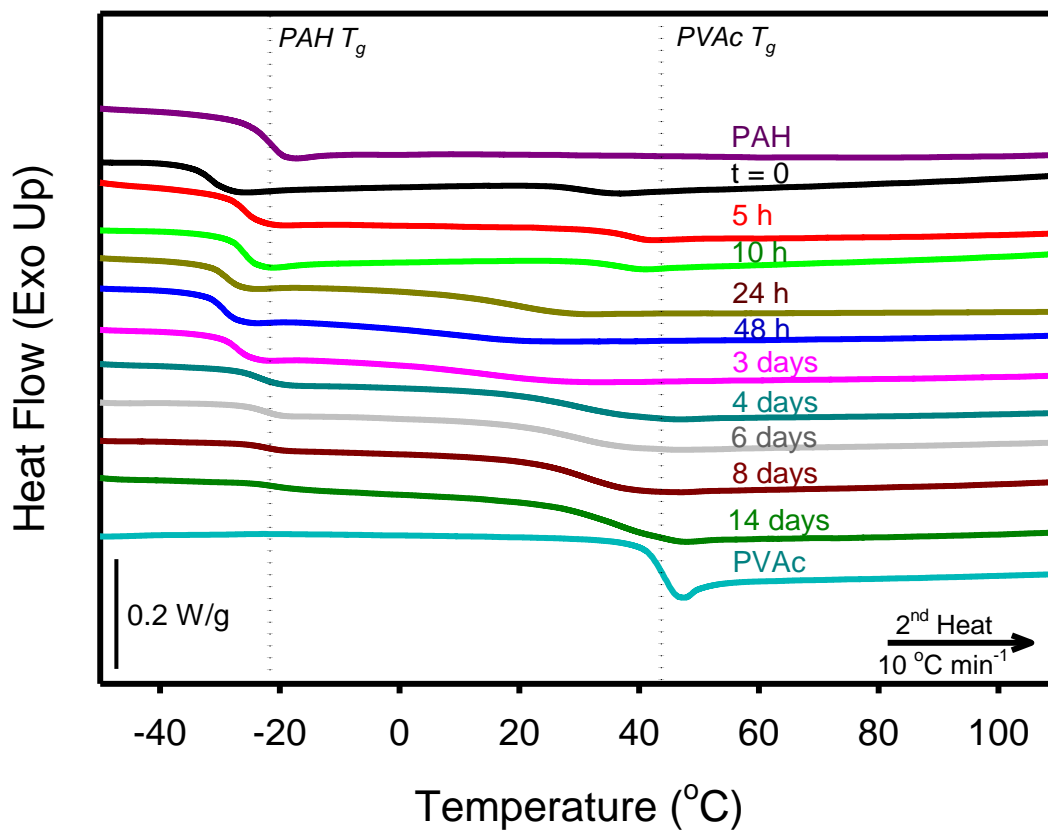


Figure 5-10. Thermal characterization by DSC of the PVAc/PAH composite following different degradation times. The dotted lines denote the glass transitions for PAH and PVAc.

Table 5-3. Fraction of PVAc in the PVAc/PAH composite as a function of degradation time.

Degradation Time (h)	T_g (PVAc)	ΔC_p (PVAc)	% PVAc
Electrospun PVAc	44.7	0.473	100
0	30.1	0.076	16
5	38.8	0.081	17
10	37.4	0.074	16
24	20.3	0.159	34
48	13.0	0.145	31
72	0.9	0.182	38
96	29.5	0.282	60
150	30.4	0.240	51
192	30.9	0.350	74
336	36.7	0.314	66

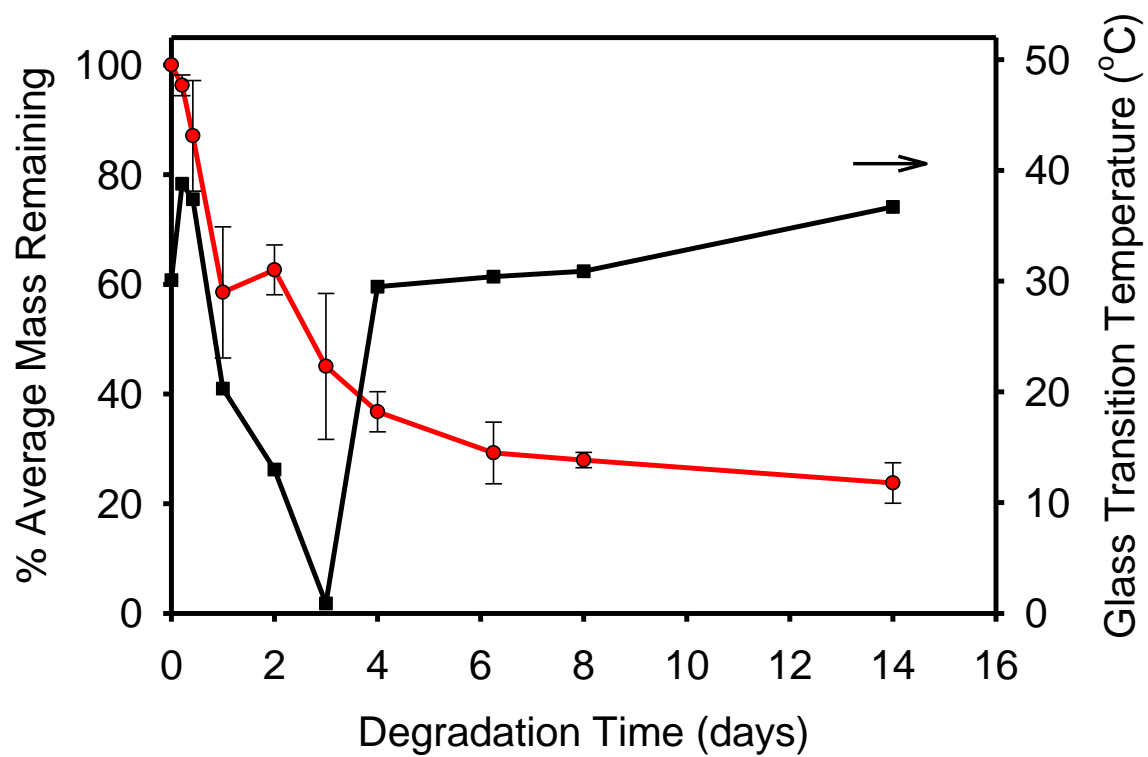


Figure 5-11. Evolution of the glass transition temperature of the PVAc component of the PVAc/PAH composite at different stages of PAH degradation.

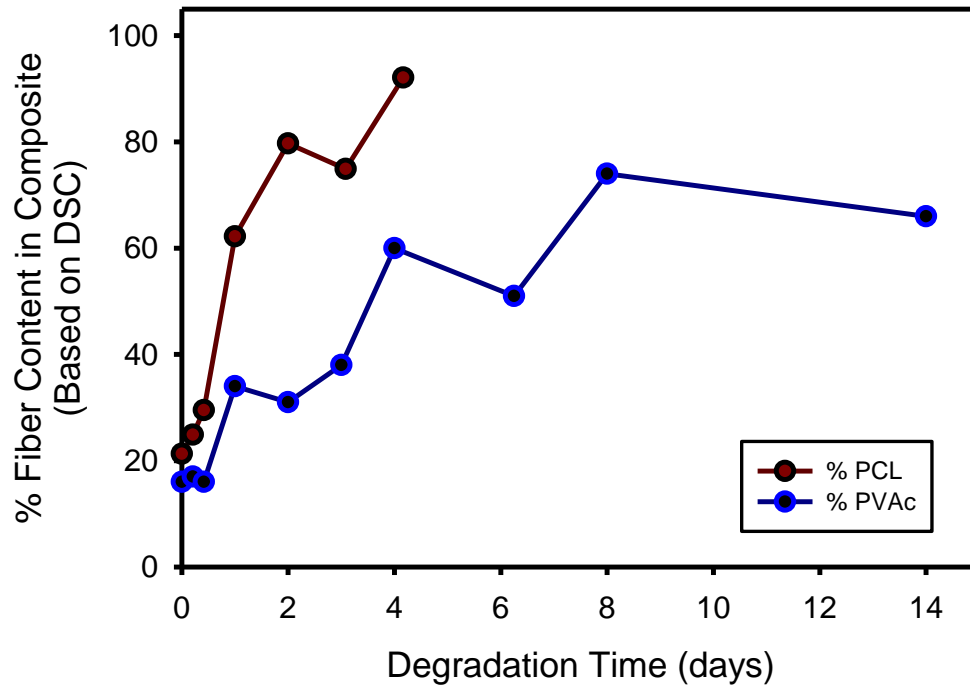


Figure 5-12. Comparison of PCL and PVAc content during degradation of the PCL/PAH and PVAc/PAH composites, respectively. The fiber composition was calculated based on the relative melting or glass transition temperatures as determined by DSC.

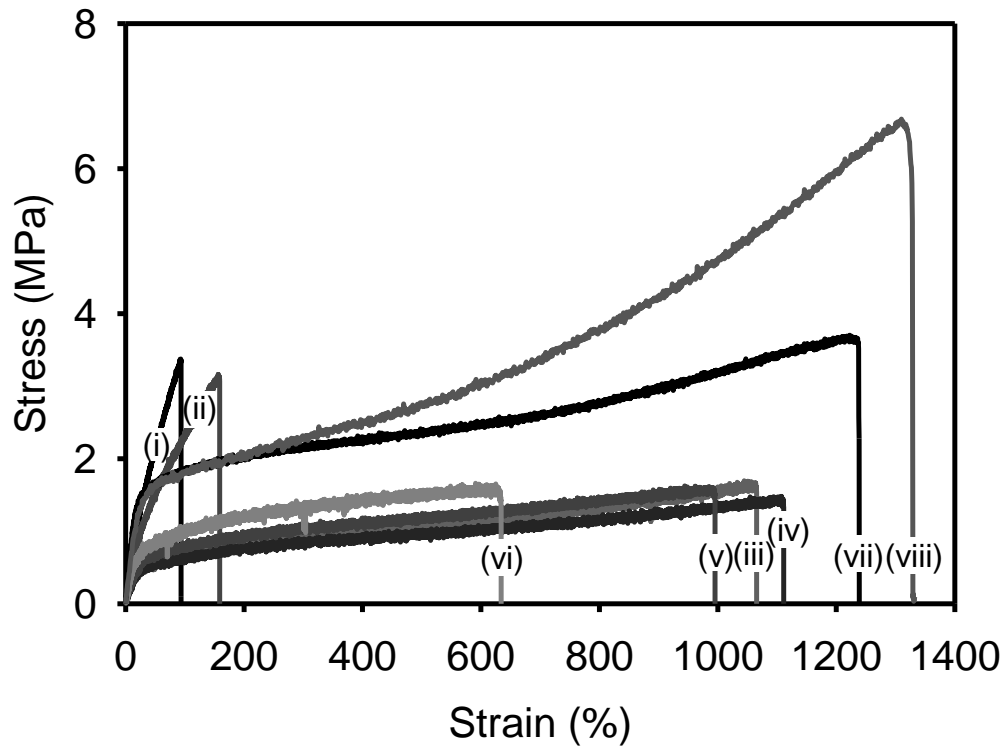


Figure 5-13. Representative engineering stress-strain plots of PCL/PAH at various degradation points of (i) as fabricated, $t = 0$, (ii) 10 h, (iii) 48 h, (iv) 72 h, (v) 96 h, (vi) 8 days, (vii) 14 days, and (viii) as-fabricated electrospun PCL for reference.

Table 5-4. Mechanical properties of PCL/PAH composite after different degradation times.

Degradation Time	Young's Modulus (MPa)	Strain-to-Failure (%)
0	7.5 ± 0.9	80 ± 40
10 h	4.6 ± 0.9	150 ± 25
48 h	3.0 ± 0.5	1000 ± 170
72 h	2.2 ± 0.8	950 ± 170
96 h	2.2 ± 1.5	900 ± 190
8 days	4.2 ± 1.5	640 ± 85
14 days	7.7 ± 3.0	1200 ± 30
Electrospun PCL	7.1 ± 3.0	1300 ± 140

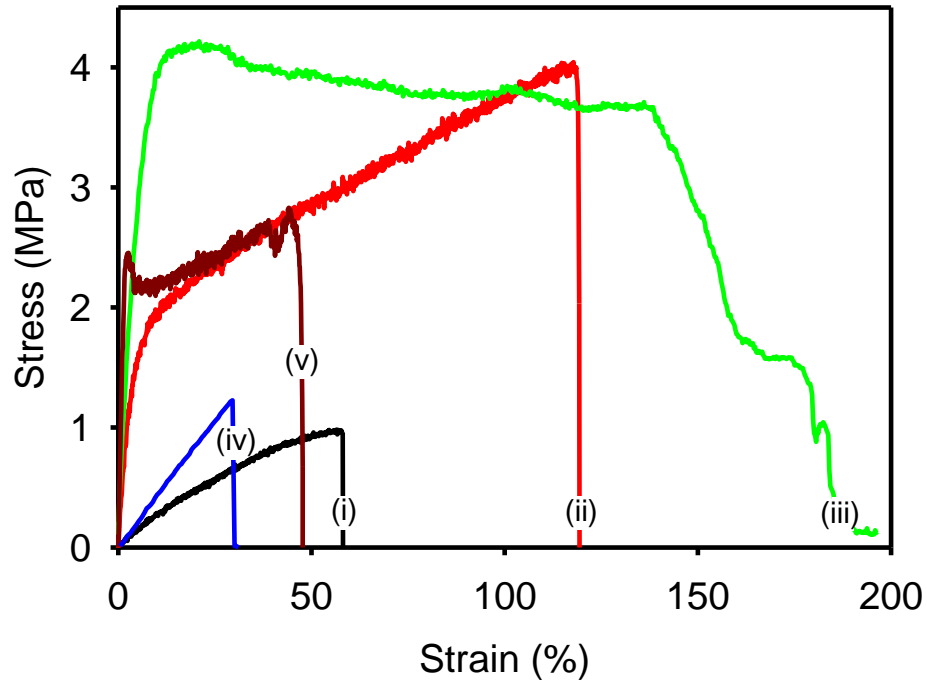
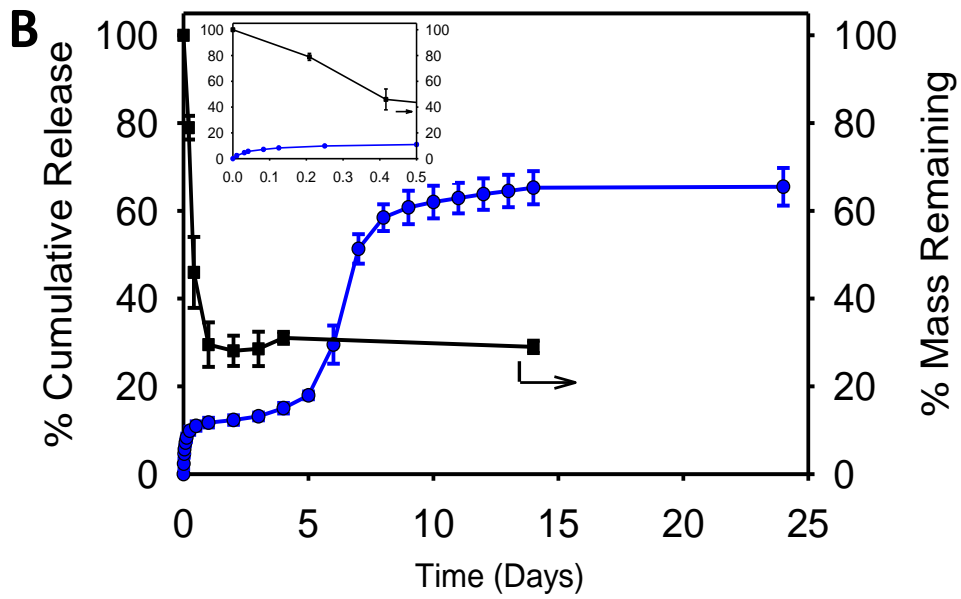
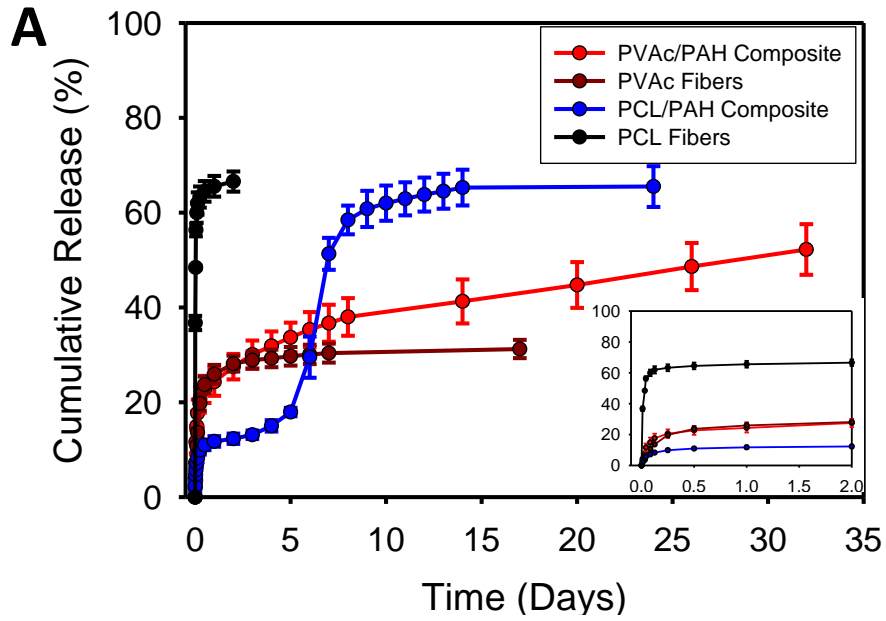


Figure 5-14. Representative engineering stress-strain plots of PVAc/PAH at various degradation points of (i) as fabricated, $t = 0$, (ii) 10 h, (iii) 48 h, (iv) PAH for reference, and (v) as-fabricated heat-treated electrospun PVAc for reference.

Table 5-5. Mechanical properties of PVAc/PAH composite after different degradation times.

Degradation Time	Young's Modulus (MPa)	Strain-to-Failure (%)
0	2.9 ± 0.5	60 ± 7
10 h	45.3 ± 3.2	140 ± 45
48 h	49.2 ± 22.5	300 ± 220
Electrospun PVAc (Heat Treated)	157.1 ± 15.2	40 ± 10



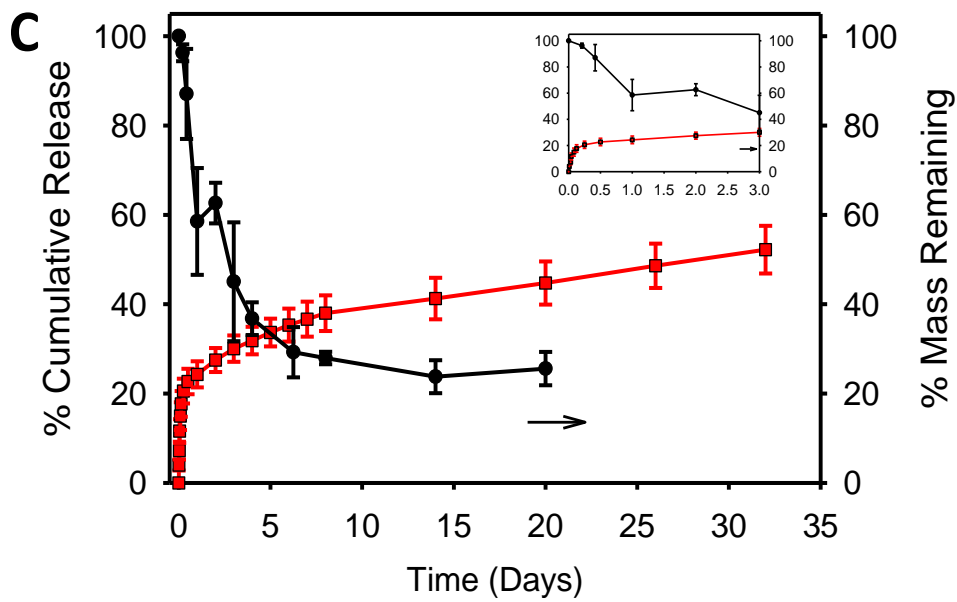


Figure 5-15. *In vitro* release of hydrophilic model drug Rhodamine B from the PCL/PAH and PVAC/PAH composites with comparisons to (A) Rhodamine B release from fibers without the PAH matrix, and with mass loss results in (B) and (C).



Figure 5-16. Qualitative demonstration of one way shape memory of the PVAc/PAH composite.

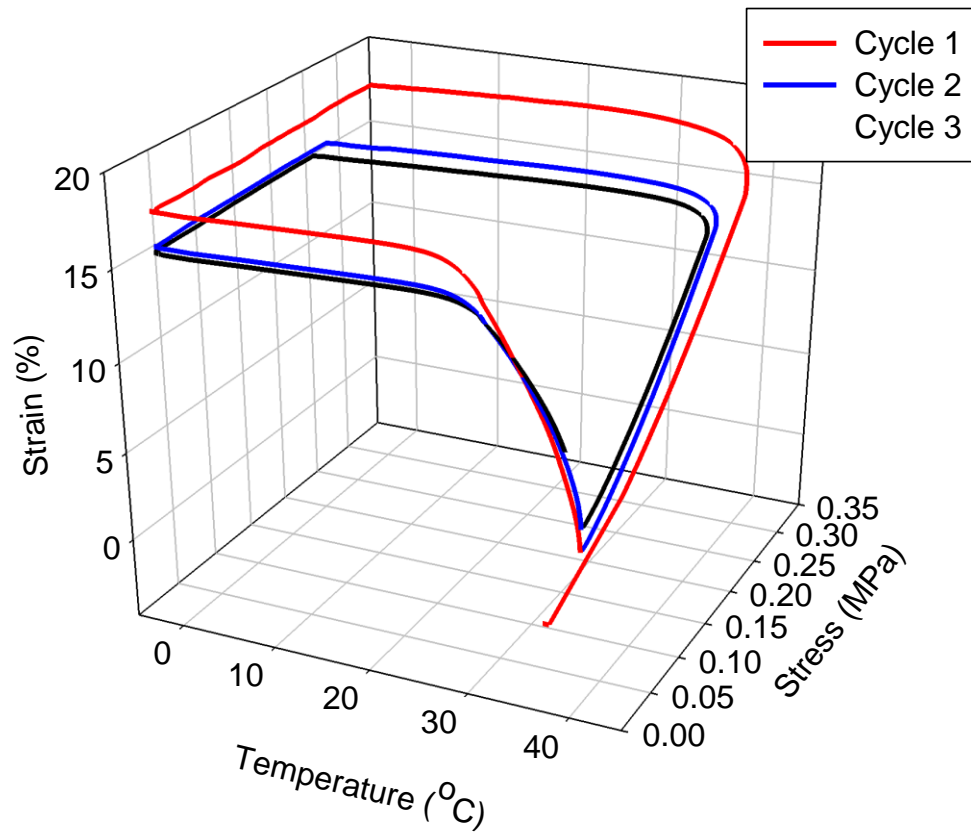


Figure 5-17. Shape memory stress-temperature-strain plot for the PVAc/PAH composite.

Table 5-6. One way shape memory fixing and recovery ratios for the PVAc/PAH composite.

Cycle	R_f (%)	R_r (%)
1	99	76
2	99	90
3	99	ND

**ND denotes no data available.*

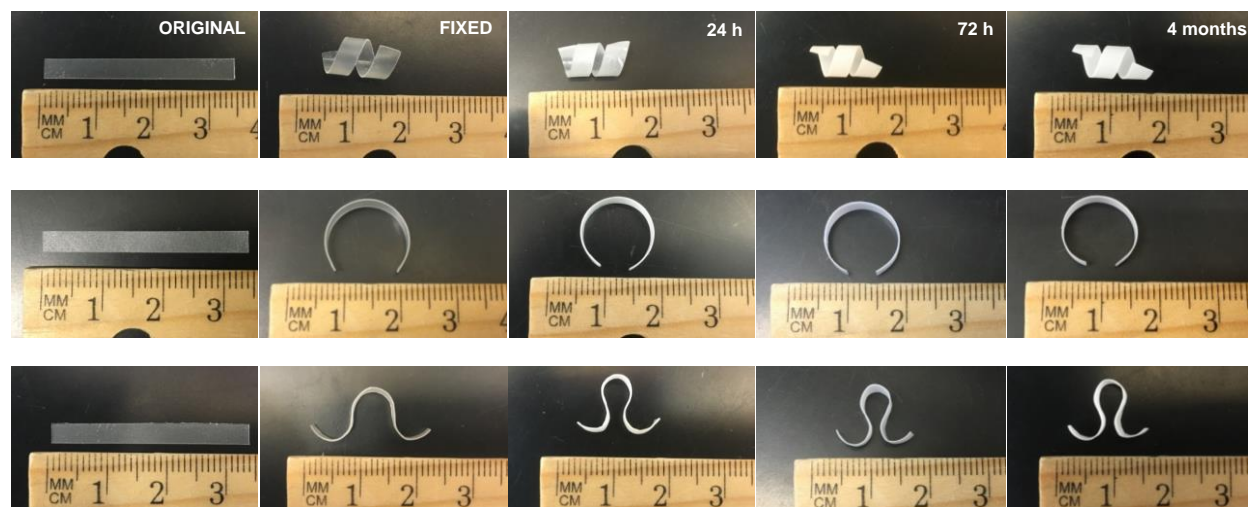


Figure 5-18. Preservation of arbitrarily deformed shapes during *in vitro* degradation of the PCL/PAH composite in PBS at 37 °C.

Chapter 6

Latent Mechanical Programming of a Shape Memory Composite with Reversible Anisotropic Actuation

6.1 Synopsis

In this chapter, the design, fabrication, and characterization of a polymeric composite composed of oriented semicrystalline polymeric fibers embedded within a crosslinked epoxy matrix is presented. While this composite inherently exhibits triple shape memory, as our group has presented in the past, we observed that introducing anisotropy enabled the construction of complex three dimensional geometries featuring latent mechanical programming. Rather than relying on specific molds to manipulate a new shape, this system instead capitalized on an induced strain to influence a new structure attained by strain conditioning above a transition temperature followed by cooling. The new geometry was then activated by strain-free exposure to this temperature, which was dictated by the orientation of the fibers across the bilayer cross-section. We investigated the effect of programming these new shapes by varying the fibrous phase orientation through multilayer laminates and studied the curvature, thermomechanical, shape memory, and microstructural properties of the composites. Additionally, we found that by compressing the oriented fibers of each ply during composite cure, the composites constructed from such plies exhibited actuation into anisotropically induced shapes. The new composite materials can have broad applications in artificial muscles, hinges, sensors, and robotics, to name a few.

6.2 Introduction

Anisotropy is found in both natural and synthetic materials and can have significant effects on material properties. In the construction, automotive and aerospace sectors, anisotropy is engineered into laminated composites in order to tailor load bearing properties, typically by specific layering of oriented laminates.¹⁻⁴ In nature, biological materials such as wood,⁵ tendons,⁶ blood vessels,⁷ sea shells,⁸ and cortical bone⁹ contain hierarchical structures that exhibit anisotropy that serve to maximize mechanical functionalities. As a result, incorporating oriented properties into composite materials has served as a great inspiration for composite material design as evidenced by the abundance of review articles, with only a few referenced here.¹⁰⁻¹⁴ Of particular interest to many are the natural anisotropic architectures within botanical materials that form complex 3D geometries.¹⁵ One specific example is the curling of pine cone scales in response to dehydration, which has been artificially mimicked by constructing bilayers containing materials that respond anisotropically to humidity.¹⁶ In another example, the twisting of orchid seed pods as a result of fibrous layers oriented $\sim 45^\circ$ relative to the long axis had been imitated by orienting stretched latex sheets at a diagonal.¹⁷

Active materials such as shape memory polymers have broad applications in many fields due to the low cost and ease of being able to create and retain articles that undergo simple temporary shape changes, yet can be returned to their original form by environmental trigger.^{18,19} These materials are seemingly a natural candidate for developing complex 3D geometries resulting from anisotropy; however only few studies have used this approach to produce such complex shapes. Lee et al. formed a variety of coil-based shapes by orienting the nematic domains within a crosslinked liquid crystalline polymer that are then thermally triggered.²⁰ In the

Mather research group, Robertson et al. introduced mechanically programming complex shapes from anisotropic soft, elastomeric shape memory composites.²¹ This was accomplished by layering amorphous composites composed of oriented electrospun poly(vinyl acetate) embedded within a Sylgard 184 silicone matrix. The composite laminates were fabricated into bilayers at differing orientations relative to each other. By uniaxially straining the bilayer composite, spontaneous room temperature curling of the samples resulted upon release of the load. While that system was capable of attaining 3D shape changes by mechanical (rather than thermal) programming, circumventing one way shape memory cycling, it was limited to immediate curling upon load release. The present investigation combines thermal triggering with mechanical programming.

We were interested in not only producing both complex shapes but also controlling when this spontaneous shape change occurred. As such, our goal was to introduce anisotropy into a similarly fibrous thermoset composite system, where the mechanically programmed shape remained dormant at room temperature until thermally prompted. We theorized that a composite material exhibiting thermal transitions above room temperature would serve to suspend a mechanically programmed shape until ready for deployment. Accordingly, we also hypothesized that these dormant mechanically programmed shapes could be tailored by the lay-up design wherein distinct layers featured orientation differences relative to each other and to the direction of mechanical programming. In order to design such a material, we turned to a versatile material combination where electrospun semicrystalline PCL was embedded within a crosslinked epoxy matrix, which had been previously developed for triple shape memory in the Mather research group.²² This particular composite was attractive due to an easily tunable glass transition

temperature through the addition reaction blend of two diepoxides, aromatic bisphenol A diglycidyl ether (DGEBA) and aliphatic diepoxide (neopentyl glycol diglycidyl) (NDGE), with a flexible diamine, Jeffamine D230.²³ Additionally, we observed that incorporating compressive stresses into the fibrous phase during fabrication led to unique reversible actuation that was unanticipated based on prior studies that demonstrated the effect for crystallizable networks²⁴ of which this is not one.

6.3 Methods

6.3.1 Materials

Poly(ϵ -caprolactone) (70,000 – 90,000 g·mol⁻¹), bisphenol A diglycidyl ether (DGEBA), neopentyl glycol diglycidyl (NDGE), Jeffamine 230, tetrahydrofuran (THF), and dimethylformamide (DMF) were purchased from Sigma Aldrich and used as received.

6.3.2 Electrospinning

Fibers were electrospun using a solution of 20 w/v % PCL dissolved in a 4:1 THF:DMF solvent mixture. The PCL solution was then transferred to a 10 ml syringe fitted with a blunt 22G needle tip. A syringe pump was used to supply a steady flow rate of 1.0 ml·h⁻¹, which was electrospun onto a grounded 50 mm drum using a distance of 7 cm between the needle tip and the drum (-500 V), and an applied voltage of 11.5 kV. To achieve oriented fibers, the drum was rotated at 5000 rpm. Typically drum rotations below 800 rpm result in randomly oriented fibers. Following electrospinning, all fiber mats were dried at room temperature under vacuum (-30 mm Hg) for 48 h to remove any residual solvent prior to further use.

6.3.3 Anisotropic Composite Fabrication

The epoxy monomers were prepared by melting DGEBA at 80 °C followed by vigorous mixing with NDGE and Jeffamine D230 (**Scheme 6-1**), which resulted in a low viscosity fluid. The weight fractions of the NDGE and DGEBA were selected to achieve a target glass transition temperature of ~35 °C, according to the Gordon-Taylor equation and prior model-fitting for this same system.²² The nomenclature used herein to refer to the epoxy formulation is DXNYD230. This refers to the weight percentage of DGEBA relative to NDGE as DX, and NDGE as NY, X and Y summing to 100. The designation “D230” denotes the Jeffamine 230 crosslinker with stoichiometric equivalence of amine protons (4 per D230 molecule) and epoxide rings (two each for DGEBA and NGDE). For example, **D41N59D230** refers to crosslinked epoxy synthesized using 41 wt% DGEBA and 59 wt% NDGE.

The cross-ply bilayer composite was prepared by layering two electrospun PCL fiber mats, one on top of the other as depicted in **Scheme 6-2**. The assembly was arranged with the aligned fibers orthogonal between top and bottom layers, yielding a “cross-ply” porous construction. Once this was arranged, the fiber mats were secured together using binder clips and infiltrated with the epoxy monomer as an assembly, followed by vacuum infiltration at RT to remove any trapped air within the fiber mats. This assembly was then clamped between two glass slides using a spacer with variable thickness, arranged as a frame defining the composite perimeter, as shown in **Scheme 6-3**. The composite was next cured for four days at 45 °C. This relatively low cure temperature was selected to preserve the PCL fiber morphology, as it is below the PCL melting transition. A spacer was used to control the sample thickness and a compression factor was quantified (*CF*), using a range from 1 to 2.6, according to:

$$CF = \frac{n * (t_{Fiber\ mat})}{t_{spacer}}, \quad (6-1)$$

where t is the thickness of the individual fiber mat or the thickness of the spacer and n is the number of fiber mats or plies used.

In a similar manner, single-ply laminae were prepared by infiltrating aligned PCL fiber mats with the epoxy monomer, followed by vacuum infiltration at RT to remove any trapped air within the fiber mats. This was then clamped between two glass slides with a spacer and cured for four days at 45 °C.

6.3.4 Thermal Analysis

Differential scanning calorimetry (DSC) was performed using a Q200 manufactured by TA Instruments, Inc. Samples weighing 2.5 – 4.0 mg were sealed in Tzero aluminum pans and heated from -60 °C to 120°C at 10 °C · min⁻¹. The melting enthalpy was calculated from the second heating cycle by integrating the melting peak, and was used to determine the fraction of PCL in the elastomeric composite by comparing the melting enthalpies according to:

$$W_{PCL} (\%) = \frac{\Delta H_m}{\Delta H_{m,0}} \times 100 \% \quad (6-2)$$

where ΔH_m is the melting enthalpy of the composite measured by DSC and $\Delta H_{m,0}$ is the melting enthalpy of pure electrospun PCL, which was 48.0 J g⁻¹, as determined by DSC.

6.3.5 Morphology

Scanning electron microscopy (SEM) was used to determine the study the morphology of the composite. All samples were sputter coated with gold for 45 s prior to SEM. A JEOL JSM-5600 SEM was used with an accelerating voltage of 4 – 6 kV. ImageJ software (version 1.46,

National Institutes of Health) was used to measure PCL fiber diameter. Fiber diameter measurements were determined by taking a minimum of 50 measurements at 5 different locations well separated in the composites. The average diameter and standard deviation were calculated using a minimum of 250 total measurements.

The cross-sections of the samples were obtained by cryogenically fracturing then solvent-etching the composites. A dogbone shaped sample prepared by punching with a die, followed by immersion in liquid nitrogen (to embrittle the specimens), followed by fracturing of the narrow section by manual flexure. The cross-section surface was then treated with THF overnight to remove the PCL phase so that the morphology of the oriented PCL fibers could be clearly distinguished – as cavities – from the epoxy matrix.

6.3.6 Thermomechanical Characterization

A TA Instruments Q800 dynamic mechanical analyzer (DMA) was used in multifrequency strain mode to measure the storage and loss moduli and tan delta. Samples were cut into rectangular strips from the cross-ply composite orientation, maintaining a ratio of length to width of 5:1. All samples were first cooled to -60 °C, followed by heating at 10 °C min⁻¹ to 90 °C as the tensile storage and loss moduli were measured at a frequency of 1 Hz.

6.3.7 Quantitative Triple Shape Memory

The triple shape behavior of the anisotropic composite was quantified using the DMA. Samples were similarly prepared as those for thermomechanical characterization in Section 6.3.6. The DMA was used in controlled force mode to stretch a dog bone sample at 75 °C to a 10% strain (or 5% for the cross-ply sample) by ramping the force at 0.05 N min⁻¹; this

temperature was above both the PCL melting and epoxy glass transitions. The temperature was then decreased at 3 °C min⁻¹ to 0 °C and held isothermal for 10 min to fix the first temporary shape. The sample was then heated at 3 °C min⁻¹ to 45 °C (below PCL T_m and above epoxy T_g) and held isothermal for 5 min. The force was then unloaded at 0.25 N min⁻¹ until it reached the preload force of 10⁻³ N. The second temporary shape was programmed by then ramping the force at 0.05 N min⁻¹ to a strain of 30% (or 10% for the cross-ply sample), followed by cooling at 3 °C min⁻¹ to 0 °C and held isothermal for 10 min to fix the second temporary shape. The force was then unloaded at 0.25 N min⁻¹ until it reached the preload force of 10⁻³ N. Finally, the permanent shape was recovered by heating at 1 °C min⁻¹ to 80 °C (or to 60 °C for the cross-ply sample), and holding isothermal for 10 min. The cross-ply samples utilized a reduced strain and melting temperature protocol due to failure at larger values.

The degree of shape fixing (R_f) and the degree of shape recovery (R_r) were quantified for each sample using the following equations:

$$R_f(\%) = \left(\frac{\varepsilon_{fixed}}{\varepsilon_{deformed}} \right) \times 100 \% \quad (6-3)$$

$$R_r(\%) = \left(\frac{\varepsilon_{fixed} - \varepsilon_{recovered}}{\varepsilon_{fixed} - \varepsilon_0} \right) \times 100 \% \quad (6-4)$$

where ε_0 is the original strain (at the beginning of each cycle), $\varepsilon_{deformed}$ is the deformed strain that occurred after cooling while still under a load, ε_{fixed} is the fixed strain that resulted following unloading, and $\varepsilon_{recovered}$ is the recovered strain following heating.

6.3.8 Latent Triggering of Mechanically Programmed, Anisotropic Shape Change

Rectangular samples of 2.5 cm by 0.3 cm were cut from the cross-ply composite fabricated using a CF of 1.1; i.e., with minimal compression. The samples were cut at different angles according to **Scheme 6-4**, resulting in a variation of the cross-ply fiber orientation relative to the long dimension of the sample. For example, samples were cut such that a cross-ply(0) sample contained one surface with fibers oriented longitudinally and the opposing surface with fibers perpendicular to the long dimension. Samples cut with a 45° angle contained a cross-hatch pattern of fibers, relative to the rectangular cut out shape, and is hereafter referred to as cross-ply(45). The thermomechanically activated shape change proceeded by securing the sample onto a custom manual stretcher and placing in an isothermal oven at 70 °C for 10 min to melt the PCL phase. While the PCL was melted, the sample was then stretched to strains of 10 %, 20 %, 30 %, or 40 % and immediately placed in an isothermal oven at 45 °C to recrystallize PCL above the epoxy T_g for 30 min, followed by cooling to room temperature. The sample was then unclamped and a temporary shape (generally flat) was observed. The mechanically programmed shape change was then activated by heating to a temperature between T_g of the epoxy but below T_m of PCL. This was accomplished by placing the unconstrained sample in an isothermal oven at 45 °C for 10 min, followed by room temperature cooling to observe the programmed shape change. Shape recovery was then triggered heating above both T_g of the epoxy and T_m of PCL. This was accomplished by placing the unconstrained sample in an isothermal oven at 70 °C for 10 min. The radius of curvature and pitch were measured at each stage to characterize the latent shape change and its dependence on the magnitude of strain during shape programming for a strain of 10% to 50%.

6.3.9 Reversible Anisotropic Actuation

Rectangular samples from the cross-ply composite were fabricated using a *CF* of 2.6 and prepared at differing cutting angles according to **Scheme 6-4**. Reversible actuation was activated by placing the unconstrained sample into a heated water bath at 75 °C until a shape change appeared and had completed. The sample was then removed from the water bath and cooled to room temperature (~ 21.8 °C to 22.5 °C) on the bench top, in response to which that samples were observed to reverse the heat-induced shape change to a great extent. This was repeated for 10 consecutive cycles and the radius of curvature was measured for each cycle.

The thermal expansion and contraction of a single-ply composite was quantified using the DMA of rectangular strips containing fibers oriented either parallel (0°) or perpendicular (90°) to the tensile axis. The DMA was used in controlled force mode to heat a rectangular sample to 75 °C at a rate of 3 °C min⁻¹ followed by an isothermal hold for 3 min. The sample was then cooled to 0 °C at a rate of 3 °C min⁻¹ and then held isothermally for 5 min.

6.4 Results

6.4.1 Composite Fabrication and Morphology

The electrospun fibers were generally oriented in the same direction, as shown in **Figure 6-1A**, with an average fiber diameter of 1.3 μm ± 0.5 μm. Following infiltration of the epoxy matrix, the surface of the composite appeared to contain a smooth layer of epoxy as shown in **Figure 6-1B**. Two cross-sections of the single-ply composite, taken perpendicularly from each other, are shown in **Figures 6-1C** and **D**. These micrographs verified both complete infiltration of the epoxy matrix, and fiber orientation relative to each ply. The PCL phase had been

successfully removed by solvent etching, leaving behind a “negative” morphology within the epoxy phase. The circular cavities shown in the micrographs are indicative of the fibers aligned in the direction toward the observer, while horizontal channels are a result of the fibers parallel to the surface. The cross-ply morphology is similarly shown in **Figure 6-1E**, confirming good coupling of the fibrous bilayers with complete epoxy infiltration with no epoxy rich layer between the two fiber mats to interfere with the anisotropic shape effect discussed later. Moreover there was no surface rich material observed that could potentially introduce bias any resulting programmed shapes in the bilayer. Superimposing the fiber mats prior to the addition of the epoxy matrix served to reduce the interface between the two layers. This allowed both fiber mats to be secured within a single epoxy matrix rather than gluing both laminates together, which can interfere with the composite properties or provide a site for delamination.

6.4.2 Thermal Analysis

Figure 6.2 and **Table 6-1** summarize the data obtained by DSC for the crosslinked epoxy with different targeted glass transitions temperatures, as well as the cross-ply composite in comparison with its individual components. The DSC results in **Figure 6-2A** show that by systematically decreasing the DGEBA weight fraction in the epoxy formulation, the T_g of the crosslinked epoxy decreased accordingly and was consistently within 8 °C of the predicted T_g from the Gordon-Taylor equation.²² As shown in **Figure 6-2B**, the epoxy T_g and the PCL T_m remained unchanged when combined in composite form, indicating minimal mixing of the two components. The addition of epoxy to the PCL fiber mat did not significantly alter the properties, which was consistent with a prior report from the Mather Research Group.²² Based on the relative enthalpies, the D41N59D230_PCL composite contained 15 % PCL. The PCL T_g was not

measured but is known to be ~ -60 °C.²⁵ The D41N59D230 epoxy formulation was selected in order to maximize the temperature interval between the epoxy T_g and PCL T_m , while maintaining the former above room temperature.

6.4.3 Thermomechanical Properties

The thermomechanical properties of the D41N59D230_PCL cross-ply(0) composite were characterized using dynamic mechanical analysis (DMA) and shown in **Figure 6-3**. The composite exhibited a much lower glass transition than measured by DSC of 12.0 °C, though the melting transition was 58.1 °C, as based on the loss modulus maxima. The storage modulus of the cross-ply(0) composite was approximately 100 MPa at 25 °C.

6.4.4 Quantitative Triple Shape Memory

The triple shape memory properties of the cross-ply(0) and the individual oriented single-ply samples were quantified using the DMA and the results are shown in **Figure 6-4**. The samples were temporarily fixed into two elongated shapes with different lengths, as indicated by the letters “F1” and “F2” in **Figure 6-4**, where F2 was more elongated than F1. The recovered shape is denoted by the letter “R” in **Figure 6-4**. These results validated that the oriented composites maintained their triple shape memory properties. The cross-ply(0) samples utilized a reduced strain and melting temperature protocol due to failure at larger values. The shape fixing and recovery ratios were calculated according to **Eqns. 6-3** and **6-4** and summarized in **Table 6-2**. Overall, the single-ply composite, whether unidirectional or cross-ply, exhibited good shape fixing, with excellent shape fixing results for the single layer samples with the fibers oriented in

the tensile direction. The recovery ratio was slightly lower than expected, albeit still good (~90%), and was slightly lower when the fibers were oriented longitudinally.

6.4.5 Latent Anisotropic Shape Change

The mechanical shape programming of the epoxy/PCL composite was the result of a mismatched alignment of fiber oriented laminae constructed in a cross-ply arrangement relative to the long dimension of a rectangular sample strip, where an external tensile mechanical stress was directed parallel to the long dimension. This mechanical programming and shape memory cycle sequence are outlined in **Figure 6-5** and the resulting programmed shapes are summarized in **Figure 6-6**. The sense of curvature and twisting actuation relative to fiber alignment distribution (top and bottom layers) was made possible by labeling of the samples with indication of fiber orientation of the top and bottom layers. Following recrystallization of PCL and vitrification of epoxy, the cross-ply samples remained elongated and flat upon release of the uniaxial tensile load. Upon heating to 45 °C, which was above the epoxy T_g and below the PCL T_m , the sample activated to the mechanically programmed shape of a circular bend, with the outer radius containing the longitudinally oriented fibers (capable of holding a PCL-fixed strain), and the inner radius comprising the fibers oriented perpendicular to the long dimension (relatively less capable of holding a PCL-fixed strain). A left-handed twist was formed for the cross-ply(45). When the cross-ply alignment was rotated 67.5° (cross-ply(67.5)), an angle between the cross-ply and the twist, the result was a hybrid shape comprising a twisted bend, where, similar to the cross-ply, the outer radius was composed of fibers oriented parallel to the long dimension.

The effect of the magnitude of strain on the resulting programmed shape is summarized in **Figure 6-7** for the cross-ply(0) oriented bilayer composite. It was observed that increasing the

magnitude of strain resulted in larger curvature, as expected from the increasing strain gradient, as recovered, through the thickness of the specimens. Programming strains beyond 40% could not be obtained due to fracture of samples. The cross-ply(45) samples showed a similar trend, where the degree of twisting increased with increased magnitude of strain, however the degree of pitch was difficult to characterize since the samples did not undergo complete twisting for the lengths tested. The pitch was estimated by extrapolating to a full rotation of the programmed shape and was estimated as 40 cm for a 10% strain and 11 cm for a strain of 40%. These pitch approximations were based on samples with an original width of 0.3 cm; the sample widths were reduced following tensile straining to approximately 0.25 cm for a 10% strain, and 0.21 cm for a 40 % strain.

6.4.6 Reversible Anisotropic Actuation

The method for controlling the clamping force during composite fabrication, as outlined in **Scheme 6-3**, following fiber infiltration with epoxy monomer, was postulated to increase fiber stress, volume fraction, orientation, or all of these. By using a spacer to control the thickness of the composite during curing, any lateral gradients of the factors postulated above were minimized. Further, decreasing the spacer height introduced compressive forces onto the layered fiber mats, which were wetted by the epoxy monomer; this was easily observable by the ensuing increase in area occupied by the fibers mats during clamping and described by the CF value (**Eq. 6-1**). Consequently, decreasing the thickness beyond that already occupied by the fiber mats led to an increase in the PCL content of the composites, which was quantified by comparing the relative melting endotherms using **Eq. 6-2**, measured by DSC. **Figure 6-8** further shows that as the CF value of the composite increased, the peak corresponding to the PCL melting endotherm

increased, indicating an increase in the PCL composition. These results are summarized in **Table 6-3**, which show that the PCL content ranged from 4% to 28% for the lowest to high CF values tested. It was also observed that when increasing the CF value to 2.6, samples deformed (curling, twisting or both) immediately upon being cut into a narrow rectangular strip from the larger parent composite sample. This is shown in **Figure 6-9**, which reveals that this behavior did not occur at a lower CF value. This deformed original shape was dependent on the orientation of the fibers across the bilayers, as observed in Section 6.4.5 above, with the exception that a bend or twist formed in the *opposite* direction as that of the programmed shape, and to a substantially smaller degree. For example, the as-cut strip was curled such that the inner radius comprised of fibers oriented longitudinal to the long dimension, rather than perpendicular. This slightly distorted original shape remained as the recoverable shape during actuation. We attribute this phenomenon to tensile stresses that exist in the constituent fibers during cure (which transpired below T_m) whose through-thickness gradient can distort slender samples for which the stresses are off-axis from principle directions of the specimen.

We suspected that reversible curvature and twisting actuation in the laminated composites might occur due to through-thickness gradients of anisotropic thermal expansion coefficient. Thus, free-standing thermal expansion/contraction measurements were conducted on single-ply composites oriented in the longitudinal and transverse directions and over a temperature range spanning both T_g and T_m . The results are presented in **Figure 6-10**, which was conducted for the first heating cycle. The longitudinally (0°) oriented sample exhibited a 6% tensile contraction upon melting of the PCL phase, which was mostly recovered with a slight elongation upon cooling that was likely due to PCL crystallization. This elongation may be due

to the preload tension of the clamps on the samples that is released upon melting of the PCL phase. In contrast, the orthogonally oriented sample (90°) exhibited a 3.7% expansion in tensile strain over a small temperature change, which then slowly returned upon cooling. As shown in **Figure 6-10**, these changes in tensile length occurred above the melting transition for PCL, indicating that this observed tensile contraction or elongation may be the result of the relieving of PCL stresses during melting. A future study should also measure the changes in tensile strain during the second heating cycle, since this initial influence of PCL tensile stresses would only occur in the first heating cycle and any anisotropic thermal expansion effects would be isolated in the subsequent heating cycles.

The actuation of the bilayer composite was conducted by cyclically exposing the sample to isothermal water-baths held at temperatures above ($T_{high} = 75\text{ }^{\circ}\text{C}$) and below ($T_{low} = 21\text{ }^{\circ}\text{C}$) the PCL melting transition and is portrayed in **Figures 6-11** for the cross-ply(0) and in **Figure 6-12** cross-ply(45) samples. Following an initial exposure to heat ($> \text{PCL } T_m$), the cross-ply sample began to bend in the direction opposite that which occurred during cutting of the specimens as described in reference to **Figure 6-9** above. In particular, heating caused curling *toward* the longitudinally oriented layer. Then, upon cooling to room temperature, the sample cooled away the longitudinally oriented layer. Successive actuation cycles advanced with the sample quickly bending in the inverted, as-cut shape upon re-immersion in a hot bath ($> \text{PCL } T_m$), and returning to the mechanically programmed shape at room temperature. In each cycle, the sample curled toward the longitudinal layer upon heating and in the opposite direction – toward the perpendicular layer upon cooling.

Reversible twisting was observed during thermal cycling of the cross-ply(45) sample. The sample began the cycle with an as-cut inverted left-handed (flattened) twist at room temperature that reversed in its twisting sense to a right-handed twisted ribbon after one cycle of heat heating ($> \text{PCL } T_m$) and cooling back to room temperature. Thereafter, this shape remained the equilibrium, “return” shape at room temperature. Actuation proceeded by the sample reversibly twisting between a right-handed ribbon in hot water ($> \text{PCL } T_m$), and the left-handed ribbon (as mechanically programmed) upon cooling to room temperature. Both the cross-ply(0) and cross-ply (45) were observed to reversibly actuate for at least 10 consecutive cycles, which was counted as beginning after the initial heat exposure (Cycle 0), which was distinct from all subsequent cycles. The radius of curvature was measured for the cross-ply sample for 10 cycles and is summarized in **Figure 6-13**, where no significant loss of shape was observed by the tenth cycle, although more repetitions should be conducted. The reversible twisting was not quantified due to technical limitations related to characterizing the complex shapes formed.

6.5 Discussion

In this chapter, we systematically altered the microstructure of an epoxy/PCL bilayer composite to influence the shape change outcome. The newly generated shapes were investigated and their dependences on the introduced strain and relative fiber orientations between laminae were studied. Additionally, an apparently new mechanical actuation mechanism for reversible curling and twisting of strips was discovered and characterized in a proof-of-concept manner.

To introduce anisotropy into a reinforced shape memory composite aligned electrospun PCL fibers were embedded within a crosslinked epoxy matrix. Two fiber mats were layered with orthogonal orientations between the plies prior to infiltration with the epoxy monomer. This

yielded bilayer composites with anisotropic properties in each layer and orientational orthogonality through the thickness. Further, variation in the principle axis of a parallelepiped strip and the orientation directions was accomplished. By assembling fibrous preforms before epoxy infiltration (rather than assembling plies already infiltrated with epoxy) use of an adhesive tie layer between the two laminae was obviated. This, in turn, prevented delamination and preserved pristine shape changing mechanics unaltered by the intervening layer. The angle formed between the fiber direction of the top and bottom fiber layers was systematically varied. The crosslinked epoxy was customized to target a glass transition temperature between room temperature and the PCL melting transition by adjusting the weight fractions of the reactants according to the Gordon-Taylor equation previously used to fit data for the same system, similar to prior work studied within the Mather research group.²² We hypothesized that positioning the glass transition within this range would enable typical temporary shape fixing of the composite, while the mechanically programmed shape remained dormant. The resulting thermal properties revealed distinctly separate thermal transitions without overlap of the thermal regimes.

The mechanical shape programming of the epoxy/PCL composite was the result of a mismatched alignment of oriented laminae constructed in a cross-ply arrangement relative to the long dimension of the a rectangular sample strip, where an external tensile mechanical stress was directed parallel to the long dimension. The phenomena of introducing mismatched strain into e bending or wrinkling is well known²⁶ This mismatching was maximal for the cross-ply(0) and triggered under a temperature change, where differences in the coefficient of thermal expansion (CTE) led to reversible bending or twisting of the composite. By introducing a uniaxial stress into two or more mismatched layers restricted by each other, residual stresses are introduced in

the layers that are then relieved by morphing into non-flat, 3D structures.²⁷ Possessing this shape change provides an advantage over previous approaches in that it broadens the applicability to include on-demand usability.

Unlike other anisotropic bilayer systems, the mechanical shape change in the PCL/epoxy composite remained dormant until thermally triggered and was also capable of retaining an arbitrary temporary shape until such activation, in part due to its inherent triple shape memory property.²² A temporary shape was established by first melting the fibrous phase and uniaxially straining the composite. Subsequent slow recrystallization of the fibers while maintaining the epoxy above its T_g was then followed by room temperature vitrification of the matrix to stabilize the fixed shape. In this temporary fixed state, the crystallized PCL fibers and vitrified epoxy (mainly the latter) maintained an arbitrary temporary shape, which was an elongated strip in this study; however, unlike traditional shape memory, internal directional stresses were stored in the composite as a result of the orthogonal anisotropy between the laminae. A mechanically programmed bend was then activated by thermally triggering the epoxy phase at a temperature between T_g and T_m in order to maintain the crystallized form of PCL. By doing so, we postulated that the compliant state of the epoxy, which was the abundant weight fraction of the composite, permitted relief of the internal stresses by allowing a curl to form preferentially toward the layer containing fibers perpendicular to the long axis. We surmised that this fiber arrangement caused local shrinkage of the epoxy near the fibers on the inside of the bend, through biased recovery of the epoxy strain, and that the outer surface exerted tensile strain. The extent of this bending was found to depend on the magnitude of strain imposed during temporary shape fixing, as manifested in the radius of curvature, where increasing the strain increased the curvature. Upon

further heating to temperature above both the epoxy T_g and fiber T_m , the sample recovered back to its original flat 2D shape and length, as was expected of a shape memory polymer.

In addition to the bending behavior of the composite, mechanical programming of a twist was also achieved. Twisting of the bilayer composite was the result of orienting the cross-ply fiber arrangement 45° relative to the long axis of the sample. The twist shape was mechanically programmed in the same manner described above for the bend shape, and remained dormant until heat exposure. Upon thermal activation, the top and bottom lamellar residual stresses were relieved in opposing orthogonal directions, thus forming a twist.²⁸ Additional angles were also investigated (**Figure 6-6**), where an angle between the 90° and 45° relative to the long axis of the sample showed an evolving shape hybrid of a bend and twist, revealing the potential for other complex shapes such as helices or combinations of bends and twists, which will be further studied in the future. Although not investigated in this study, we surmised that the handedness of the twist can be switched by mirroring the cutting angle of the cross-ply relative to the sample dimensions.

The reversible actuation behavior of the mechanically programmed geometries was achieved by incorporating additional internal stresses into the anisotropic bilayer composite during fabrication. More specifically, external compressive forces, as defined by CF (**Eqn. 6-1**), were imposed on the fibrous laminae by increasing the clamping force used to construct the composite (**Scheme 6-4**). A slip condition between the PCL fiber/epoxy monomer liquid assembly and the mold surfaces was evident, facilitating stretching of the PCL fibers while the assembly was squeezed and prior to the crosslinking reaction. Furthermore, we postulated that the residual stresses incurred during the epoxy crosslinking reaction likely contributed to

additional compression at the fiber interface due to chemical shrinkage.²⁹ We hypothesized that the epoxy CTE was greater in the direction orthogonal to the PCL fibers, with no strong dependence on PCL melting or crystallization. These combined effects on the fibrous phase promoted the internal stresses that served to further strain and align the percolating channels occupied by the fibers within the epoxy matrix. Consequently, the restricted geometry of these channels likely supported the crystal orientation recovery, and may even serve as a template for oriented recrystallization during thermal cycling.³⁰ Moreover, it has been reported in the literature that polymer crystal nucleation tends to proceed parallel to the surface of the substrate, which would be the strained anisotropic channels, in our case.³¹ We attributed the cyclic melting and cooling of the PCL crystalline domains within the anisotropic channels as driving the actuation, where upon melting of the PCL crystals, directional contraction occurred, whereas during cooling, the confined recrystallization induced anisotropic expansion. This recrystallization within conflicting pathways among the bilayers led to reversible restoration of the mechanically programmed bend or twist observed in the non-actuating samples above.

The concept of reversible actuation directed by anisotropic crystallizable domains was previously investigated by Behl et al. in semicrystalline copolymers exhibiting very broad melting transitions ($\sim\Delta T_m$ over 65 °C),³² however, in contrast to our system, the actuation in those copolymers was controlled by polymer chain expansion during melting and contraction during crystallization. Bothe et al., on the other hand, developed a polyurethane elastomer that exhibited this very phenomena in the crystalline domains, which was applied to thermally triggered actuation.³³ That system, however, was limited to simple bidirectional shape change and required thermomechanical training of the polymer before actuation can be stimulated. Other

examples using this type of driving mechanism use shape memory materials that are also limited to simpler shape changes.³⁴ Unlike other systems, the PCL used in this composite was not crosslinked,³⁵ and complete melting of the fibrous phase was established through exposure well above T_m . This provision further confirmed that partial melting was not driving actuation as had been observed in other crystallizable thermosets exhibiting reversible actuation.³⁶ The reversible actuation for the PCL/epoxy composite was found to proceed over multiple cycles without diminishing curvature and appeared to be limited by the elected the number of testing cycles (**Figure 6-12**). Additional studies on the crystalline morphologies and actuation properties should be investigated in future work.

6.6 Conclusions

In this work, mechanically programmable 3D shapes were produced by introducing anisotropy into an epoxy/PCL bilayer composite. These mechanically programmed shapes remained dormant until thermally triggered. The prominence of these shapes depended on the magnitude of the imposed strain used to program these shapes. We also demonstrated reversible thermal actuation of the composite between its equilibrium and mechanically programmed shapes around the PCL melting transition. This actuation behavior was activated upon the increase of stored stresses of the fibrous phase imparted during composite fabrication. We hypothesized that this actuation was driven by the melt-induced expansion and oriented recrystallization generated contraction of the PCL crystalline domains within the composite.

6.7 References

1. Wulfsberg, J., Herrmann, A., Ziegmann, G., Lonsdorfer, G., Stoess, N. & Fette, M. Combination of carbon fibre sheet moulding compound and prepreg compression moulding in aerospace industry. *Procedia Engineering* **81**, 1601 (2014).
2. Friedrich, K. & Almajid, A. A. Manufacturing aspects of advanced polymer composites for automotive applications. *Applied Composite Materials* **20**, 107 (2013).
3. Vasiliev, V. V., Barynin, V. A. & Razin, A. F. Anisogrid composite lattice structures—Development and aerospace applications. *Composite Structures* **94**, 1117 (2012).
4. Zhang, J., Chaisombat, K., He, S. & Wang, C. H. Hybrid composite laminates reinforced with glass/carbon woven fabrics for lightweight load bearing structures. *Materials & Design* **36**, 75 (2012).
5. Diddens, I., Murphy, B., Krisch, M. & Muller, M. Anisotropic elastic properties of cellulose measured using inelastic X-ray scattering. *Macromolecules* **41**, 9755 (2008).
6. Netti, P., D'amore, A., Ronca, D. & Ambrosio, L. Structure-mechanical properties relationship of natural tendons and ligaments. *Journal of Materials Science: Materials in Medicine* **7**, 525 (1996).
7. Holzapfel, G. A., Gasser, T. C. & Ogden, R. W. A new constitutive framework for arterial wall mechanics and a comparative study of material models. *Journal of elasticity and the physical science of solids* **61**, 1 (2000).
8. Lin, A., Meyers, M. A. & Vecchio, K. S. Mechanical properties and structure of *Strombus gigas*, *Tridacna gigas*, and *Haliotis rufescens* sea shells: a comparative study. *Materials Science and Engineering: C* **26**, 1380 (2006).
9. Swadener, J. G., Rho, J. Y. & Pharr, G. M. Effects of anisotropy on elastic moduli measured by nanoindentation in human tibial cortical bone. *Journal of Biomedical Materials Research* **57**, 108 (2001).
10. Chen, P. Y., Lin, A., Lin, Y. S., Seki, Y., Stokes, A. G., Peyras, J., Olevsky, E.A., Meyers, M.A. & McKittrick, J. Structure and mechanical properties of selected biological materials. *Journal of the Mechanical Behavior of Biomedical Materials* **1**, 208 (2008).
11. Woltman, S. J., Jay, G. D. & Crawford, G. P. Liquid-crystal materials find a new order in biomedical applications. *Nature Materials* **6**, 929 (2007).
12. Gloria, A., Ronca, D., Russo, T., D'Amora, U., Chierchia, M., De Santis, R., Nicolais, L. & Ambrosio, L. Technical features and criteria in designing fiber-reinforced composite

materials: from the aerospace and aeronautical field to biomedical applications. *Journal of Applied Biomaterials & Functional Materials* **9**, 151 (2011).

13. Chen, P. Y., McKittrick, J. & Meyers, M. A. Biological materials: functional adaptations and bioinspired designs. *Progress in Materials Science* **57**, 1492 (2012).

14. Meyers, M. A., McKittrick, J. & Chen, P. Y. Structural biological materials: critical mechanics-materials connections. *Science* **339**, 773 (2013).

15. Burgert, I. & Fratzl, P. Plants control the properties and actuation of their organs through the orientation of cellulose fibrils in their cell walls. *Integrative and Comparative Biology* **49**, 69 (2009).

16. Reyssat, E. & Mahadevan, L. Hygromorphs: from pine cones to biomimetic bilayers. *Journal of the Royal Society Interface* **6**, 951 (2009).

17. Armon, S., Efrati, E., Kupferman, R. & Sharon, E. Geometry and mechanics in the opening of chiral seed pods. *Science* **333**, 1726 (2011).

18. Mather, P.T., Luo, X. & Rousseau, I.A. Shape Memory Polymer Research. *Annual Review of Materials Research* **39**, 445 (2009).

19. Lendlein, A., Jiang, H., Jünger, O. & Langer, R. Light-induced shape-memory polymers. *Nature* **434**, 879 (2005).

20. Lee, K. M., Bunning, T. J. & White, T. J. Autonomous, hands-free shape memory in glassy, liquid crystalline polymer networks. *Advanced Materials* **24**, 0935 (2012).

21. Robertson, J. M., Torbati, A. H., Rodriguez, E. D., Mao, Y., Baker, R.M., Qi, H.J. & Mather, P.T. Mechanically programmed shape change in laminated elastomeric composites. *Soft Matter* **11**, 5754 (2015).

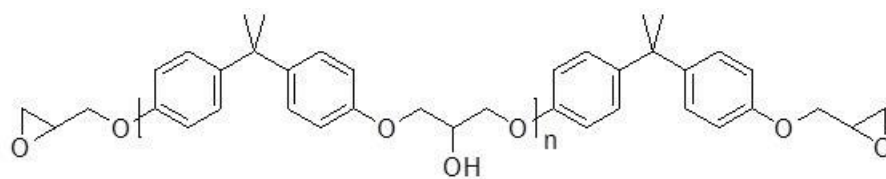
22. Luo, X. & Mather, P. T. Triple-shape polymeric composites (TSPCs). *Advanced Functional Materials* **20**, 2649 (2010).

23. Xie, T. & Rousseau, I. A. Facile tailoring of thermal transition temperatures of epoxy shape memory polymers. *Polymer* **50**, 1852 (2009).

24. Chung, T. & Romo, A. Two-way reversible shape memory in a semicrystalline network. *Macromolecules* **41**, 184 (2008).

25. Hutmacher, D. W., Schantz, T., Zein, I., Ng, K.W., Teoh, S.H. & Tan, K.C. Mechanical properties and cell cultural response of polycaprolactone scaffolds designed and fabricated via fused deposition modeling. *Journal of Biomedical Materials Research* **55**, 1097 (2001).

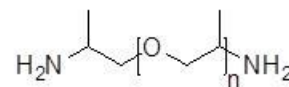
26. Chen, Z., Huang, G., Trase, I., Han, X. & Mei, Y. Mechanical self-assembly of a strain-engineered flexible layer: wrinkling, rolling, and twisting. *Physical Review Applied* **5**, 017001 (2016).
27. Chun, I. S., Challa, A., Derickson, B., Hsia, K. J. & Li, X. Geometry effect on the strain-induced self-rolling of semiconductor membranes. *Nano Letters* **10**, 3927 (2010).
28. Seo, D. K., Kang, T. J., Kim, D. W. & Kim, Y. H. Twistable and bendable actuator: a CNT/polymer sandwich structure driven by thermal gradient. *Nanotechnology* **23**, 075501 (2012).
29. Russell, J. D., Madhukar, M. S., Genidy, M.S. & Lee, A.Y. A new method to reduce cure-induced stresses in thermoset polymer composites, part III: correlating stress history to viscosity, degree of cure, and cure shrinkage. *Journal of Composite Materials* **34**, 1926 (2000).
30. Cauda, V., Torre, B., Falqui, A., Canavese, G., Stassi, S., Bein, T. & Pizzi, M. Confinement in oriented mesopores induces piezoelectric behavior of polymeric nanowires. *Chemistry of Materials* **24**, 4215 (2012).
31. Hu, Z., Baralia, G., Bayot, V., Gohy, J. F. & Jonas, A. M. Nanoscale control of polymer crystallization by nanoimprint lithography. *Nano Letters* **5**, 1738 (2005).
32. Behl, M., Kratz, K., Noechel, U., Sauter, T. & Lendlein, A. Temperature-memory polymer actuators. *Proceedings of the National Academy of Sciences* **110**, 12555 (2013).
33. Bothe, M. & Pretsch, T. Bidirectional actuation of a thermoplastic polyurethane elastomer. *Journal of Materials Chemistry A* **1**, 14491 (2013).
34. Li, J., Rodgers, W. R. & Xie, T. Semi-crystalline two-way shape memory elastomer. *Polymer* **52**, 5320 (2011).
35. Stroganov, V., Al-Hussein, M., Sommer, J.U., Janke, A., Zakharchenko, S. & Ionov, L. Reversible thermosensitive biodegradable polymeric actuators based on confined crystallization. *Nano Letters* **15**, 1786 (2015).
36. Zotzmann, J., Behl, M., Hofmann, D. & Lendlein, A. Reversible Triple-Shape Effect of Polymer Networks Containing Polypentadecalactone- and Poly (ϵ -caprolactone)-Segments. *Advanced Materials* **22**, 3424 (2010).



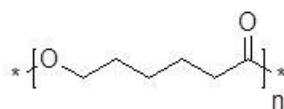
Diglycidyl ether of bisphenol A (DGEBA)



**Neopentyl glycol diglycidyl ether
(NDGE)**

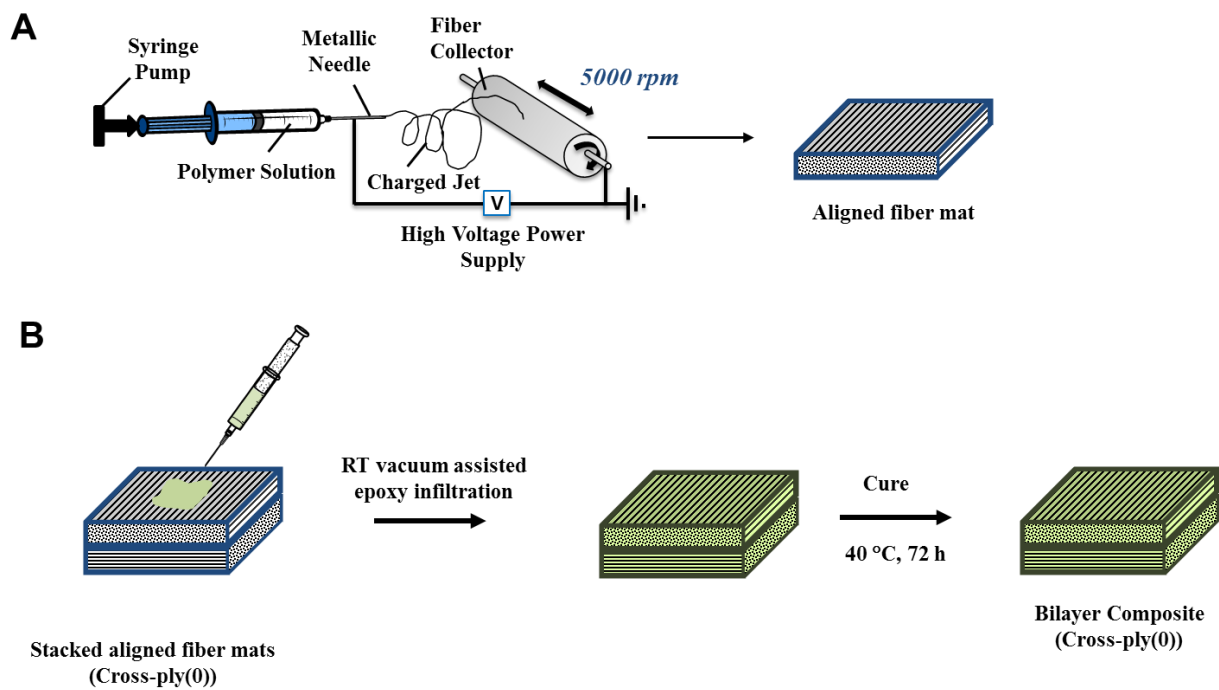


Jeffamine D230

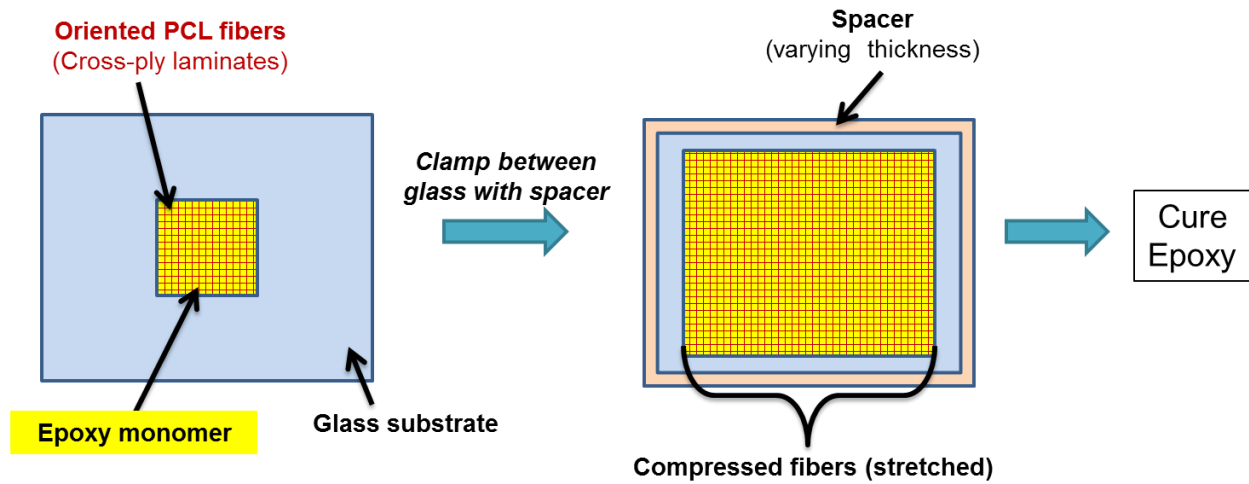


Poly(ε-caprolactone)

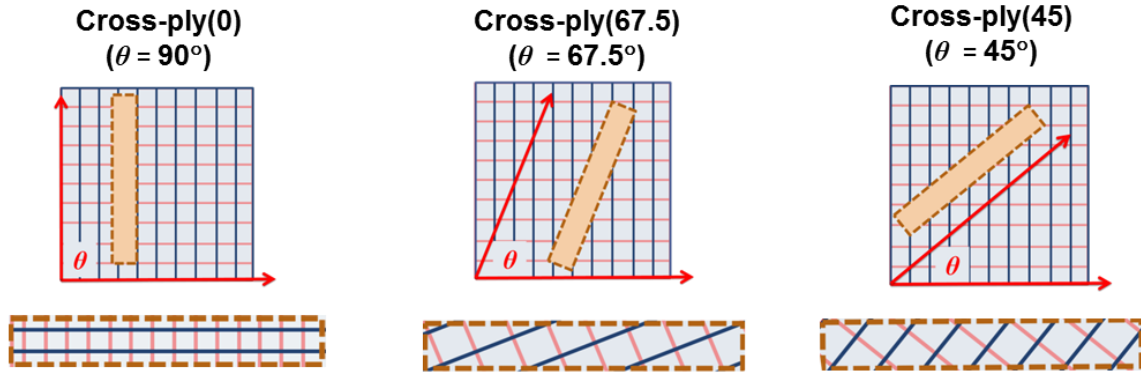
Scheme 6-1. The chemical structures of the epoxy components and PCL used to fabricate the PCL/epoxy composite.



Scheme 6-2. Fabrication of the bilayer anisotropic epoxy-PCL composite by (A) first electrospinning aligned PCL fibers followed by (B) infiltration of aligned PCL fiber mats in the cross-ply(0) orientation.



Scheme 6-3. Method for controlling clamping force by varying the spacer thickness during epoxy/PCL composite fabrication.



Scheme 6-4. Various cutting angles (top row) of rectangular samples (bottom row) used to mechanically program 3D shapes. The blue lines correspond to the fiber direction of the top layer and the red lines were maintained on the bottom layer.

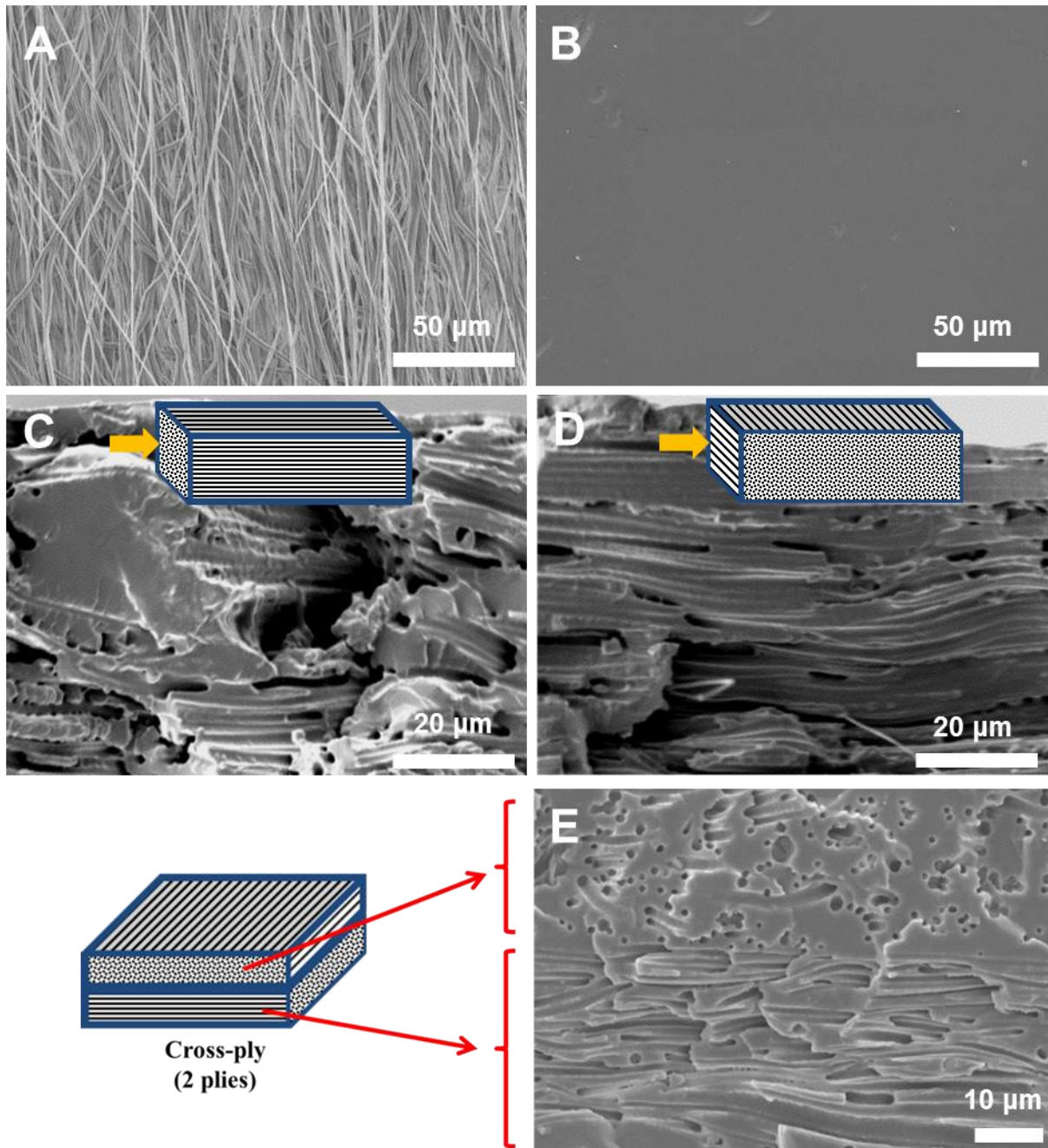


Figure 6-1. Representative SEM micrographs of the (A) aligned electrospun PCL fibers, (B) PCL/epoxy composite surface, (C) cross-section of the single-ply composite with fibers aligned longitudinally (0° to long dimension), (D) cross-section of the single-ply composite with fibers aligned perpendicular (90° to long dimension), and (E) cross-section of the cross-ply(0) bilayer composite. The micrographs in (B) – (E) were visualized following removal of the PCL phase.

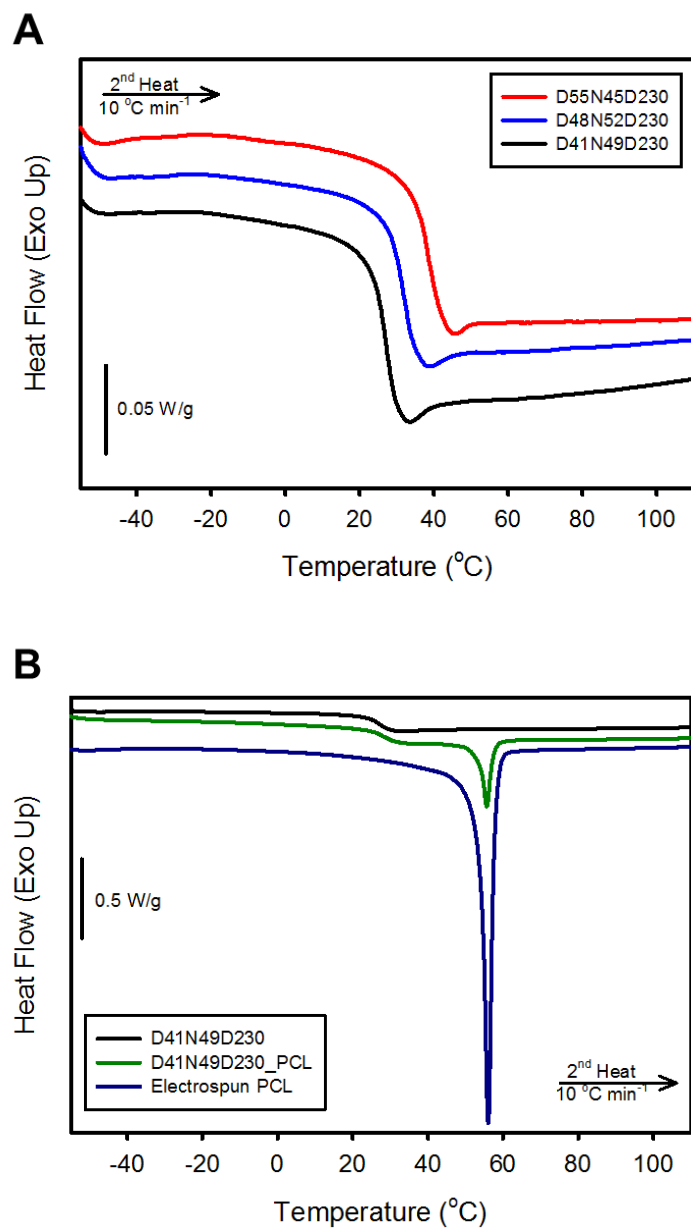


Figure 6-2. DSC thermograms of (A) the crosslinked epoxy using different relative weight fractions of DGEBA and NDGE, and (B) the PCL/epoxy composite and its individual components.

Table 6-1. Thermal transitions of the different crosslinked epoxy formulations, the epoxy/PCL composite and the electrospun PCL component. All measurements were taken from the second heating cycle. *NM* denotes not measured and *N/A* means not applicable.

Formulation	Target T_g (°C)	T_g (°C)	T_m (°C)
D55N45D230	45	38.2	<i>N/A</i>
D48N52D230	40	31.9	<i>N/A</i>
D41N59D230	35	27.2	<i>N/A</i>
D41N59D230_PCL (Cross-ply(0))	35	27.9	55.7
Electrospun PCL	<i>N/A</i>	<i>NM</i>	56.1

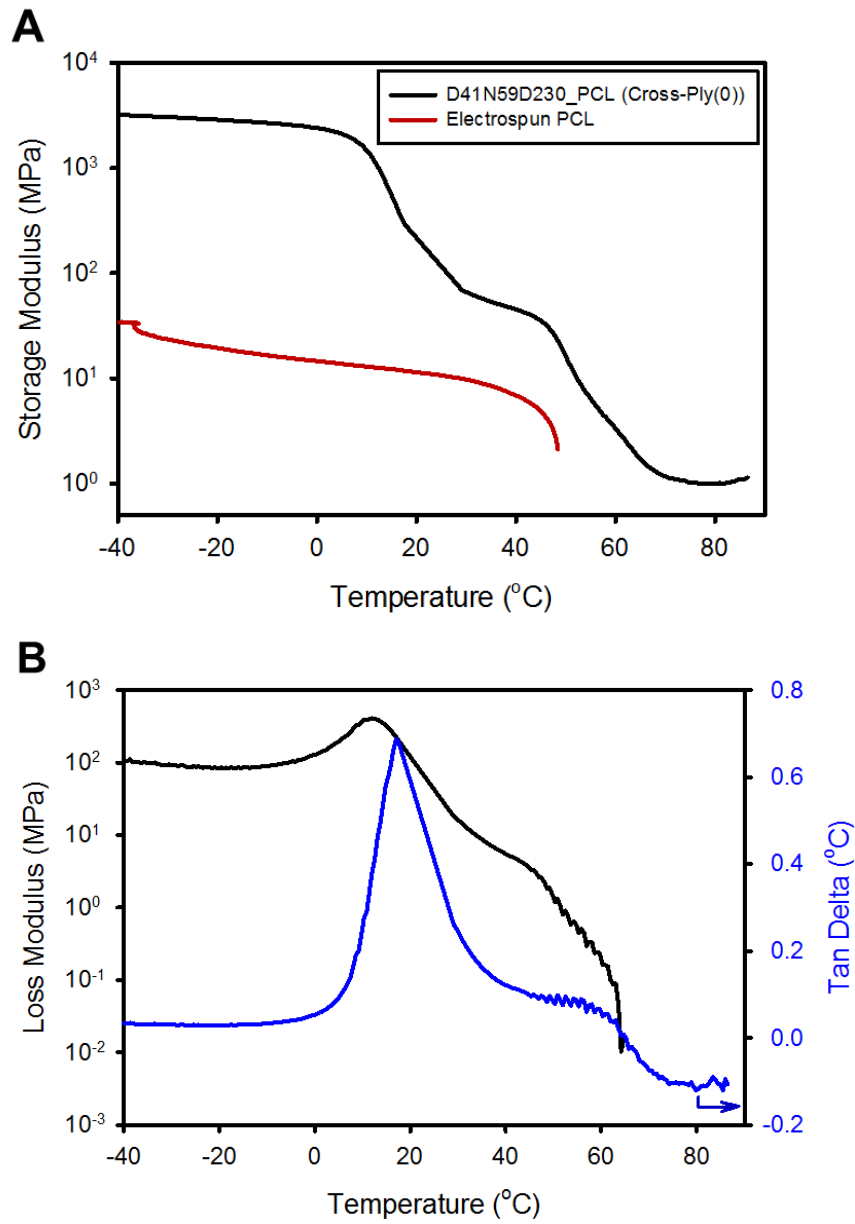
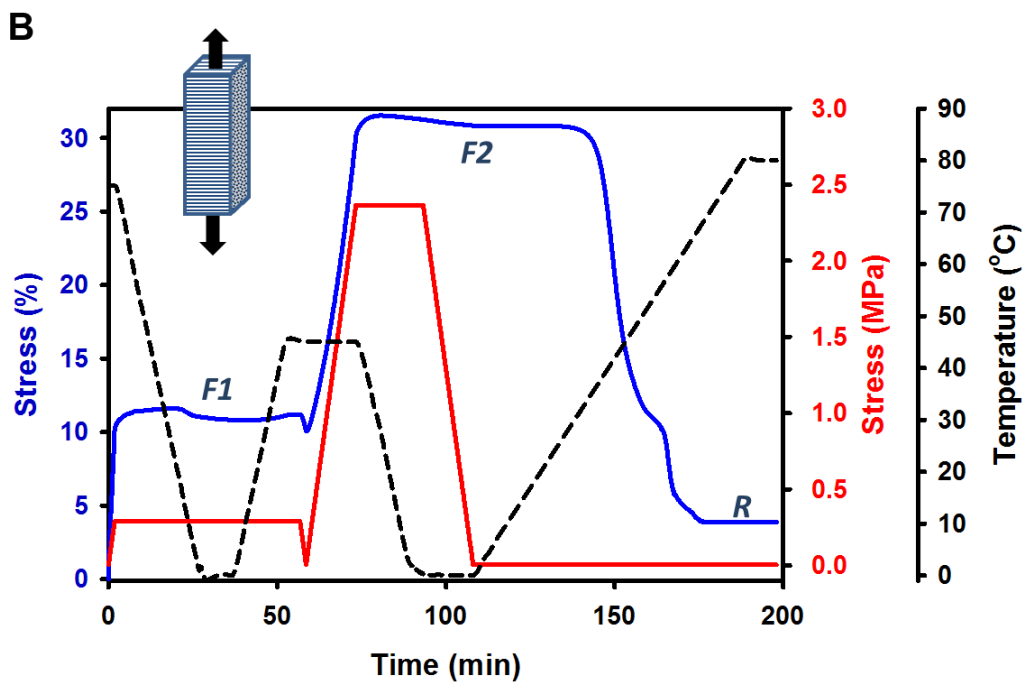
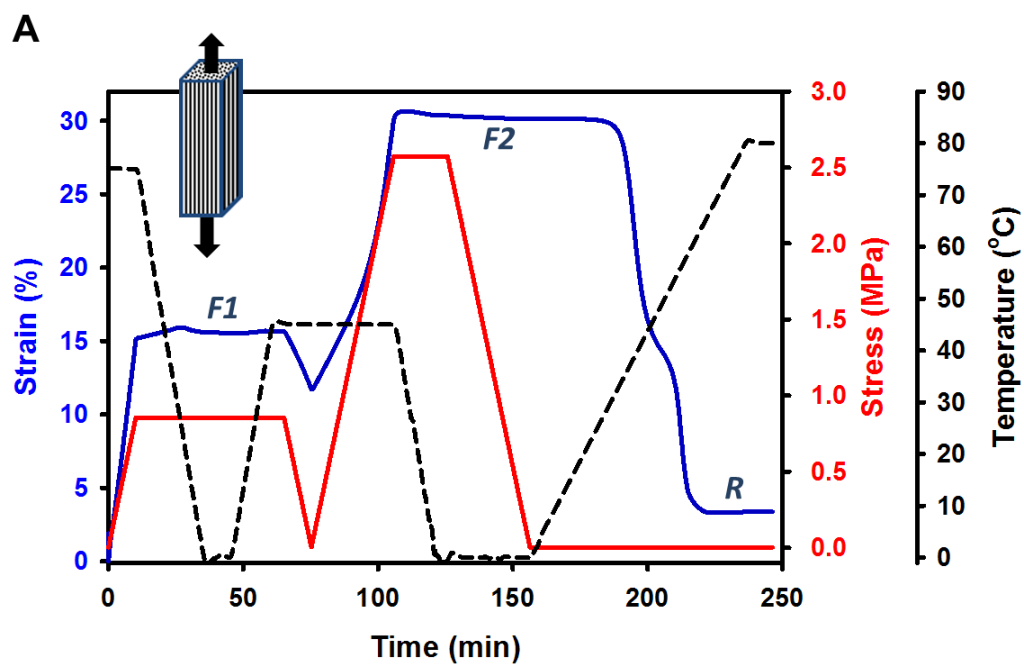


Figure 6-3. Thermomechanical characterization of the D41N59D230 epoxy/PCL cross-ply(0) composite fabricated using a compression factor of 1.1 showing (A) the storage modulus and (B) the loss modulus and tan delta.



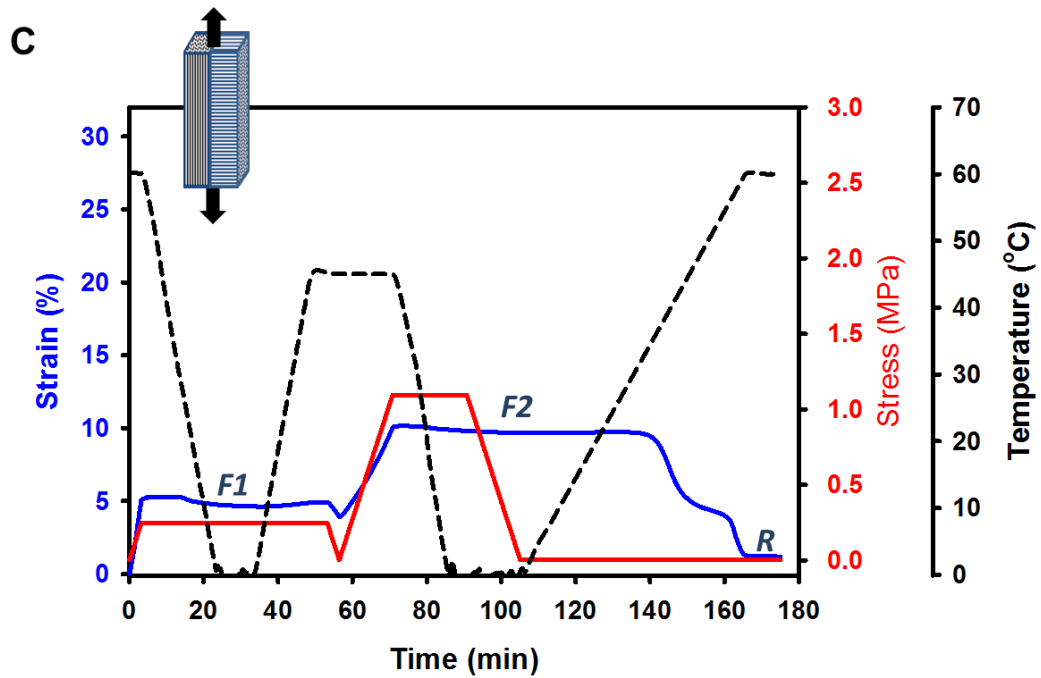


Figure 6-4. Triple shape memory quantification of the epoxy/PCL composite (A) single-ply with fibers oriented parallel to the uniaxial strain (0°), (B) single-ply with fibers oriented perpendicular to the uniaxial strain (90°), and (C) the cross-ply(0) bilayer composite. The annotations denote the first fixed shape (F1), second fixed shape (F2) and the recovered shape (R).

Table 6-2. Fixing and recovery ratios for the triple shape memory quantification of the epoxy/PCL composite as single-ply with fibers oriented parallel to the uniaxial strain (0°) or perpendicular to the uniaxial strain (90°), and the cross-ply(0) bilayer composite.

Sample	$R_{f,1}$ (%)	$R_{f,2}$ (%)	R_r (%)
0° Fiber Alignment (Single-ply)	99.8	99.6	79.0
90° Fiber Alignment (Single-ply)	90.8	97.1	87.4
Cross-ply(0) (Bilayer)	92.8	95.6	87.8

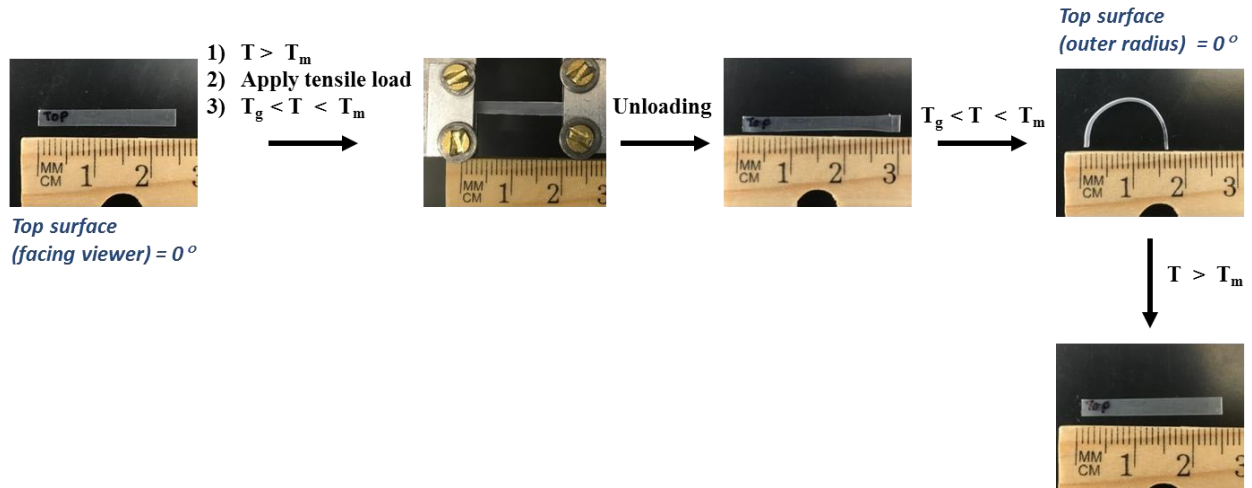


Figure 6-5. Example of mechanical shape programming sequence with shape recovery (shown for the cross-ply(0) composite), where 0° refers to the layer containing longitudinally oriented fibers.

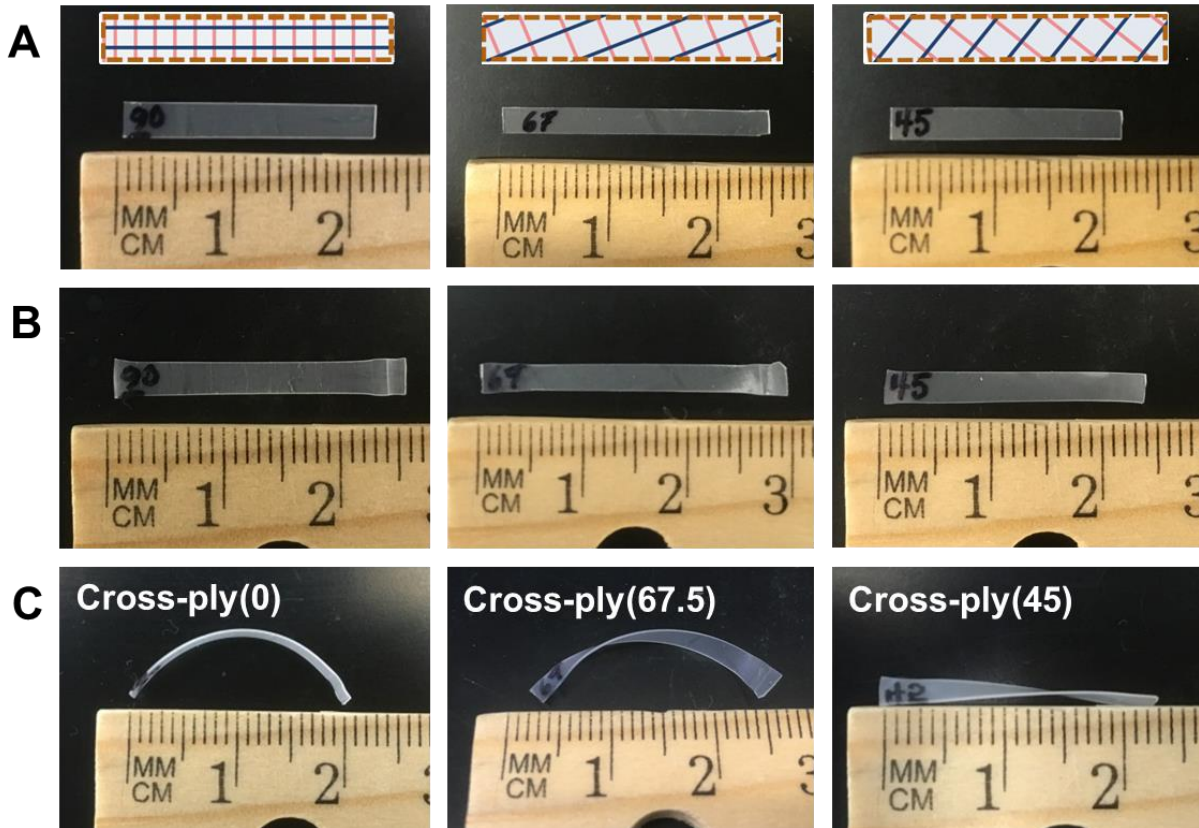


Figure 6-6. Various fiber orientations between the top and bottom fibrous phases within the composite and resulting shapes. (Row A) original shape with fiber orientation depiction (blue = top layer/red = bottom layer) (Row B) and original shapes (Row C) temporary fixed shape

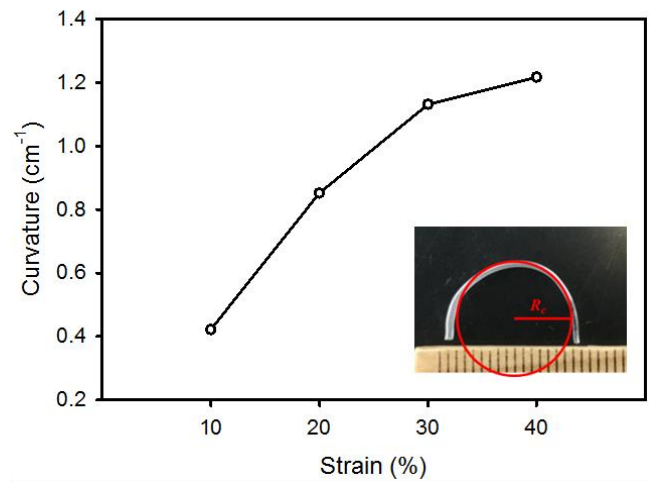
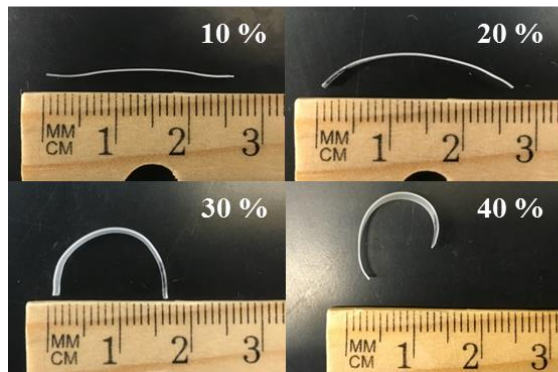


Figure 6-7. Effect of strain during mechanical shape programming on the cross-ply(0) composite.

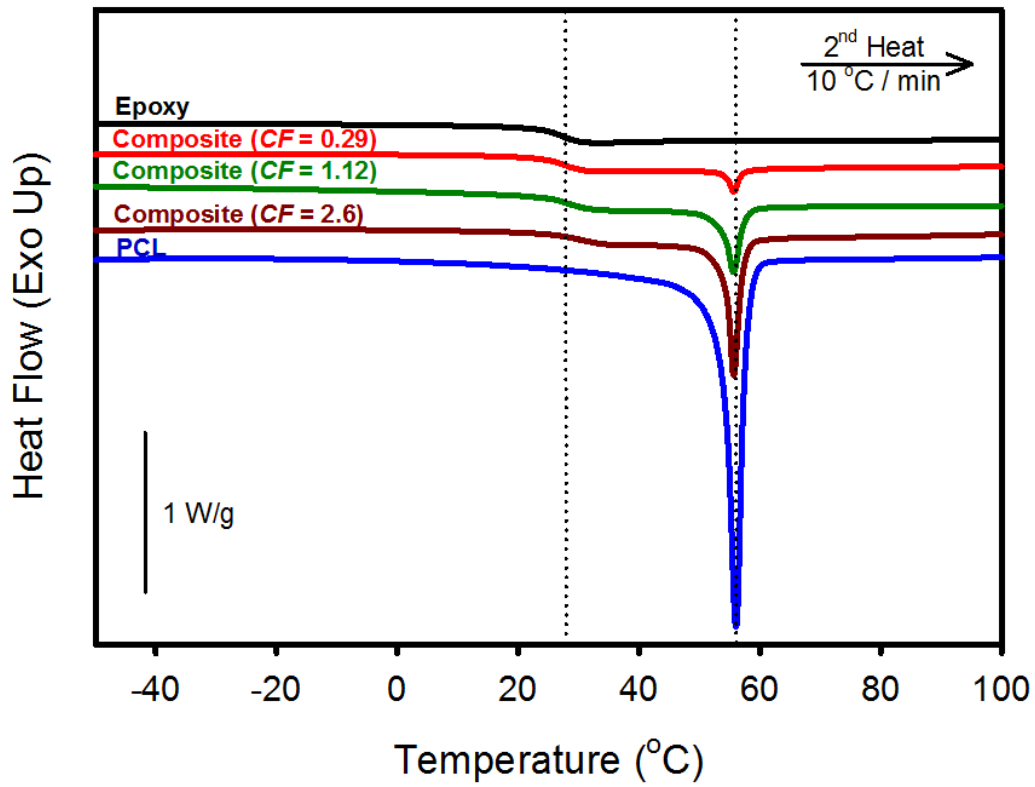


Figure 6-8. DSC thermograms for epoxy/PCL cross-ply(0) composites fabricated using different compression factors.

Table 6-3. Thermal characterizations for epoxy/PCL composites fabricated using different compression factors. *NM* denotes not measured and *N/A* means not applicable.

Compression Factor	T_g (°C)	T_m (°C)	ΔH (J/g)	Amount of PCL (%)
0.29	27.8	55.6	1.8	4%
1.12	27.9	55.7	7.6	15%
2.60	29.5	55.7	13.7	28%
Epoxy	27.1	<i>N/A</i>	<i>N/A</i>	<i>N/A</i>
PCL Fibers	<i>NM</i>	56.1	49.7	100%

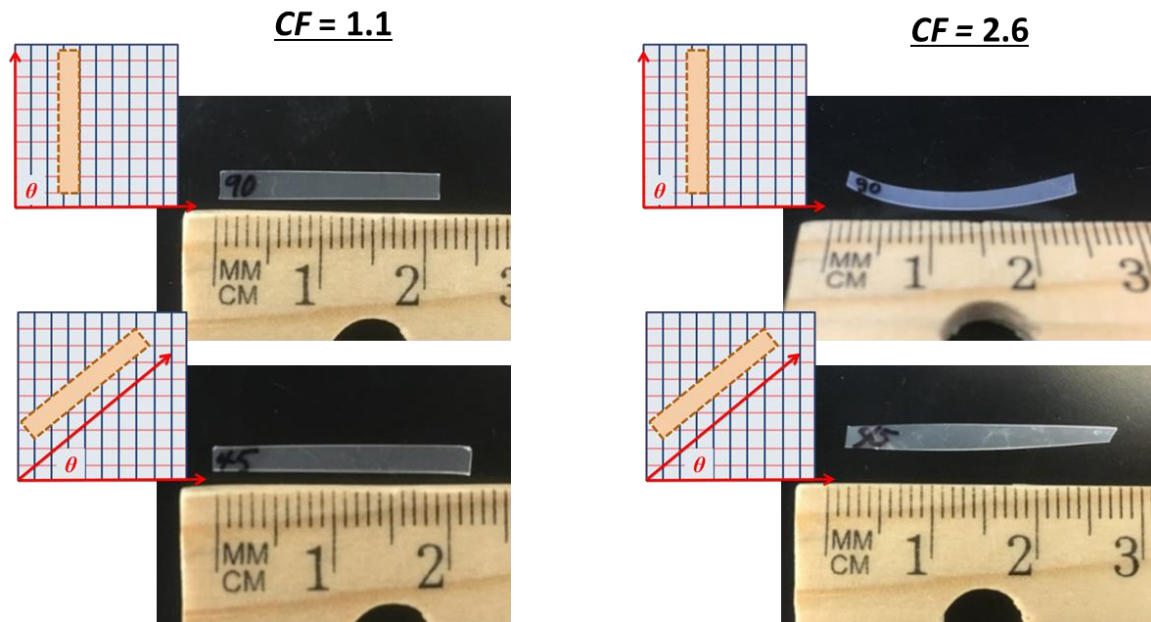


Figure 6-9. Upon increasing the compression factor (CF) of the fiber mats within the composites, the samples begin to immediately change shape when strips are cut from the parent composite batch. The fiber orientation is depicted such that the blue vertical lines are the top layer and the red horizontal lines indicate the bottom layer)

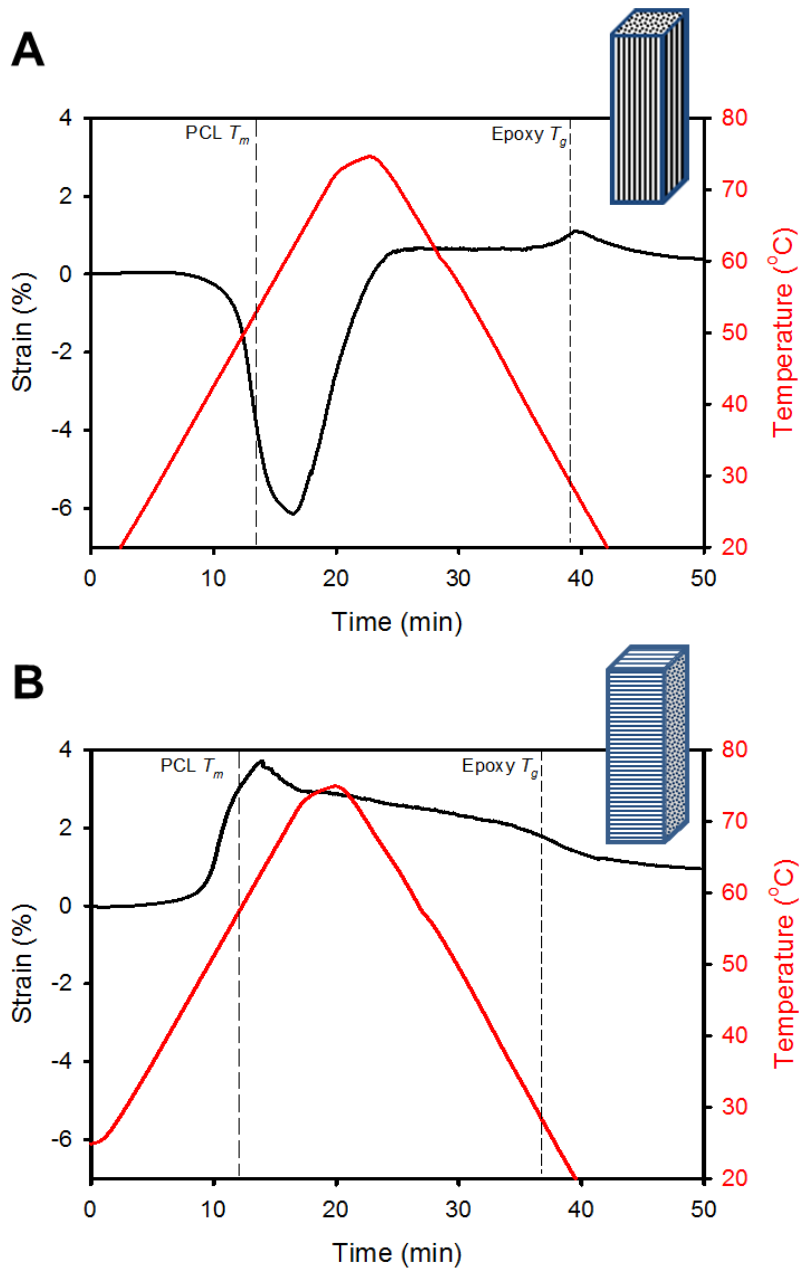


Figure 6-10. Stress-free strain of single-ply oriented epoxy/PCL composites in response to heating and cooling for fiber alignment oriented (A) longitudinal and (B) perpendicular to the long axis.

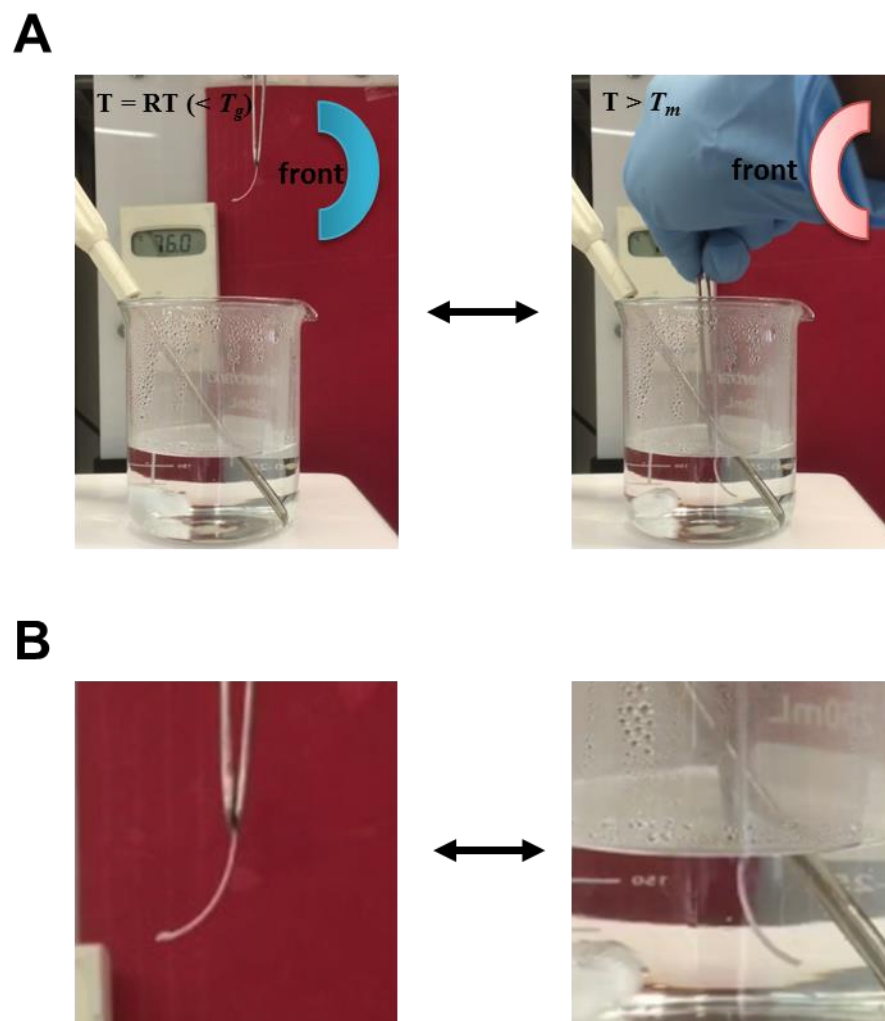


Figure 6-11. Actuation behavior of the epoxy/PCL bilayer composites upon thermal cycling with the cross-ply(0) sample showing the (A) testing set-up and (B) magnification of the samples during actuation.

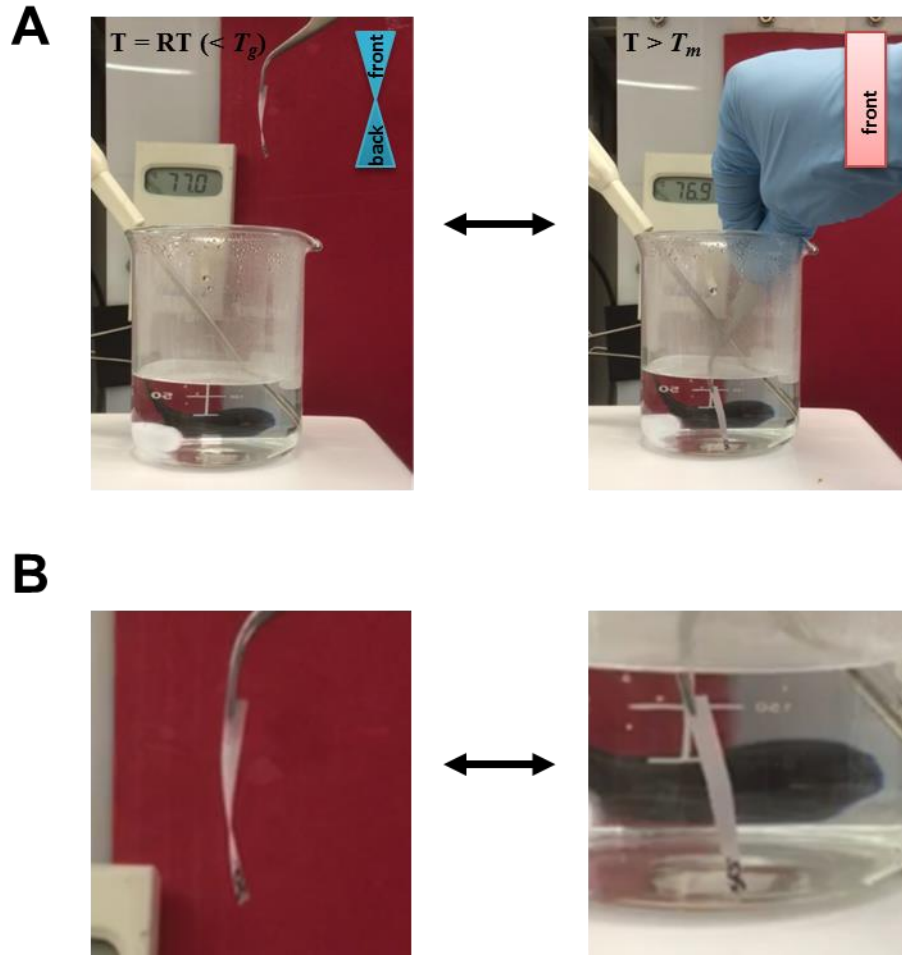


Figure 6-12. Actuation behavior of the epoxy/PCL bilayer composites upon thermal cycling with the cross-ply(45) sample showing the (A) testing set-up and (B) magnification of the samples during actuation.

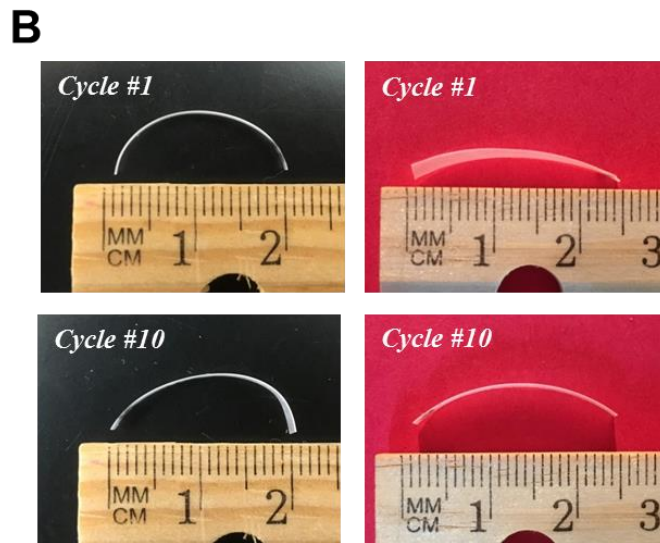
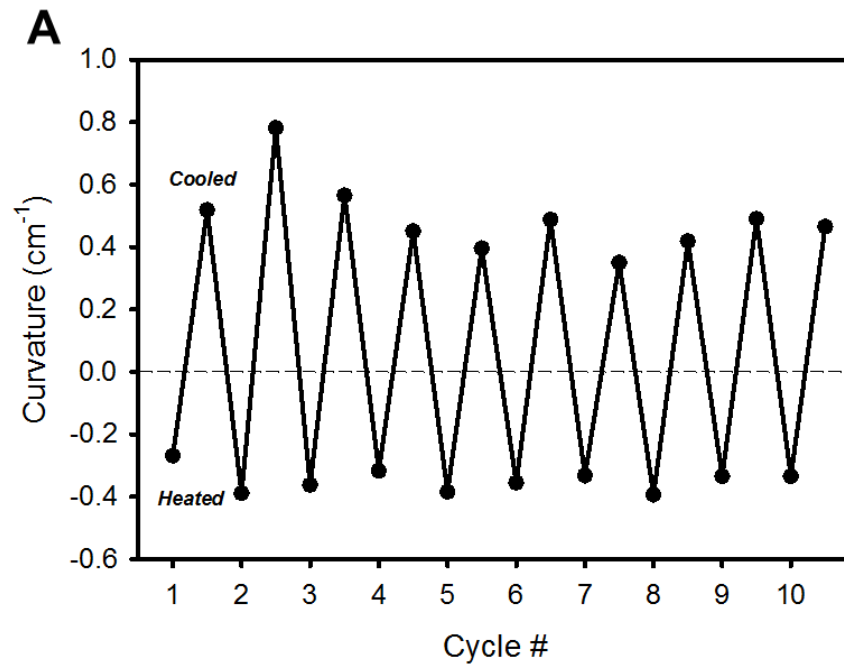


Figure 6-13. (A) Curvature of the cross-ply(0) bilayer epoxy/PCL composite after 10 consecutive actuation cycles for the shape at room temperature (cooled) and the shape upon heating. (B) Representative photos of the shape change under cooling (left column) and heating (right column) conditions. The curvature of the heated activated shape was opposite to that of the cooled shape, as indicated by the negative curvature value.

Chapter 7

Conclusions & Future Work

7.1 Overall Conclusions

This dissertation examined the design, development and characterization of electrospun shape memory polymeric composites with tailorable properties for various applications. Several features were designed into these composites including one way shape memory, controlled drug delivery, reconfigurable shape memory, degradation, latent mechanical programming and reversible actuation.

In **Chapters 2** and **3**, a drug molecule was combined with PCL and then electrospun into fibers that were then embedded within a PDMS matrix. The *in vitro* controlled release characteristics of two different hydrophilic drugs in PBS under physiological conditions were investigated. In both chapters, the addition of the PDMS elastomer served to control the initial burst release as well as extend and improve overall drug release. **Chapter 2** demonstrated controlled release of a hydrophilic model drug, Rhodamine B, and it was ascertained that the crystallinity of the fibers had a greater effect on the drug release than did the size of the fibers, such that the crystallization mechanism guided drug release. We attributed this behavior to phase separation of the hydrophilic drug within the hydrophobic PCL fiber that either expelled the drug to the fiber surface during fiber formation or toward the fiber core during post-electrospinning crystallization. Furthermore, we postulated that the addition of the PDMS elastomer displaced air occupying the voids within the fiber mats, thus enabling further release of buried drug due to additional aqueous contact with the fibers. The tensile mechanical properties of this composite

demonstrated usefulness for soft material applications owing to its elasticity, low modulus, and multi-stage load bearing response typically associated with native soft tissues.

Encouraged by the results in **Chapter 2**, the work in **Chapter 3** extended the development of the PCL/PDMS composite for use as a small diameter synthetic vascular graft. A nitric oxide (NO) releasing donor compound was added to the PCL fibrous phase and controlled release of NO was demonstrated for over ten weeks. Here, it was observed that increasing the concentration of the hydrophilic NO donor molecule reduced drug release on a percentage basis, which we attributed to the phase separation effect between the drug and the PCL fiber carrier. This composite exhibited good suture retention characteristics that were comparable to native blood vessels, and a burst pressure strength that exceeded commercially available options. The NO-releasing composite also demonstrated good cytotoxicity when using a reduced concentration of the tin catalyst employed to crosslink the PDMS matrix, with no impact on the tensile mechanical properties. The addition of the NO donor compound counteracted both the catalytic activity and cell toxicity caused by the catalyst. The NO-releasing composite also promoted significant endothelial cell migration, which was revealed using an *in vitro* chemotaxis assay. We expect that this composite material is a good candidate for blood vessel prosthetics such as AV or bypass grafts where long term mechanical and anti-thrombogenic properties are desired.

In **Chapter 4**, a new shape memory composite was developed by substituting the PDMS component with a crosslinked PAH to make a fully degradable and biocompatible composite. We determined that coupling these materials in this manner gave rise to reconfigurable shape memory such that the original shape can be permanently altered due to dynamic covalent

exchange between the anhydride groups. The use of a PCL thermoplastic urethane enabled one way shape memory to be implemented without interference with the permanent reconfiguration programming, owing to its relatively low melting point. Additionally, since shape memory occurs at physiological temperatures, the potential exists for many biomedical applications such as degradable implants with deploying mechanisms, self-healing applications, and dynamic surfaces for tissue engineering.

The degradation properties of the reconfigurable composite developed in **Chapter 4** were explored in **Chapter 5**, where two different electrospun fiber compositions were separately embedded in crosslinked PAH. The degradation of the polyanhydride matrix was dependent on the composition of the fibrous phase, where erosion proceeded more rapidly when the composite contained the more hydrophobic PCL fibers compared to hygroscopic, amorphous PVAc, since PVAc competed with the degrading PAH for water. The presence of a fibrous structure infiltrating through the PAH film altered the erosion dynamics from heterogeneous to homogenous. PAH continued to remain on the fibers as a protective sheath for both composite compositions. It was determined that the PVAc fibers were plasticized by the PAH, which remained in the fibers, and this resulted in prolonged degradation and enhanced the duration of sustained drug delivery of hydrophilic model drug Rhodamine B. The drug releasing properties of this composite would be advantageous for infection management following surgical intervention or minimizing thrombosis on the surface of an implant. This composite possesses tailorable degradation, reconfigurable shape memory, controlled drug release, and long-term shape retention and can thus provide an enabling technology with broad biomedical applications such as smart implants and tissue engineering scaffolds.

Lastly, in **Chapter 6**, mechanically programmable 3D shapes were produced by introducing anisotropy into an epoxy/PCL bilayer composite. These mechanically programmed shapes remained dormant until thermally triggered. The distinction of these shapes depended on increasing the magnitude of the imposed strain used to program these shapes. Reversible thermal actuation of the composite was also demonstrated between its equilibrium and mechanically programmed shapes around the PCL melting transition. This actuation behavior was activated upon the increase of stored stresses of the fibrous phase imparted during composite fabrication. We hypothesized that this actuation was driven by the melt-induced expansion and oriented recrystallization-generated contraction of the PCL crystalline domains within the composite. The new composite materials can have broad applications in artificial muscles, hinges, sensors, and robotics.

7.2 Future Directions

7.2.1 Shape Memory Elastomeric Composite with Controlled Drug Release of a Hydrophilic

Drug Model

The drug releasing SMEC system developed and characterized in **Chapter 2** focused only on release of a hydrophilic model drug. This particular composite system lends itself well to studying other types of drug molecules by mixing with PCL prior to electrospinning. The drug releasing capabilities of this composite can be expanded to include release of other water-soluble drugs with varying hydrophilicities such as acetaminophen, an anti-inflammatory agent. Additional work can also be conducted using hydrophobic drugs such as dexamethasone and ketoprofen, both of which are useful anti-inflammatory agents. Even more interesting would be the ability to release two drugs, each with independent release. This can be achieved by co-

spinning two PCL solutions, each containing a different drug followed by imbibing with the siloxane matrix. This approach would promote controlled mixing of the drug populations and even mediate gradient concentrations through the fiber mat cross-section. For example, a combination of two anticancer drugs, doxorubicin hydrochloride and paclitaxel can provide an enhanced therapeutic effect.¹ We anticipate slower or more incomplete release of hydrophobic drugs in the PCL/PDMS composite due to the greater solubility between the drug and the composite materials. To account for this, the hydrophilicity of the fibrous phase can be adjusted by substituting with electrospun PCL copolymerized with poly(ethylene glycol) (PEG) and a chain extender to create a PCL-PEG multi-block copolymer thermoplastic polyurethane (TPU). This TPU has been previously developed in the Mather Research group for shape memory.² PEG is a widely studied hydrophilic biocompatible polymer that can be used to conduct a series of PCL-PEG compositions with gradually increasing PEG content until a desired drug release rate is reached. Considering that PEG is also crystalline, competing crystallization patterns between PCL and PEG may yield interesting interactions with the encapsulated drug than was reported in **Chapter 2**. Furthermore, more than one fibrous composition can be co-spun such that differences in hydrophobicity would gate drug release such that in the case of a single drug, one polymer can provide immediate drug release while the other can engage in late stage drug release.

Alternatively, co-spinning of PCL with Pellethane 5863–80A (Lubrizol), an aromatic polyether thermoplastic polyurethane elastomer could allow for a variety of drug releasing options. This SMEC was previously developed for its shape memory properties, however, drug release was not studied.³ Here, Pellethane would replace PCL as the fibrous phase while

electrospun PCL would become the matrix following hot pressing the fiber mat above the PCL melting transition. Some initial work was conducted that supported the feasibility of this system, as shown in **Figure 7-1**, where controlled release of RhB was observed. Additional work is required to study the weight fraction, microstructural and morphological effects of this composite composition in comparison to the PDMS-based one. Pellethane was determined to absorb considerably more water than PDMS, as shown in **Figure 7-2**. As such, we expect that RhB release would be quicker; however, the crystalline PCL matrix could counter that quicker release by providing a physical barrier to water uptake to the Pellethane channels due to its poor water absorption properties. In a separate study, the drug can be added to the Pellethane phase rather than the PCL matrix. Additionally, another way to combine Pellethane with PCL would be by coaxial electrospinning of these polymers, which to our knowledge, has not been done before. In this arrangement, PCL can contain RhB and serve as the core that is encapsulated in a Pellethane sheath, rather than in a non-porous matrix. Beyond drug release, this composite morphology can potentially lead to interesting mechanical properties since it would retain a fully fibrous format and thus be a good candidate for tissue engineering applications.

7.2.2 Nitric Oxide Releasing Shape Memory Elastomeric Composite for Vascular Graft Applications

The application of the drug release SMEC system in **Chapter 2** was also studied specific to vascular graft development. As suggested in Section 7.2.1, dual spinning of an additional fibrous population containing another drug can yield some useful effects. Specific to this endeavor, other drugs shown to aid in preventing thrombosis such as heparin or an antiplatelet agent such as aspirin can be electrospun in combination with electrospun DETA-NO/PCL or

similar material to extend drug release benefits. Aspirin has been studied for this application in combination with electrospun PCL and demonstrated a promising reduction in platelet adhesion, however, the effect was short term of up to ~ 2 d.⁴ Additional application specific evaluations could be considered for the DETA-NO/PCL/PDMS composite such as hemocompatibility assessment. An initial study was conducted in collaboration with Dr. Eric Finkelstein and REU student Emily Mihalko. PCL/PDMS samples both with and without DETA-NO were placed in contact with whole human blood and the clotting time and hemolysis assays were evaluated according to established protocols.⁵ **Figure 7-3** reveals promising results, where the NO releasing samples showed a slight reduction in clotting compared to the control groups. This work can be expanded by adjusting the DETA-NO concentration and conducting a platelet adhesion assay according to methods prescribed in the literature.^{6,7} Lastly, further optimization of the *in vitro* chemotaxis study in **Chapter 3**, can be conducted utilizing a co-culture of both the smooth muscle cells and endothelial cells to better simulate *in vivo* conditions and capture any synergistic effects between the two cell populations and NO releasing materials. Also, considering that NO is a natural antimicrobial, the antimicrobial activity of the NO-releasing PCL/PDMS composites can be studied to assess the infection resistant potential of this composite.⁸

7.2.3 Anhydride-Based Reconfigurable Shape Memory Elastomeric Composite

The results in **Chapter 4** indicated that the reconfigurable nature of the PAH anhydride groups may be exploited for developing re-moldable thermoset materials and self-healing of cracks or fractures through heating of select PAH surfaces. **Figure 7-4A** shows the potential of remolding crosslinked PAH cubical pellets into a larger object. This was accomplished by

applying a force and heat above the reconfiguration temperature in a mold substrate. Additional work to further this concept would include optimizing the molding process to improve the moldability of small features as well as characterization of the material properties following molding. Similarly, in **Figure 7-4B**, the PAH/PCL Re-SMEC exhibited similar abilities, with the ability to be recycled following grinding into a film. The resulting morphology would no longer contain percolating fibers. The newly blended, molded material morphology would need to be investigated alongside the post-molding mechanical and shape memory properties. The effect of the volume fraction of PCL should be determined, where it is anticipated that an upper limit could be reached such that the presence of PCL may interfere with shape memory if the PAH continuity through the sample volume is significantly disrupted. **Figure 7-5** further shows healing potential of a composite containing PAH, where two fragmented pieces of the PCL/PAH composite are repaired following coupling of the pieces under pressure and heat. The reverse plasticity shape memory should be quantified and optimized by varying the relative fractions of the composite constituents or composition of the fibrous phase. Additionally, the shape memory of an embossed surface can be studied to determine the minimum resolution and its dependence on the PAH fraction in the composite. The degradability of an embossed feature in the surface may be useful for studying cell-material interactions under dynamic surfaces or even altered drug releasing properties through the increased macroscopic surface areas.

7.2.4 Biodegradable Shape Memory Elastomeric Composites with Controlled Model Drug

Release of a Model Drug

Additional degradation work can be conducted to complete the degradation of the PCL/PAH composite through enzymatic degradation of PCL, which would also liberate any

remaining drug molecules. The substitution of Pellethane as the fibrous phase in combination with the PAH matrix could prompt a different type of shape memory effect in a fully elastomeric composite. Specifically, the PAH matrix can be used to fix a temporary shape through the thermally reconfigurable bond exchange mechanisms, while the Pellethane fibers would serve to remember the original/permanent shape. Shape recovery would then proceed by degradation of the PAH using methods described in **Chapter 5**. A feasibility study was conducted, in collaboration with Tackla S. Winston, that revealed the possibility of this type of shape memory, as depicted in **Figure 7-6**, where a rectangular strip of electrospun Pellethane imbued by PAH was shaped into a curl and the original flat geometry was recovered following degradation of the PAH matrix. While immersed in PBS at 37 °C, the curled shape unfolded back into the rectangular strip within 24 h, while the composite visually reverted to the original opaqueness of the electrospun Pellethane fiber mat. SEM of the degraded composite verified the preservation of the Pellethane fibrous morphology as well as the absence of the PAH matrix following a 24 h degradation induced shape recovery cycle. Additional work to complete this investigation includes quantification of a temporary shape over degradation time (i.e. radius of curvature evolution for a curled shape), effect of fiber volume fraction, mechanical and thermal characterizations as well as thermomechanical quantification of the new composite and controlled drug release can be explored. We also anticipate that quick drug release for a hydrophilic drug would occur due to the combined effects of PAH degradation and the greater water absorption properties for Pellethane, as described in Section 7.2.1.

7.2.5 Latent Mechanical Programming of a Shape Memory Composite with Reversible Anisotropic Actuation

The programmed shapes studied in **Chapter 6** were fabricated using a bilayer composite containing a cross-ply orientation that was varied relative to the direction of mechanical strain. Future work can include varying the orientations of the fibers with respect to each other as well as combining additional anisotropic lamina for multilayer composites with a goal of producing latent programming of complex shapes. Complex shapes can also result from gradient mechanical programming of the bilayer composites at different orientations. With the innate delayed shape triggering only activated by temperature, a temperature gradient can also be introduced such that the hotter end of a strip will express a tighter curl or twist that would gradually decrease in magnitude until it reaches the position below the thermal activation temperature. Since the epoxy/PCL composite is a tough material (**Appendix A1**), it has the potential to apply a force and manipulate an external object such as by pushing or lifting. We would expect the direction and range of motion to depend on the programmed shape. **Figure 7-7** demonstrates the ability of a flat strip to lift a 20 mm x 20 mm glass cover slip upon thermal activation into the bend shape. Further studies are needed to quantify the mass ratio limit that this composite can displace an object and the ability to tune that limit. Moreover, the thermally reversible actuation mechanisms can also be engaged to manipulate external objects. The development of more complex shapes as described above will also enable more complex actuation movement. Lastly, the shape dependence on the fiber orientations and mechanical programming can be modeled to predict the resulting shapes.

7.3 References

1. Xu, X., Chen, X., Wang, Z. & Jing, X. Ultrafine PEG–PLA fibers loaded with both paclitaxel and doxorubicin hydrochloride and their in vitro cytotoxicity. *European Journal of Pharmaceutics and Biopharmaceutics* **72**, 18 (2009).
2. Gu, X. & Mather, P. T. Entanglement-based shape memory polyurethanes: Synthesis and characterization. *Polymer* **53**, 5924 (2012).
3. Robertson, J. M., Nejad, H. B. & Mather, P. T. Dual-spun shape memory elastomeric composites. *ACS Macro Letters* **4**, 436 (2015).
4. Del Gaudio, C., Ercolani, E., Galloni, P. & Santilli, F. Aspirin-loaded electrospun poly (ϵ -caprolactone) tubular scaffolds: potential small-diameter vascular grafts for thrombosis prevention. *Journal of Materials Science: Materials in Medicine* **24**, 523 (2013).
5. Punnakitikashem, P., Truong, D., Menon, J. U. & Nguyen, K. T. Electrospun biodegradable elastic polyurethane scaffolds with dipyridamole release for small diameter vascular grafts. *Acta biomaterialia* **10**, 4618 (2014).
6. Frank, R. D., Dresbach, H. & Thelen, H. Glutardialdehyde induced fluorescence technique (GIFT): A new method for the imaging of platelet adhesion on biomaterials. *Journal of Biomedical Materials Research* **52**, 374 (2000).
7. Bohl, K. S. & West, J. L. Nitric oxide-generating polymers reduce platelet adhesion and smooth muscle cell proliferation. *Biomaterials* **21**, 2273 (2000).
8. Nablo, B. J. & Schoenfisch, M. H. Antibacterial properties of nitric oxide–releasing sol-gels. *Journal of Biomedical Materials Research Part A* **67**, 1276 (2003).

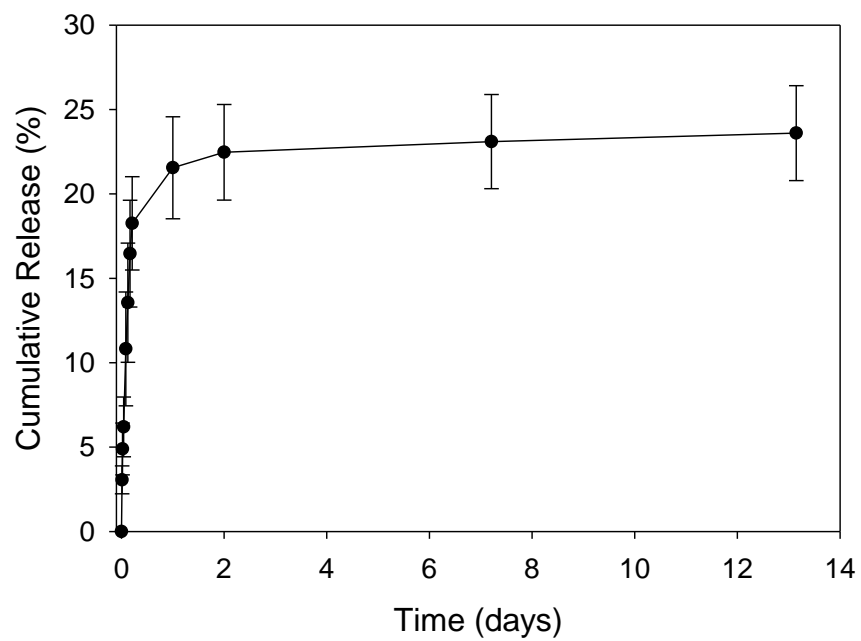


Figure 7-1. Cumulative release of RhB from PCL/Pellethane composite. RhB diffusion originated from the PCL matrix.

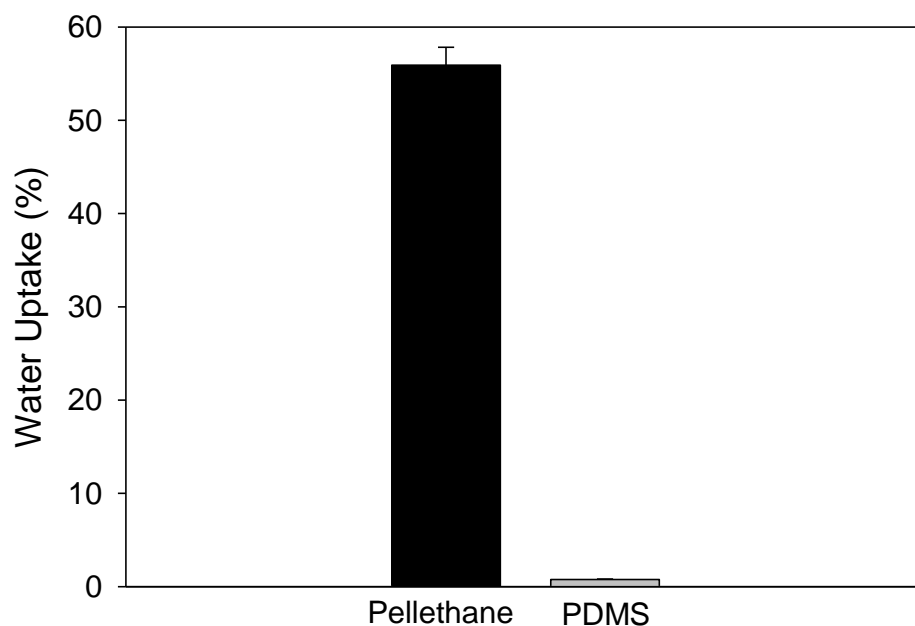


Figure 7-2. Water uptake comparison between electrospun Pellethane and crosslinked silanol-terminated PDMS film following 24 h immersion in water. Sample size of three per group was used. The water uptake was calculated by dividing the difference in the mass of the wet and dried samples by the mass of the dried sample.

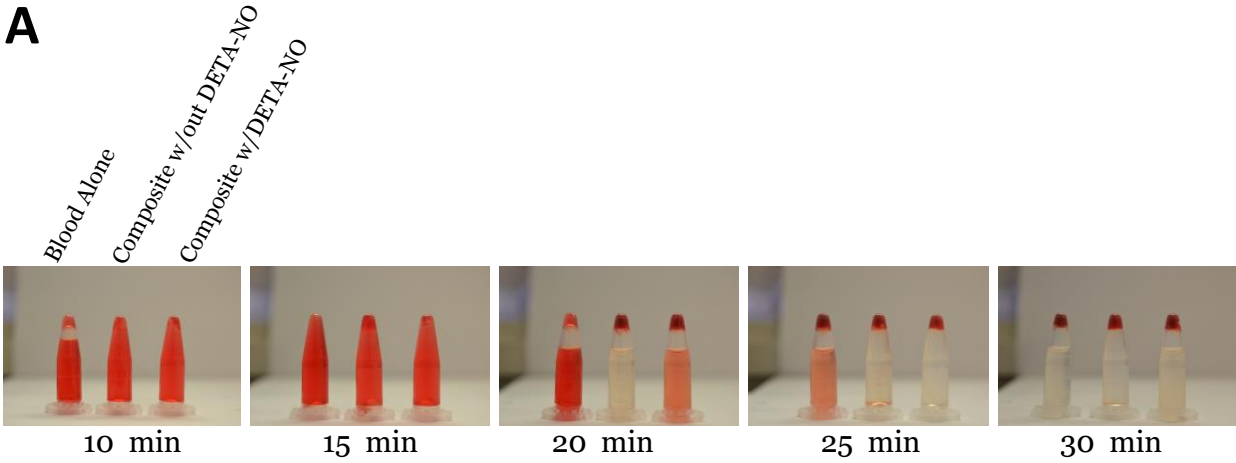
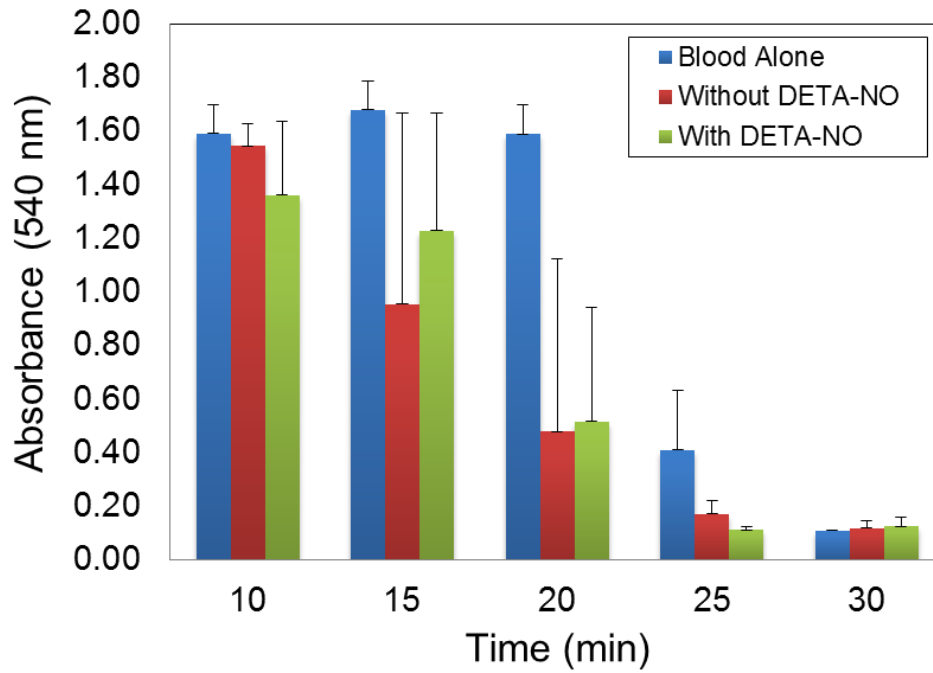
A**B**

Figure 7-3. Results of hemolysis assay showing (A) photos of human blood clot formation over time comparing blood exposure to no samples (blood alone), the PCL/PDMS composite without drug, and the DETA-NO/PCL/PDMS composite, and (B) lysate absorbance values from the clotting assay.

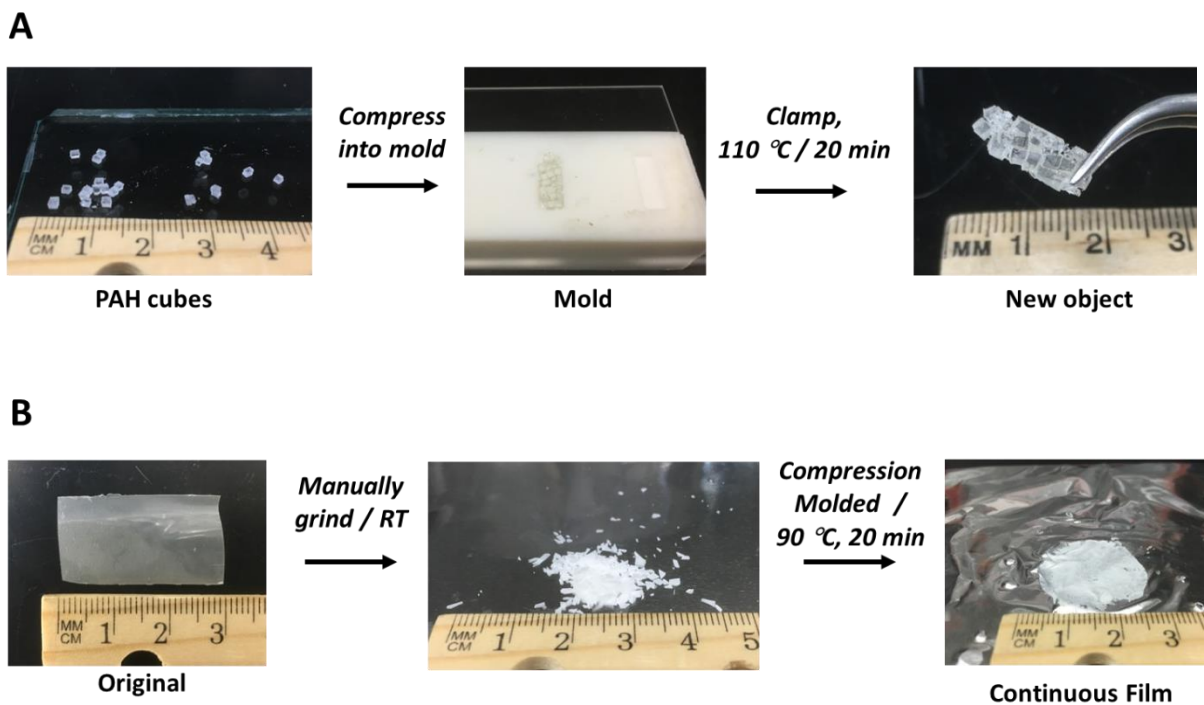


Figure 7-4. Feasibility of remolding PAH-based materials following grinding. (A) A crosslinked PAH film is cut into small cubes that are then compression molded into a single object, and (B) the PAH/PCL composite is grinded and then compression molded into a film.

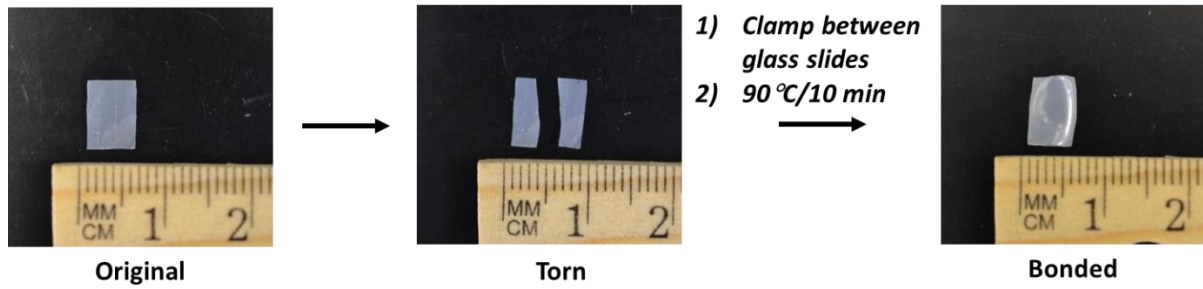


Figure 7-5. Healing potential of the PAH/PCL composite. A rectangular sample is fragmented into two pieces and then repaired back into a single piece following applying heat and pressure to the fractured surfaces under constant contact.

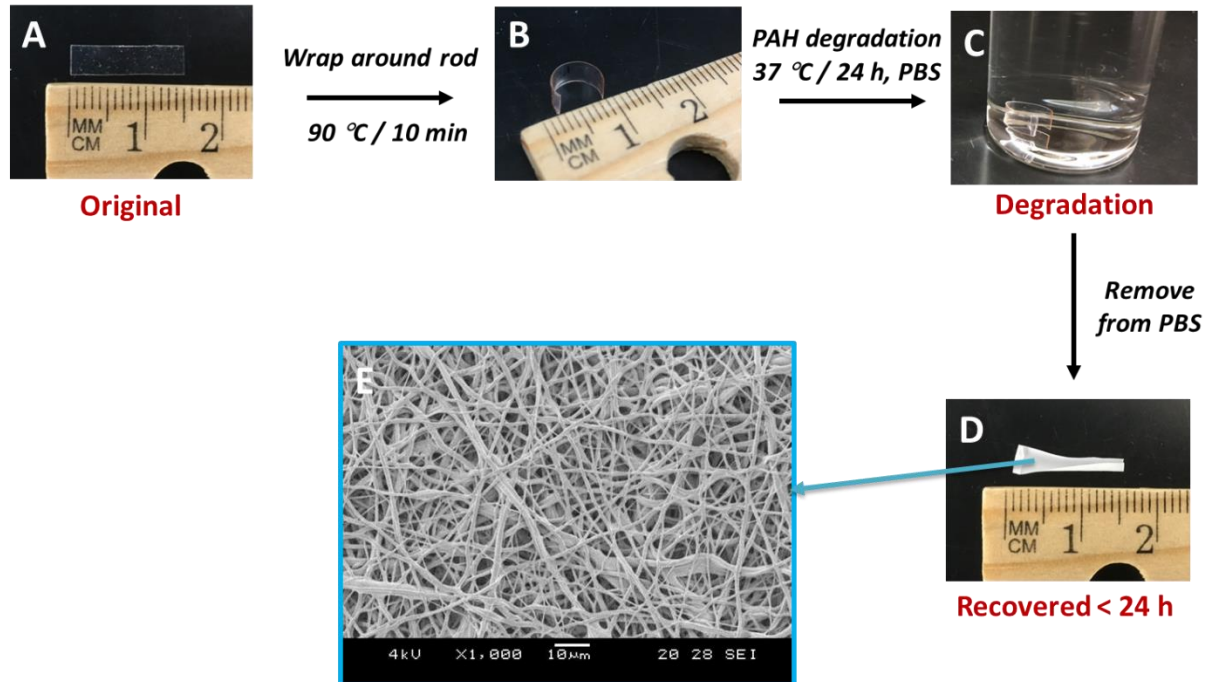


Figure 7-6. Sequence for attaining degradation-induced shape recovery for the electrospun Pellethane fibers imbibed in PAH composite showing: (A) original shape, (B) arbitrarily thermally programmed shape, (C) degradation of the newly shaped composite (D) recovery of the original shape following PAH matrix degradation, and (E) retention of fibrous morphology following degradation of the PAH matrix.

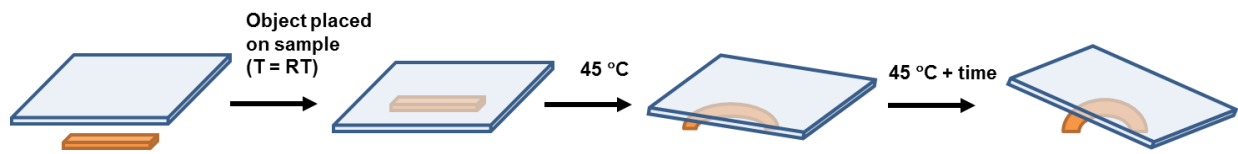


Figure 7-7. Time-lapsed mechanically programmed displacement of an object by the anisotropic PCL/epoxy composed of oriented PCL arranged orthogonally. A rectangular strip was topped with a glass cover slip and placed on a hot plate at 45 °C. As the mechanically programmed shape was thermally activated, the sample began to curl and lift the glass slide in under 30 s. The schematic above demonstrates the thermally activated sequence of free-standing object displacement by the sample shown below.

Appendix 1

Properties and Ballistic Performance of Epoxy-Based Thermoset-Thermoplastic Composites

A1.1 Background

An epoxy/(poly(ϵ -caprolactone) (PCL) composite previously developed by the Mather research group for triple shape memory properties has the potential to provide suitable mechanical properties with self-healing ballistic damage.¹⁻³ We contemplated that the addition of the more ductile, semicrystalline PCL phase to a brittle epoxy matrix may support energy dissipation during high strain rate impact, thus improving fracture resistance. Moreover, the temperature dependent moduli of this composite can be tuned through facile adjustment of the glass transition temperature of the epoxy phase was considered a practical utility. We were interested in studying the method of integrating PCL into the epoxy matrix as it can institute profoundly diverse structural characteristics. Given these possibilities, we were motivated to study the effect of varying the microstructural properties of the epoxy/PCL composite by altering the formulation and fabrication scheme such as by polymerization-induced phase separation (PIPS) or fibrous PCL coupled with epoxy imbibing.

A1.2 Experimental Methods

Materials

Poly(ϵ -caprolactone) (43,000 – 50,000 g·mol⁻¹) was purchased from Polysciences. Jeffamine D230 was purchased from Huntsman. Diglycidyl ether of bisphenol A (DGEBA) and neopentyl glycol diglycidyl (NDGE), poly(propylene glycol) bis(2-aminopropyl ether)

(Jeffamine® 230), tetrahydrofuran (THF), and dimethylformamide (DMF) were purchased from Sigma Aldrich. All materials were used as received.

Fabrication of Polymerization-Induced Phase Separation (PIPS) Composite

The mass ratios of the epoxy components were calculated according to a targeted glass transition temperature guided by the Gordon Taylor relation and prior model-fitting for this same system.² The Jeffamine D230 was calculated for stoichiometric equivalence of amine protons (four per D230 molecule) and epoxide rings (two each for DGEBA and NDGE). The PIPS composite was prepared by first melting DGEBA at 80 °C in an isothermal oven and combined with NDGE and PCL in a three-neck flask. The components were then stirred using an overhead motorized mixer (~150 rpm) at 60 °C under a nitrogen purge until a homogenous transparent mixture was observed. This was followed by degassing of the mixture under vacuum before cooling to 40 °C under continuous stirring. At this stage, the Jeffamine 230 was added and allowed to continue stirring under vacuum until homogenous, for approximately 10 min. The mixture was then immediately casted in stainless steel molds (6 in. x 6 in. x 0.25 in.) previously treated with Frekote 55NC release agent and pre-heated to the selected cure temperature; this was immediately followed by degassing under vacuum. The epoxy/PCL mixture was then cured at either 80 °C for 4 h, 90 °C for 4 h, 100 °C for 4 h, 130 °C for 2 h, 150 °C for 30 min. All batches were then post-cured at 120 °C for 2 h followed by 150 °C for 2 h. The nomenclature used herein to refer to the PIPS formulation is DXNYD230/PCLMWk(Z), X and Y summing to 100. This describes the weight fraction of DGEBA relative to NDGE as DX, and NDGE as NY. The designation “D230” denotes the Jeffamine 230 crosslinker. The terms “MW” and “Z” denote

the molecular weight and wt% of PCL relative to the epoxy. For example, D₄₁N₅₉D230/PCL45k(20) refers to crosslinked epoxy synthesized using 41 wt% DGEBA, 59 wt% NDGE and 20 wt% PCL. The chemical structures are presented in **Scheme A1-1**.

Fabrication of Laminated Electrospun PCL/Epoxy Composite

PCL fibers were electrospun (**Scheme A1-2A**) using a customized electrospinning system (Spraybase®, Profector Life Sciences, Dublin, Ireland). A 35 w/v % solution was prepared by dissolution of PCL in THF:DMF (4:1) and then transferred to the syringe ejection system equipped with three emitters, each fitted with blunt 22G needle tips. The needle tips were adjusted to a distance of 7 cm from the receiving drum and the PCL was electrospun at a rate of 1 ml h⁻¹ onto the drum rotating at 250 rpm with an applied voltage of 6.5 kV. Following electrospinning, the fiber mats were dried at room temperature under vacuum overnight to remove any residual solvents. The dried fiber mats were then cut into two squares of 5.375 in. x 5.375 in. and separately imbibed with an epoxy monomer mixture prepared using 55 wt % DGEBA, 45 wt % NDGE and stoichiometric Jeffamine D230 (described above), followed by exposure to vacuum at room temperature to complete infiltration of the monomer within the fiber mats by air removal (**Scheme A1-2B**). Excess monomer was manually removed from the surfaces and the two fiber mats were superimposed and fitted in an unheated stainless steel molds (6 in. x 6 in. x 0.25 in.) pre- treated with Frekote 55NC release agent. The sample was cured then at 40 °C for 48 h (below PCL melting transition) followed by a post cure of 90 °C for 24 h.

Cryogenic Treatment

Small-scale samples for x-ray diffraction and thermal characterizations were cryogenically treated by exposure to -60 °C for 5 min. Larger samples prepared for ballistics testing were cryogenically treated to induce crystallization of the PCL phase by placing in a freezer at -30 °C, which is above the PCL glass transition temperature, for approximately 72 h.

Scanning Electron Microscopy (SEM)

The morphology of the various formulations and cure conditions were assessed using SEM. All samples were sputter-coated (Denton Desk-5) with gold-palladium for 45 s using a current of 45 mA. A Hitachi S-4700 SEM was used to visualize the surfaces using an accelerating voltage of 1.0 kV. ImageJ software (version 1.46r, National Institutes of Health) was used to measure PCL fiber diameter. Fiber diameter measurements were determined by taking a minimum of 50 measurements at five different sites. The average diameter and standard deviation were calculated using a minimum of 250 total measurements.

The cross-sections of the samples were obtained by cryogenically fracturing then solvent removal of the PCL phase from the composite. A dogbone shaped sample was prepared and immersed in liquid nitrogen followed by fracturing of the narrow section. The cross-section surface was then treated with THF overnight to remove the PCL phase by molecular dissolution.

Thermal Characterization

Differential scanning calorimetry (DSC) was performed using a Discovery DSC manufactured by TA Instruments, Inc. Samples weighing 2.5 – 4.0 mg were sealed in Tzero aluminum pans and heated and cooled from -60 °C to 120 °C at 10 °C · min⁻¹ for each cycle.

Thermomechanical Characterization

A TA Instruments Q800 dynamic mechanical analyzer (DMA) was used in the multifrequency strain mode to measure the storage and loss moduli and tan delta. Samples were cut into rectangular strips, maintaining a 5:1 ratio of length to width. All samples were first cooled to -60 °C and held isothermally for 5 min followed by heating at 3 °C min⁻¹ to 100 °C.

X-Ray Diffraction

The crystalline structural properties of the composites were studied using both wide angle and small angle x-ray scattering (WAXS and SAXS). Wide-angle (WAXS) and small-angle (SAXS) x-ray scattering experiments were conducted to ascertain the molecular and nano-scale ordering and orientation of the various crosslinked polymeric samples. For this purpose, a Rigaku S-MAX3000 pinhole camera system was utilized, with a Micromax-007HF rotating anode source operating with Cu K α emission ($\lambda = 1.5406$), voltage of 40 kV and current of 20 mA. Wide-angle scattering patterns were collected at a sample-detector distance of 117 mm, as calibrated using corundum (NIST SRM 676a) and using Fujifilm image plates (CR HR-V) with a Raxia-Di Image Plate reader at a scan resolution of 100 μ m. Small angle scattering patterns were collected at a sample-detector distance of 1525 mm, as calibrated using silver behenate, on a 2D Multiwire Area Detector. Exposure times were 900 s for WAXS patterns and 600 s for SAXS patterns.

Ballistics Testing

Ballistic testing was conducted according to a previously established protocol.⁴ The sample was cut into squares of 62.5 mm x 62.5 mm x 6.4 mm (total of 12 per test group) and clamped between two aluminum plates with a circular aperture diameter of 50.8 mm. A witness plate composed of aluminum foil with a 0.0108 mm thickness was placed at a distance of 50.8 mm behind the target. A stainless steel ball bearing (Type 302) with a diameter of 5.56 mm and a mass of 0.69 g was discharged from a 22 caliber gas gun. The speed of the projectile was measured using a Doppler radar (BR-3502, Infnition, Inc.). Ballistic failure was defined as either when the projectile or a fraction of the sample penetrated the witness plate; therefore, ballistic failure can manifest without projectile penetration. The impact velocities were recorded and used to calculate the V_{50} ballistic limit, which represents the projectile velocity at which there is a 50 % probability for target failure. This value was calculated by taking the average of the top three highest passing and lowest failed impact velocities. The kinetic energy was then calculated from the V_{50} value ($KE = 0.5 m V_{50}^2$, where m is the mass of the projectile) and is reported.

A1.3 Preliminary Results

The morphological effect of increasing the PCL concentration in the PIPS blend composite was examined in **Figure A1-1**. At PCL concentrations of 20% and below, the microstructure comprised of a percolating epoxy rich matrix with regularly dispersed PCL droplets, which appeared to generally increase in diameter as the PCL fraction was increased. This microstructure was substantially altered when the PCL concentration was increased to 25 %, where the morphology of both phases became heterogeneous such that both the PCL and

epoxy mutually formed droplets and interconnected capillaries. At 30 % PCL, the epoxy transitioned into regularly dispersed spheres embedded within a continuous PCL matrix.

A cure study was conducted by varying the initial curing profile and maintaining the same post-cure conditions and formulation (D₅₅N₄₅D230/PCL45k(20)). The resulting PIPS composites exhibited increasing optical clarity as the cure temperature was increased, with apparent translucence occurring for cure temperatures of 100 °C to 150 °C (**Figure A1-2**). Cure temperatures greater than 150 °C resulted in visual degradation of the samples and were not studied further. This change in opacity was accompanied by a shift in morphology shown in **Figure A1-3**, from a distinct two phase microstructure containing spherical particles, which then appeared to coalesce when the cure temperature was increased to 100 °C and above. At higher cure temperatures, the morphology was smooth and homogenous, with no clear difference between curing at 130 °C and 150 °C. This was suggestive of PCL arrest in the amorphous state during higher epoxy crosslinking temperatures. This postulation was further supported by the thermal analyses in **Figure A1-4**, where PCL was markedly more crystalline for the cooler curing conditions below 100 °C; this microstructural state persisted even pursuant to a second heating cycle (**Figure A1-4C**), where the melting endotherm was substantially smaller and broader for the amorphous PCL, asserting that PCL may be suppressed from fully recrystallizing. Consequently, we hypothesized that a more aggressive crystallization protocol would enable PCL recrystallization and initiate nanoscale domains for high performance impact protection. A cure temperature of 130 °C was thus selected for further study due its ease of fabrication and reproducibility, with no significant difference in properties compared to the composite cured at higher temperatures. **Figure A1-5** summarizes the thermomechanical analyses, exposing that the

glass transition temperature decreased as the curing temperature was increased. The target T_g was 45 °C, which was attained using the original cure profile (80 °C). We attributed this plasticization effect to the highly dispersed PCL within the epoxy matrix, which while in an amorphous state, mediated greater epoxy chain mobility.

Cryogenically treating the D₅₅N₄₅D230/PCL45k(20) PIPS samples cured at 130 °C corroborated our hypothesis when a significant increase in crystallization materialized, as revealed by the DSC thermograms in **Figures A1-6** and **A1-7**. This observation demonstrated high reproducibility across several synthesis batches. A comparison of the samples by WAXS (**Figure A1-8**) verified the amorphous nature of PCL at greater curing temperatures which then became more crystalline following cryogenic exposure by observing that the ring pattern becomes sharper and additional peaks are liberated in the scattering profile (**Figure A1-9**). The SAXS data in **Figures A1-10** and **A1-11** similarly confirm these elucidations, indicating long range order of the cryogenically induced PCL lamellae formation.

The ballistic performance presented in **Figures A1-12** and **A1-13** was significantly improved by the addition of PCL to the epoxy matrix, in comparison to the neat epoxy, which resulted in complete penetration of the projectile with radial cracks. A comparison of the epoxy/PCL PIPS compositions showed that increasing glass transition, by addition of the aromatic diepoxide (DGEBA), aided in withstanding greater impact; however, this gain in KE₅₀ was also made by simply curing the composite at a higher temperature. Interestingly, these higher cure samples had a tendency to capture the projectile without crack initiation. The highest KE₅₀ value (V_{50} of 293 m s⁻¹) of this series was attained by the cryogenically treated, high cure sample, though this provided only a marginal improvement beyond the untreated samples.

Further investigation is warranted to gain additional insight into the fraction mechanism differences relative to the microstructural properties observed in this work.

Lastly, a fiber reinforced epoxy matrix was prepared by combining two layers of electrospun non-woven PCL fibers within the crosslinked epoxy. The electrospun PCL fibers were randomly oriented with an average fiber diameter of $2.4 \mu\text{m} \pm 0.8 \mu\text{m}$ (**Figure A1-14**) and a resulting thickness of ~ 2.8 mm. Preliminary ballistics testing conducted on a limited number of samples revealed complete penetration of the projectile with radial cracking and fragmental delamination between the fiber mats (**Figure A1-15**); we postulated that this failure was likely due to entrapped air pockets between laminae, which can be improved through optimization of the fabrication process. The estimated KE_{50} value was $16 \text{ kg m}^2 \text{ s}^{-2}$ (based on a $V_{50} \sim 215 \text{ m s}^{-1}$), though more trials were needed to support this calculation. These results were a slight improvement over the neat epoxy samples, though not as resilient as those prepared by PIPS.

A1.4 Conclusions & Future Directions

In this work, the effect of the microstructural properties of an epoxy/PCL composite on ballistic performance was investigated. Increasing the weight fraction of PCL in the PIPS blend was shown to impart significant morphological changes. We determined that increasing the temperature of the cure of this epoxy/PCL PIPS composite affected optical clarity and considerably inhibited the formation of crystalline domains, while also having a plasticizing effect. The addition of PCL to the crosslinked epoxy significantly improved ballistic performance, where samples formulated with a greater glass transition temperature, and those processed with highly dispersed PCL cryogenically induced crystallized domains showing greatest improvements. The ballistic results for electrospun PCL imbibed within crosslinked

epoxy were not as satisfactory as the blended samples; however, additional process optimization is merited. The thermally triggered self-healing of the blends can be studied to ensure preservation of mechanical properties following impact by a ballistics projectile. The cure effect described here can also be investigated for other PIPS formulations, with determination of rheological constraints. Transmission electron microscopy can be employed to examine the morphological transitions affected by curing parameters in greater detail. Finally, characterization of the mechanical properties such as tensile stress-strain and fracture toughness can be conducted.

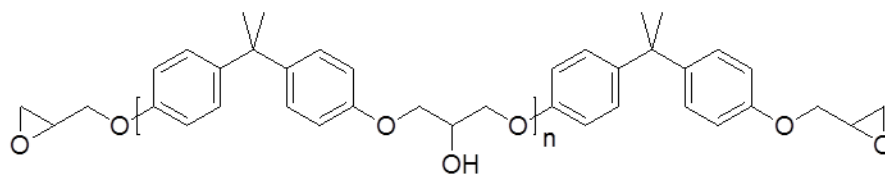
A1.5 Acknowledgements

This work was conducted at the Army Research Laboratory (ARL) in Aberdeen Proving Ground, MD, in collaboration with Dr. Joseph L. Lenhart of the Macromolecular Science and Technology Branch (ARL/MTSB) in the Weapons and Materials Research Directorate. The SEM imaging was conducted by Dr. Eric Laird (ARL) and ballistics testing by Dr. Jian H. Yu (ARL). Dr. Patrick T. Mather conducted all x-ray scattering characterizations. Dr. Rick Beyer of ARL/MSTB is acknowledged for assistance and discussion concerning x-ray scattering measurements.

A1.6 References

1. Nejad, H. B., Garrison, K. L. & Mather, P.T. Comparative analysis of shape memory-based self-healing coatings. *Journal of Polymer Science Part B: Polymer Physics* **54**, 1415 (2016).
2. Luo, X. & Mather, P. T. Triple-shape polymeric composites (TSPCs). *Advanced Functional Materials* **20**, 2649 (2010).

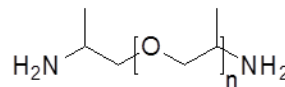
3. Torbati, A. H., Nejad, H. B., Ponce, M., Sutton, J. P. & Mather, P. T. Properties of triple shape memory composites prepared via polymerization-induced phase separation. *Soft Matter* **10**, 3112 (2014).
4. V50 ballistic test for armor MIL-STD-662F Standard. *US Department of Defense* (1997).



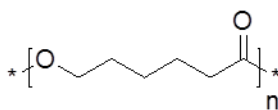
Diglycidyl ether of bisphenol A (DGEBA)



**Neopentyl glycol diglycidyl ether
(NDGE)**



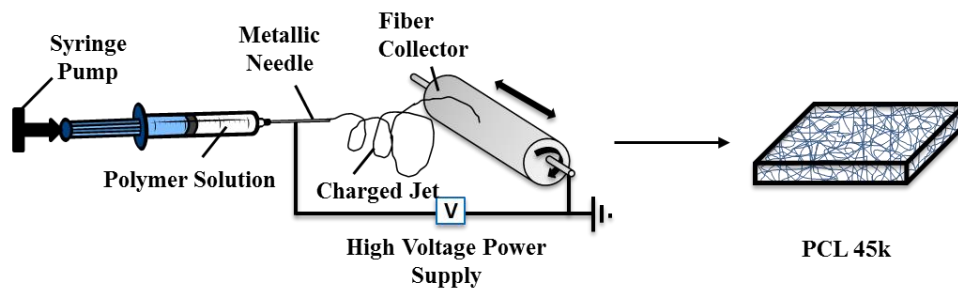
Jeffamine D230



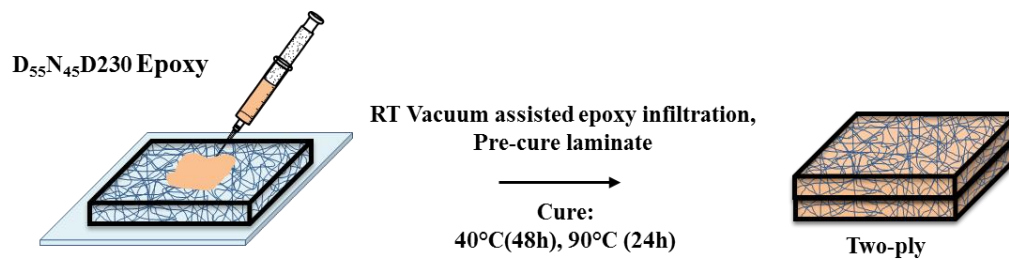
Poly(ε-caprolactone)

Scheme A1-1. Chemical structures used to synthesize epoxy-PCL composites.

A



B



Scheme A1-2. (A) Electrospinning of PCL and (B) subsequent preparation of epoxy imbibed laminated PCL fiber mats .

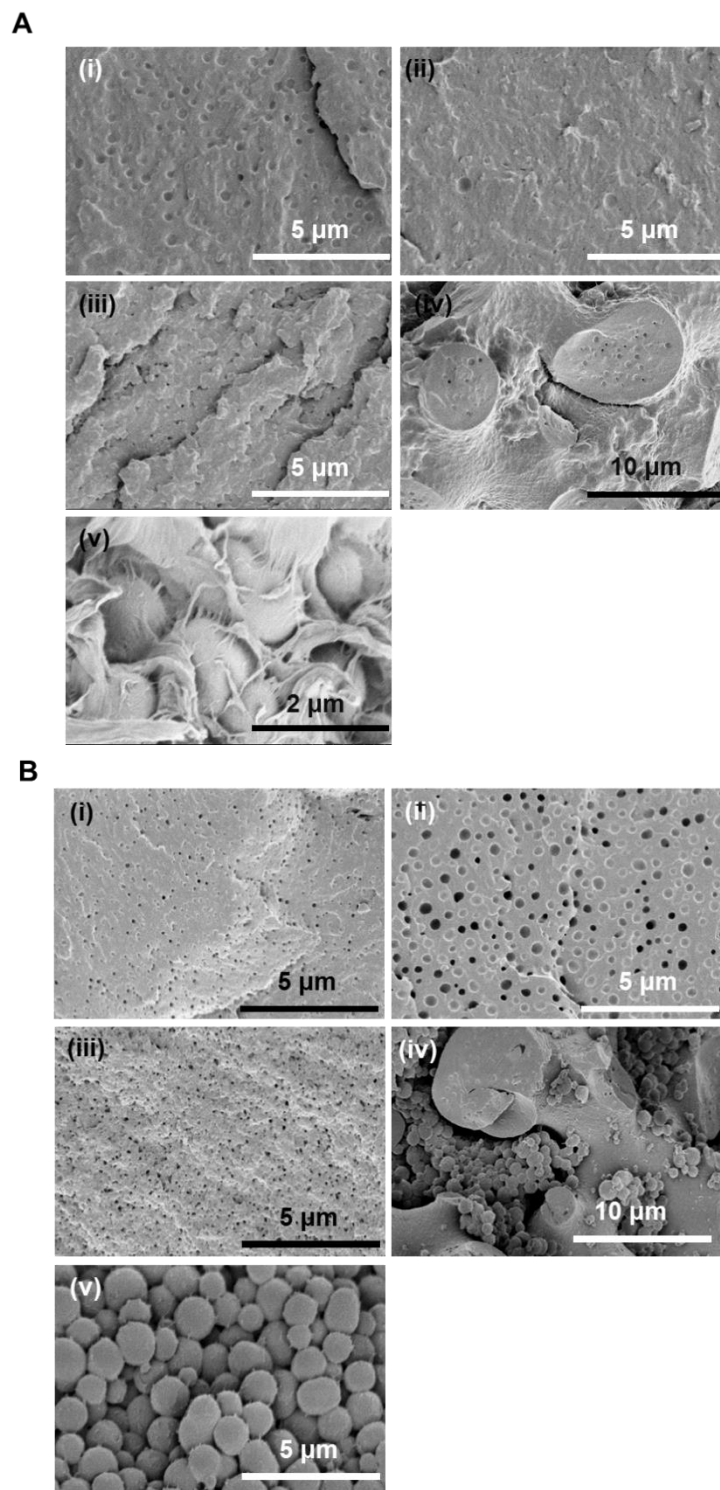


Figure A1-1. Microstructure of varying PCL concentration in $D_{62}N_{38}D230/PCL45k$ as revealed by SEM of both (A) as fabricated and (B) post-etching of PCL, for (i) 10 %, (ii) 15 %, (iii) 20 %, (iv) 25 %, (v) 30 %. The scale bar represents 5 μm .

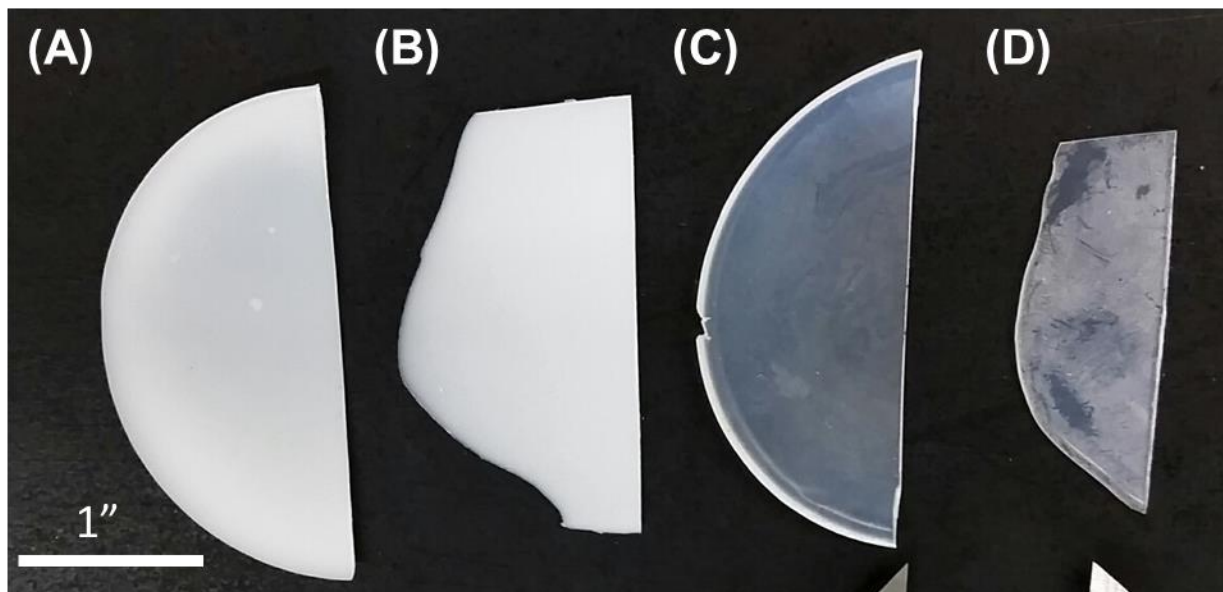


Figure A1-2. Photographs of cure temperature effect on appearance of $D_{55}N_{45}D230/PCL45k(20)$ for an initial cure temperature of (A) 80 °C, (B) 90 °C, (C) 100 °C, (D) 130 °C.

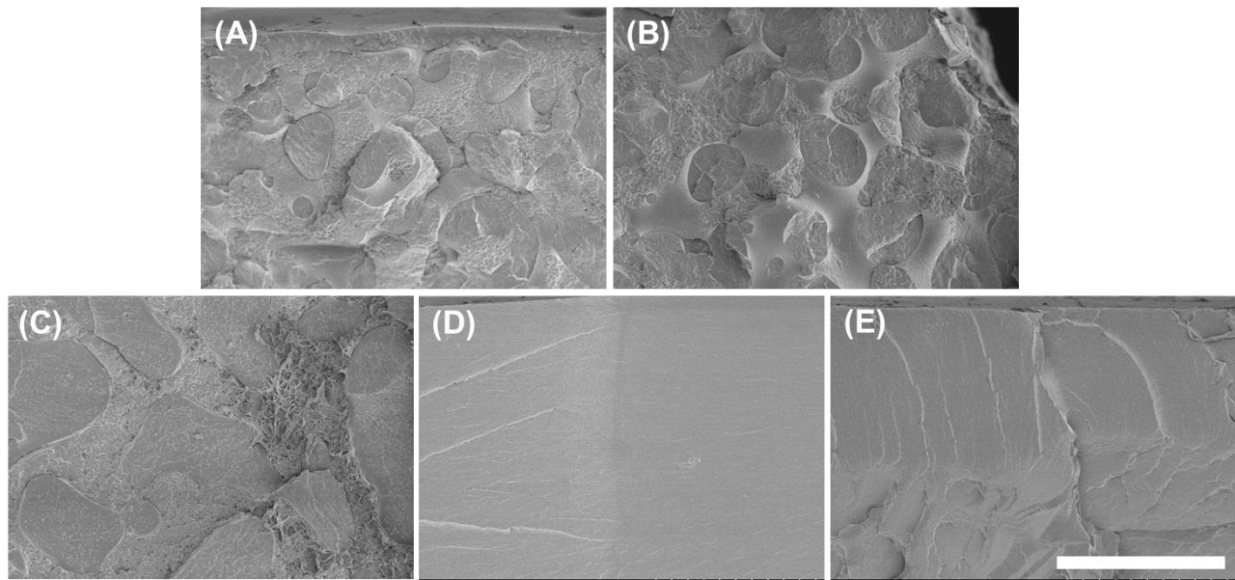
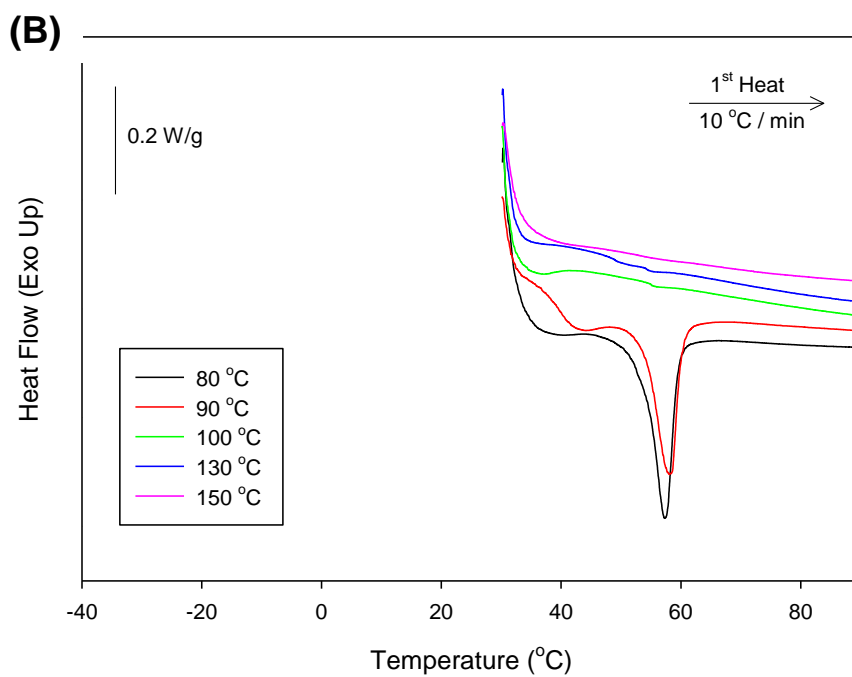
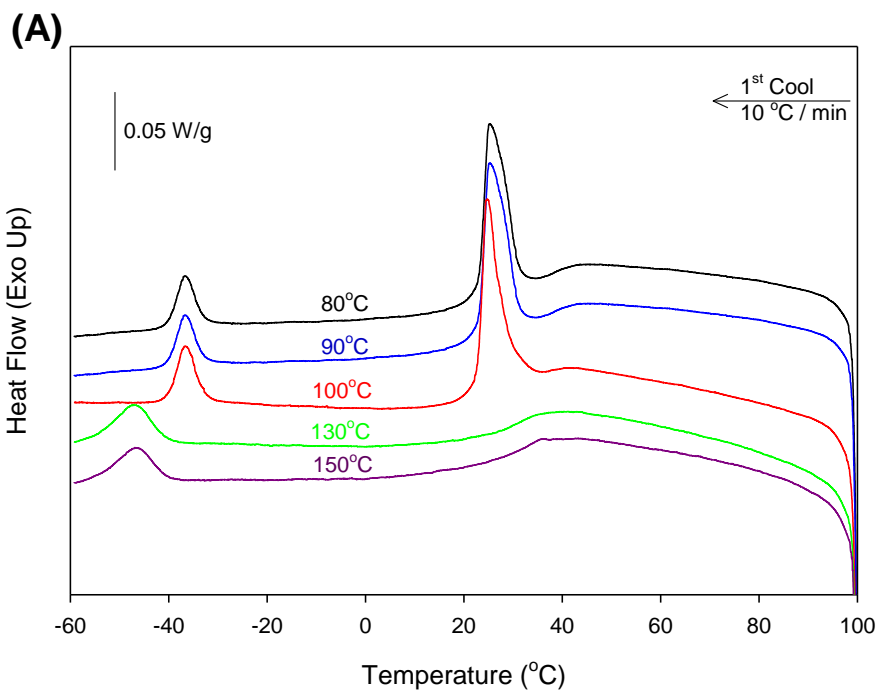


Figure A1-3. Microstructure of $D_{55}N_{45}D230/PCL45k(20)$ cross-sections as revealed using SEM for initial cure temperature of: (A) 80 °C, (B) 90 °C, (C) 100 °C, (D) 130 °C, (E) 150 °C . The scale bar represents 50 μm .



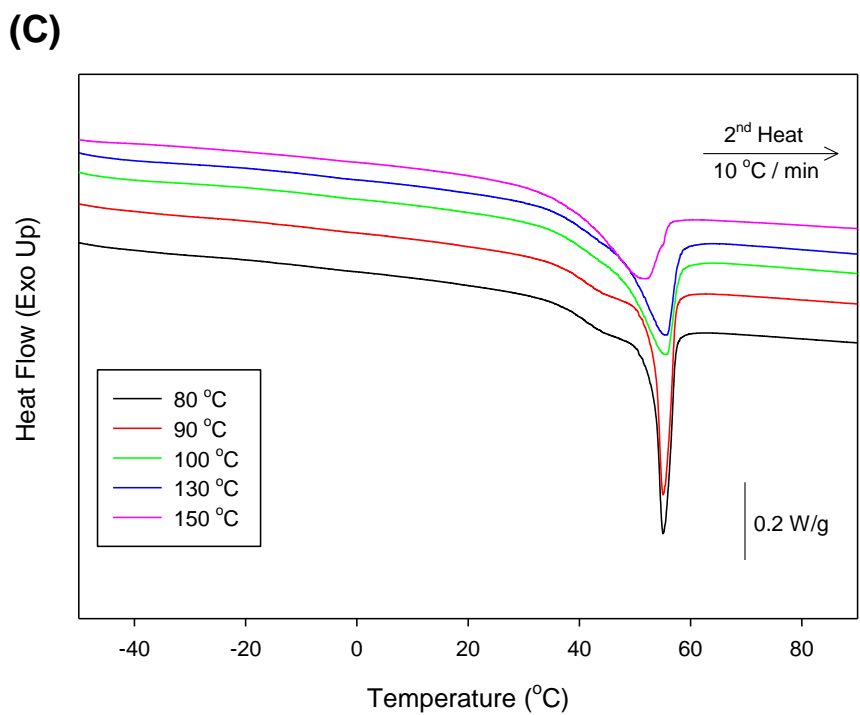
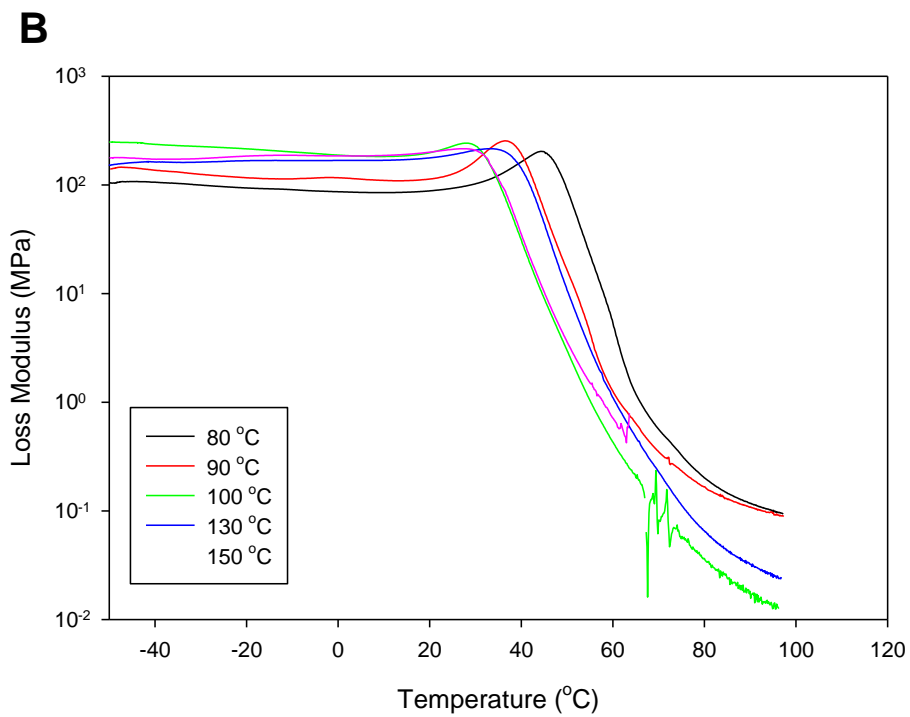
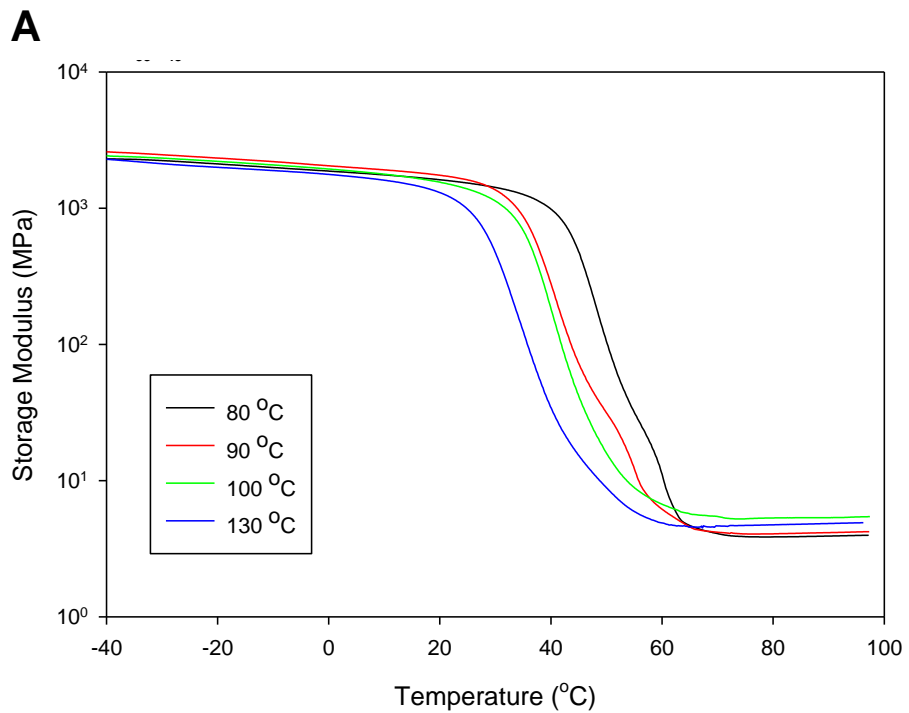


Figure A1-4. DSC characterization of D₅₅N₄₅D230/PCL45k(20) at various cure temperatures demonstrating that PCL becomes more amorphous with increased cure temperature for the (A) first cool, (B) first heat, (iii) second heat cycles.



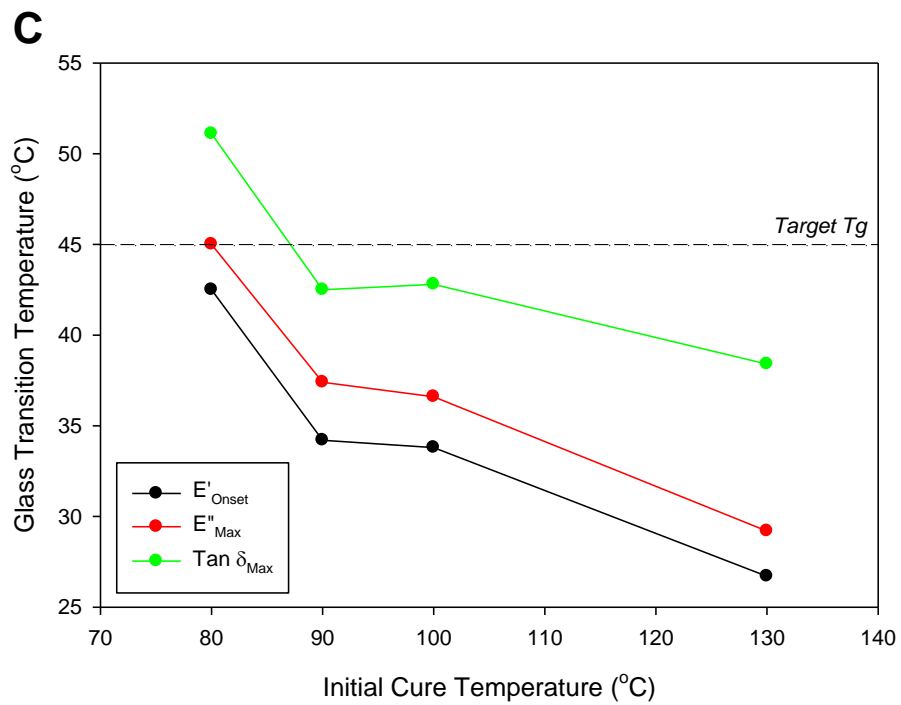


Figure A1-5. DMA characterization of D₅₅N₄₅D230/PCL45k(20) showing (A) the storage moduli, (B) loss moduli at various cure temperatures. The plot is (C) shows that the glass transition temperature decreased with increased cure temperature.

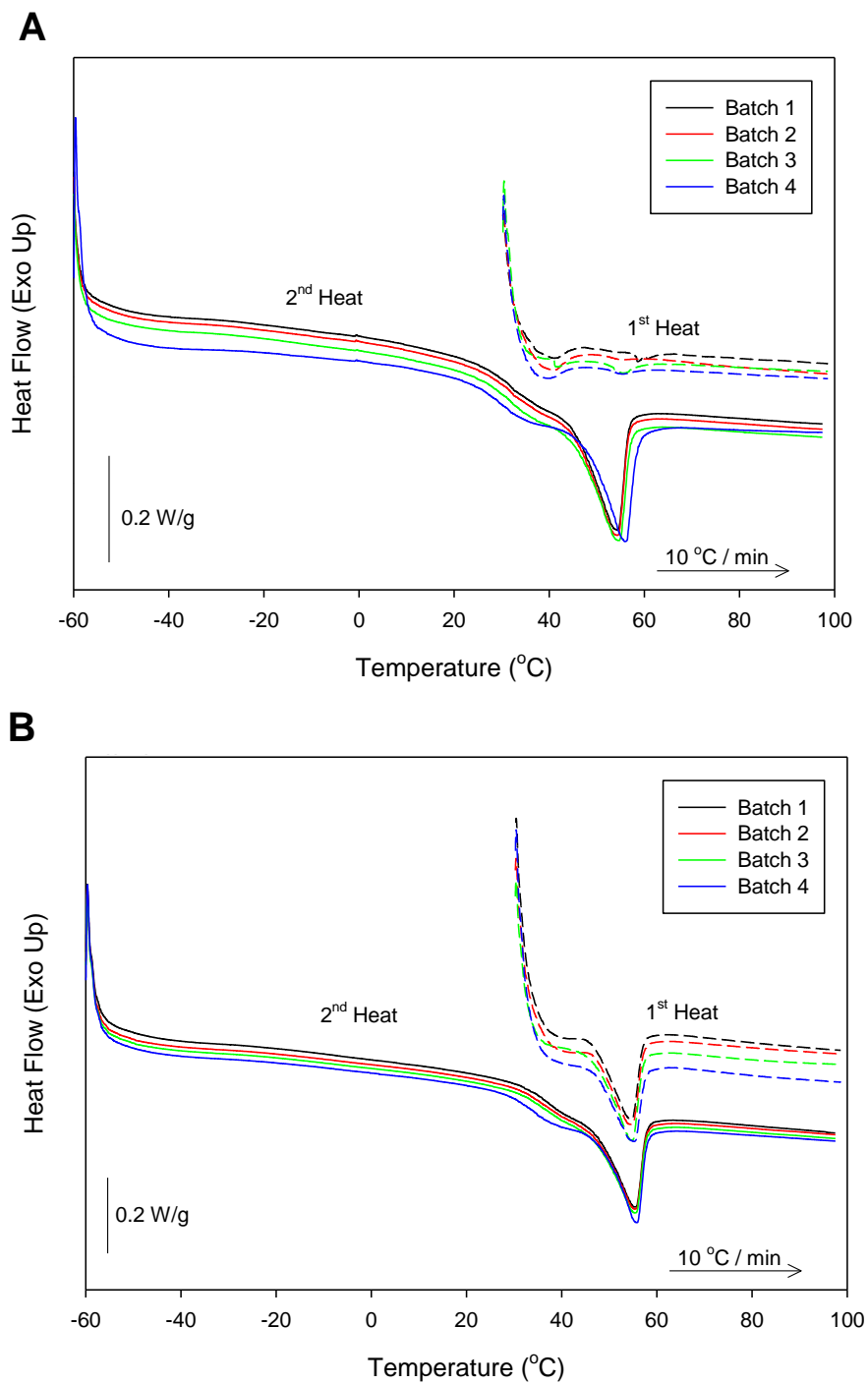


Figure A1-6. DSC first and second heat characterizations of D₅₅N₄₅D230/PCL45k(20) (A) before and (B) after cryogenic treatment and demonstrating reproducibility across synthesis batches.

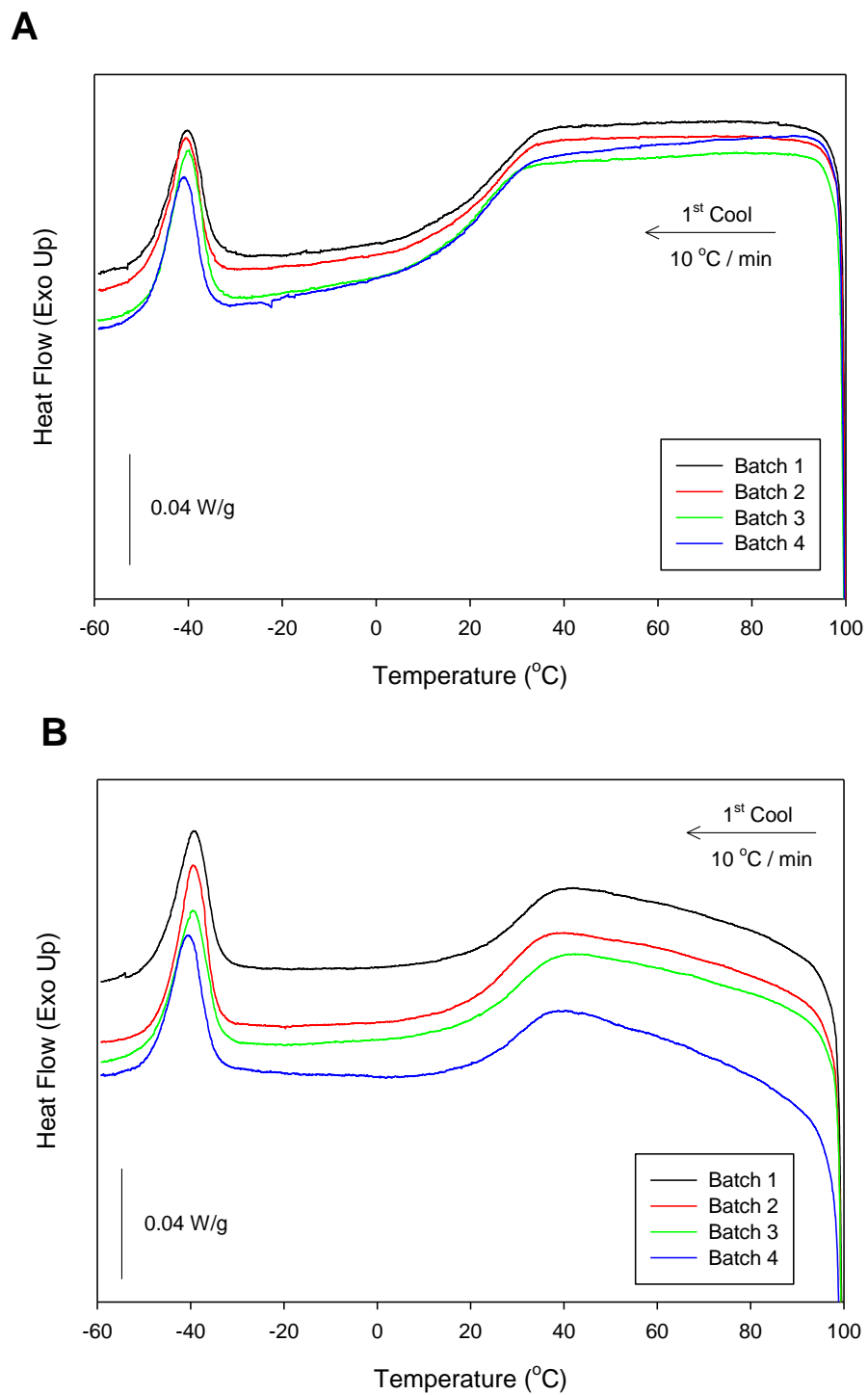


Figure A1-7. DSC first cooling characterizations of $D_{55}N_{45}D_{230}/PCL_{45k(20)}$ (A) before and (B) after cryogenic treatment and demonstrating reproducibility across synthesis batches.

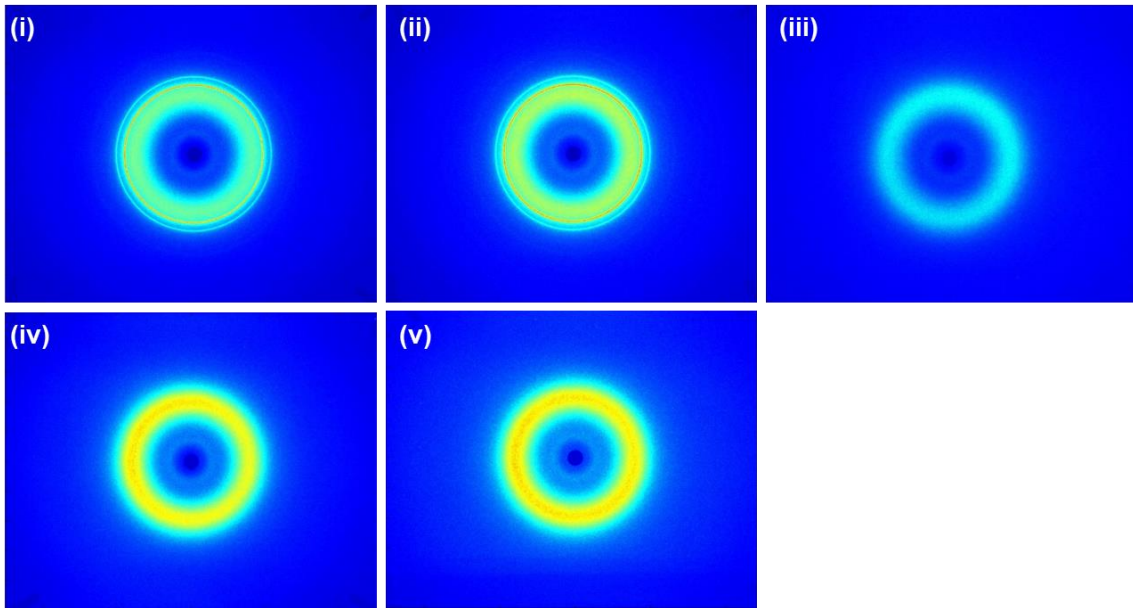
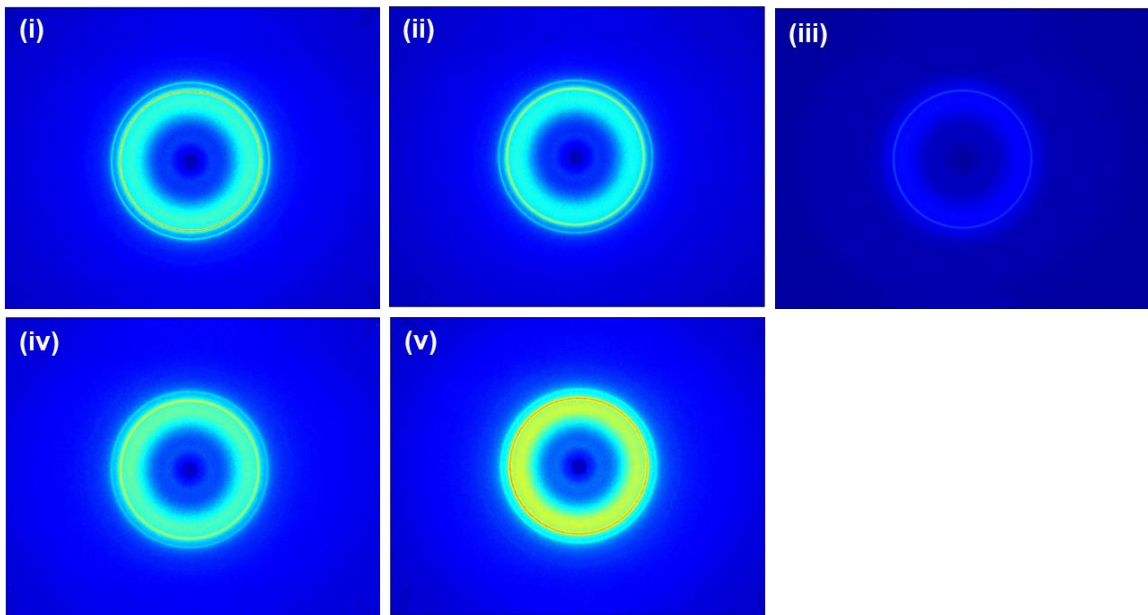
A**B**

Figure A1-8. Microstructure of $D_{55}N_{45}$ D230/PCL45k(20) as revealed using WAXS for the composite (A) as-cured and (B) cryogenically treated, for an initial cure temperature of: (i) 80 °C, (ii) 90 °C, (iii) 100 °C, (iv) 130 °C, (v) 150 °C.

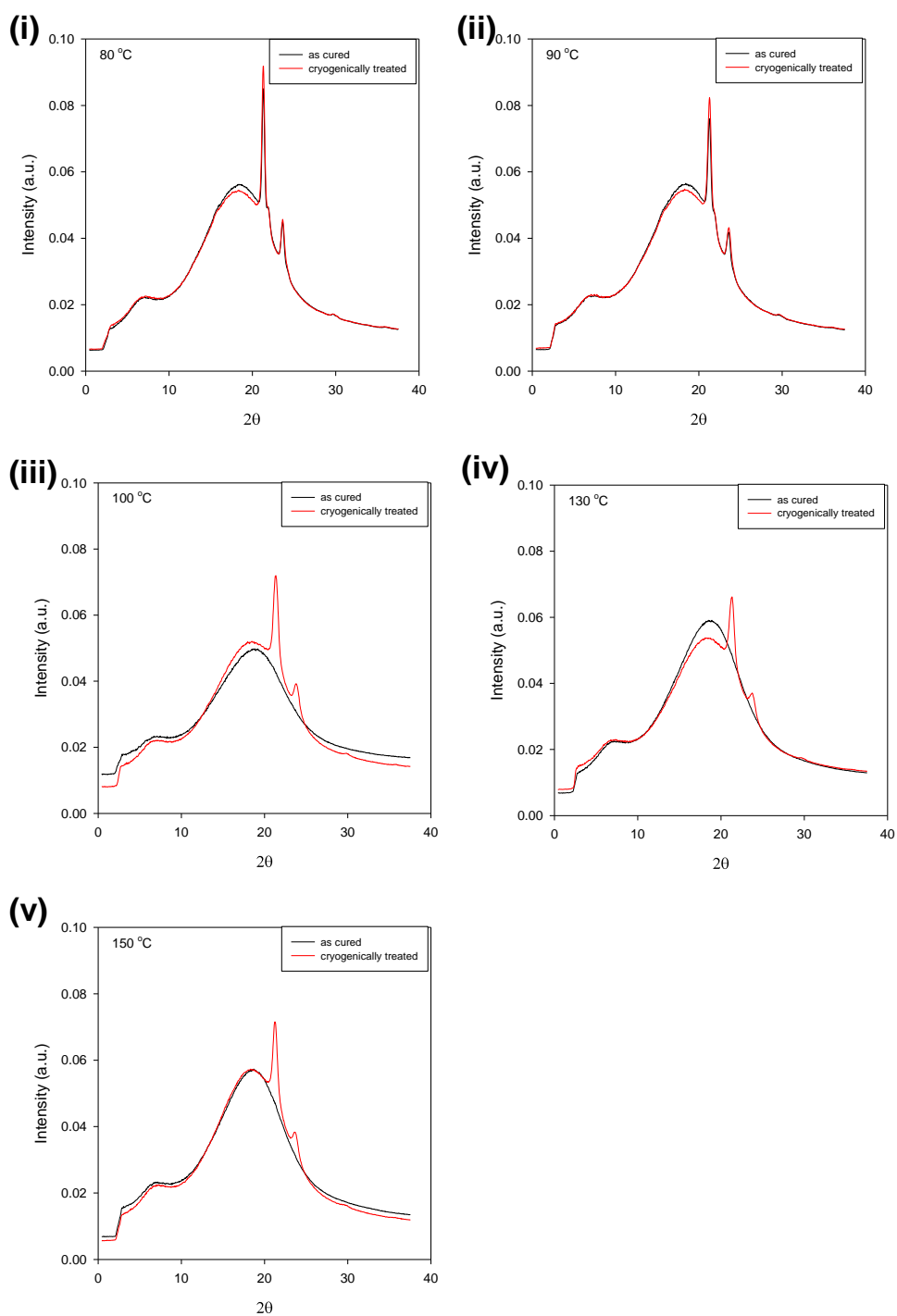


Figure A1-9. WAXS diffractograms revealing crystalline peaks for the $D_{55}N_{45}D_{230}/PCL_{45k(20)}$ the composite comparing both as-cured (black trace) and cryogenically treated (red trace), for an initial cure temperature of: (i) 80 °C, (ii) 90 °C, (iii) 100 °C, (iv) 130 °C, (v) 150 °C.

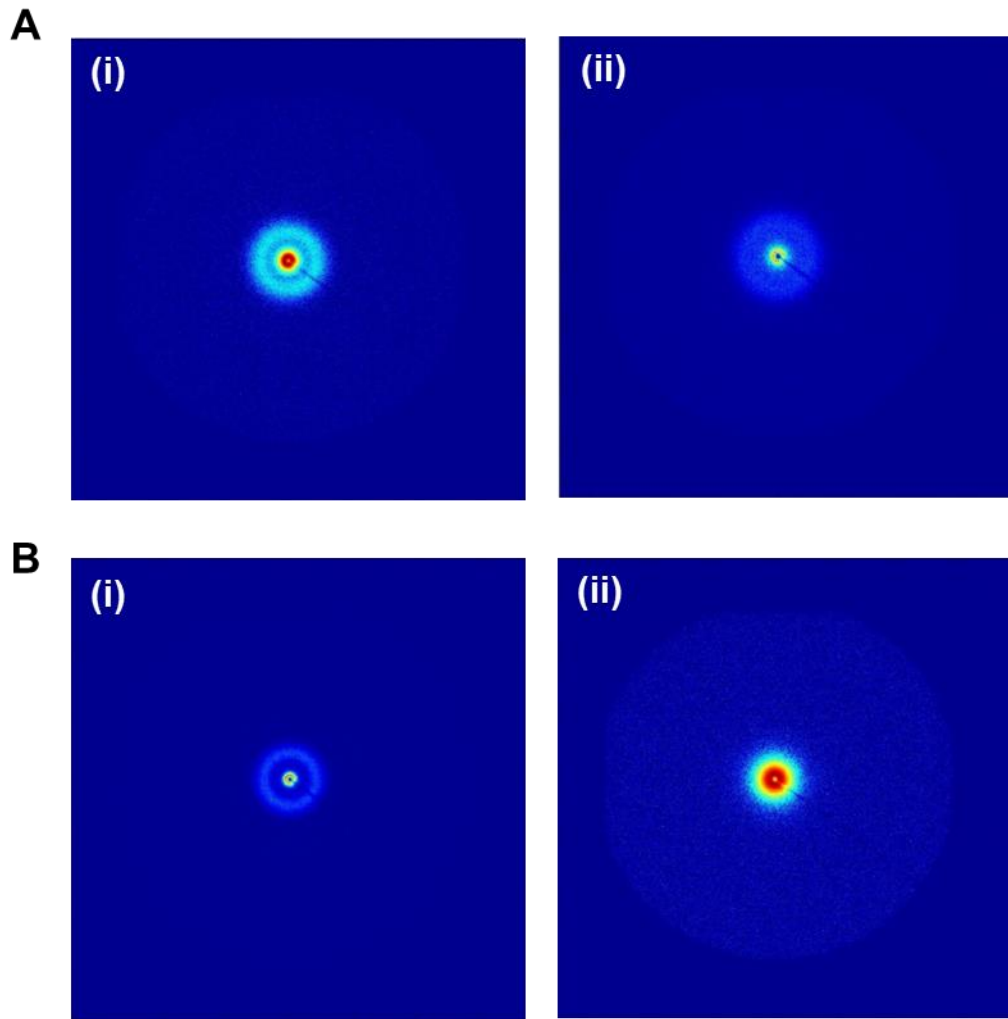


Figure A1-10. Effect of post-cure cryogenic treatment of $D_{55}N_{45}D230/PCL45k(20)$ as revealed using SAXS for the composite (A) as-cured and (B) cryogenically treated, for an initial cure temperature of: (i) 80 °C, (ii) 130 °C.

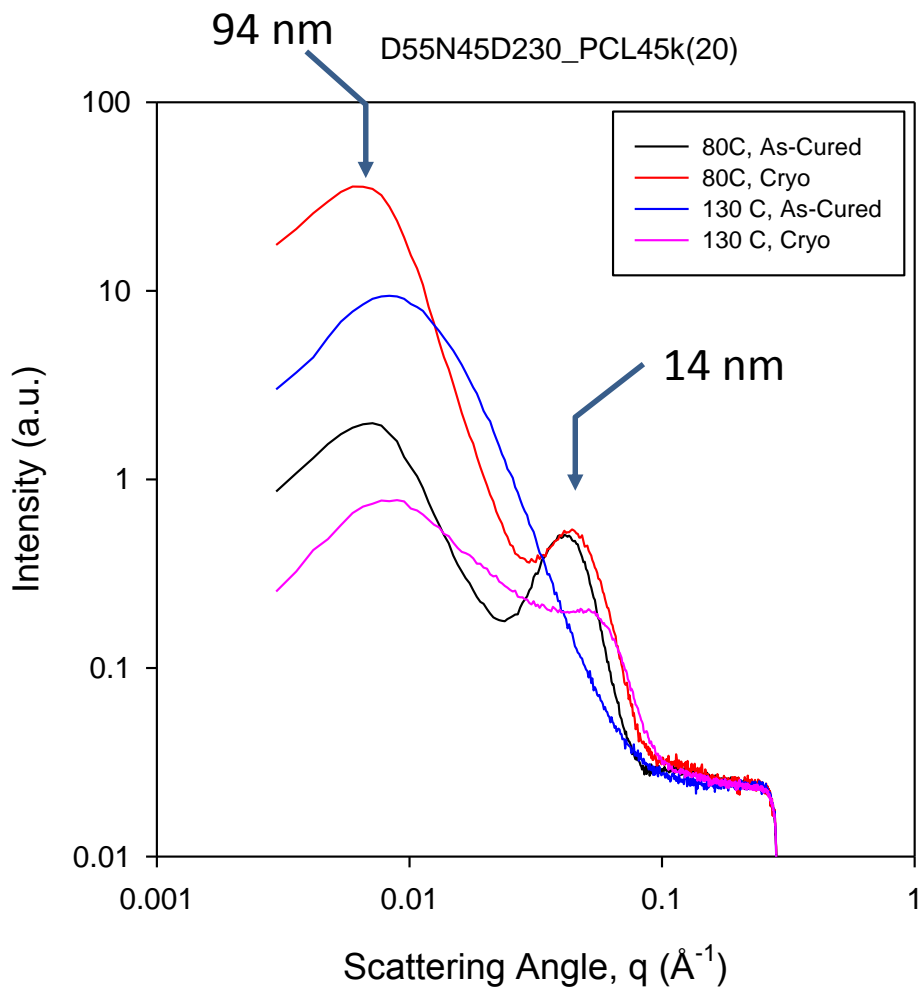


Figure A1-11. WAXS diffractograms comparing crystalline peaks for the D₅₅N₄₅D230/PCL45k(20) before and after cryogenically treatment.

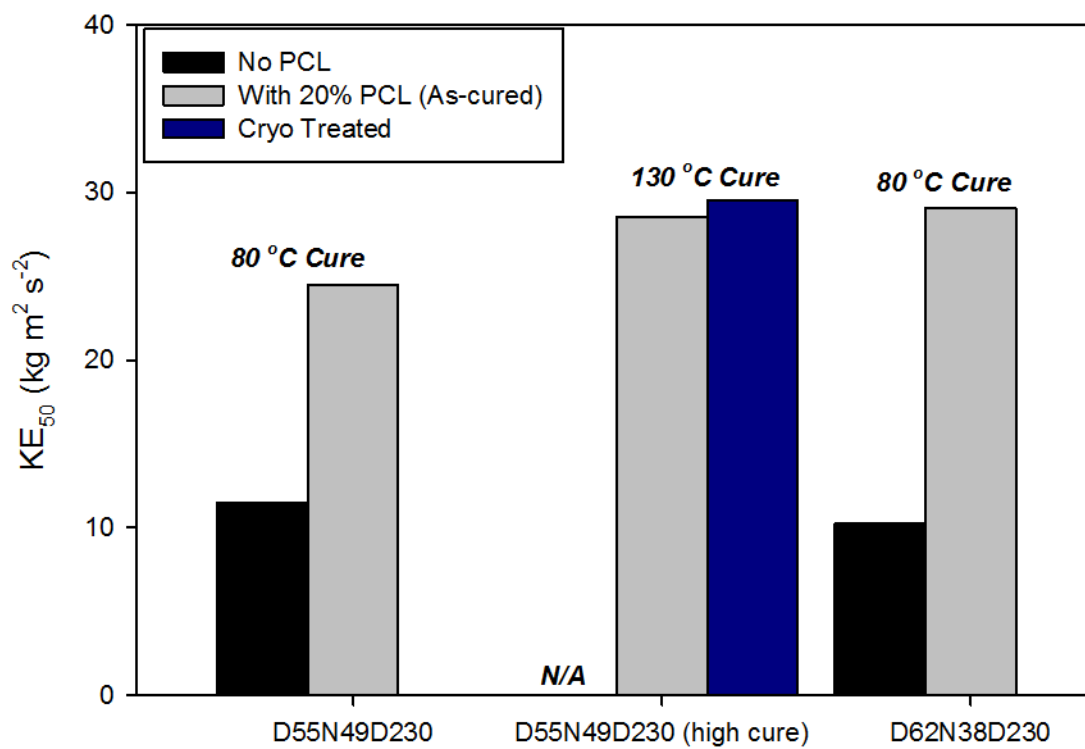


Figure A1-12. Ballistic results of the $D_{55}N_{45}D_{230}$ $D_{62}N_{38}D_{230}$ formulations synthesized with and without 20 % PCL at two different cure temperatures. The cryogenically treated sample is also included for comparison.

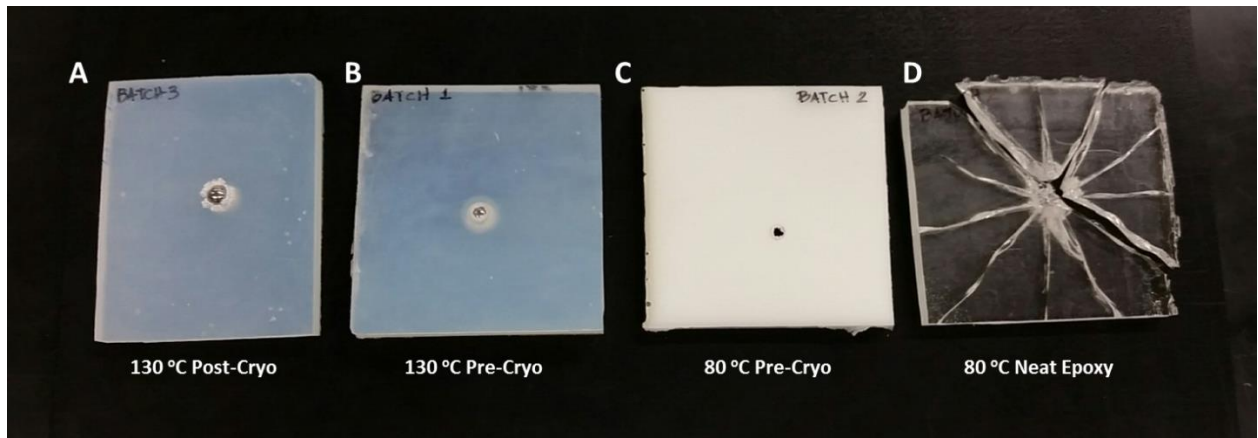


Figure A1-13. Photographs following ballistic testing of $D_{55}N_{45}D_{230}/PCL_{45k}(20)$ for cure at (A) at 130 °C, (B) 130 °C post-cryo, (C) 80 °C, and (D) untreated neat epoxy, cured at 80 °C.

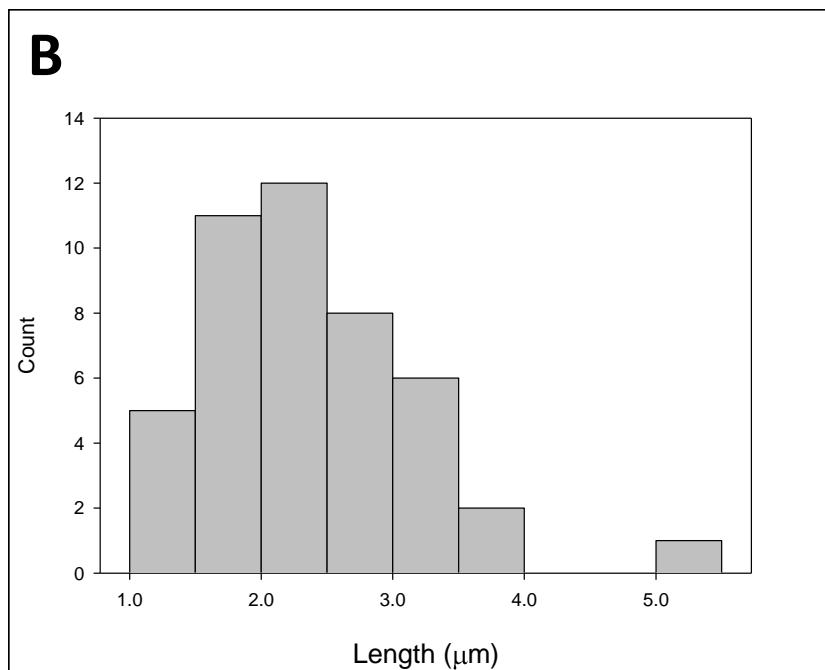
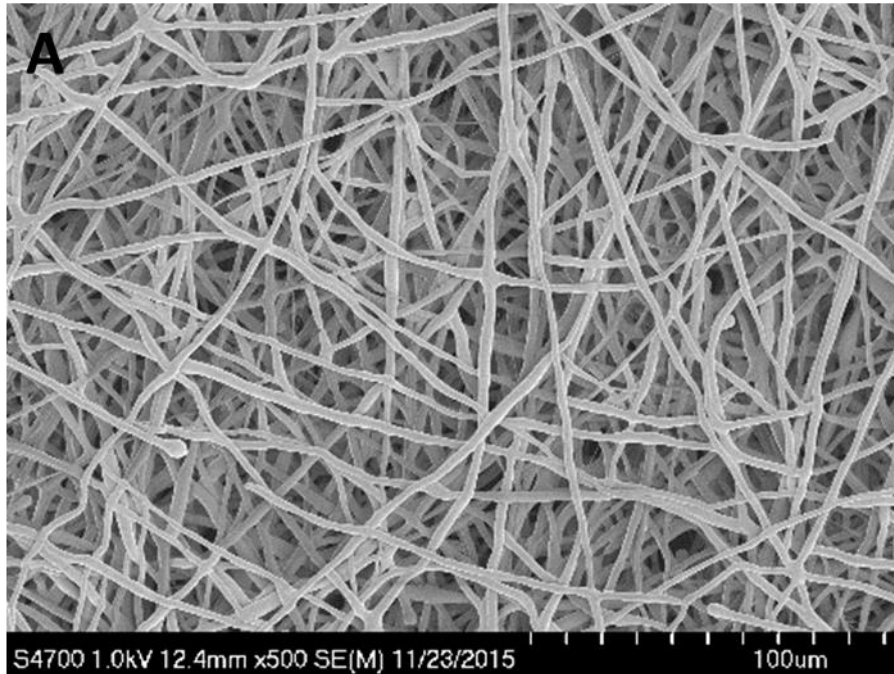


Figure A1-14. SEM micrograph of (A) electrospun PCL45k and (B) resulting fiber diameter distribution.

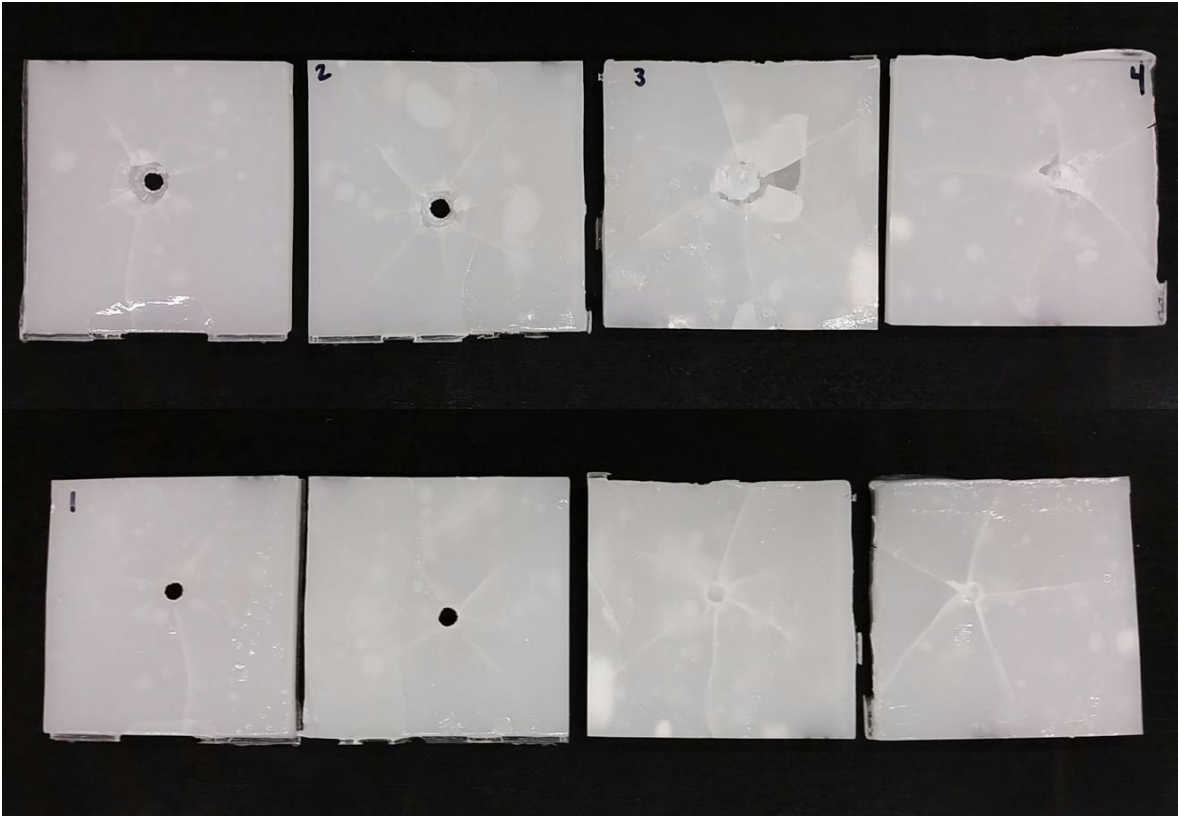


Figure A1-15. Photographs following ballistic testing of laminated epoxy/PCL composites prepared using electrospun PCL fibers for the same sample group with the reverse side of the top row shown in the bottom row.

VITA

NAME OF AUTHOR: Melodie I. Lawton

PLACE OF BIRTH: New York, NY, USA

EDUCATION:

B.S. in Chemical Engineering, Polytechnic University (2004)

M.S. in Materials Science and Engineering, Rochester Institute of Technology (2010)

Ph.D. in Bioengineering, Syracuse University (2018)

SELECTED PUBLICATIONS AND PRESENTATIONS:

Lawton, M. I., Tillman, K. R., Mohammed, H. S., Kuang, W., Shipp, D. A., Mather, P. T., "Anhydride-Based Reconfigurable Shape Memory Elastomers," *ACS Macro Lett.* (2016), 5, 203-207.

Lawton, M. I. and Mather, P. T., "Controlled Drug Delivery of a Hydrophilic Drug Model from a Fibrous Elastomeric Composite with Shape Memory Properties," *Proceedings of the Annual Technical Conference & Exhibition Society of Plastics Engineers* (2015), ISBN: 978-0-9850112-7-7, pp. 2370-2374.

Lawton, M. I., and Mather, P. T., *Anisotropic Triple Shape Memory Polymers*. 252nd American Chemical Society National Meeting & Exposition, POLY: Advanced Functional Biopolymers & Biomaterials, Philadelphia, PA, August 24, 2016.

Lawton, M. I., Tillman, K. R., Mohammed, H. S., Kuang, Wenbin, Shipp, D.A., Mather, P. *Biodegradable Anhydride-Based Reconfigurable Shape Memory Elastomer*. World Biomaterials Congress, Montreal, Quebec, Canada, May 18, 2016.

Lawton, M. I. and Mather, P. T. *Controlled Drug Delivery of a Hydrophilic Drug Model from a Fibrous Elastomeric Composite with Shape Memory Properties* SPE ANTEC, Orlando, Florida, March 24, 2015.

(Formerly published as Melodie I. Torres)

Torres, M. and Santhanam, K.S.V., "Quality Control of Silicone Hydrogel Contact Lenses by Impedance Spectroscopy," *Materials Research Society Proceedings* (2014) doi:10.1557/opl.2014.201.

Torres, M.I., Onyejekwe, I.U., Finkelstein, E.B., Maier, K.G., Gahtan, V., Mather, P.T. *A Biomimetic Approach to Developing Anti-Thrombotic Small Caliber Prosthetic Vascular Grafts*. Arteriosclerosis, Thrombosis and Vascular Biology 2014, Toronto, Ontario, May 2, 2014 (poster).